

540
BA1

T327

COMPUTATIONAL STUDIES OF THE PROPERTIES OF BARE AND ZEOLITE SUPPORTED GOLD CLUSTERS

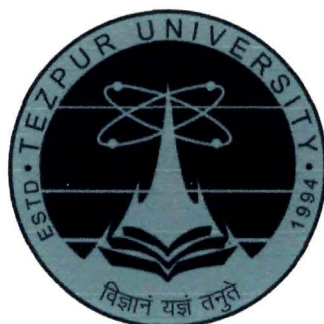
A thesis submitted in partial fulfillment of the
requirements for the degree of

Doctor of Philosophy

by

Subhi Baishya

Registration No. 038 of 2010



Department of Chemical Sciences

School of Sciences

Tezpur University

NAPAAM, TEZPUR - 784028

ASSAM, INDIA

December, 2014

Dedicated To..

Ma & Deuta

COMPUTATIONAL STUDIES OF THE PROPERTIES OF BARE AND ZEOLITE SUPPORTED GOLD CLUSTERS

Abstract

With its alluring golden yellow hue, gold has fascinated mankind since ages, mostly for its widespread use in jewellery. In addition, it finds application in numerous fields ranging from investment and monetary exchange, electronics, dentistry, medical and chemical field, aerospace industry and as a symbol of status. Gold possess excellent properties that it does not tarnish on exposure to atmosphere and retains its beautiful lustre undiminished for years. Its resistance to oxidation and corrosion in air as well as its chemical inertness towards various reactions contributes largely to the noble behaviour of gold.

However, the nobility diminishes when bulk gold is reduced to the nano dimension, thereby making it one of the excellent catalysts for reactions such as low temperature CO oxidation, direct formation of hydrogen peroxide etc. This makes the study of gold particularly interesting. The use of nanogold dates back to ancient ages and the most famous example is the Lycurgus Cup which was manufactured in the 5th to 4th century B.C and is now exhibited in the British Museum. In 1857, the legendary work of Michael Faraday on the formation of deep red solutions of colloidal gold by reduction of an aqueous solution of chloroaurate AuCl_4^- using phosphorus was the first scientific investigation on finely divided gold. Since, then synthesis and application of gold nanoparticle in fields of catalysis, biological labelling, optical and electronic devices etc have been steadily growing.

The earliest report on the use of gold as a catalyst dates back to 1906 when Au gauzes were reported as catalysts for H₂ oxidation. The work of Bone and Andrew in 1925 is one of the earliest reference where Au had been reported as catalyst for CO oxidation. Years later, Huber *et al.* in 1977 reported CO oxidation on Au atom based model and attempted to interrelate the results with actual heterogeneous oxidations of CO to CO₂. In the subsequent years, pioneering work of Haruta *et al.* demonstrated the catalytic activity of transition metal oxide supported ultrafine gold towards low temperature CO oxidation. This opened up new dimension towards catalytic activity of supported gold clusters. The catalytic activity has been attributed to various physico-chemical parameters such as cluster size of gold particles, morphology, site-specificity and electronic state of gold clusters. Small gold particles differ significantly from the bulk due to the presence of low coordination atoms and the adoption of geometries which lead to more reactive electronic structures. Thus, catalytic properties of gold nanoparticles can be attributed partly to their geometric structures. Modification of the electronic properties by the support has been considered as an important factor in supported gold clusters.

The concept of single atom catalysis has recently gained impetus in the field of contemporary catalytic research so as to maximize the efficiency of metal utilization. It is believed that catalysts with well-defined single active centres are necessary to understand the catalytic mechanisms better unlike the multiple active sites of subnanoclusters which are not always the most desirable centres for catalytic processes. Single atom catalysts have evolved as an effective way to utilize each and every metal atom of supported metal clusters.

In this thesis, we have employed density functional theory to explore the catalytic activity of neutral and charged gas phase gold clusters towards CO oxidation. Further, the catalytic activity of zeolite sup-

ported neutral and charged gold monomer towards CO oxidation and water gas shift reaction has been studied with hybrid DFT method. The adsorption of CO and O₂ on zeolite supported Au and the effect of the presence of moisture on their adsorption has been investigated. We also explore the structure and electronic properties of gas phase hydrogenated gold clusters with the aid of density functional theory. The reactivity properties have been investigated with DFT based global reactivity descriptors. The structure of zeolite supported hydrogenated gold and palladium clusters obtained due to reverse hydrogen spillover from bridging OH groups of the zeolite to the metal clusters has been studied.

The thesis consists of seven (7) chapters:

Chapter 1 gives a brief introduction about clusters with a special emphasis on gold clusters and its unique properties such as presence of aurophilic interactions and large relativistic effect. Gold clusters undergo substantial structural transition with increase in cluster size such that the small clusters are planar while larger clusters exhibit compact core-shell structure. The size and the charge state of the host gold cluster and presence of specific low coordination binding sites have been identified as some factors that on which the adsorption of O₂ and CO depends. On oxide supported gold clusters, O₂ preferentially adsorbs on the metal-support interface rather than the gold particles and with sufficient charge transfer, activation of O₂ to superoxo state O₂⁻ is observed. Gold clusters as small as a single Au atom is an excellent catalyst towards carbon monoxide oxidation. However, the inevitable presence of moisture in practical catalytic systems can affect the adsorption behaviour of CO and O₂ and consequently the catalytic activity towards CO oxidation. One of the emerging trends in the field of catalytic research is the concept of single atom catalysis. Single Au atoms supported on zeolites, oxides, BN-monolayer exhibit potential as catalysts for CO oxidation, water gas shift reaction etc. We have

included these aspects in the introductory chapter of the thesis. The objectives of the present work are included in this chapter.

Chapter 2 describes the computational tools like molecular mechanics (MM), quantum mechanics (QM), density functional theory (DFT), and various basis sets and functionals used within the realm of DFT. Hybrid quantum mechanics/molecular mechanics (QM/MM) methods are discussed in detail. We have also included the concepts of potential energy surface, electron correlation etc in this chapter. DFT, hybrid QM/MM methods have been utilized in our calculations.

Chapter 3 is divided into two sections: *Section 3.1* presents the results of the DFT investigation of the structures, electronic and reactivity properties of Au_6H_n ($n = 1 - 12$) clusters. In this study, we have calculated different parameters like bond lengths, average Hirshfeld charges, electronic properties like HOMO-LUMO gap, chemical hardness, vertical ionization potential, adiabatic ionization potential and binding energy. DFT based reactivity descriptors have been used to calculate the reactivity properties of the hydrogenated clusters. *Section 3.2* summarizes the results of reverse hydrogen spillover from bridging OH groups of the faujasite support to Pd_6 and Au_6 clusters using DFT. We utilize the distorted octahedral structures for Pd_6 and Au_6 and the geometries of the model clusters are optimized without imposing symmetry constraints. To investigate the reactivity of the metal clusters with the OH groups of the zeolite fragment, we have calculated the energy of reverse hydrogen spillover from bridging OH groups to the metal cluster, M_6 and Hirshfeld population analysis (HPA) has been used to characterize the electronic charge distribution.

Chapter 4 investigates the catalytic activity of neutral and charged gold hexamer, Au_6 cluster towards CO oxidation which elucidates the effect of cluster charge state on the catalytic activity. We also present

the results of CO and O₂ adsorption on neutral, anionic and cationic Au₆ clusters. For our study, we have considered the conventional bimolecular Langmuir-Hinshelwood mechanism with co-adsorbed CO and O₂ at the neighbouring sites in all the clusters.

Chapter 5 presents the results of hybrid quantum mechanics molecular mechanics calculations on the adsorption of small molecules such as CO and O₂ on faujasite supported gold monomer in three oxidation states viz. 0, +1 and +3. We have considered three different modes viz. top, bridge and dissociative for O₂ adsorption. The parameters such as bond length, binding energy, amount of charge transferred to O₂ and CO are calculated. These results are summarized in *Section 5.1*. We have also considered the adsorption of CO and O₂ on Auⁿ/FAU (n = 0, +1 and +3) in the presence of pre-adsorbed water using QM/MM method and the results are summarized in *Section 5.2*. The effect of the pre-adsorbed H₂O on CO and O₂ adsorption accompanied by the changes in binding energies, mode of adsorption and structural changes encountered are presented. We have also investigated the process of proton sharing between H₂O and O₂ and consequently forming a hydroperoxyl-hydroxyl species on the supported Au monomer. The barrier involved in H₂O dissociation is calculated.

Chapter 6 discusses the catalytic activity of faujasite supported gold monomer towards reactions like CO oxidation, water-gas shift reaction using hybrid quantum mechanics molecular mechanics method. *Section 6.1* focuses on the activity of faujasite supported neutral (Au⁰) and cationic (Au⁺ and Au³⁺) gold monomer towards CO oxidation ($2\text{CO} + \text{O}_2 \rightarrow 2\text{CO}_2$). We have considered different CO-O₂ co-adsorption configurations and their interaction energies have been determined. Based on that different oxidation pathways have been appraised for this study and the catalytic activity of neutral and cationic Au monomer has been compared. The results of hybrid quan-

tum mechanics molecular mechanics calculations on the activity of neutral and cationic gold monomer towards water-gas shift reaction ($\text{CO} + \text{H}_2\text{O} \rightarrow \text{CO}_2 + \text{H}_2$) are summarized in *Section 6.2*. We have initially considered two different CO – H₂O co-adsorption configurations for all the oxidation states viz. Au⁰/FAU, Au⁺/FAU and Au³⁺/FAU. The parameters such as bond length, binding energy of CO/H₂O in presence of pre-adsorbed H₂O/CO have been calculated. The reaction mechanism has been investigated with the more favourable co-adsorbed configuration and the catalytic activity of the different Au oxidation states has been compared.

Chapter 7 recapitulate the salient observations of the entire work presented in the thesis and presents future prospects to refine and reinforce the research work.

Declaration

This thesis entitled "**Computational Studies of the Properties of Bare and Zeolite Supported Gold Clusters**" being submitted to the Department of Chemical Sciences, Tezpur University, is a presentation of the original research work carried out by me. Any contribution (text, figure, result or design) of others, wherever involved, is appropriately referenced in order to give credit to the original author(s). All sources of assistance have been duly acknowledged. I affirm that neither this work as a whole nor a part of it has been submitted to any other university or institute for any other degree, diploma or award.

Date: 30-12-2014

Place: Tezpur University

Subhi Baishya
(Subhi Baishya)



TEZPUR UNIVERSITY
(A Central University established by an Act of Parliament)

NAPAAM, TEZPUR- 784028
DISTRICT: SONITPUR, ASSAM, INDIA

Ph: 03712 - 267008
03712 - 267009
Fax: 03712 - 267005
03712 - 267005
e-mail: ramesh@tezu.ernet.in

Prof. Ramesh C. Deka
Professor
Department of Chemical Sciences
Tezpur University

This is to certify that the thesis entitled "**Computational Studies of the Properties of Bare and Zeolite Supported Gold Clusters**" submitted to the School of Sciences, Tezpur University in partial fulfilment for the award of the degree of Doctor of Philosophy in Chemical Sciences is a record of research work carried out by **Ms. Subhi Baishya** under my supervision and guidance. She has been duly registered (Reg. No. 038 of 2010) and the thesis presented is worthy of being considered for the Ph. D Degree. All help received by her from various sources have been duly acknowledged. No part of this thesis has been submitted elsewhere for award of any other degree.

Date: 30.12.2014

Place: T.U.

(Prof. R. C. Deka)

Professor

Dept. of Chemical Sciences
Tezpur University-784028



तेजपुर विश्वविद्यालय

(केन्द्रीय विश्वविद्यालय)

नपाम, तेजपुर - 784 028, असम, भारत

TEZPUR UNIVERSITY

(A Central University)

Napaam, Tezpur - 784 028, Assam, India

CERTIFICATE OF THE EXTERNAL EXAMINER
AND ODEC

This is to certify that the thesis entitled "**Computational Studies of the Properties of Bare and Zeolite Supported Gold Clusters**" submitted by Ms. Subhi Baishya to the Department of Chemical Sciences under the School of Sciences, Tezpur University in partial fulfilment for the award of the degree of Doctor of Philosophy in Chemical Sciences has been examined by as on and found to be satisfactory.

Signature of:

Supervisor

External Examiner

Date:

Date:

Acknowledgements

At the very outset, I extend my heartiest thanks to Prof. Ramesh C. Deka, Department of Chemical Sciences, Tezpur University; my teacher and research supervisor, for selecting me as a Ph.D student under his guidance. I truly acknowledge his support and help during my research work. I am indebted to him for providing me the opportunity to visit University College London, London and work with Prof. C. Richard A. Catlow and his group during my research tenure.

I am grateful to Prof. Mihir Kanti Chaudhuri, honourable Vice-Chancellor, Tezpur University for endowing me with the opportunity to carry out my research in a cordial and scientific environment. Furthermore, my sincere gratitude goes to the entire university fraternity for providing me all the basic necessities to make my stay in the campus comfortable during this period.

I truly thank my Doctoral Committee members, Dr. Ruli Borah and Dr. Ashim J. Thakur, Associate Professors, Department of Chemical Sciences, Tezpur University for their valuable suggestions and help during my research period. I thank all the faculty members and staff of the Department of Chemical Sciences, Tezpur University for their cooperation and help at various times.

I thank the Council of Scientific and Industrial Research, New Delhi and Department of Science and Technology, New Delhi for their financial support.

I am deeply thankful to one of the great teachers of my life, G. R. Lalitha, ex-principal, Vivekananda Kendra Vidyalaya, Golaghat whose inspiration and encouragement led me to pursue a career in the field of research. Her spirituality, generosity, kind, affectionate and intense love boosted me with moral support at some of my very crucial moments. I thank all my teachers from Vivekananda Kendra Vidyalaya, Golaghat, Kendriya Vidyalaya, Nagaon and Debraj Roy College, Golaghat who made me capable enough to pursue higher studies.

I thank the Computer Centre, Tezpur University for giving me the opportunity to carry out some of my calculations in the Altix machine and help me solve any

computer related issue.

I am glad to acknowledge Dr. Pusphita Ghosh, Indian Association for Cultivation of Science, Kolkata for her help in providing me innumerable and valuable research literature at different times.

I profoundly thank the reviewers of my manuscripts for their valuable comments and suggestions which helped me to improve my research work.

I especially thank my friend, Ms. Papia Dutta, whose congenial company made my stay in this campus so pleasant. I must acknowledge the immense help, support and encouragement she gave me at many difficult moments.

I thank all my labmates, research scholars of the Department of Chemical Sciences and friends from other departments-Priyakshi, Julee, Pratisha for helping time to time.

I must thank all the hostel menials who made me feel at home with their love and affection during my stay in the hostel. I must mention their unconditional care during my ill health.

It is difficult to jot down in mere words my gratitude towards Mr. Shantanu Konwar for his immense help and constant support. I am very grateful indeed to the Almighty for having a friend like him in my life who stood firm by my side at every moment.

Last but not the least, I must thank Ma, Deuta and my sister, Jupi for their love, support, blessings and scoldings which has helped me to overcome all the hurdles that came across my path and kept alive my zeal to continuously focus on my research work. Special thanks goes to Tarun jethpeha, Lily jethai and Dolly ba for their help and continuous enthusiasm.

I would like to thank all the well-wishers for their blessings and prayers which encouraged me to complete this work.

Date: 30-12-2014

Place: Jexpur University.

Subhi Baishya
(Subhi Baishya)

Table of Contents

<i>Contents</i>	<i>Page</i>
Abstract	i
List of Abbreviation	xviii
List of Tables	xix
List of Figures	xxii
1 Introduction	1
1.1 Clusters	1
1.1.1 Types of Clusters	3
1.2 Gold Clusters	4
1.2.1 Aurophilicity	5
1.2.2 Relativistic Effects	6
1.2.3 Structure of Gold Clusters	7
1.2.4 Magic Number Clusters	9
1.3 Adsorption of small molecules on gold clusters	10
1.3.1 Adsorption of O ₂ and CO on gas phase gold clusters	10
1.3.2 Adsorption of O ₂ and CO on supported gold clusters	13
1.3.3 Effect of water on CO and O ₂ adsorption	14
1.4 Catalysis By Gold	16
1.4.1 Bare gold clusters in CO oxidation	16
1.4.2 Supported gold clusters in CO oxidation	18
1.4.3 Zeolite supported gold clusters	19
1.4.3.1 Zeolites-Structure and Property	19

1.4.3.2	CO oxidation on zeolite supported Au	21
1.4.4	Activity of gold clusters towards water-gas shift reaction	23
1.5	Single Atom Catalysis	26
1.6	Objectives of The Present Work	27
2	Basic Electronic Theory	29
2.1	Introduction	29
2.2	Computational Chemistry Perspective	30
2.3	Potential Energy Surface	31
2.4	Molecular Mechanics	33
2.5	Quantum Mechanics	35
2.5.1	Hartree-Fock Method	35
2.5.2	Semi-empirical Methods	41
2.5.3	Density Functional Theory	44
2.5.3.1	Hohenberg-Kohn Theorems	45
2.5.3.2	Kohn-Sham Method	46
2.5.3.3	Exchange-Correlation Energy Functionals	49
2.5.3.4	Performance of DFT functionals	52
2.5.4	Basis Sets	53
2.5.4.1	Slater Type Orbitals (STO)	53
2.5.4.2	Gaussian Type Orbitals (GTO)	53
2.5.4.3	Single-zeta, Multiple-zeta basis sets	54
2.5.4.4	Split-valence basis sets	54
2.5.4.5	Polarization functions	55
2.5.4.6	Diffuse functions	55
2.5.4.7	Numerical basis sets	56
2.5.4.8	Effective Core Potentials (ECP)	56
2.6	Quantum Mechanics/Molecular Mechanics (QM/MM) Methods	57
3	Density Functional Studies on Hydrogenated Gold Clusters	60
3.1	Structure, Electronic and Reactivity Properties of Au ₆ H _n (n=1-12) Clusters	61
3.1.1	Introduction	61

3.1.2	Computational Details	62
3.1.3	Results and Discussion	65
3.1.3.1	Geometric Structures of Au ₆ H _n (n=1-12) clusters	65
3.1.3.2	Variation of Electronic Properties	68
3.1.3.3	Fukui Function	73
3.1.4	Salient Observation	74
3.2	Reverse Hydrogen Spillover on Zeolite Supported Pd ₆ and Au ₆ clusters	76
3.2.1	Introduction	76
3.2.2	Computational Details	78
3.2.3	Results and Discussion	80
3.2.3.1	Zeolite supported bare Pd ₆ and Au ₆ clusters	80
3.2.3.2	Zeolite supported hydrogenated Pd ₆ clusters	82
3.2.3.3	Zeolite supported hydrogenated Au ₆ clusters	84
3.2.4	Salient Observation	87
4	Adsorption of CO, O₂ on Gas Phase Gold Clusters and CO Oxidation	89
4.1	Introduction	90
4.2	Computational Details	91
4.3	Results and Discussion	92
4.3.1	Structural features of optimized Au ₆ ⁿ clusters (n= 0, -1 and +1)	92
4.3.2	Adsorption of O ₂ and CO on Au ₆ ⁿ clusters (n= 0, -1 and +1)	93
4.3.3	Co-adsorption of CO and O ₂ on Au ₆ ⁿ clusters (n= 0, -1 and +1)	96
4.3.4	CO oxidation on neutral Au ₆ cluster	97
4.3.5	CO oxidation on anionic Au ₆ cluster	99
4.3.6	CO oxidation on cationic Au ₆ cluster	101
4.4	Salient Observation	103
5	Adsorption of CO and O₂ on Zeolite Supported Gold Monomer and the Effect of Moisture	105
5.1	Adsorption of CO and O ₂ on faujasite supported gold monomer	106

5.1.1	Introduction	106
5.1.2	Computational Details	107
5.1.3	Results and Discussion	109
5.1.3.1	Faujasite supported gold monomer	109
5.1.3.2	CO adsorption on faujasite supported gold monomer	110
5.1.3.3	O ₂ adsorption in the top mode on faujasite supported gold monomer	112
5.1.3.4	O ₂ adsorption in the bridge mode on faujasite supported gold monomer	113
5.1.3.5	O ₂ adsorption in the dissociative mode on faujasite supported gold monomer	115
5.1.4	Salient Observation	116
5.2	Role of water on the adsorption of CO and O ₂ on faujasite supported gold monomer	119
5.2.1	Introduction	119
5.2.2	Computational Details	120
5.2.3	Results and Discussion	121
5.2.3.1	Water adsorption on faujasite supported gold monomer	121
5.2.3.2	Adsorption of CO on faujasite supported gold monomer in presence of pre-adsorbed H ₂ O	123
5.2.3.3	Adsorption of O ₂ in the top mode on faujasite supported gold monomer in presence of pre-adsorbed H ₂ O	124
5.2.3.4	Adsorption of O ₂ in the bridge mode on faujasite supported gold monomer in presence of pre-adsorbed H ₂ O	130
5.2.3.5	Adsorption of O ₂ in the dissociative mode on faujasite supported gold monomer in presence of pre-adsorbed H ₂ O	134
5.2.4	Salient Observation	136
6	Activity of Zeolite Supported Gold Monomer Towards CO Oxidation and Water Gas Shift Reaction	138

6.1	CO oxidation on faujasite supported gold monomer	139
6.1.1	Introduction	139
6.1.2	Computational Details	141
6.1.3	Results and Discussion	142
6.1.3.1	Adsorption of CO and O ₂ on faujasite supported Au monomer	142
6.1.3.2	CO oxidation reaction energy profile with dissoci- ated O ₂	143
6.1.3.3	CO oxidation reaction energy profile with gas phase O ₂	150
6.1.3.4	CO oxidation reaction energy profile with gas phase CO	153
6.1.4	Salient Observation	155
6.2	Water Gas Shift reaction on faujasite supported Au monomer . . .	158
6.2.1	Introduction	158
6.2.2	Computational Details	159
6.2.3	Results and Discussion	160
6.2.3.1	Adsorption of CO and H ₂ O on faujasite supported Au monomer	160
6.2.3.2	Water gas shift reaction on Au ⁰ /FAU	161
6.2.3.3	Water gas shift reaction on Au ⁺ /FAU and Au ³⁺ /FAU	164
6.2.4	Salient Observation	169
7	Conclusions and Future Scopes	172
	Bibliography	180
	List of Publications	200
	List of Conferences Attended	201
	Appendices	203
A	Structural Isomers of Au₆H_n (n=1-12) clusters	204

B Structures of O₂ and CO adsorption on Au₆ⁿ (n=0,-1 and +1) Clusters	215
C Frontier Molecular Orbitals for Different Auⁿ/FAU (n=0, +1 and +3) systems	218
D Structures of Different Species for CO Oxidation pathways	225

List of Abbreviation

AMBER	Assisted Model Building and Energy Refinement
B3LYP	Combination of Becke exchange functional, three-parameter and Lee-Yang-Parr correlation functional
BSSE	Basis Set Superposition Error
CHARMM	Chemistry at HARvard Molecular Mechanics
CVFF	Consistent Valence Force Field
DFT	Density Functional Theory
DNP	Double Numerical basis set with Polarization function
ECP	Effective Core Potential
ER	Eley-Rideal mechanism
FAU	Faujasite zeolite
GAMESS	General Atomic Molecular Electronic Structure System
HOMO	Highest Occupied Molecular Orbital
IRC	Intrinsic Reaction Coordinate
LANL2DZ	Los Alamos National Laboratory (LANL) ECP with Double Zeta valence basis set
LH	Langmuir-Hinshelwood mechanism
LUMO	Lowest Unoccupied Molecular Orbital
MM2, MM3	Molecular Mechanics force field
NBO	Natural Bond Orbital
QM	Quantum Mechanics
QM/MM	Quantum Mechanics/Molecular Mechanics
SIMOMM	Surface Integrated Molecular Orbital Molecular Mechanics
VWN	Vosko-Wilk-Nusair correlation functional
WGS	Water Gas Shift reaction
ZSM-5	Zeolite Socony Mobil-5
η	Global Hardness

List of Tables

<i>Tables</i>	<i>Page</i>
1.1 Classification of clusters according to the nature of bonding	4
3.1.1 Computed Au-H and Au-Au bond lengths of Au ₆ H _n (n=1-12) clusters.	68
3.1.2 Calculated electronic properties of the Au ₆ H _n (n=1-12) clusters. . .	71
3.1.3 Averaged atomic Hirshfeld charges on H atom in Au ₆ H _n (n=1-12) clusters.	73
3.2.1 Computed geometrical parameters and Hirshfeld charges of selected atoms of faujasite supported bare Pd ₆ and Au ₆ clusters.	81
3.2.2 Computed geometrical parameters, Hirshfeld charges of selected atoms and reverse spillover energy per transferred hydrogen of faujasite supported hydrogenated Pd ₆ and Au ₆ clusters.	87
4.1 Computed bond lengths (Å) for Au ₆ ⁿ clusters (n= 0, -1 and +1). . .	92
4.2 Computed CO and O ₂ binding energies (eV), C-O and O-O distances (Å), C-O and O-O stretching frequencies (cm ⁻¹) for Au ₆ ⁿ clusters (n= 0, -1 and +1).	95
4.3 Computed bond lengths (Å) and interaction energies (eV) for the co-adsorbed complexes in the neutral, anionic and cationic Au ₆ clusters.	97
4.4 Bond lengths (Å) and bond angle for all the species involved in CO oxidation catalyzed by neutral Au ₆ cluster.	99
4.5 Bond lengths (Å) and bond angle for all the species involved in CO oxidation catalyzed by anionic Au ₆ cluster.	101
4.6 Bond lengths (Å) and bond angle for all the species involved in CO oxidation catalyzed by cationic Au ₆ cluster.	103

4.7	Comparison of the barriers (eV) involved in the different steps of CO oxidation over neutral and charged Au ₆ clusters.	104
5.1.1	Bond lengths (Å) and NBO charges on faujasite supported Au monomer in three oxidation states.	109
5.1.2	Geometrical parameters, binding energies and vibrational frequency of CO adsorbed on Au ⁿ /FAU (n=0, +1 and +3).	111
5.1.3	Geometrical parameters, binding energies and vibrational frequency of O ₂ adsorbed on Au ⁿ /FAU (n=0,+1 and +3)	117
5.1.4	Computed NBO charges in the different modes of O ₂ adsorption on Au ⁿ /FAU (n=0, +1 and +3).	118
5.2.1	Computed bond length (Å), binding energy (eV) and NBO charges of H ₂ O adsorbed on Au ⁿ /FAU, n=0, +1 and +3.	122
5.2.2	Computed bond lengths (Å), stretching frequency, ν_{C-O} (cm ⁻¹), binding energy of CO (eV) and NBO charges for CO adsorption on Au ⁿ /FAU, n=0, +1 and +3 with pre-adsorbed H ₂ O.	125
5.2.3	Computed bond lengths (Å), stretching frequency, ν_{C-O} (cm ⁻¹) and binding energy of O ₂ (eV) for O ₂ adsorption on Au ⁿ /FAU, n=0, +1 and +3 with pre-adsorbed H ₂ O.	127
5.2.4	Computed NBO charges for O ₂ adsorption in the top mode in presence of pre-adsorbed H ₂ O (R), the hydroperoxyl-hydroxyl species formed (H) and the transition state involved (TS) in Au ⁿ /FAU (n=0, +1 and +3).	129
5.2.5	Computed bond lengths (Å) of the transition states and the hydroperoxyl species, the barriers involved, ΔE (eV) and the imaginary frequency for the transition states in Au ⁿ /FAU, n=0, +1 and +3.	131
5.2.6	Computed NBO charges for O ₂ adsorption in the bridge mode in presence of pre-adsorbed H ₂ O (R), the hydroperoxyl-hydroxyl species formed (H) and the transition state involved (TS') in Au ⁿ /FAU, n=0, +1 and +3.	134
5.2.7	Computed NBO charges for O ₂ adsorption in the dissociative mode on Au ⁿ /FAU (n=0, +1 and +3) in the presence of pre-adsorbed H ₂ O.	135

6.1.1 Computed interaction energies (in eV) for different initial configurations containing CO and O ₂ on Au ⁿ /FAU (n=0, +1 and +3).	142
6.1.2 Computed geometrical parameters (Å), barriers values (eV) and the imaginary frequency (cm ⁻¹) for transition states in the Eley-Rideal pathway with dissociated O ₂ on Au ⁰ /FAU.	144
6.1.3 Computed geometrical parameters (Å), barriers values (eV) and the imaginary frequency (cm ⁻¹) for transition states in the Eley-Rideal (η^1 -carbonate) pathway with dissociated O ₂ on Au ³⁺ /FAU.	147
6.1.4 Computed geometrical parameters (Å), barriers values (eV) and the imaginary frequency (cm ⁻¹) for transition states in the Eley-Rideal pathway with gas phase O ₂ on Au ³⁺ /FAU.	151
6.1.5 Computed geometrical parameters (Å), barriers values (eV) and the imaginary frequency (cm ⁻¹) for transition states in the Eley-Rideal pathway with gas phase CO on Au ³⁺ /FAU.	154
6.1.6 Comparison of the barriers involved in the different pathways for CO oxidation on Au ⁿ /FAU (n=0, +1 and +3).	156
6.2.1 Computed geometrical parameters and the binding energy of water in the CO pre-adsorbed Au ⁿ /FAU (n=0, +1 and +3) (R1').	161
6.2.2 Computed geometrical parameters (Å), energy barriers (eV) and the imaginary frequency (cm ⁻¹) associated with the transition states in the various steps of the water gas shift reaction on Au ⁰ /FAU.	166
6.2.3 Computed geometrical parameters (Å), energy barriers (eV) and the imaginary frequency (cm ⁻¹) associated with the transition states in the various steps of the water gas shift reaction on Au ⁺ /FAU.	170
6.2.4 Computed geometrical parameters (Å), energy barriers (eV) and the imaginary frequency (cm ⁻¹) associated with the transition states in the various steps of the water gas shift reaction on Au ³⁺ /FAU.	171

List of Figures

<i>Figures</i>	<i>Page</i>
1.1 Schematic representation of cluster placed in between atom, molecule and bulk material	2
1.2 Examples of different clusters	3
1.3 Optimized TPSS/7s5p3d1f structures of the lowest energy 2D and 3D isomers of Au ₁₁	8
1.4 Ground state geometry of Au ₁₉ and Au ₂₀	8
1.5 Compact core shell of Au ₂₅ ⁻	9
1.6 Optimized structures of O ₂ adsorption complex on metal-support interface.	11
1.7 Structures of primary and secondary building block of zeolites.	20
1.8 Framework structure of faujasite zeolite.	20
2.1 Various stationary points on an intrinsic reaction coordinate.	32
2.2 Annual occurrence of the phrase 'DFT' in Journals	44
2.3 Jacob's Ladder of density functional approximations.	52
2.4 Behaviour of e^r and e^{r^2} for s-type function.	54
2.5 Partitioning a chemical system in to inner part (I) and an outer part (O).	58
3.1.1 Optimized structures of the pristine Au ₆ cluster and the Au ₆ H _n (n=1-12) clusters at PBE/DNP level of calculation.	67
3.1.2 Variation of electronic properties of the Au ₆ H _n (n=1-12) clusters with the number of hydrogen atoms.	70
3.1.3 The HOMO and LUMO orbitals of Au ₆ , Au ₆ H ₂ , Au ₆ H ₄ , Au ₆ H ₆ , Au ₆ H ₈ , Au ₆ H ₁₀ and Au ₆ H ₁₂ clusters.	72

3.2.1 Faujasite model with three bridging OH groups.	79
3.2.2 Optimized structures of faujasite supported bare Pd ₆ and Au ₆ clusters	81
3.2.3 Optimized structures of faujasite supported hydrogenated Pd ₆ clusters, Pd ₆ H _n /FAU(3-n); n=1-3.	84
3.2.4 Optimized structures of faujasite supported hydrogenated Au ₆ clusters, Au ₆ H _n /FAU(3-n); n=1-3.	86
4.1 Optimized structure of Au ₆ cluster at the BLYP/DNP level of calculation.	92
4.2 Optimized structures of O ₂ and CO adsorbed on (a) Au ₆ ⁰ (b) Au ₆ ⁻ (c) Au ₆ ⁺ clusters.	94
4.3 Optimized structures of CO and O ₂ co-adsorbed complexes of (a) Au ₆ ⁰ (b) Au ₆ ⁻ (c) Au ₆ ⁺ clusters.	97
4.4 Energy profile diagram for CO oxidation on neutral Au ₆ cluster. . .	99
4.5 Energy profile diagram for CO oxidation on anionic Au ₆ cluster. . .	101
4.6 Energy profile diagram for CO oxidation on cationic Au ₆ cluster. . .	103
5.1.1 The faujasite model used in our calculations.	108
5.1.2 Optimized structures of faujasite supported Au monomer.	110
5.1.3 Optimized structures of CO adsorbed on Au ⁿ /FAU (n=0, +1 and +3).	110
5.1.4 Optimized structures of O ₂ adsorbed in the top mode on Au ⁿ /FAU (n=0, +1 and +3).	113
5.1.5 Optimized structures of O ₂ adsorbed in the bridge mode on Au ⁿ /FAU (n=0, +1 and +3).	114
5.1.6 Optimized structures of O ₂ adsorbed in the dissociative mode on Au ⁿ /FAU (n=0, +1 and +3).	115
5.2.1 Optimized structures of H ₂ O adsorbed on Au ⁿ /FAU (n=0, +1 and +3).	123
5.2.2 Optimized structures of CO adsorbed on Au ⁿ /FAU (n=0, +1 and +3) in the presence of pre-adsorbed H ₂ O.	124
5.2.3 Optimized structures of O ₂ adsorbed in the top mode on Au ⁿ /FAU (n=0, +1 and +3) in the presence of pre-adsorbed H ₂ O.	126

5.2.4 Energy profile diagram for the formation of hydroperoxyl-hydroxyl species from O ₂ (adsorbed in the top mode) and H ₂ O on Au ⁿ /FAU (n=0, +1 and +3).	128
5.2.5 Optimized structures of O ₂ adsorbed in the bridge mode on Au ⁿ /FAU (n=0, +1 and +3) in the presence of pre-adsorbed H ₂ O.	130
5.2.6 Energy profile diagram for the formation of hydroperoxyl-hydroxyl species from O ₂ (adsorbed in the bridge mode) and H ₂ O on Au ⁿ /FAU (n=0, +1 and +3).	132
5.2.7 Optimized structures of O ₂ adsorbed in the dissociative mode on Au ⁿ /FAU (n=0, +1 and +3) in the presence of pre-adsorbed H ₂ O. .	135
6.1.1 Energy profile diagram for the Eley-Rideal pathway with dissociated O ₂ on Au ⁰ /FAU.	145
6.1.2 Energy profile diagram for the Eley-Rideal (η^1 -carbonate) pathway with dissociated O ₂ on cationic systems.	148
6.1.3 Energy profile diagram for the Eley-Rideal pathway with gas phase O ₂ on Au ⁿ /FAU (n=0, +1 and +3).	152
6.1.4 Energy profile diagram for the Eley-Rideal pathway with gas phase CO on Au ⁿ /FAU (n=0, +1 and +3).	155
6.2.1 Optimized structures of H ₂ O adsorbed on CO pre-adsorbed Au ⁿ /FAU (n=0, +1 and +3).	161
6.2.2 Energy profile diagram for the water-gas shift reaction on Au ⁰ /FAU.	163
6.2.3 Frontier molecular orbitals illustrating interaction between the Au centre and C atom in the <i>cis</i> -COOH intermediate (I ₂ ^{0,+3+}).	164
6.2.4 Energy profile diagram for the water-gas shift reaction on Au ⁺ /FAU and Au ³⁺ /FAU.	168

Chapter 1

Introduction



Richard Phillips Feynman
(May 11, 1918 - Feb 15, 1988)

1.1 Clusters

The famous talk entitled "There's Plenty of Room at the Bottom", presented by Richard Feynman to the American Physical Society in Pasadena on December 1959 focussed on the wide range of possibilities of manipulation at the atomistic level. His talk is considered to be a groundbreaking event in the history of nanoscience. In the early 1960s, F. A. Cotton coined the term '*cluster*' to define aggregates of three to several hundreds of thousands atoms or molecules with interactions ranging from very weak van der Waals contacts to strong ionic bonds. Nowadays, in a broader purport, aggregates with two to several hundreds of thousands entities are defined within the realm of clusters. Clusters form an intermediate state between atomic and bulk size regime. This is depicted in Figure 1.1. In addition, they serve as a bridge among various disciplines by combining ideas of atomic, molecular, and condensed matter and nuclear physics as well as among physical, organic, and analytical chemistry [1,2]. The earliest investigations on clusters by

Rayleigh recognized that the colour of stained glasses was due to the scattering of light by small metal particles embedded in the glass [3]. The independent works of Bentley [4] and Henkes [5] in 1961 detected jet-generated clusters of carbon dioxide using mass spectrometers which marks the beginning of the modern era of cluster science. In the following years, field of cluster science gained momentum with the development of new experimental sources for production of clusters [6-10]. In 1974, Prof. Norio Taniguchi coined the term nano-technology to describe semiconductor processes such as thin film deposition and ion beam milling exhibiting characteristic control on the order of a nanometer.

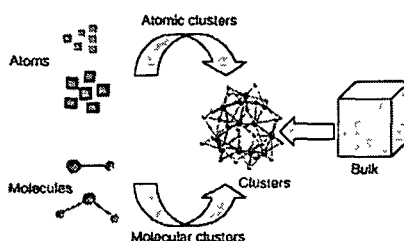


Figure 1.1: Schematic representation of cluster placed in between atom, molecule and bulk material. The dimension increases from left to right in the figure [11].

The physical and chemical properties of clusters differ significantly from their bulk counterparts. The size-dependent specificity and selectivity of their physical and chemical properties or in other words, the ability to modify the cluster properties by changing the size of the system, one at a time, makes them particularly interesting. Delocalization of electrons in bulk metals which imbue them with high electrical and thermal conductivity, light reflectivity and mechanical ductility may be wholly or partially absent in metal nanoclusters, while new properties develop in them [12]. Metal clusters have lower melting point compared to the corresponding bulk material. The unique relationship of cluster properties with the size has been attributed to physical aspects such as high surface to volume ratio, quantum size effects etc. The increased surface to volume ratio in clusters compared to the bulk materials enhances their reactivity towards reactions occurring on the surfaces. Moreover, the low-coordinated atoms present in the surface of clusters have a tendency to form additional bonds with ligands which impart extra stability to clusters. Within the realm of the nanoscale, the electronic nature of the clusters

differs considerably from the macroscopic particles and quantization effects due to confinement of the electron movement appear. This leads to discrete energy levels intrinsic to every cluster size which can be modelled by quantum mechanical treatment of a particle in a box. The phenomenon is defined as *quantum size effect* that leads to new electronic properties in metal clusters.

Clusters find wide range of applications that include photonic devices [13,14], electronic devices [15,16], ultrasensitive biological detection and fluorescent biological imaging [17,18]. Thus, clusters form one of the most fascinating materials and the interest in cluster science to identify potent applications in different areas is ever increasing with the improvements in experimental techniques and computational tools.

1.1.1 Types of Clusters

Clusters can be classified according to the constituents in the aggregate and the nature of bonding present in the cluster which can be ionic, covalent, metallic, van der Waals etc. Table 1.1 summarizes the various cluster types according to the nature of bonding [11]. According to the nature of the constituents, clusters can be classified as:

Homo-atomic (or Homo-molecular) clusters: Clusters with identical constituent atoms/molecules. Example: Au_n , $(H_2O)_n$ (n is the number of atoms/molecules).

Hetero-atomic (or Hetero-molecular) clusters: Clusters with two or more different constituents. Example: Pd_nPt_m (n and m are the number of atoms). Figure 1.2 shows some of the cluster types.

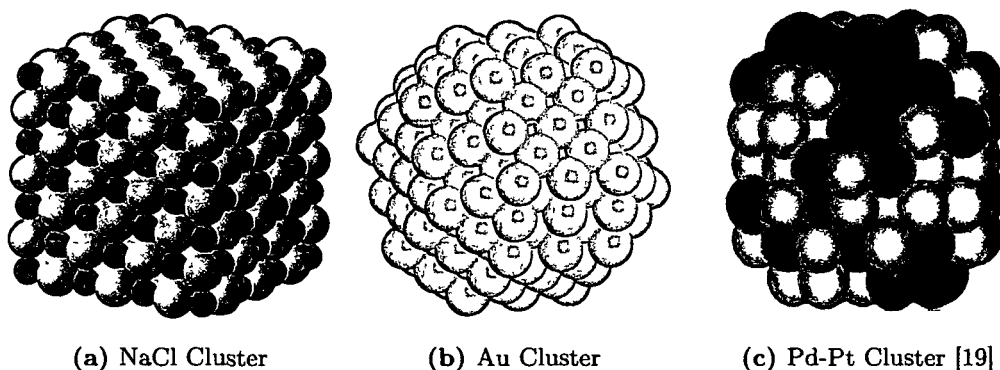


Figure 1.2: Examples of different clusters

Table 1.1: Classification of clusters according to the nature of bonding

Type	Example	Nature of Binding	Binding Energy/Mole (kcal)
Ionic Clusters	$(\text{NaCl})_n, (\text{CsI})_n$	Ionic Bonds (Strong Binding)	$\sim 50 - 100$
Covalent Clusters	$\text{C}_{60}, \text{Si}_n$	Covalent Bonding (Strong Binding)	$\sim 20 - 100$
Metal Clusters	$\text{Na}_n, \text{Fe}_n, \text{Au}_n$	Metallic Bonding (Moderate to Strong Binding)	$\sim 10 - 50$
Molecular Clusters	$(\text{H}_2\text{O})_n$	Molecular interactions, hydrogen bonding, Van der Waals, etc.	< 10
Van der Waals Clusters	Ar_n, Xe_n	Polarization Effects (Weak bindings)	< 5

1.2 Gold Clusters

Gold has fascinated mankind since ages. It finds widespread consumption in jewellery across the world owing to its excellent properties that it does not tarnish on exposure to atmosphere and retains its beautiful lustre undiminished for years.

Its resistance to oxidation and corrosion in air as well as its chemical inertness towards various reactions contributes largely to the noble behaviour of gold.

What makes gold particularly very interesting is the fact that the most noble metal loses its nobility to become one of the excellent catalyst for reactions such as low temperature CO oxidation, direct formation of hydrogen peroxide etc, when the size is reduced to nano dimension. The use of nanogold dates back to ancient ages and the most famous example is the Lycurgus Cup which was manufactured in the 5th to 4th century B.C and is now exhibited in the British Museum. It is ruby red in transmitted light and green in reflected light, due to the presence of gold particles [20]. In the Vedic period of ancient India, gold containing ashes (gold *bhasma*) was prepared for medicinal purposes by usually secret recipes [21]. In 1857, the legendary work of Michael Faraday [22] on the formation of deep red solutions of colloidal gold by reduction of an aqueous solution of chloroaurate (AuCl_4^-) using phosphorus was the first scientific investigation on finely divided gold. Since then, synthesis and application of gold nanoparticles in fields such as biological labelling, optical and electronic devices etc have been steadily growing. In addition, very large relativistic effects and the presence of aurophilic interactions, makes gold unique compared to the other coinage metal counterparts. These effects are discussed in the following sections.

1.2.1 Aurophilicity

Aurophilicity or *Aurophilic Interactions* play a central role in the area of gold chemistry [23,24]. The terms, introduced in 1987 by Schmidbaur, is used to describe various kinds of Au-Au interactions within and between gold compounds [25]. Aurophilic interactions are cohesive interactions occurring among formally closed shell gold atoms (Au^I centres with $5d^{10}$ configuration) inside a molecule, or between such atoms in different molecules. These interactions are characterized by metal-metal distances shorter ($2.7\text{-}3\text{\AA}$) than the sum of two van der Waals radii (3.7\AA) and that the bond energy is usually small but higher than the energy of standard van der Waals contacts. An outcome of aurophilicity is that several gold atoms can assemble in polynuclear gold species resulting in dimers, oligomers or infinite two-dimensional sheets. Temperature dependent NMR spectroscopy mea-

surement of the strength of interaction between per Au pair of atoms is observed in the range of 29-46 kJmol⁻¹, comparable to hydrogen bond [26] and such interactions has been suggested to be intermediate between conventional covalent/ionic and van der Waals interactions [27]. The behaviour of aurophilic interaction varies as a function of R^{-6} at large distances which provide evidence for the dispersion character of these interactions [28]. Aurophilic interactions can coexist with other kind of bonding such as covalent bonding [29] and hydrogen bonding [30]. Theoretical studies have indicated that when an aurophilic attraction is present, the hydrogen bonding losses strength and directionality to retain the gold-gold interaction [31]. From a theoretical point of view, the aurophilic interaction has been attributed to electron-correlation strengthened by relativistic effects rather than classical theory of chemical bonding [26,32,33].

1.2.2 Relativistic Effects

The unique chemistry of gold has been largely attributed to the impact of large relativistic effects (larger than any other element with $Z < 100$). Relativistic effects occur due to the high speeds of all electrons when they move near a heavy nucleus and as a consequence of relativity, will lead to an increase in mass. This mass increase results in radial contraction observed predominantly in case of s and p orbitals. Thus, contraction of these orbitals leads to a stronger screening of the nuclear attraction, and consequently destabilization and expansion of d and f orbitals. The relativistic effects scale roughly as Z^2 (Z is the full nuclear charge), thus becoming more important in the heavier elements. Large relativistic effects in gold accounts for the differences in properties between gold and the other coinage metals, most notably silver. Schmidbaur and co-workers established the smaller size of Au(I) compared to Ag(I) [34,35]. The high electron affinity of gold relative to silver and the existence of aurides (eg, Cs^+Au^-) which are non-metallic semiconductors have been attributed to relativistic effects [36]. Moreover, these effects are responsible for much higher first ionization potential of gold than silver (IP1 for Au 9.225 eV, IP1 for Ag 7.576 eV) [37]. The tighter binding of the s electron of gold accounts for higher cohesion energy of gold metal and higher melting point. The yellow colour of gold (absorption beginning at 2.38 eV) associated with tran-

sitions from the 5d orbital to the Fermi level (largely 6s in character) results from the raising of the Au 5d orbital and the lowering of the valence 6s orbital unlike absorption observed in the ultraviolet region in case of silver [38]. Over the years, impact of relativistic effect on the chemistry of gold has been studied in detail [39-42].

1.2.3 Structure of Gold Clusters

A unique feature of gold clusters is the presence of relativistic effect which induces s-d hybridization by reducing the 6s-5d energy gap thereby making gold clusters strikingly different from Cu and Ag counterparts. Thus, investigating the structure of gold clusters has been an interesting aspect of both experimental [43-50] and theoretical studies [51-57]. For neutral and anionic Au clusters, the transition from planar to three dimensional structure has been observed in the size range $n=11-14$ [58-63]. The crossover size in case of neutral gold clusters is constantly debated by different groups and no definite consensus has been achieved. Li *et al.* [58] studied the structure and stability of Au clusters with up to 14 atoms using DFT and suggested that the transition from planar to 3D structure for neutral gold clusters occur at Au_{12} . However, Deka *et al.* [59] indicated the lowest energy structures to be planar till Au_{13} in their study on Au clusters with 2-13 atoms using DFT. In a recent study by Johansson *et al.* [61], the transition for neutral Au clusters was suggested to occur at Au_{11} (Figure 1.3) from the global optimizations of Au_n , $n = 9 - 13$ clusters using a genetic algorithm and a meta-generalized density functional theory. On the other hand, Assadollahzadeha and Schwerdtfeger [62] observed Au_{14} to be the first cluster size where 3D structure is the global minimum.

Unlike neutral Au clusters, the transition from 2D to 3D structure for anionic clusters has been suggested to occur at Au_{12}^- by different studies. Häkkinen *et al.* [63] observed the 2D to 3D transition for anionic gold clusters at $n = 12$ from combined experimental and theoretical investigation in agreement with ion mobility measurements conducted earlier [64]. For cationic clusters, planarity was retained till $n = 7$ and three dimensional structures form at Au_8^+ as revealed from ion mobility and density functional calculations [65]. In agreement with the above

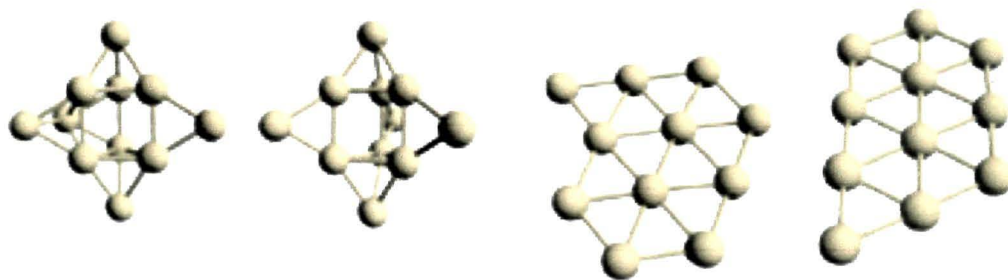


Figure 1.3: Optimized TPSS/7s5p3d1f structures of the lowest energy 2D and 3D isomers of Au_{11} [61].



Figure 1.4: Ground state geometry of Au_{19} and Au_{20} [71].

observations, Madsen and co-workers [66] observed 2D-3D transition at $n=8$ and $n=12$, respectively for cationic and anionic Au clusters from density functional calculations using meta-GGA functional. Johansson *et al.* [61] also observed the 2D-3D crossover for cationic and anionic clusters at Au_8^+ and Au_{12}^- , respectively.

On moving to the higher clusters, it has been observed that the structure of gold clusters undergo transition to flat-cage structures observed for Au_{15} , Au_{16} while spherical hollow cage structures have been found to dominate in case of Au_{17} , Au_{18} [52,67-69]. This transition from flat cage to hollow cage structure has been suggested to take place at Au_{17} for neutral clusters and at Au_{16}^- for anionic clusters. Studies have shown that Au_{19} and Au_{20} possess pyramidal structures with Au_{20} having a tetrahedral symmetry. Au_{19} differs from Au_{20} by a single missing vertex atom of the tetrahedron and has C_{3v} symmetry (Figure 1.4). The symmetries of both the clusters have been found to same in the anionic counterparts [70-73].

Structural transition from pyramidal to hollow tubular type has been observed in Au_{24}^- and further to compact core-shell structure at Au_{25}^- (Figure 1.5)[74]. For clusters larger than Au_{25}^- , experiments in conjugation with theoretical investigation

have indicated low-symmetry core-shell structures as the global minimum with the number of core atoms increasing as the cluster size increases [75]. Jalbout *et al.* [76] have suggested higher stability of low symmetry (disordered) isomers for Au_{32}^- unlike the most stable cage structure as proposed by others [75,77]. It was observed that Au_{32}^- possess a three-atom triangular core while Au_{33}^- to Au_{35}^- and Au_{36}^- to Au_{38}^- possess a four-atom tetrahedral core [75,78]. Cage like structure has also been identified as the global minimum for neutral Au clusters [79,80].

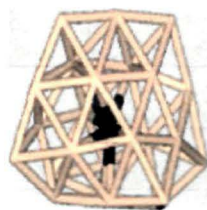


Figure 1.5: Compact core shell of Au_{25}^- [74]

1.2.4 Magic Number Clusters

One key concept in the field of cluster science is the magic number clusters which was originally introduced in alkali metal clusters with $(ns)^1$ configuration [81]. The electronic magic-number clusters are near-spherical metal clusters with specific number of valence electrons, e.g., 8, 18, 20, 34, 40, 58, ..., and are very robust because of their closed electronic shells. These clusters possess high stability and much higher abundance in mass spectrometric studies than other sizes of metal clusters. The electronic magic-number clusters typically have much larger HOMO-LUMO gap than their neighbouring-size clusters. The highly symmetric clusters such as those clusters with icosahedral symmetry may be viewed as geometric magic-number clusters [82]. It has been established that magic number gold clusters are obtained when the number of valence electrons is equal to or near the value of 2, 8, 18, 32, 50, ... that stabilizes the spherical structures. The magic gold clusters have been studied using experimental techniques as well as theoretical methods [83,84]. Au_{20} is a near-double magic cluster with a large HOMO-LUMO gap and a highly symmetric tetrahedral structure [85] while among the medium sized gold clusters, the electronic magic cluster Au_{34} has a large HOMO-LUMO gap but a low symmetry structure [45].

1.3 Adsorption of small molecules on gold clusters

1.3.1 Adsorption of O₂ and CO on gas phase gold clusters

The exceptional catalytic activity of gold at the nanoscale regime prompted interest in understanding the chemical reactivity of gas-phase gold clusters towards adsorption of various molecules. CO oxidation is one of the most extensively studied reactions in which gold clusters exhibit excellent catalytic activity. Among the various factors affecting the catalytic activity, adsorption of CO and O₂ on gold clusters is one of the key issues and has been a subject of numerous experimental and theoretical investigations. An oft-studied process is the variation of the adsorption behaviour of O₂ with the number of electrons in the host gold cluster and consequently its activation which is essential for CO oxidation. This is apparent from the large number of experimental [86-91] and theoretical [92-101] studies on O₂ adsorption on gold clusters. Salisbury *et al.* [86] investigated the adsorption-desorption equilibria of di-oxygen (O₂) on gold cluster anions (Au_N⁻, N=2-22) in the high-pressure limit by pulsed flow-reactor methods at ambient temperature. They observed measurable adsorption of single O₂ molecule for certain clusters (N= 2, 4, 6, 8, 10, 12, 14, 18, 20). Their results suggested that O₂ acts as a single electron acceptor yielding adsorbed superoxide (O₂⁻) species. However, from density functional calculations, Metiu and co-workers [92] observed binding of the second O₂ molecule to clusters with odd number of electrons with binding energy lower than the first O₂ molecule. The anionic gold clusters with odd number of electrons bind O₂ more strongly than neutral clusters with odd number of electrons and clusters with even number of electrons. The effect of surface roughness on the binding of O₂ on Au clusters and Au(111) surface was studied by Mills *et al.* [93] using DFT. From the calculations, they observed that O₂ does not bind to a flat facet while roughening of the Au(111) surface by depositing Au clusters, leads to binding. Localization of the HOMO in clusters and in rough surfaces provides higher electron density at site where O₂ binds; thus facilitates the charge transfer to the π^* of O₂. Over the years, exploring the adsorption characteristics

of O_2 remains an interesting topic of research. Boronat and Corma [97] considered different conformations for O_2 adsorption on extended gold surfaces, isolated gold nanoparticles and small gold clusters supported on TiO_2 and concluded that the mode of O_2 adsorption and its activation does not depend on particle size but on particle morphology. They suggested that the dissociation of O_2 depends on the arrangement of gold surface atoms. For Au/TiO_2 catalysts, it was observed that O_2 preferentially adsorbed on the metal-support interface rather than the gold particles and are the most active sites for O_2 dissociation (Figure 1.6).

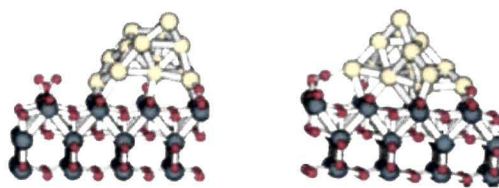


Figure 1.6: Optimized structures of O_2 adsorption complex on metal-support interface [97].

On the basis of density functional calculations, Roldán *et al.* [98] suggested that the presence of charge has a small effect on the bond strength and activation of O_2 for up to about 20-25 atoms. While for larger clusters such as Au_{55} and Au_{79} considered in their work, it was observed that the nuclearity and the shape of the gold cluster are much more important than the charge state, such that bond strengths and activation modes are independent of their charge. Larger nanoparticles with more than 30 atoms consist of positively charged core and a negatively charged shell and were found to simultaneously activate several oxygen molecules owing to the negative charge on the surface [99]. Sun *et al.* [100] proposed that atomic oxygen prefers multifold hole sites on gold surfaces and forms the most stable linear $O - Au - O$ structure which accounts for the observed high diffusion barrier of an oxygen atom. Spectroscopic evidence for the formation of a superoxo species bound to a formally cationic gold cluster as a result of charge-transfer complex in odd sized Au_nO_2 ($n=7,9,11,21$) was presented by Woodham *et al.* [91]. DFT calculations indicated that the charge transfer induces significant rearrangement of the gold cluster such that it more closely resembles the structure of the cation. Thus, they suggested that structural flexibility plays an important role for oxygen activation by small gold particles.

The adsorption behaviour of CO on gold clusters has been another important issue of experimental [102-105] and theoretical [106-114] investigations. The CO adsorption is affected by the cluster charge as reflected from the study by Wu *et al.* [106] where they observed stronger CO adsorption on cationic clusters than on neutral and anionic counterparts. Neumaier *et al.* [103] studied room temperature CO adsorption on isolated gold cluster cations (Au_N^+ , $1 < N < 66$) in a Fourier transform ion cyclotron resonance mass spectrometer. The binding energies were found to decrease with increasing cluster size and at cluster sizes beyond 30 atoms, CO binding energies appeared to approach those found for gold single-crystal surfaces. The decreasing bond energy was attributed to the increasingly "diluted" charge in the metal particle. CO binding to Au atoms with low coordination number of two or three in the head-on fashion has been characterized as the most stable isomer. 2D-3D transition of gold clusters as a result of CO binding was reported by Li and co-workers [108] where they showed that on adsorption of two CO molecules, the planar structure of Au_4^+ is no longer retained; thus signifying a 2D-3D transition. Moreover, DFT based molecular dynamics calculations by Manzoor *et al.* [109] shed light on the effect of cluster charge and ligand on the temperature behaviour of Au_6 cluster. Their simulations revealed that the neutral cluster is stable up to much higher temperature (1100 K) compared to charged clusters (500 K). Higher stability of the neutral cluster has been attributed to enhanced s-d hybridization, higher HOMO-LUMO energy gap and the bonding of the negatively charged inner triangle atoms to the positively charged outer atoms. Their work demonstrated that on chemisorption of CO, the neutral and anionic ground state conformations are stable up to nearly 800K whereas the cationic counterpart collapses at room temperature.

Thus, the charge state, cluster size and presence of specific low coordination binding sites in gold clusters are some of the factors that have been identified on which the adsorption of O_2 and CO depends as revealed by the various experimental and theoretical studies. Presence of supports such as metal oxides, zeolites etc. might alter the adsorption behaviour and has been a subject of investigations. Moreover, the presence of moisture in practical catalytic systems can also affect the adsorption of O_2 and CO and in turn influence the catalytic properties of

supported gold clusters.

1.3.2 Adsorption of O₂ and CO on supported gold clusters

One of the rudimentary processes in understanding the catalytic activity of supported gold clusters towards CO oxidation is the adsorption of O₂ and CO on these catalysts and activation of O₂ is an essential step in CO oxidation. Thus, various experimental [115-119] and theoretical [97,120-126] studies have been made on O₂ adsorption on supported gold clusters. Stiehl *et al.* [115] provided evidence for the presence of molecularly chemisorbed O₂ on both TiO₂(110) supported gold clusters and Au(111) using thermal desorption (TDS), adsorption/reaction-induced desorption and collision-induced desorption (CID). It was observed that O₂ adsorbs much more readily on Au particles than on the Au(111) surface possibly due to the higher concentration of low coordinated sites in the former. From DFT calculations, Rasmussen *et al.* [120] suggested that the adsorption of O₂ on reduced rutile surface was possible only in the presence of bridging oxygen vacancies unlike on stoichiometric rutile TiO₂(110) surface where adsorption was observed to be endothermic. Molina and Hammer [121] observed weaker binding of O₂ and lesser charge transfer on Au₆ cluster supported at a MgO-F⁺ centre compared to free anionic Au₆.

Adsorption of CO on various supported gold clusters has also been investigated by both experimental [127-130] and theoretical [131-136] studies. Gates and co-workers [128] provided the first evidence of Au⁰(CO)₃ species present on the low-coordinated zerovalent Au atoms at the surface of zeolite supported gold nanoclusters from IR data. The sample initially prepared by them consisted of mononuclear gold complexes in zeolite NaY and observed the formation of zero-valent gold nanoparticles during CO treatment. Three new ν_{CO} bands were observed during CO treatment; characteristic of Au⁰-carbonyls and have been assigned to Au⁰(CO)₃ species. Using quantum mechanics/molecular mechanics method, Thomson and co-workers [131] reported favourable adsorption of CO on the Au clusters in TS-1 but the adsorption energies are weakly dependent on the cluster size and on the TS-1 site. Activation of the C-O bond as indicated by the red-shift in CO vibrational frequency results from the electron back-donation

into antibonding orbital in CO. The charge transfer mechanism as proposed by the authors involves first losing of electron density by the TS-1 framework to the adsorbed Au clusters. This excess negative charge on the clusters is then donated to the antibonding CO orbital upon its adsorption. Sierraalta *et al.* [132] studied the interaction of CO molecule with Au-exchanged mordenite catalysts, Au/MOR using hybrid quantum mechanics/molecular mechanics method. It was perceived from their study that the position of Al in the mordenite affects the degree of the back bonding between Au⁺ and the CO molecule such that different ν_{CO} are obtained for CO adsorbed on Au at sites T1 and T4. Moreover, for Au-T1 site, the CO adsorption energy was observed to be slightly greater than for the Au-T4 site because of the stronger overlap between the Au and the CO orbitals. Deka *et al.* [133] studied the adsorption of CO on gas phase and faujasite supported gold monomer in three oxidation states 0, +1 and +3 using DFT. They observed an increase in CO binding energy in gas phase monomer with increase in Au oxidation state. The calculations revealed red-shift in CO vibrational frequency for AuCO and Au³⁺CO complex while blue-shift for Au⁺CO. In case of supported clusters, CO facilitated stronger interaction of gold with the support which increased with oxidation state. The strongest binding of CO to the gold monomer was observed in the +1 oxidation state and ν_{CO} value increases with increasing Au oxidation state.

The studies so far reported thus imply that with sufficient charge transfer, activation of O₂ to superoxo state (O₂⁻) is observed, and O₂ preferentially adsorbs on the metal-support interface rather than the gold particles. On zeolite supported gold clusters, red-shift in ν_{CO} value was observed that indicates CO activation and CO adsorption energy increases with Au oxidation state. Both CO and O₂ prefer low coordination sites of Au clusters for adsorption.

1.3.3 Effect of water on CO and O₂ adsorption

The presence of moisture is inevitable in practical catalytic systems such as supported gold clusters and can affect the adsorption of O₂ and CO on such catalytic systems; in turn, altering their catalytic activity towards CO oxidation. Various studies have investigated the co-adsorption of O₂/CO and H₂O or the effect of pre-

adsorbed water on adsorption of O₂ and CO [137-146]. Gao *et al.* [139] suggested that the promotional effect of water on the catalytic activity of TiO₂ supported Au particles is mainly due to activation of molecular oxygen rather than carbonate decomposition. It was suggested that the binding energy of CO decrease in presence of water. DFT calculations by Zhang and Lindan [140] on the co-adsorption of water and oxygen on the TiO₂ (110) surface indicated enhancement in water binding in presence of co-adsorbed O and a new feasible path for water dissociation was observed. First-principle investigations by Bongiorno and Landman [142] revealed a significant enhancement of the binding and activation of O₂ resulting from the co-adsorption of O₂ and water on small Au clusters (Au₈) supported on defect-free MgO(100), as well as on gas-phase neutral clusters (Au₈ and Au₃₀). The water enhanced activity of gold clusters towards CO oxidation has been attributed to the formation of a complex which involves partial sharing of a proton between the co-adsorbed molecules resulting in a hydroperoxyl-like intermediate. The O-O bond is observed to be highly activated in this complex attaining bond length values characteristic of superoxo or peroxy like states. Reaction with a gaseous CO molecule either via Eley-Rideal or Langmuir-Hinshelwood mechanism (depending on the adsorption site) involved low reaction barriers. Su *et al.* [143] studied the effect of water on the adsorption of O₂, O, CO, dissociation of O₂ and CO oxidation on the Ag(111) and Au(111) surfaces using density functional theory. For the co-adsorption of H₂O and atomic oxygen, significant stabilization with respect to the adsorption of atomic oxygen was observed in presence of water. Strong lateral interaction between water and atomic oxygen on both Ag(111) and Au(111) surfaces has been attributed to the formation of the H bonds and the charge transfer from H₂O to the atomic O mediated through the substrate. For the co-adsorption of H₂O and O₂, the stabilization of the adsorbates has been attributed to the charge transfer mediated through the substrate rather than H bonding interaction which was found to be modest. For H₂O and CO co-adsorption, they observed moderate stabilization of the adsorbates as compared to O₂ and atomic O. Recently, Ito *et al.* [145] demonstrated the enhancement in the adsorption of CO and O₂ molecules on gold dimer cation, Au₂⁺ due to pre-adsorption of a H₂O molecule using tandem mass spectrometry and ion trap methods. They observed adsorption

of up to two O₂ molecules in presence of pre-adsorbed H₂O and has attributed the enhancement effect to partial electron transfer from O atom in H₂O to Au₂⁺.

1.4 Catalysis By Gold

Traditionally, gold is viewed as an element of beauty and wealth and has been appreciated for its luster, malleability and nonreactivity and noncorrosive durability. The earliest report on the use of gold as a catalyst dates back to 1906 when Au gauzes were reported as catalysts for H₂ oxidation [147]. The work of Bone and Andrew [148] in 1925 is one of the earliest reference where Au has been reported as catalyst for CO oxidation. Years later, Huber *et al.* [149] in 1977 reported CO oxidation on Au atom based model and attempted to interrelate the results with actual heterogeneous oxidations of CO to CO₂. In the subsequent years, pioneering work by Haruta *et al.* [150,151] on low temperature CO oxidation opened up new dimension towards catalytic activity of supported gold clusters. Their work showed that ultrafine gold particles dispersed on transition metal oxides were highly active for CO oxidation at temperatures as low as -70°C. The catalytic activity has been attributed to cluster size [152-154] of gold particles. Apart from this, morphology [155], site-specificity [156,157] and electronic state [158-160] of gold clusters are identified as other physicochemical parameters which contribute to the activity of gold. A striking difference of small particles of gold from the bulk is the presence of low coordination atoms [161] and the adoption of geometries which lead to more reactive electronic structures [162]. Thus, catalytic properties of gold nanoparticles can be attributed partly to their geometric structures [163]. In case of supported gold clusters, modification of the electronic properties by the support has been considered as an important factor [150,164,165]. A focus on all the above mentioned factors and the important features in gold catalysis has been well documented [166,167].

1.4.1 Bare gold clusters in CO oxidation

The sensational catalytic performance of bare gold clusters for CO oxidation has been a subject of a number of experimental [168-170] studies. Using pulsed flow

reactor and mass spectrometric techniques, Wallace and Whetten [168] observed cooperative co-adsorption of CO and O₂ on anionic gold clusters in the gas phase, Au_N⁻. Under CO and O₂ co-adsorption conditions, the new peaks that arise in the mass spectrum of Au₆⁻ has been attributed to CO₂ and it is found that Au₆⁻ is capable of oxidizing CO at 100 times higher rate than reported for commercial or model gold catalysts. The evidence for low temperature catalytic oxidation of CO by Au₂⁻ was provided from the combined experimental and theoretical study of Landman and co-workers [169].

Density functional theory based studies [171-177] have played an important role in the exploration of underlying facts and understanding the mechanism involved in CO oxidation on gold clusters. The catalytic activity of a single gold atom has been demonstrated by Fang *et al.* [171] at the CCSD(T)/aug-cc-pVTZ//mPW2PLYP/aug-cc-pVTZ level of theory. They observed a barrier of 4.8 kcal mol⁻¹ at 0K for the first oxidation step and 1.6 kcal mol⁻¹ for the second step. An associative mechanism was observed to be more favourable for CO oxidation while breaking of the O-O bond (dissociative mechanism) involves a very high energy barrier of 68.8 kcal mol⁻¹. Häkkinen and Landman [172] identified di-gold-carbonate as the key intermediate in CO oxidation on Au₂⁻ from the density functional calculations. Reaction of a CO molecule with this intermediate Au₂CO₃⁻ produces two CO₂ molecules simultaneously and an activation barrier of 0.5 eV was identified. On subnanometer Au₁₆-Au₃₅ clusters, Gao *et al.* [173] observed stronger adsorption of O₂ as well as the co-adsorption of CO and O₂ in the anionic clusters and consequently lower reaction barrier as compared to the neutral counterparts. Relatively small cone angle (<110°) associated with each surface site has been identified as another important geometric indicator of relatively strong adsorption strength of CO or O₂. To provide an insight into the catalytic activity of large-sized nanoclusters, Tang and Hu [174] studied the charge and spin state effect on the catalytic activity of Au₅₅ towards CO oxidation. The formation of a peroxo-type (OOCO) intermediate was predicted as the rate limiting step in the Langmuir-Hinshelwood mechanism and the catalytic activity of the anionic cluster was better than the neutral and cationic counterparts. However, the triplet pathway involved lower barriers than the singlet pathway in case of

Au₅₅⁻. DFT study on three decahedral Au clusters (Au₇₅, Au₁₀₁ and Au₁₄₆) by Liu *et al.* [175] included the effect of an external electric field on their catalytic activity. Au₇₅ corresponds to the moderate stable structure while Au₁₄₆ is the most stable. Their work showed that looser binding of the reactants could benefit for catalyzing CO oxidation. Among the three clusters, Au₇₅ performs the best in this catalytic reaction due to the weakest adsorption capacity and the large activation barriers in the higher clusters. A moderate intensity negative field balances between exothermic adsorption and low activation energy; thus making it a better option. With the advancement in computational methods and experimental techniques, the urge to study the catalytic properties of gold clusters ranging in size from small to large clusters continues so as to obtain an improved realistic catalyst.

1.4.2 Supported gold clusters in CO oxidation

Gold clusters supported on various transition metal oxides and zeolites have been recognized as exceptionally active catalysts for low temperature CO oxidation. The major breakthrough in understanding the catalytic activity of supported gold clusters originated with the work of Haruta *et al.* [150,151] on 3d-transition metal oxide supported ultra-fine gold particles. Since then, the activity of gold clusters supported on various oxides towards CO oxidation has been studied with different experimental techniques [178-185]. Among the various factors such as particle shape, nature of support etc. on which the catalytic activity of Au nanoparticles for CO oxidation depends, particular emphasis has been laid on the size of Au clusters. A marked increase in the catalytic activity of supported Au clusters was observed when the diameter of the Au clusters is decreased below ~ 3.5 nm. However, a further decrease in the cluster diameter to below ~ 3 nm decreases the catalytic efficiency [185]. Aguilar-Guerrero and Gates [178] observed the initially synthesized mononuclear cationic gold species on CeO₂ to be slightly active as a catalyst for CO oxidation. But after a short period of operation, the catalyst underwent activation to form clusters as small as Au₆, on average, and was inferred to be non-metallic. Their work proposed better catalytic activity of the clusters, at least on the CeO₂ support. Gold octamer cluster Au₈ supported on defect

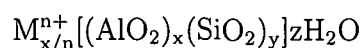
rich MgO(001) has been identified as the smallest cluster to catalyze the low temperature CO oxidation to CO₂. The catalytic activity has been attributed to the charging of the metal cluster caused by partial transfer of charge from the substrate oxygen vacancy F-centre defect into the deposited cluster. On the other hand, the same cluster bound to a MgO surface without oxygen vacancy has been found to be catalytically inert for CO oxidation [180,181].

Over the years, density functional theory based calculations have helped in understanding the various factors influencing the catalytic activity of supported gold catalysts such as the importance of low coordinated sites [186-188], size and shape of supported gold clusters [189], role of oxide support [190-193], perimeter sites [194], oxidation state of Au [195] etc. The urge to investigate the catalytic activity of various gold-based catalysts supported on different metal oxides continues and everyday new research has been focused in developing such catalysts.

1.4.3 Zeolite supported gold clusters

1.4.3.1 Zeolites-Structure and Property

An appealing and unique class of host materials with well-defined cavities and channels is *zeolites* which bestow them with excellent shape- and size-selectivity property. Zeolites are crystalline aluminosilicates with the general composition



where M^{n+} is a cation with charge $n+$ and x, y, z are numbers [196]. The term zeolite, originally coined by Swedish mineralogist *Axel Fredrik Cronstedt* in 1756 means *boiling stone*. These porous crystalline materials are composed of SiO₄ and AlO₄ tetrahedra which combine in a variety of ways to give rise to different structures. When twenty-four primary building blocks, SiO₄ and AlO₄ arrange to form a truncated octahedron, the resulting secondary building block is known as sodalite cage (Figure 1.7).

In faujasite zeolites, each sodalite cage is connected to four other sodalite cages and each connecting unit is six bridging oxygen ions (form hexagonal prism) that



Figure 1.7: Structures of (a) primary building block, SiO_4 tetrahedra and (b) secondary building block, sodalite cage of zeolites.

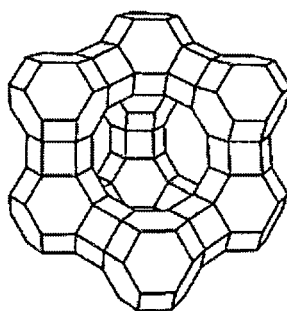


Figure 1.8: Framework structure of faujasite zeolite.

link the hexagonal faces of two sodalite cages. Sometimes, the tetrahedra can arrange to form chain-type building block which then connect to form a layer. Such structure consists of rings with five O atoms and hence the name pentasil is used to describe them. Examples of zeolites included in this category are: Silicalite, ZSM-5, ZSM-11. Faujasites find largest-scale application in catalysis and includes Zeolite X and Zeolite Y. The three-dimensional pore structure is relatively large with a diameter of 0.74 nm and comprises of twelve membered oxygen rings such that selective transport of molecules are allowed. The supercage has a diameter of 1.2 nm and is surrounded by 10 sodalite cages. The framework structure of faujasite zeolite is shown in Figure 1.8. When a Si atom of the zeolite framework is replaced with an Al atom, it generates an excess negative charge which when compensated with a proton attached to the oxygen atom connecting neighbouring Si and Al atom results in a Brønsted acid site. Four positions in the faujasite zeolites have been identified for charge compensating cations: in the centers of hexagonal prisms, in the sodalite cages across the hexagonal faces, in the supercages near unjoined hexagonal faces and in supercages but farther from hexagonal faces.

The cations located in the supercages are easily accessible to reactants and hence are involved in catalysis [197]. These cations act as Lewis acid site and the negative charge bearing framework oxygen atoms behave as basic sites. As the amount of aluminium in the zeolite structure increases the concentration of acid sites also increases while the strength of the acid sites is greater when the amount of aluminium is lower. Thus, the Si/Al ratio is an important factor in acidity of zeolites. Zeolites find widespread application as cracking catalysts of higher hydrocarbons [198-202]. Over the years, both experimental [203-206] and theoretical [207-211] studies have been made on various aspects of zeolites.

1.4.3.2 CO oxidation on zeolite supported Au

With pores and cavities of molecular dimensions and adjustable acidic properties, zeolites form a fascinating class of solid support. Their ability to disperse gold, because of the internal distribution of the pores and the aptness to control particle size, makes them a promising type of solid support for gold nanoparticles. The catalytic activity of gold nanoparticles supported on zeolites towards CO oxidation has been studied using different experimental methods [212-222]. The earliest report concerning zeolite supported gold clusters was the work of Boudart and Meitzner [212]. The size of the gold particles in Y-zeolite was found to be compatible with their location inside the zeolite lattice. The size of the clusters increased with thermal treatment and the authors attributed this to the migration of the particles to the outside of the zeolite crystallite. Later, Fraissard and co-workers proposed [213], for the first time, a method to prepare small, thermally stable gold particles located inside NaHY zeolite. The effects of preparation conditions such as chloroauric acid concentration, pH of gold solution, solution temperature, and mixing time on zeolite supported gold (Au/Y) for CO oxidation was studied by Lin and Wan [214]. Higher catalytic activity of Au/Y catalyst was found with gold species prepared in the supercage of Y-type zeolite. Chen *et al.* [215] prepared nano-gold in Y, β and mordenite zeolites and observed that Y-zeolite with more aluminium loading showed no aggregation of the gold particles with size around 1 nm. The high activity of Au/Y catalyst and its stability for CO oxidation has been attributed to the cage-like pores in Y-zeolite with high aluminium content

that prevented sintering of gold and the hydrophilic surface favoured activation of gold species. Roduner and co-workers [216] observed the stabilization of the unusual Au(II) oxidation state in zeolite Y supercage for the first time using electron spin resonance (ESR). The authors concluded that confinement within the zeolite pores stabilized this unusual oxidation state of Au and prevented it from undergoing disproportionation.

The oxidation state of the active gold species in zeolite supported gold catalysts remains controversial [217-219]. The role of cationic gold in CO oxidation catalysis was investigated by Fierro-Gonzalez and Gates [218] in their work on mononuclear Au^{III} and Au^I complexes bonded to NaY zeolite but without zerovalent gold. It was observed that reduction of Au^{III} to Au^I was accompanied by the consequent decrease in catalytic activity which implied that Au^I is less reactive than Au^{III} at 298 K under the studied reaction conditions. The EXAFS spectrum indicated that gold remained in the mononuclear form without forming clusters. The crystalline structure of the zeolites limited the migration of the entrapped gold clusters (formed when the supported gold complexes were treated at very high temperatures) [220]. However, Simakov *et al.* [219] have identified two types of active sites of gold in Y-zeolite for CO oxidation- partly charged gold clusters Au_n^{δ+} and gold nanoparticles Au_m⁰. Using aberration corrected scanning transmission electron microscopy (STEM), Lu *et al.* [221] demonstrated that zeolite serve as a suitable catalyst for dispersed gold catalyst with a high degree of uniformity. The catalytic sites were identified as site-isolated gold complexes and that the site-isolation of the gold complexes was retained after CO oxidation catalysis which supports the inference that the gold species were stabilized by their confinement in the zeolite channels.

In comparison to the large volume of the experimental work on the catalytic activity of zeolite supported Au towards CO oxidation, theoretical investigations are quite scarcer and some studies have been focused on CO adsorption on zeolite supported gold [135, 223-225]. Griffe *et al.* implemented density functional calculations to study CO oxidation on silicoaluminophosphates (SAPO) molecular sieves supported Au, Au₂ [224] and Au₃₋₅ [225]. Their results indicated exothermicity of the oxidation reaction on both Au/SAPO-11 species and an Eley-Rideal

mechanism where gas phase O_2 reacts with adsorbed CO [224]. CO adsorption and oxidation was studied on $Au_{3-5}/SAPO-11$ using hybrid QM/MM method [225]. Lack of theoretical understanding of the catalytic CO oxidation on zeolite supported Au clusters necessitates it to be properly addressed. The present thesis attempts to provide a theoretical insight into the CO oxidation mechanism over zeolite supported small Au clusters.

1.4.4 Activity of gold clusters towards water-gas shift reaction

The water gas shift reaction, $WGSR(CO + H_2O \rightarrow CO_2 + H_2)$ plays a pivotal role in providing high-purity hydrogen for fuel cell and numerous industrial applications [226,227]. The commercially available low-temperature heterogeneous WGS catalysts do not meet the stringent requirements of high activity and structural stability in air and in cyclic operations [228]. The commercially used WGS catalyst, Cu-ZnO suffers from drawbacks such as its sensitivity to temperature excursions, air exposure (pyrophoric), and water condensation during shutdown; thus making it unsuitable for fuel cell applications [229]. Alternative to Cu-ZnO, cerium oxide based catalysts have been investigated for WGS. Presence of a small amount of a transition metal significantly enhances the reducibility and catalytic activity of ceria and platinum (Pt) was one of the earliest metal additives with considerable effect on ceria reducibility [230]. The high cost associated with Pt-based catalysts and the deactivation of Pt – CeO_2 catalysts when used in realistic WGS streams [231] made it desirable to develop useful alternatives to it. Li *et al.* [232] have reported a Cu-ceria catalyst that is more stable than Cu-ZnO-based LTS catalysts and exhibits high WGS activity and structural stability at temperatures as high as 600°C.

The unusual and unanticipated catalytic properties of nano sized gold in contrast to bulk gold makes it one of the central tenant in the field of catalytic research. The high activity of gold catalysts towards WGS reaction was first made by Andreeva *et al.* [233,234] using Au/Fe_2O_3 at low temperatures. Under same conditions, Au/Fe_2O_3 catalyst exhibited better activity than the most efficient low temperature WGS catalyst, $CuO/ZnO/Al_2O_3$. Excellent WGS catalyst

resulting from Au supported on ceria was first reported by Fu *et al.* [235] and since then this catalytic system has been extensively studied [228,236-239]. Experimental evidence pertaining to the role of oxidized Au in the WGS reaction was provided and it was proposed that the metallic Au⁰ particles are mere spectators [228]. They characterized the active species as Au cations using x-ray photoelectron spectroscopy (XPS). Liu *et al.* [240] concluded from DFT studies that the active sites in the Au-ceria catalysts are neither single Au atoms nor sizeable Au particles, but ultra-small Au clusters. In a recent work by Song and Hensen [241], it was shown that the CeO₂(110) supported Au nanorod exhibits better activity than the single Au atom for WGS reactivity. The carboxyl mechanism has been proposed as the dominant pathway for the low temperature reaction instead of the redox mechanism. A novel and more active Au/TiO₂ catalyst which exhibits low temperature activity for both forward and reverse water-gas shift reactions was reported by Haruta and co-workers [242]. Apart from this, catalytic activity of gold particles dispersed on titania has been investigated by different experimental and theoretical studies [242-244]. In addition, Au particles supported on various other oxides such as ZrO₂, Al₂O₃ etc. as well as mixed oxides have been used as catalysts for WGS reaction [245-247]. Although the WGS reaction on different supported gold catalysts has been extensively studied, no definite consensus on the mechanism as well as the active gold site has been reached. The various factors affecting the WGS reaction on supported gold catalysts such as the effect of particle size, effect of the support, preparation method, active site [248,249], location of the gold species which is critical both in terms of stability and low temperature activity, detailed insight into the reaction mechanism [250] have been reviewed in detail.

In comparison to the large volume of work reporting the activity of gold supported on different metal oxides towards WGS reaction, investigation of zeolite supported gold is very meagre. Mohamed and Ichikawa [251] used *in situ* FTIR spectroscopy to identify the adsorbed species derived from CO + H₂O and CO + O₂ reactions on H-mordenite-encapsulated gold catalysts. On Au/H-mordenite, they characterized a monodentate formate species while performing WGS reaction from the well-developed absorption bands in the 3000 to 2800 cm⁻¹ range along with

the 1690 and 1340 cm^{-1} asymmetric and symmetric stretching bands of the COO^- group, respectively. Contrary to this, on H-mordenite WGS reaction proceeded through the formation of a bidentate formate species. It was observed that the activation energy for the formate decomposition to products, CO_2 and H_2 , was lower in Au/H-mordenite (40.1 kJmol^{-1}) compared to H-mordenite (63.3 kJmol^{-1}) emphasizing the higher decomposition rate in the former. It was thus, suggested that the reaction is more facile when Au is encapsulated in the H-mordenite zeolite. In another study by the same group [252], reaction intermediates in the WGS reaction on Au^{n+} ($1 \leq n \leq 3$) incorporated into NaY, Na-mordenite, and Na-ZSM-5 zeolites has been studied by means of *in situ* FT-IR spectroscopy. They have identified a unidentate formate species on Au^+/NaY from the characteristic bands observed at 1620 and 1340 cm^{-1} which further decomposed to CO_2 and H_2 . Au^+ has been identified as the active site that interacts with the dissociative H_2O molecules giving monodentate formate as the intermediate. They observed that on the Au/NaY surface, formate species formed exclusively while on Au/Na-mordenite, carbonate and organic-like carbonate species also formed. This has been attributed to the lower Si/Al ratio in NaY, leading to a lower average negative charge sitting on the lattice oxygen atoms to decrease considerably the amount of formed carbonate species. The highest activity towards WGS reaction was observed in NaY catalyst and involved activation energy of 64.1 kJ mol^{-1} . Participation of the Au^+ and Au^0 dual site for WGS reaction when encapsulated inside NaY zeolite was suggested. Much higher concentration of water was found to decrease the catalytic activity because of the masking of the active sites.

A few theoretical studies have investigated the catalytic activity of unsupported Au nanoparticles such as Au_2 , Au_{38} etc. towards WGS reaction. DFT study by Wang *et al.* [253] on the WGS reaction promoted by neutral and charged gold dimer clusters signified the role of cluster charge on the catalytic activity. The barriers calculated for the neutral and anionic clusters were higher than those in the cationic clusters and on all the three clusters, irrespective of the charge state; the formate mechanism was feasible rather than the redox mechanism. Liu and Rodriguez [254] have attributed the presence of low coordinated corner and edge sites in addition to the fluxionality of the particles as factors contributing to the

higher activity of nanoparticles[Au₂₉ and Cu₂₉] than their parent bulk surfaces [Au(100) and Cu(100)]. In all the systems, water dissociation remained the rate limiting step. DFT study on the catalytic activity of Au₃₈ cluster towards WGS reaction indicated better activity of this cluster when compared to Au(100) and Au₂₉ based on the lower barrier associated with the rate limiting water dissociation step (Au₃₈: 31.41 kcal mol⁻¹; Au(100): 35.28 kcal mol⁻¹ and Au₂₉: 32.05 kcal mol⁻¹). Desorption of H₂ was observed to occur more readily on the Au₃₈ cluster [255].

1.5 Single Atom Catalysis

The concept of single atom catalysis has recently gained impetus and has become one of the central tenants in the field of catalytic research which is reflected from the numerous reports [256-259] on the activity of single atom supported on different materials towards reactions such as CO oxidation. The attraction towards single atom catalysis has evolved so as to maximize the efficiency of metal utilization. It has been proposed that catalysts with well-defined single active centres are necessary to understand the catalytic mechanisms better unlike the multiple active sites of subnanoclusters which are not always the most desirable centres for catalytic processes. Single atom catalysts have evolved as an effective way to utilize each and every metal atom of supported metal clusters [260]. A novel iron oxide supported single Pt atom catalyst was synthesized by Qiao *et al.* [261] which exhibited excellent stability and high catalytic performance for both CO oxidation and preferential oxidation of CO in H₂.

Catalysis by single gold atom has also been reported for reactions such as CO oxidation, water gas shift reaction etc. Recently, Mao *et al.* [262] reported catalytic activity of a single Au atom embedded in a 2D h-BN monolayer using density functional theory along with molecular dynamics and microkinetic analysis. Activation of O₂ involved low barrier and the rate determining step was the formation of two CO₂ molecules from an OOCAuCOO intermediate obtained in their work. They concluded from their study that this supported single Au atom has a potential for CO oxidation. In another recent work, Li *et al.* [263]

observed the catalytic activity of single Au atoms supported on aluminium oxide clusters using mass spectroscopy and density functional calculations. Gates *et al.* [218,220] have identified single cationic Au centre as the active site for CO oxidation on mononuclear Au^{III} and Au^I complexes supported on faujasite using experimental techniques. Bare single gold atom has been demonstrated to be good catalyst towards CO oxidation by Fang *et al.* [171] at the CCSD(T)/aug-cc-pVTZ//mPW2PLYP/aug-cc-pVTZ level of calculation. The adsorption and catalytic activation of O₂ which is an important step for oxidation reactions has been observed on Au and Au₂ supported on h-BN surface as a consequence of charge transfer [264]. The catalytic activity of isolated Au atoms supported on titania has been reported for water gas shift reaction at low temperatures and the catalyst exhibited good stability at temperatures up to 473 K [244]. An important point that needs to be considered is that the availability of only a single site in these catalysts can at some times limit the applicability of single atom catalysts for processes requiring multiple active sites. However, deeper insight in utilizing the novel properties derived from single atom catalysts will provide new dimension in the field of heterogeneous catalysis. It is believed that investigation of such fundamental aspects at the atomic level will help understand these phenomena at larger clusters better.

1.6 Objectives of The Present Work

The present Ph.D. work was undertaken with the following objectives:

1. DFT studies on hydrogenated gold clusters and the phenomenon of reverse hydrogen spillover on zeolite supported gold and palladium clusters.
2. Theoretical studies of the adsorption of carbon monoxide and oxygen on gas phase gold clusters and carbon monoxide oxidation.
3. Theoretical studies of the adsorption of carbon monoxide and oxygen on zeolite supported gold monomer in three oxidation states and the effect of moisture on their adsorption using hybrid QM/MM methodology.

4. DFT studies of CO oxidation and Water-Gas Shift reaction on zeolite supported gold monomer in three oxidation states using hybrid QM/MM methodology.

Chapter 2

Basic Electronic Theory

Quantum Physics thus reveals a
basic oneness of the universe

Erwin Schrödinger

2.1 Introduction

Quantum mechanics is the explicit mathematical description of the behaviour of very small particles such as electrons and nuclei of atoms and molecules and thus of the chemistry. In theory, quantum mechanics can predict any property of an individual atom or molecule exactly. It was formulated over 100 years ago and emerged as an outcome of the failure of classical mechanics to describe the behaviour of atomic and sub-atomic particles. On one hand, the *ab-initio* and *semi-empirical* approaches are quantum mechanical methods which calculate molecular wave function and thus represent wave function methods. Density functional theory (DFT), on the other hand is based on the premise that the energy of an electronic system can be defined in terms of electron probability density. Dating back to the foundations of density functional theory in 1920s with the early works of Thomas and Fermi, DFT has evolved as one of the most powerful quantum mechanical methods for the electronic structure calculations of molecular and condensed matter systems. It was developed in the 1960s with the work of Hohenberg, Kohn and Sham

and since then density functional theory has been widely used. The 1998 Nobel Prize for chemistry was awarded to Walter Kohn for the development of density functional theory along with John Pople for his role in developing practical wave function based methods. In this chapter, we shall provide a brief insight in to the various computational approaches used for electronic structure calculations of materials.

2.2 Computational Chemistry Perspective

Computational methods are a bridge between theoretical models and experimental results. Apart from providing results comparable with experimental values, e.g. to equilibrium geometries, binding energies, vibrational frequencies or photoelectron spectra, they also offer supplementary information that are not available directly from experiment. Computational chemistry can be defined as the implementation of chemical, mathematical and computing expertise to obtain solution of interesting chemical problems. Useful information such as properties of molecules or simulated experimental results is generated by computers. In simpler words, one can define computational chemistry as chemistry performed with computer rather than chemicals. The behaviour of real systems can be simulated with the use of intellectual models and improving these models help in describing the atoms and molecules in the real world more accurately. Computational chemistry software can be utilized to perform:

- determination of electronic structure
- geometry optimizations
- frequency calculations
- definition of transition structures and reaction paths
- protein calculations, i.e. docking
- calculations of electron and charge distributions
- calculations of potential energy surfaces (PES)

- calculations of rate constants for chemical reactions (kinetics)
- thermodynamic calculations- heat of reactions, energy of activation, etc
- calculation of many other molecular and bulk physical and chemical properties.

Ab-initio, semi-empirical, molecular mechanics, molecular dynamics and Monte Carlo are the most important numerical techniques and understanding these techniques is crucial to understand the use of computational methods in chemistry. In the present thesis, we have employed density functional theory (DFT) based quantum mechanics (QM) and hybrid quantum mechanics/molecular mechanics (QM/MM) methods to perform all the calculations. A brief discussion of the methods is given in the following sections. Before moving into the various methods, another important concept that occupies a central position in the field of computational chemistry calculations is the Potential Energy Surface.

2.3 Potential Energy Surface

Potential Energy Surface (PES) can be defined as a mathematical or graphical representation between the energy of a molecule (or a collection of molecules) and its geometry. Or in other words, potential energy surface is mathematical function that gives the energy of a molecule as a function of its geometry (one or more geometrical parameter(s)). Example: For a di-atomic molecule A-B, the only parameter on which the change in energy with changing geometry depends is the bond length. The graph representing the change in potential energy of the di-atomic molecule with change in bond length is a 1D-PES. Likewise, if the energy of the molecule depends on two parameters, the resulting PES is a 2D-PES. An important characteristic of a PES is the *stationary point*; which can be defined as a point on the PES at which the surface is flat i.e. parallel to the horizontal line (or plane) corresponding to the geometrical parameter(s).

Mathematically, the first derivative of the potential energy with respect to each geometrical parameter at the stationary point is zero:

$$\frac{\partial E}{\partial q_i} = 0 \quad (2.1)$$

Minima are those stationary points that correspond to actual molecules with a finite lifetime while transition states are points on the PES that exist for an instant. The lowest energy minimum on the whole PES is the *global minimum* while a minimum relative to the neighboring points on the PES is a *local minimum*. The lowest energy pathway linking two minima is the *Intrinsic Reaction Coordinate* (IRC) with a saddle shape. A transition state is called a *saddle point* (at the center of the saddle-shaped surface) links two minima and represents a maximum along the IRC, but along all other directions it is a minimum. A minimum, on the other hand, is a minimum along all the directions.

From the second derivatives, for a minimum,

$$\frac{\partial^2 E}{\partial q^2} > 0 \text{ for all } q$$

For transition state:

$$\frac{\partial^2 E}{\partial q^2} < 0 \text{ along IRC}$$

$$\frac{\partial^2 E}{\partial q^2} > 0 \text{ for all } q, \text{ except IRC}$$

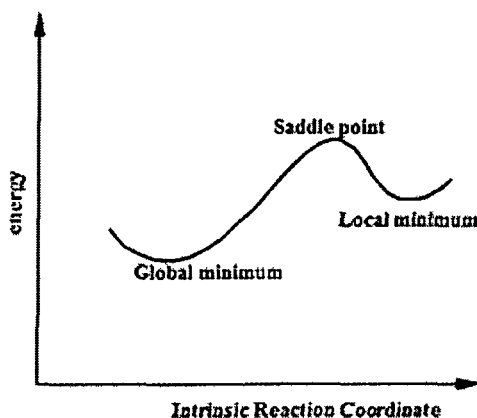


Figure 2.1: Various stationary points on an intrinsic reaction coordinate.

The saddle point on the IRC for which the second derivative of energy with respect to one and only one geometric coordinate is negative is a transition state whereas points where the second derivative is negative with respect to more than one coordinate are called *higher-order saddle points* or *hilltops*. Figure 2.1 shows the various stationary points on an intrinsic reaction coordinate.

2.4 Molecular Mechanics

Molecular mechanics employs a model of a molecule comprising of spheres of different masses (atoms) held together by a variety of springs of different lengths and stiffness (bonds) and is thus referred to as the ball and spring model. Molecular mechanics uses the parameters such as bond stretching and bond bending force constants and also interaction between non-bonded atoms to construct a potential energy expression that is a function of the atomic positions. It predicts equilibrium geometries and relative energies by minimizing the potential energy expression for various conformers. Westheimer, Hendrickson, Wiberg, Allison, Warshel and others have been accredited for development of the method, and is applicable to ground electronic states. Electrons are not considered explicitly but each atom (the atomic nucleus and the associated electrons of the atom) is treated as a single particle in molecular mechanics and hence, electronic effects get involved in the force fields through parameterization. Therefore, molecular mechanics is not very useful in chemical problems wherein electronic effects are critical viz. bond-breaking or bond-forming. Instead, it is appreciated in large systems for predicting the potential energy of a particular conformation. The quantum aspects of nuclear motion is neglected and the dynamics of the atoms is treated by classical mechanics i.e. Newton's second law. The Born-Oppenheimer approximation is implicitly used so that nucleus experience a static attractive force, whether from electrons or springs and henceforth, the molecule has a distinct geometry. The principle behind molecular mechanics is to express the energy of a molecule as a function of its resistance toward bond stretching, bond bending, and atom crowding, and to use this energy equation to find the bond lengths, angles, and dihedrals corresponding to the minimum-energy geometry or more precisely, to the various possible potential energy surface minima. Mathematically, the total potential energy or steric energy is expressed as the sum of the bond stretching energy E_{str} , angle bending energy E_{bend} , torsion energy E_{tors} , out of plane bending E_{oop} , interaction between these motions E_{cross} , van der Waals attraction and repulsion between non-bonded atoms E_{vdW} and electrostatic interaction between atoms E_{ele}

$$E = E_{str} + E_{bend} + E_{oop} + E_{tors} + E_{cross} + E_{vdW} + E_{ele} \quad (2.2)$$

The explicit expressions for the potential energy terms contain parameters and the specified set of equations and parameters is defined as molecular mechanics force field since the derivatives of potential energy functions determine the forces on the atoms.

A force field assigns the atoms in a molecule to the available atom types depending on the atom's atomic number and molecular environment. The various force fields available vary with respect to three factors viz. the functional form of each energy term, of cross terms included, and the type of information used for fitting the parameters. Examples of some commonly used force fields include MM2, MM3, AMBER, CHARMM, CVFF, CFF91, and UFF. Some of the main applications of MM can be outlined as:

1. To calculate geometries and energies of systems with thousands of atoms viz. biological macro-molecules like DNA, proteins, organic compounds and polymers.
2. To calculate geometries and energies of transition states.
3. To generate the potential energy function under which molecules move for molecular dynamics calculations.

Advantages

1. Molecular mechanics calculations are fast and can be carried on with limited resources-computationally not expensive.
2. Treat large systems such as bio-molecules.
3. With good parameters, appreciable prediction of geometries and relative energies can be made within a short span.

Disadvantages

1. Do not calculate electronic properties and processes involving electronic effects such as bond breaking and bond making.

2. Applicable to a limited class of molecules.
3. Force field methods are zero dimensional. The probable error cannot be accessed within the method. It relies on experimental (or *ab-initio*) data for parameters.

2.5 Quantum Mechanics

Ab initio calculation focuses on solving the Schrödinger equation without relying on calibration against measured chemical parameters and hence its name meaning "from the first" [Latin], from first principles. Hartree-Fock (HF), Möller-Plesset perturbation theory (MP), Configuration Interaction (CI), Coupled Cluster (CC) method and Density Functional theory (DFT) are *ab initio* methods. Born-Oppenheimer approximation forms an indispensable part to solve the Schrödinger equation by simplifying the calculations as the electrons are considered to move in a field of fixed nuclei. The ground for such approximation is that the nucleus is much more sluggish than the electrons (a hydrogen nucleus is 1837 times more massive than an electron). Thus, solving the electronic Schrödinger equation with nuclear positions as parameters forms the essential computational task. For complex many-electron systems, each electron is assumed to perceive all others as an average field that is the fundamental assumption of Hartree-Fock theory. Although this has satisfactory accuracy but neglecting electron correlation can have profound chemical consequences in determining accurate wavefunctions and properties derived from it. Hartree-Fock theory constitutes a stepping stone for the more refined subsequent theories that come closer to the accurate solution of the Schrödinger equation.

2.5.1 Hartree-Fock Method

The many-body time-independent Schrödinger equation can be expressed as:

$$\hat{H}\psi_i(\vec{x}_1, \vec{x}_2, \dots, \vec{x}_N, \vec{R}_1, \vec{R}_2, \dots, \vec{R}_M) = E_i\psi_i(\vec{x}_1, \vec{x}_2, \dots, \vec{x}_N, \vec{R}_1, \vec{R}_2, \dots, \vec{R}_M) \quad (2.3)$$

where \hat{H} is the Hamiltonian operator for a molecular system consisting of M nuclei and N electrons in the absence of magnetic or electric fields. The differential

operator \hat{H} represents the total energy given as:

$$\hat{H} = -\frac{1}{2} \sum_{i=1}^N \nabla_i^2 - \frac{1}{2} \sum_{A=1}^M \frac{1}{M_A} \nabla_A^2 - \sum_{i=1}^N \sum_{A=1}^M \frac{Z_A}{r_{iA}} + \sum_{i=1}^N \sum_{j>i}^N \frac{1}{r_{ij}} + \sum_{A=1}^M \sum_{B>A}^M \frac{Z_A Z_B}{R_{AB}} \quad (2.4)$$

Here, A and B denote M nuclei, while i and j denote the N electrons in the system. The first two terms describe the kinetic energy of the electrons and the nuclei, respectively and the Laplacian operator ∇_q^2 can be defined as a sum of differential operators:

$$\nabla_q^2 = \frac{\partial^2}{\partial dx_q^2} + \frac{\partial^2}{\partial dy_q^2} + \frac{\partial^2}{\partial dz_q^2} \quad (2.5)$$

The rest of the terms represents the potential part and the third term stands for nucleus-electron attractive electrostatic interaction while the other two for the electron-electron and nucleus-nucleus repulsive interactions, respectively.

$\psi_i(\vec{x}_1, \vec{x}_2, \dots, \vec{x}_N, \vec{R}_1, \vec{R}_2, \dots, \vec{R}_M)$ stands for the 'i' th state of the system and depends on 3N spatial coordinates $\{\vec{r}_i\}$ and N spin coordinates $\{S_i\}$ of the electrons, which are collectively denoted by $\{\vec{x}_i\}$. It also depends on 3M spatial coordinates of the nuclei $\{\vec{R}_i\}$. The wavefunction ψ_i contains all the information that can possibly be known about the quantum system and E_i is the numerical value of the energy of the state described by ψ_i .

As a consequence of the Born-Oppenheimer approximation, kinetic energy of the nuclei is zero and the potential energy due to the nucleus-nucleus repulsion is a constant. Thus, the Schrödinger equation can be expressed as:

$$\hat{H}_{elec} = -\frac{1}{2} \sum_{i=1}^N \nabla_i^2 - \sum_{i=1}^N \sum_{A=1}^M \frac{Z_A}{r_{iA}} + \sum_{i=1}^N \sum_{j>i}^N \frac{1}{r_{ij}} \quad (2.6)$$

Equation 2.6 is the electronic Hamiltonian. The nucleus-nucleus repulsion is added as a separate constant term later. The total energy is then the sum of electronic energy, E_{elec} and the constant nuclear repulsion term. In Hartree-Fock method, an approximation to the many-electron wavefunction is done by considering the N-electron wavefunction as an anti-symmetric product of N one-electron wavefunctions, $\chi_i(x_i)$. This product is referred to as the Slater determinant, Φ_{SD} and has been used as an approximation to the exact wavefunction, ψ_{exact} .

$$\Phi_{SD} = \frac{1}{\sqrt{N!}} \begin{vmatrix} \chi_1(\vec{x}_1) \chi_2(\vec{x}_1) \dots \chi_N(\vec{x}_1) \\ \chi_1(\vec{x}_2) \chi_2(\vec{x}_2) \dots \chi_N(\vec{x}_2) \\ \dots \dots \dots \\ \chi_1(\vec{x}_N) \chi_2(\vec{x}_N) \dots \chi_N(\vec{x}_N) \end{vmatrix} \quad (2.7)$$

or,

$$\Phi_{SD} = \frac{1}{\sqrt{N!}} \left| \chi_1(\vec{x}_1) \chi_2(\vec{x}_2) \dots \chi_N(\vec{x}_1) \right| \quad (2.8)$$

One-electron functions $\chi_i(x_i)$ are called spin orbitals which are composed of spatial orbital $\phi_i(r_i)$ and one of the two spin functions $\alpha(s)$ or $\beta(s)$. The physical significance of spin orbitals is that $|\chi(\vec{x})|^2 dx^2$ represents the probability of finding the electron with spin given by σ within the volume element dr . The pre-factor $\frac{1}{\sqrt{N!}}$ is given so that Φ_{SD} fulfills the normalization condition. The anti-symmetry of the Slater determinant is decided from the fact that upon exchange of two rows or columns the determinant changes sign. In order to find the best Slater determinant, Φ_{SD} that will yield the lowest energy, variational principle is used keeping in view that the spin orbitals remain orthonormal.

$$E_{HF} = \min_{\Phi_{SD} \rightarrow N} E[\Phi_{SD}] \quad (2.9)$$

The final Hartree-Fock energy is given by:

$$E_{HF} = \left\langle \Phi_{SD} | \hat{H} | \Phi_{SD} \right\rangle = \sum_i^N (i|\hat{h}|i) + \frac{1}{2} \sum_i^N \sum_j^N (ii|jj) - (ij|ji) \quad (2.10)$$

where,

$$(i|\hat{h}|i) = \int \chi_i^*(\vec{x}_1) \left\{ -\frac{1}{2} \nabla_2^2 - \sum_A^M \frac{Z_A}{r_{1A}} \right\} \chi_i(\vec{x}_1) d\vec{x}_1 \quad (2.11)$$

Equation (2.9) gives the contribution to the kinetic energy of electron and nucleus-electron attraction.

$$(ii|jj) = \int \int |\chi_i(\vec{x}_1)|^2 \frac{1}{r_{12}} |\chi_j(\vec{x}_2)|^2 d\vec{x}_1 d\vec{x}_2 \quad (2.12)$$

$$(ij|ji) = \int \int \chi_i(\vec{x}_1) \chi_j^*(\vec{x}_1) \frac{1}{r_{12}} \chi_j(\vec{x}_2) \chi_i^*(\vec{x}_2) d\vec{x}_1 d\vec{x}_2 \quad (2.13)$$

Equations (2.12) and (2.13) are the so-called *columb* and *exchange* integrals, respectively and represent the interaction between two electrons. E_{HF} in equation (2.10) is a functional of the spin orbitals

$$E_{HF} = E[\{\chi_i\}] \quad (2.14)$$

The condition that the spin orbitals must remain orthonormal during energy minimization introduces the Lagrangian multipliers, ϵ_i in the resulting Hartree-Fock equations which yield the best spin orbitals giving the lowest E_{HF} value.

$$\hat{f}\chi_i = \epsilon_i\chi_i \quad i = 1, 2, \dots, N \quad (2.15)$$

Equation (2.15) yields a set of eigenvalue equations; where Lagrangian multipliers, ϵ_i are eigenvalues of the operator and gives the orbital energies. The one-electron Fock operator, is defined as:

$$\hat{f} = -\frac{1}{2}\nabla_i^2 - \sum_A^M \frac{Z_A}{r_{iA}} + V_{HF} \quad (2.16)$$

The first term in equation (2.16) is for kinetic energy and the second for nucleus-electron attraction. The Hartree-Fock potential $V_{HF}(i)$ is the average potential experienced by the i^{th} electron due to the remaining $N-1$ electrons. $V_{HF}(i)$ takes into account the average electron-electron repulsion and replaces the two electron repulsion operator $\frac{1}{r_{ij}}$ in the Hamiltonian. Thus, each electron is considered to be moving in the field of the nucleus and the average field of the other $n-1$ electrons in Hartree-Fock theory. The two components of $V_{HF}(i)$ are:

$$V_{HF}(\vec{x}_1) = \sum_j^N \left\{ \hat{J}_j(\vec{x}_1) - \hat{K}_j(\vec{x}_1) \right\} \quad (2.17)$$

where, the *columb* operator is defined as:

$$\hat{J}_j(\vec{x}_1) = \int |\chi_j(\vec{x}_2)|^2 \frac{1}{r_{12}} d\vec{x}_2 \quad (2.18)$$

and the *exchange* operator is:

$$\hat{K}_j(\vec{x}_1)\chi_i(\vec{x}_1) = \int \chi_j^*(\vec{x}_2) \frac{1}{r_{12}} \chi_i(\vec{x}_2) d\vec{x}_2 \chi_j(\vec{x}_1) \quad (2.19)$$

The *columb* operator represents the potential experienced by an electron at position \vec{x}_1 due to the average charge distribution of another electron in spin orbital, χ_j .

On the other hand, *exchange* operator refers to the exchange of electrons within two spin orbitals. The exchange terms results from the antisymmetry of the Slater determinant. The Slater determinant is an eigen function of a Hamiltonian operator defined as the sum of the one-electron Fock operators:

$$\hat{H}_{HF}\Phi_{SD} = E_{HF}^0\Phi_{SD} = \sum_i^N \hat{f}_i\Phi_{SD} = \sum_i^N \epsilon_i\Phi_{SD} \quad (2.20)$$

Thus, Slater determinant is the exact wave function of N non-interacting electrons moving in the field of the effective potential, V_{HF} . The Fock operator \hat{f}_i , depends on the Hartree-Fock potential which in turn depends on spin orbitals. Thus, in the eigenvalue equation (2.13), we need to know χ_i , which itself is unknown, in order to have the Fock operator. This is a pseudo-eigenvalue problem and has to be solved iteratively. Since the orbitals are derived from their own effective potential, it is known as the Self Consistent Field (SCF) method. Starting from an initial guess set of orbitals, the Hartree-Fock equations are solved. Using these functions the operator \hat{f}_i , is constructed which is then allowed to operate on the guess functions to yield energy levels along with new, improved functions. The resulting new set of orbitals is then used in the next iteration and so on until convergence is obtained.

Restricted Hartree-Fock (RHF) method deals with closed shell system with doubly occupied spatial orbitals, i.e. there are two spin orbitals, χ_p and χ_q that share the same spatial orbital, φ_p connected with an α - and β - spin function, respectively and have the same orbital energy. *Restricted Open Shell Hartree-Fock* (ROHF) method is applicable for systems with unpaired electrons, where electrons occupy molecular orbitals in pairs as in the RHF method, except for the unpaired electron(s). But sometimes, α - and β - spin electrons are allowed to occupy separate spatial orbitals giving two sets of molecular orbitals one for α and one for β electrons. This is *Unrestricted Hartree-Fock* (UHF) method.

Electron Correlation

Hartree-Fock method takes into account the average effect of electron repulsion, but not the explicit electron-electron interaction. Within Hartree-Fock theory, as a consequence of central field approximation, the probability of finding an

electron at some location around an atom is determined by the distance from the nucleus but not the distance to the other electrons. In reality, the electrons in an atom tend to correlate their positions so as to acquire a stable state of minimum potential energy i.e. if one electron is near the nucleus the other will remain as far as possible. This is electron correlation. As a consequence, the motion of an electron in a real atom or molecule is more complicated than that for an electron moving in a smeared-out field and the electrons are thus better able to avoid one another. Thus, the electron-electron repulsion is really smaller than predicted by a Hartree-Fock calculation, i.e. the electronic energy is in reality lower (more negative). Actually, Hartree-Fock method allows for some electron correlation because of the antisymmetry requirement of the wavefunction. In accordance with the variational principle, the energy obtained by approximating wavefunction to represent the ground state is greater than the exact ground state energy i.e. $E_{HF} > E_0$. The correlation energy is defined as the difference between exact ground state energy, E_0 and the Hartree-Fock energy, E_{HF}

$$E_C^{HF} = E_0 - E_{HF} \quad (2.21)$$

The correlation energy is a negative quantity.

The post-Hartree-Fock calculations (correlated calculations) treat correlated electron motion better than does the Hartree-Fock method. Such methods include Møller-Plesset perturbation theory (MP n , where n is the order of correction), the generalized valence bond (GVB) method, multi-configurational self-consistent field (MCSCF), configuration interaction (CI), and coupled cluster theory (CC). Together, these methods are referred to as correlated calculations.

The accuracy of the molecular orbitals becomes better with the increasing number of basis functions. The solution of the Hartree-Fock equations with an infinite basis set becomes similar to those obtained by numerical Hartree-Fock methods. This yields the best solution to the Schrödinger equation and is defined as the *Hartree-Fock limit*. Actually, this limit can never be reached in actual practice.

2.5.2 Semi-empirical Methods

Similar to Hartree-Fock calculations, semi-empirical calculations are set up with the same general structure comprising of a Hamiltonian and a wave function. Within this framework, parameters replace the omitted integrals and the core electrons are not included. Parameters obtained by fitting the results to experimental data or *ab initio* calculations account for correction of the errors introduced by the omitting part of the calculation. The advantage of semi-empirical calculations is that they are much faster (about 100-1,000 times) than *ab initio* calculations whereas inconsistency of the results and reliable prediction of fewer properties are its disadvantages. Parameterization and approximations drastically reduce the number of integrals to be calculated, thereby, making semi-empirical calculations much less demanding of computer power than *ab initio* ones. The results depend on the availability of the parameters for the molecule being computed, or in other words, if the molecule being computed is similar to molecules in the database used to parameterize the method, then the results may be very good. However, semi-empirical methods are not as sensitive to the parameterization set as are molecular mechanics calculations.

Semi-empirical methods differ from *ab initio* calculations in (1) treating only valence or π electrons, (2) the mathematical functions used to expand the MOs (the nature of the basis set functions), (3) evaluation of the core and two-electron repulsion integrals, and (4) the treatment of the overlap matrix. Some of the most commonly used semi-empirical methods are:

1. *The Pariser-Parr-Pople (PPP) Method*: The PPP method (1953) was the first semi-empirical SCF-type method to gain widespread use. It is an extension of the Hückel method that allows heteroatoms other than hydrogen. Similar to Hückel method, it is limited to π electrons, with the other electrons forming a σ framework holding the atomic p orbitals in place.
2. *The Complete Neglect of Differential Overlap (CNDO) Method*: Unlike PPP method, CNDO is the first semi-empirical SCF-type method to go beyond just π electrons (ca. 1966). It is not limited to planar π systems and was a general geometry method.

3. *The Intermediate Neglect of Differential Overlap (INDO) Method*: Presently, INDO is used mostly only for calculating UV spectra, in specially parameterized versions called INDO/S and ZINDO/S.; although it is more accurate than CNDO.
4. *The Modified Intermediate Neglect of Differential Overlap (MINDO) Methods*: There are three MINDO methods viz. MINDO/1, MINDO/2, and MINDO/3. Among these, MINDO/3 method is by far the most reliable and has yielded qualitative results for organic molecules.
5. *The Neglect of Diatomic Differential Overlap (NDDO) Methods*: NDDO methods are benchmark methods in general-purpose semi-empirical calculations. These methods are basis of the currently popular semi-empirical methods developed by M. J. S. Dewar and by coworkers.
6. *The modified neglect of diatomic overlap (MNDO) Method*: MNDO has been found to give reasonable qualitative results for many organic systems.
7. *The Austin Model 1 (AM1) Method*: AM1 was developed at the University of Texas at Austin and was introduced by Dewar, Zoebisch, Healy and Stewart in 1985. It generally predicts the heats of formation, ΔH_f more accurately than MNDO, although a few exceptions involving Br atoms have been documented but is still popular for modeling organic compounds.
8. *The Parameterization Method 3 (PM3)*: PM3 differs from AM1 basically in the way parameterization is done. It is more accurate than AM1 for hydrogen bond angles, but AM1 is more accurate for hydrogen bond energies. The availability of algorithms for including solvation effects in PM3 and AM1 methods makes them more popular than other semi-empirical methods. Some of the extended PM3 methods include PM3(tm), PM5 and PM6.
9. *The Semi Ab Initio Method Number 1 (SAM1)*: SAM1 is essentially a modification of AM1 and is the last semi-empirical method to be reported (1993) by Dewar's group. Since the success in treating hydrogen bonding with AM1 and MNDO methods was only limited, so, SAM1 evolved as an improvement.

It appears to be the first semi-empirical parameterization to handle a wide variety of hydrogen bonded systems correctly.

Some of the *applications* of semi-empirical methods are:

1. Determination of geometries.
2. Calculation of frequencies and vibrational spectra.
3. Calculation of dipole moments, charges and bond orders.
4. Calculation of ultra-violet spectra, ionization energies and electron affinities.

Strength of semi-empirical methods:

1. Very fast compared to *ab initio* and even to DFT with a tolerable loss of accuracy.
2. Semi-empirical geometries of normal molecules and even transition states are often adequate
3. Reaction and activation energies, although not accurate (except by chance cancellation of heat of formation errors), will probably expose any marked trends in a series.
4. AM1 and PM3 usually give fairly realistic geometries and useful relative energies for cations, radicals, anions, strained molecules, and even transition states.

Weakness of semi-empirical methods:

1. Poor results for molecules for which parameters are unavailable.
2. Heats of formation are subject to large errors and consequently affect the heats (enthalpies) of reaction and activation energies.
3. AM1 and PM3 underestimate steric repulsions, overestimate basicity and underestimate nucleophilicity, and can give unreasonable charges and structures.
4. Semi-empirical errors are less systematic than *ab initio*, and thus harder to correct for.

2.5.3 Density Functional Theory

The past decades have seen enormous rise in popularity of density functional theory (DFT) as a powerful quantum mechanical method in the calculations of the structure of atoms, molecules, crystals, surfaces, and their interactions [265]. The pioneering work of Hohenberg, Kohn and Sham in the 1960s led to the widespread use of DFT as a leading tool for electronic structure calculations. Figure 2.2 shows the increasing number of occurrence of DFT in journals from 1990 till 2011.

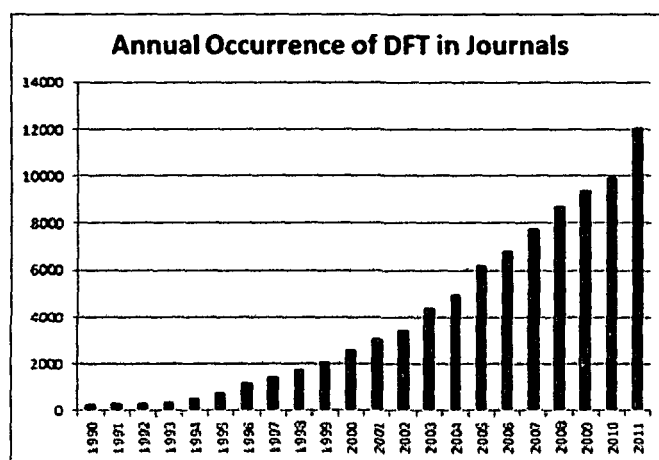


Figure 2.2: Annual occurrence of the phrase 'DFT' in Journals

According to DFT formalism, the ground-state electronic energy is determined completely by the electron density, ρ in a system of non-interacting electrons.

$$\rho(\vec{r}) = N \int \dots \int |\psi(\vec{x}_1 \vec{x}_2 \vec{x}_3 \dots \vec{x}_N)| dx_1 dx_2 \dots dx_N \quad (2.22)$$

where $\rho(\vec{r})$ determines the probability of finding any of the N electrons within a volume element dr_1 with arbitrary spin while the other $N-1$ electrons have arbitrary positions and arbitrary spin in the state represented by ψ . $\rho(\vec{r})$ is a non-negative function of position only, i.e. of only three spatial variables for an N electron system. Contrary to it, wave function (ψ) is a function of $4N$ variables (three spatial variables and one spin variable for each electron). Thus, the complexity of the wave function increases with the number of electrons while electron density remains a function of three variables. Apart from this, unlike wave function, the electron density is an observable and can be measured experimentally e.g. X-ray diffraction or electron diffraction [266].

2.5.3.1 Hohenberg-Kohn Theorems

The theoretical formulation of DFT is based on the Hohenberg-Kohn theorems. The first Hohenberg-Kohn theorem [267], also known as the 'existence theorem' states that any ground state property of a molecule is a functional of the ground state electron density function, e.g. if we consider the energy, then, $E = F[\rho_0] = E[\rho_0]$. Thus, this theorem assures that there is a way to calculate molecular properties from electron density. However, it merely says that a functional, F exists (and hence the name existence theorem) but does not tell how to find it.

The second Hohenberg-Kohn theorem [267] says that any trial electron density function will give an energy higher than the true ground state energy. This is in principle, the DFT analogue of the variation theorem (in context of *ab initio* method). In DFT, the electronic energy from a trial electron density function is the energy of the electrons moving under the influence of the external potential $[v(r)]$ of the atomic nuclei. Thus,

$$E_v[\rho_t] \geq E_0[\rho_0] \quad (2.23)$$

where, E_v is the energy of the trial electron density under the influence of external potential, $v(r)$, $[\rho_t]$ is the trial electron density, $E_0[\rho_0]$ is the true ground state energy corresponding to the true electron density, ρ_0 . Thus, the total electronic energy of a system can be expressed as:

$$E = E[\rho(r)] = T[\rho(r)] + E_{Ne}[\rho(r)] + E_{ee}[\rho(r)] \quad (2.24)$$

where, T is the kinetic energy of all the electrons, E_{Ne} is the potential energy due to the nucleus-electron attraction, E_{ee} is the electron-electron interaction which consists of the classical Coulomb term and other non-classical terms. Equation (2.23) can be further written as:

$$E[\rho(r)] = \int \rho(\vec{r}) V_{Ne} d\vec{r} + F_{HK}[\rho] \quad (2.25)$$

The potential energy due to the nucleus-electron attraction, E_{Ne} can be expressed as:

$$E_{Ne}[\rho(r)] = \int \rho(\vec{r}) V_{Ne} d\vec{r}$$

and $F_{HK}[\rho]$ is:

$$F_{HK}[\rho] = T[\rho(r)] + E_{ee}[\rho(r)]$$

Since, the functional forms of both the terms in $F_{HK}[\rho]$ are unknown thus; implementation of Hohenberg-Kohn theorems is not an easy task.

2.5.3.2 Kohn-Sham Method

The introduction of orbitals, as suggested by Kohn and Sham [268] forms the foundation for the use of DFT methods in computational chemistry. The first Kohn-Sham (KS) theorem tells us that it is necessary to find a way to calculate molecular properties from the electron density. The second theorem suggests that a variational approach might yield a way to calculate the energy and electron density. The key problem in DFT is that the correct energy functional is unknown since the accurate electron density function is not available. These two problems are alleviated by the Kohn-Sham approach (1965) to DFT. The two basic ideas behind the KS approach are:

1. To express the molecular energy as a sum of terms and a relatively small term among these involves the "unknown" functional. Thus, even moderately large errors in this term will not introduce large errors into the total energy.
2. To use an initial guess of the electron density ρ in the Kohn-Sham equations to calculate an initial guess of the KS orbitals and energy levels.

The initial guess orbitals are then used to refine these orbitals and energy levels in an iterative manner, similar to the HF SCF method. The final KS orbitals are used to calculate an electron density that in turn is used to calculate the energy.

The Kohn Sham approach to DFT introduces a fictitious *non-interacting reference* system in which the ground state electron density distribution, ρ_r is exactly the same as that in the real ground state system i.e. $\rho_r = \rho_0$. The ground state electronic energy of the real molecule can be expressed as:

$$E_0 = \langle T[\rho_0] \rangle + \langle V_{Ne}[\rho_0] \rangle + \langle V_{ee}[\rho_0] \rangle \quad (2.26)$$

where, $\langle T[\rho_0] \rangle$ is the electron kinetic energy, $\langle V_{Ne}[\rho_0] \rangle$ is the nucleus-electron attraction potential energy and $\langle V_{ee}[\rho_0] \rangle$ is the electron-electron repulsion potential

energy. The energy terms are expressed as the expectation values and each is a functional of the ground state electron density. Equation (2.26) can be written as:

$$E_0 = \langle T[\rho_0] \rangle + \int \rho_0(r) \nu_r dr + \langle V_{ee}[\rho_0] \rangle \quad (2.27)$$

where, $\nu(r)$ is the external potential (in the context of the attraction between nucleus and electron). In order to solve equation 2.27 (since the functionals in $\langle T[\rho_0] \rangle$ and $\langle V_{ee}[\rho_0] \rangle$ are not known), Kohn and Sham incorporated the idea of reference system of non-interacting electrons. The deviation of the real kinetic energy from the reference system can be defined by $\Delta\langle T[\rho_0] \rangle$:

$$\Delta\langle T[\rho_0] \rangle \equiv \langle T[\rho_0] \rangle - \langle T_r[\rho_0] \rangle \quad (2.28)$$

The deviation of the real electron-electron repulsion energy from classical electrostatic repulsion energy is defined by $\Delta\langle V_{ee}[\rho_0] \rangle$

$$\Delta\langle V_{ee}[\rho_0] \rangle \equiv \langle V_{ee}[\rho_0] \rangle - \frac{1}{2} \int \int \frac{\rho_0(r_1)\rho_0(r_2)}{r_{12}} dr_1 dr_2 \quad (2.29)$$

The classical electrostatic repulsion energy $\frac{1}{2} \int \int \frac{\rho_0(r_1)\rho_0(r_2)}{r_{12}} dr_1 dr_2$ is the summation of the repulsion energies for a pair of infinitesimal volume elements $\rho_0(r_1)dr_1$ and $\rho_0(r_2)dr_2$. Thus,

$$E_0 = \int \rho_0(r) \nu_r dr + \langle T_r[\rho_0] \rangle + \frac{1}{2} \int \int \frac{\rho_0(r_1)\rho_0(r_2)}{r_{12}} dr_1 dr_2 + \Delta\langle T[\rho_0] \rangle + \Delta\langle V_{ee}[\rho_0] \rangle \quad (2.30)$$

The sum of the kinetic energy deviation from the reference system and the electron-electron repulsion energy deviation from the classical system is called the exchange-correlation energy, E_{XC} . E_{XC} can also be defined as the correction to the kinetic energy term arising from the interacting nature of electrons and all non-classical corrections to the electron-electron repulsion energy[269].

$$E_{XC}[\rho_0] = \Delta\langle T[\rho_0] \rangle + \Delta\langle V_{ee}[\rho_0] \rangle \quad (2.31)$$

$\Delta\langle T \rangle$ and $\Delta\langle V_{ee} \rangle$ terms represent the kinetic correlation energy of the electrons and the exchange energy, respectively. The correlation term refers to the interaction between electrons of opposite spin and the exchange term is connected with electrons of same spin. Using equation (2.31) in (2.30), gives:

$$E_0 = \int \rho_0(r) \nu_r dr + \langle T_r[\rho_0] \rangle + \frac{1}{2} \int \int \frac{\rho_0(r_1)\rho_0(r_2)}{r_{12}} dr_1 dr_2 + E_{XC}[\rho_0] \quad (2.32)$$

More precisely, electronic energy of the ground state of a system comprising n electrons and N nuclei can be written as:

$$E_0 = - \sum_{X=1}^N \int \frac{Z_X}{r_{X_i}} \rho(r_1) dr_1 - \frac{1}{2} \sum_{i=1}^n \int \psi^*(r_1) \nabla_i^2 \psi_i r_1 dr_1 + \frac{1}{2} \int \int \frac{\rho_0(r_1) \rho(r_2)}{r_{12}} dr_1 dr_2 + E_{XC}[\rho_0] \quad (2.33)$$

where, ψ_i ($i = 1, 2, 3, \dots, n$) are the Kohn-Sham orbitals.

$$\int \rho_0(r) v(r) dr = - \sum_{X=1}^N \int \frac{Z_X}{r_{X_i}} \rho(r_1) dr_1$$

and,

$$\langle T_r[\rho_0] \rangle = - \frac{1}{2} \sum_{i=1}^n \int \psi_i^*(r_1) \nabla_i^2 \psi_i r_1 dr_1$$

The biggest challenge in DFT is devising an accurate exchange-correlation functional (the last term in equation 2.33).

The ground state electron density ρ_0 can be written as a set of Kohn-Sham orbitals (the one-electron orbitals):

$$\rho_0 = \sum_{i=1}^n |\psi_i(r)|^2 \quad (2.34)$$

The significance of the Kohn-Sham orbitals is that they allow calculating density from the above equation. The Kohn-Sham orbitals are determined by solving the Kohn-Sham equations.

$$\hat{h}_i \psi_i(r_1) = \epsilon_i \psi_i(r_1) \quad (2.35)$$

In equation (2.35), \hat{h}_i represents the Kohn-Sham Hamiltonian and ϵ_i is the associated Kohn-Sham orbital energy. The Kohn-Sham Hamiltonian can be written as:

$$\hat{h}_i = - \frac{1}{2} \nabla_1^2 - \sum_{X=1}^N \frac{Z_X}{r_{X_i}} + \int \frac{\rho(r_2)}{r_{12}} dr_2 + V_{XC}(r_1) \quad (2.36)$$

V_{XC} in the above equation is the functional derivative of the exchange-correlation energy with respect to ρ and is given as:

$$V_{XC}[\rho] = \frac{\delta E_{XC}[\rho]}{\delta \rho} \quad (2.37)$$

V_{XC} can be readily obtained once E_{XC} is known. The Kohn-Sham equations will give the exact energy, if the exchange-correlation energy as a functional of density is exactly known. Several approximations to E_{XC} exist but there is still no systematic way to improve E_{XC} . Similar to Hartree-Fock method, the Kohn-Sham equations are solved in a self-consistent fashion.

2.5.3.3 Exchange-Correlation Energy Functionals

A. Local Density Approximation (LDA)

The simplest approximation to the exchange-correlation functional is given by the Local Density Approximation (LDA). LDA applies to a uniform electron gas and within its framework; the exchange-correlation energy at any point in space is a function of the electron density at that point only. The exchange-correlation energy is given as:

$$E_{XC}^{LDA}[\rho] = \int \rho(r) \epsilon_{XC}(\rho) dr \quad (2.38)$$

where, the integral is over all the space, dr stands for dx, dy, dz and ϵ_{XC} is the exchange-correlation energy per electron in an uniform electron density, ρ . The functional derivative of E_{XC}^{LDA} gives,

$$\nu_{XC}^{LDA} = \frac{\partial E_{XC}^{LDA}}{\partial \rho} = \epsilon_{XC}[\rho(r)] + \rho(r) \frac{\partial E_{XC}^{LDA}(\rho)}{\partial \rho} \quad (2.39)$$

ϵ_{XC} can be bifurcated in to the exchange and correlation contributions:

$$\epsilon_{XC}[\rho] = \epsilon_X[\rho] + \epsilon_C[\rho] \quad (2.40)$$

where,

$$\epsilon_X[\rho] = -\frac{3}{4} \left(\frac{3}{\pi}\right)^{\frac{1}{3}} [\rho(r)]^{\frac{1}{3}} \quad (2.41)$$

$\epsilon_X[\rho]$ is the exchange energy of an electron in a homogenous electron gas and is given by Dirac functional [270]. For the $\epsilon_C[\rho]$ part, highly accurate values have been determined from Quantum Monte Carlo (QMC) calculations using interpolation formula to provide an analytical form for $\epsilon_C[\rho]$. Such interpolation is performed with the widely used Vosko-Wilk-Nusair (VWN) [271] and Perdew-Wang (PW) [272] approximations and these are considered to be accurate fits. LDA suffers from some typical deficiencies, such as the inadequate cancellation of self-interaction contributions. It underestimates atomic ground-state energies and ionization energies while binding energies are overestimated. The computationally convenient LDA improves with the size of the system, being worse for small molecules and it favors high-spin state structures [269].

Introducing electron spin in to LDA results in a more general approximation, the *Local Spin Density Approximation (LSDA)*. Initially proposed by J. C. Slater [273], LSDA assigns different spatial orbitals to the α and β spin electrons in the homogenous electron gas. LSDA is useful for open-shell systems, like radicals and molecular geometries near dissociation. For closed-shell systems, LSDA is equivalent to LDA. LSDA yield reasonably good molecular equilibrium geometries, vibrational frequencies and dipole moments, even for transition metal compounds. However, atomization energies are very inaccurate and dissociation energies require improved functionals than LSDA.

B. *Generalized-Gradient Approximation (GGA)*

Any real molecular system is spatially non-uniform; i.e. the electron density varies greatly from place to place. So, it is not surprising that the LDA approach will have limitations. One obvious way to improve is to make exchange and correlation energies dependent on both density and its gradient, $\Delta\rho$ (first derivative with respect to position). Inclusion of the density gradient along with density yields gradient corrected functionals and are defined as *Generalized Gradient Approximation (GGA)*. The exchange-correlation energy can be expressed as:

$$E_{XC}^{GGA}[\rho] = \int \rho(r)\epsilon_{XC}(\rho, \Delta\rho)dx \quad (2.42)$$

Basically, there are two groups of the exchange functional in GGA method; the first one was developed by Becke [274-279] and is empirical in nature. Exchange functionals such as Becke88 (B) [280], Perdew-Wang (PW) [281], modified Perdew-Wang (mPW) [281,282], OptX (O) [283] and X [284] are included in this group. The second group which is more rational-based was proposed by Perdew [285,286]. They contain no empirically optimized parameters and consider that the exchange-correlation functionals should be based on the quantum mechanical principles. Becke86 (B86) [274], Perdew 86 (P) [287], Perdew-Burke-Ernzerhof (PBE) [288] and modified Perdew-Burke-Ernzerhof (mPBE) [288,289] are included in this group. For the correlation functional, corrections to the correlation energy density include Becke88 (B88) [290], Perdew 86 (P86) [287], and Perdew-Wang (PW91) [291]

and the widely popular Lee-Yang-Parr (LYP) [292].

GGA methods yield better total energies [293], atomization energies [272], reliable bond distances and binding energies [294]. Moreover, although GGA methods give a correct description of covalent, ionic, metallic and hydrogen bridge bonds but these methods fail for van der Waals interactions [295,296].

An improvement in the GGA functionals was made by incorporating additional semi-local information beyond the first order density gradient contained in GGA functionals. These sophisticated semi-local functionals that depend explicitly on higher order density gradients or alternatively the orbital kinetic energy density are termed *Meta- Generalized Gradient Approximation (meta-GGA)*. M-GGA functionals exhibit significant improvement over GGA functional in the determination of properties such as atomization energies. Examples of meta-GGA include B95 [278], KCIS [297], TPSS [298] and VSXC [299].

C. Hybrid Functional

Hybrid DFT functionals (H-GGA) couple the exchange-correlation of a GGA method with a percentage of Hartree-Fock (or exact) exchange leading to a better description of the exchange part. The Hartree-Fock exchange cannot be assigned from the first principles and is thus fitted semiempirically. Hybrid functionals are extensively used owing to the significant improvement in results over conventional GGAs. Examples of hybrid functionals include B3LYP [278,280,292], B3P86 [278,280,287], mPW3LYP [282,291,292]. The B3LYP functional is defined as:

$$E_{XC}^{B3LYP} = (1 - a_0 - a_x)E_X^{LDSA} + a_0E_X^{HF} + a_xE_X^{B88} + (1 - a_c)E_C^{VWN} + a_cE_C^{LYP} \quad (2.43)$$

The values of the parameters are: $a_0 = 0.20$, $a_x = 0.72$, $a_c = 0.81$

Another class of functionals that has been developed in the past years starts from the meta-GGA functionals and incorporate the Hartree-Fock exchange, electron density and its gradient and the kinetic energy density. These functionals are known as Hybrid-meta GGA (HM-GGA) methods. B1B95 [278,280], BB1K [278,280,300], MPW1B95 [278,282,291,301].

2.5.3.4 Performance of DFT functionals

Starting from the local density approximation, each time the subsequent functionals have been improved (inclusion of additional exact constraints into approximations) with the goal to attain chemical accuracy. This progress in the field of density functionals has been termed as the *Jacob's Ladder* by Perdew [302]. In Perdew's perception of Jacob's ladder of density functional approximations, earth is the Hartree approximation and heaven is the realm of chemical accuracy. The angels are the users, climbing or descending the ladder and choosing the rung according to their needs for precision and computational resources available. The five rungs representing the hierarchy of density functional approximations are given as: LDA (lowest or first rung), GGA (second rung), meta-GGA (third rung), hybrid-GGA and hybrid meta-GGA (fourth rung) and fully non-local description (fifth rung). The first three rungs are computationally efficient semi local functionals while the more accurate fourth and fifth rungs are computationally expensive nonlocal functionals [303]. The outcome of such ladder strategy is a steady improvement in the accuracy of the results with a compromise in the associated computational cost on moving from lower to higher rungs. Figure 2.3 represents the Jacob's Ladder of density functionals presented by J. Perdew at the DFT2000 symposium in Menton, France.

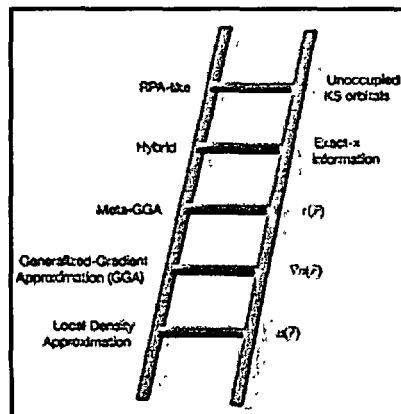


Figure 2.3: Jacob's Ladder of density functional approximations. On the left, the rungs are labeled and on the right on their added ingredients are shown [303].

2.5.4 Basis Sets

A basis set is a set of mathematical functions used to represent atomic orbitals and the employed mathematical functions describe the radial and angular distribution of electron density. Linear combination of atomic orbitals or basis functions centered at each atomic nucleus within the system yields molecular orbitals. Basis sets can be classified into the following types:

2.5.4.1 Slater Type Orbitals (STO)

The idea of basis sets in computation was first introduced by J. C. Slater [304] in 1930. These are known as Slater Type Orbitals (STO) with the following functional form:

$$f^{STO}(r) = \left(\frac{\zeta^3}{\pi}\right)^{0.5} \exp(-\zeta r) \quad (2.44)$$

STOs describe fairly well the radial electron distribution and closely resemble hydrogenic atomic orbitals. However, STOs are difficult to handle as they do not converge. Also, the evaluation of the integrals is a tedious calculation. As an alternative, Gaussian Type Orbitals were developed by S. F. Boys [305] in 1950.

2.5.4.2 Gaussian Type Orbitals (GTO)

The functional form of Gaussian Type Orbital (GTO) can be given as:

$$f^{GTO}(r) = \left(\frac{2\alpha}{\pi}\right)^{0.5} \exp(-\alpha r^2) \quad (2.45)$$

GTOs are convenient from the viewpoint of computational efficiency and are easier to handle as they converge easily. However, they describe the radial electron distribution less satisfactorily. Figure 2.4 shows the behaviour of STOs and GTOs with respect to the radial decay of s-type functions. For STO, the radial decay is exponential in r while for GTO it is exponential in r^2 ; resulting in a rapid reduction of amplitude with distance.

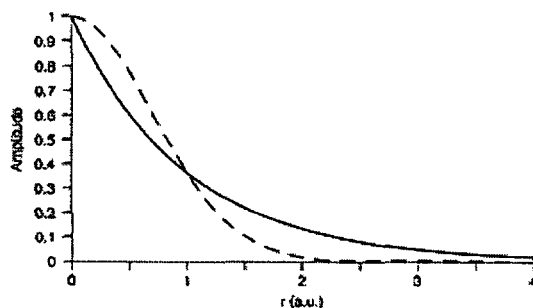


Figure 2.4: Behaviour of e^{-r} (solid line, STO) and e^{-r^2} (dashed line, GTO) for s-type function [306].

In order to achieve accuracy comparable to that of STOs along with the computational efficiency, GTOs are used as a linear combination to provide the best fit to an STO. A basis function obtained as a linear combination of GTOs is referred to as 'contracted' basis function and the constituent Gaussians from which it is formed are called as 'primitive' Gaussians. These can be represented as STO-NG (Slater Type Orbitals approximated by N Gaussians).

2.5.4.3 Single-zeta, Multiple-zeta basis sets

When only one basis function is employed for each type of orbital (core to valence); the basis set is defined as a *single* - ζ basis set, or, more commonly, a *minimal basis set*. Example: STO-3G. When each basis function of minimal basis set is replaced by two basis functions i.e. each orbital is treated separately as the sum of two STOs with different ζ values in equation (2.44); the basis set is defined as the *double-zeta (DZ) basis set*. Similarly, when each basis function of minimal basis set is replaced by three and four basis functions, this gives *triple-zeta (TZ)* and *quadruple-zeta basis set (QZ)*, respectively. However, the multiple zeta basis sets involve rigorous calculations and thus will cause a problem for calculation of larger molecules.

2.5.4.4 Split-valence basis sets

From a chemical standpoint, the core orbitals are only weakly affected by chemical bonding whereas the valence orbitals can vary widely as a function of chemical bonding. Thus, using a single basis function for the core orbitals and more than

one for valence orbitals will reduce the computational expenses. This type of basis sets are called *split-valence basis sets*.

Example: 6-31G is a split-valence basis set where the valence shell orbitals are composed of two basis functions; one is a linear combination of three Gaussian type orbitals and the other consists of one Gaussian type orbital. The core orbitals are represented by one basis function composed of six Gaussian type orbitals. Some other split-valence basis sets include 3-21G, 4-31G.

2.5.4.5 Polarization functions

Inclusion of polarization functions increases the size of the basis set to improve the accuracy of the calculation. A polarization function is any higher angular momentum orbital used in a basis set that is not normally occupied in the separated atom. Polarization functions improve the flexibility of the basis set by allowing atomic electron densities to be polarized in order to better represent the electron density of the molecule. As atoms are brought close together, their charge distribution causes a polarization effect which distorts the shape of the atomic orbitals. For instance, 's' orbitals begin to have a little of the 'p' flavour and 'p' orbitals that of 'd' flavour. Example: 6-31G*. A 6-31G* calculation on C atom will include the polarization (six d orbitals) functions. A 6-31G** calculation will include the polarization (p) functions in H and He atoms in addition to the d-functions on the heavy atoms.

2.5.4.6 Diffuse functions

In order to overcome the significant errors in energies and other molecular properties that might arise if a basis set does not have the flexibility necessary to allow weakly bound electrons of highly excited states, anions etc. to localize far from the remaining density; standard basis sets are often augmented with *diffuse basis functions*. The presence of diffuse functions is indicated by '+' in the basis set name. When elements having p or higher occupied orbitals are augmented with diffuse functions, one '+' is used and two '++' when diffuse functions are used for both heavy and light elements. Example: 6-31+G(d), 6-311++G(3df, 2pd).

2.5.4.7 Numerical basis sets

Within the realm of DMol³ program [307], *Numerical basis sets* are given as numerical values on an atomic-centered spherical-polar mesh, rather than as analytical functions (i.e. Gaussian orbitals). These basis functions are generated by solving the atomic Kohn-Sham equations numerically with the corresponding approximate exchange-correlation functional. Because of the better quality of the atomic orbitals, basis set superposition errors are minimized and an excellent description of even weak bonds are possible. Larger basis sets yield better accuracy by providing greater variational freedom. Double-numerical (DN) basis set (N is used to emphasize the numerical nature of the orbitals) refers to the generation of an entire second set of functions resulting in doubling the size of the basis set.

2.5.4.8 Effective Core Potentials (ECP)

From about the third row of the periodic table, the large number of electrons begins to significantly decelerate the conventional *ab initio* calculations because of the concomitant requirement to use a large number of basis functions to describe them. Moreover, core electrons are less significantly affected by chemical bonding. *Effective Core Potentials* (ECP) or pseudopotentials allow treatment of the core electrons as some average potential while the valence electrons are considered explicitly. ECPs take in to account the relativistic effects which are prominent in heavy elements. Electrons near the very positive nucleus of a heavy element experience a larger relative attraction than for lighter elements, which accelerates the electrons close to the speed of light. According to Einstein's theory of special relativity, this will cause an increase in mass of the electrons and consequently will have an effect on the shape of the atomic orbitals. The core orbitals are contracted and enhance nuclear shielding causing valence orbitals to increase in energy. Such changes have considerable impact in geometries and properties of heavy -atom molecules and inclusion of relativistic effect is necessary. Example: Los Alamos national Laboratory (LANL) ECP with DZ valence basis set. The overall combination is known as LANL2DZ basis set [308,309].

2.6 Quantum Mechanics/Molecular Mechanics (QM/MM) Methods

With an increase in the size of the chemical system, the need for computational resources also increases which hampers the application of *ab-initio* methods for treatment of large systems such as surfaces, biomolecules etc. To combat this problem, hybrid methods have been designed, where the active site (the bond breaking/bond formation, adsorption etc. takes place) is treated quantum mechanically (usually semi-empirical, low-level *ab initio* or density functional methods) and rest of the system by molecular mechanics. This methodology is often denoted as *Quantum Mechanics-Molecular Mechanics (QM/MM)*. The 2013 Nobel Prize in Chemistry has been awarded to A. Warshel, M. Levitt and M. Karplus; credited for their development of hybrid QM/MM [310] strategy to model complex chemical systems.

The QM/MM approach divides the energy of the whole system, S into three parts- QM energy of the inner or active part, I, MM energy of the outer or inactive part, O and an interaction energy term, I-O.

$$E_{QM-MM}(S) = E_{QM}(I) + E_{(MM)}(O) + E(I - O) \quad (2.46)$$

Figure 2.5 (a) shows the active inner part (I) and the outer inactive part (O) of a chemical system. In Figure 2.5 (b), A-B is a bond which is broken on separating the system into I and O parts. L is the link atom used to saturate the inner part for QM calculations.

The key issue in the QM/MM scheme is defining the interaction between the QM and MM part, i.e. $E(I - O)$. Several approaches have been forwarded to describe this interaction, which can be divided into two categories viz. subtractive and additive coupling. Further, the additive coupling incorporates various embedding schemes such as mechanical embedding, electrostatic embedding and polarizable embedding; each having its own merits and de-merits. Apart from these, elastic polarizable environment [311] (EPE) embedding has been developed for ionic oxides where the QM cluster is terminated with capping atoms represented by effective core potentials without basis functions. The EPE approach

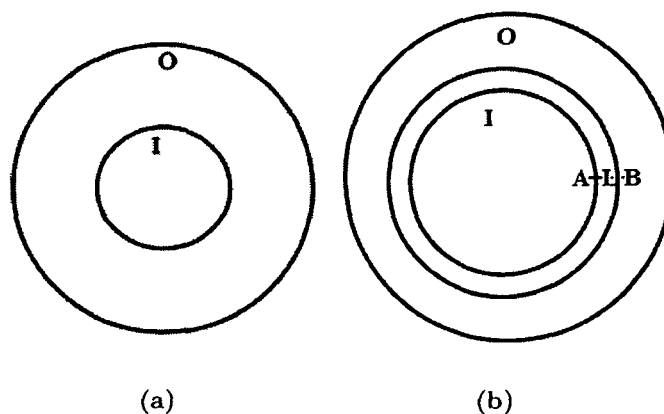


Figure 2.5: Partitioning a chemical system into inner part (I) and an outer part (O).

has been extended to covalent elastic polarizable environment [312] (covEPE) embedding for systems with directional polar covalent bonds. The QM cluster in the covEPE scheme is saturated by specially constructed monovalent "pseudoatoms", referred to as bonding atoms that represent real atoms of the material which simultaneously belong to both QM and MM regions. However, for practical calculations, when QM and MM parts are connected by chemical bonds, defining the QM part explicitly requires cutting of the bonds. This creates one or more unpaired electrons (dangling bonds) in the QM subsystem which must be properly terminated; otherwise, the chemical behaviour of the inner region will be dramatically different from the real system. Usually, these dangling bonds are terminated by adding "link" atoms or capping atoms, typically hydrogen. The QM calculation is performed for a cluster, C , comprising of the active part and the link atoms, i.e. $C = L + I$. The successful termination of dangling bonds with hydrogen for clusters of silica or zeolite has been attributed to the role played by terminating H atoms as "a quarter of a silicon atom (for O-H termination) or as "one-half of an oxygen atom" (for Si-H termination) [313]. The electronegativity of H is between that of Si and O; so that H accepts electrons from Si (as O does) and donates electrons to O (as Si does). For application of hybrid QM/MM methods to surface models, Shoemaker *et al.* [314] modified the original IMOMM method of Maseras and Morokuma to *Surface Integrated Molecular Orbital Molecular Mechanics Method (SIMOMM)*. The total energy of the entire system under the SIMOMM scheme is given as:

$$E_{SIMOMM}(S, L) = E_{QM}(C) + E_{MM}(O) + E_{MM}(I - O) \quad (2.47)$$

The MM part is calculated crossing out the terms applicable to the inner part from the expression for the entire system:

$$E_{MM}(S) = E_{MM}(I) + E_{MM}(O) + E_{MM}(I - O)$$

or,

$$E_{MM}(O) + E_{MM}(I - O) = E_{MM}(S) - E_{MM}(I) \quad (2.48)$$

Thus, the actual working equation is:

$$E_{SIMOMM}(S, L) = E_{QM}(C) + E_{MM}(S) - E_{MM}(I) \quad (2.49)$$

In SIMOMM method, the constraints on the link atoms are lifted and are allowed to move according to the forces obtained from equation (2.50):

$$\frac{\partial E_{SIMOMM}(S)}{\partial L_i} = \frac{\partial E_{QM}(C)}{\partial L_i} \quad (2.50)$$

The forces on the I and O atoms are obtained by differentiating equation (2.50):

$$\frac{\partial E_{SIMOMM}(S)}{\partial I_i} = \frac{\partial E_{QM}(C)}{\partial I_i} + \frac{\partial E_{MM}(I - O)}{\partial I_i} \quad (2.51)$$

$$\frac{\partial E_{SIMOMM}(S)}{\partial O_i} = \frac{\partial E_{MM}(S)}{\partial O_i} \quad (2.52)$$

The SIMOMM method is implemented within the TINKER [315] and GAMESS [316] programs.

Hybrid QM/MM methods find application in studying properties of large systems like zeolites, biomolecules, adsorption on metal oxide surfaces, organometallic reactions and homogeneous catalysis, structure, reactivity and bond energies of large organic molecules including fullerenes, nanotubes, and enzyme-catalyzed reactions.

In our present work, we have performed density functional theory based quantum mechanical calculations on gas phase gold clusters using DMol³ program and quantum mechanics-molecular mechanics calculations on zeolite supported gold clusters using GAMESS program. The results of these investigations are summarized in the following chapters.

Chapter 3

Density Functional Studies on Hydrogenated Gold Clusters

All that glitters is not gold

English Proverb

Overview

This chapter is divided into two sections, 3.1 and 3.2. Section 3.1 deals with the detailed investigation of the structures, electronic and reactivity properties of Au_6H_n ($n=1-12$) clusters using density functional theory. We have found that the adsorption of hydrogen atoms stabilizes the Au_6 cluster retaining the Au_6 planar triangular structure till Au_6H_6 . Further addition of H atoms distorts the structure such that the structure of Au_6H_{12} is non-planar. Odd-even alternation in electronic properties like HOMO-LUMO gap, chemical hardness, vertical ionization potential, adiabatic ionization potential and binding energy has been observed. Potential sites for electrophilic and nucleophilic attack have been identified for all the hydrogenated clusters using DFT based reactivity descriptors [Baishya, S. & Deka, R. C. *Comput. Theor. Chem.* **1002**, 1--8, 2012].

In the next part, we intend to study the effect of zeolite on the stable Au_6 cluster and faujasite has been chosen as the zeolite of our interest. This section

(Section 3.2) summarizes the results of density functional study of reverse hydrogen spillover from bridging OH groups of the faujasite support to Pd₆ and Au₆ clusters. The hydrogenated clusters, M₆H_n/FAU(3-n); M= Pd, Au and n=1-3 resulting due to the process of proton transfer from the bridging OH groups are energetically preferable over faujasite supported bare clusters, M₆/FAU(3H). The calculated reverse hydrogen spillover energy per transferred hydrogen atom for faujasite supported Pd₆H₃ and Au₆H₃ are -29.33 kJmol⁻¹ and -24.50 kJmol⁻¹, respectively. For both the metals, it is found that hydrogen migration results in partial oxidation of the metal atoms with concomitant reduction of H⁺ to H⁻ [Deka, R. C. & Baishya, S. *Catal. Today* **198** (1), 110--115, 2012].

3.1 Structure, Electronic and Reactivity

Properties of Au₆H_n (n=1-12) Clusters

3.1.1 Introduction

The noble metal, gold acquires a central stage in the field of material research. This can be attributed to its interesting property to act as a wonderful catalyst when the size is reduced to the nano regime. The physical and chemical properties of gold nanoclusters are found to have pronounced dependence on their structures. Gold has an atomic configuration [Xe] 4f¹⁴5d¹⁰6s¹ and exhibits properties similar to alkali metals due to the single valence s-electron. However, it possess significant relativistic effect which is larger than any other element with Z<100 in the periodic table. Presence of relativistic effect reduces the s-d energy gap thus inducing hybridization of the atomic 5d-6s energy levels and causing an overlap of the 5d shells of the neighboring atoms in the cluster. For instance, presence of relativistic effect has led to the uniqueness of gold in having stable planar 2D clusters up to n=12 [63,64].

Hydrogen has an atomic configuration of 1s¹ similar to gold that makes it interesting to study the interaction of small gold clusters with hydrogen atoms [317]. Gold hydrides have attracted considerable attention as they serve as important intermediates in gold catalyzed reactions [318-320] such as hydrogenation [321],

hydrosilylation [322], C-H bond activation [323], aerobic oxidation of alcohols [324] etc. The study of gold hydride clusters is important to understand the adsorption of hydrogen on to metal surfaces. Moreover, the gold hydrides serve as archetype to study the relativistic effects. The chemistry of gold has been demonstrated by several theoretical and experimental works [325,326] to have significant resemblance to that of the hydrogen atom. In 1978, *ab initio* studies were performed by Hay *et al.*[327] on diatomic gold hydride using relativistic effective core potentials. A number of experimental and theoretical studies have been reported about the interaction of the gold clusters with hydrogen [328-331]. Phala performed DFT calculation to study the interaction of small Au_n ($n=1-13$) clusters with H and CO [332]. Buckart *et al.* [333] presented that the spectra of Au_n^- and $Au_{n-1}H^-$ showed identical features for $n>2$ in their photoelectron spectra; thus suggesting that hydrogen behaved as protonated species. Even though a large number of studies have been devoted towards gold cluster hydrides involving a single hydrogen atom, but multi-hydrogen atom interaction has been rarely studied [334]. In addition to understanding the interaction between hydrogen and gold cluster, investigation of the reactivity of Au cluster and the reacting sites within them with the aid of DFT based reactivity descriptors is also important. Such exploration of the reactive sites in hydrogen adsorbed gold clusters is however, still lacking behind.

3.1.2 Computational Details

The density functional calculations reported here are carried out using DMol³ [307] package utilizing PBE functional [288] incorporating the Perdew, Burke, Ernzerhof correlation at the generalized gradient approximation (GGA) level. The DNP numerical basis set has been chosen for our calculations and is the highest quality set available in DMol³. DNP basis functions are the double numerical sets containing a polarization d-function on heavy atoms and polarization p-function on hydrogen. Although the size is comparable to 6-31G** basis set but the numerical basis set of given size are much more accurate than Gaussian basis set of same size. Relativistic calculations in gold are important and are performed with scalar relativistic corrections to valence orbitals relevant to atomic bonding

properties via a local pseudopotential (VPSR) [335]. For matrix integrations fine grid mesh points are employed. Convergence criterion of 10^{-6} a.u. has been used for self-consistent field procedures on energy and electron density. The vibrational frequency calculations at the optimized structures have been performed at the same level in order to verify the stationary points as minima.

The stability and the electronic properties of the clusters have been determined from the binding energy per atom, binding energy per H-atom, the vertical ionization potential and the chemical hardness values. For a given cluster, the binding energy is a measure of its thermodynamic stability. We calculate the average binding energies using the following formulas:

$$E_b = \frac{[6E(\text{Au}) + nE(\text{H}) - E(\text{Au}_6\text{H}_n)]}{(n + 6)} \quad (3.1.1)$$

$$E_b^a = \frac{[E(\text{Au}_6) + nE(\text{H}) - E(\text{Au}_6\text{H}_n)]}{n} \quad (3.1.2)$$

where E_b is the binding energy per atom and, E_b^a is the binding energy per H-atom, $E(\text{Au})$ and $E(\text{H})$ are the energies of Au and H atoms respectively, $E(\text{Au}_6)$ and $E(\text{Au}_6\text{H}_n)$ are the energies of Au_6 and Au_6H_n clusters respectively and n is the number of H atoms in a given cluster.

The Vertical Ionization Potential (VIP) is calculated as:

$$VIP = E(\text{Au}_6\text{H}_n)^+ - E(\text{Au}_6\text{H}_n) \quad (3.1.3)$$

where, $E(\text{Au}_6\text{H}_n)^+$ is the energy of the cationic cluster at the optimized geometry of the neutral cluster. Generally, larger Vertical Ionization Potential implies deeper HOMO energy level leading to lesser reactivity or higher chemical stability. A useful parameter for examining the kinetic stability of the clusters is the HOMO-LUMO gap (HLG).

$$HLG = E(LUMO) - E(HOMO) \quad (3.1.4)$$

Larger HOMO-LUMO gap corresponds to higher energy for perturbing the electronic structure thus indicating higher stability of electronic structure. The reactivity of a system can be described in terms of its chemical hardness. The second derivative of energy (E) with respect to the number of electrons (N) at

constant external potential, $\nu(\vec{r})$ defines hardness, η .

$$\eta = \frac{1}{2} \left(\frac{\partial^2 E}{\partial N^2} \right)_{\nu(\vec{r})} = \frac{1}{2} \left(\frac{\partial \mu}{\partial N} \right)_{\nu(\vec{r})} \quad (3.1.5)$$

where μ is the chemical potential of the system.

Applying three point finite difference approximation, hardness can be approximated as:

$$\eta = \frac{IP - EA}{2} \quad (3.1.6)$$

where IP is the Ionization potential and EA is the electron affinity of the system. Within the framework of Density Functional Theory, applying Koopmans approximation, hardness can be expressed as:

$$\eta = \frac{E(LUMO) - E(HOMO)}{2} \quad (3.1.7)$$

Condensed Fukui functions in a finite difference approximation have been proposed by Yang *et al.* [336] to describe the site reactivity or site selectivity and are given as:

$$f^+ = q(N + 1) - q(N) \text{ for nucleophilic attack} \quad (3.1.8a)$$

$$f^- = q(N) - q(N - 1) \text{ for electrophilic attack} \quad (3.1.8b)$$

$$f^0 = \frac{1}{2}[q(N + 1) - q(N - 1)] \text{ for radical attack} \quad (3.1.8c)$$

$q(N)$, $q(N + 1)$ and $q(N - 1)$ are the electronic populations for atoms with (N) , $(N + 1)$ and $(N - 1)$ electrons, respectively.

Roy *et al.* [337] proposed relative nucleophilicity as:

$$f_{nu} = \frac{f^-}{f^+} \quad (3.1.9)$$

and relative electrophilicity as:

$$f_{ele} = \frac{f^+}{f^-} \quad (3.1.10)$$

These are useful to identify the reactive site at which the reaction shall take place. In a molecule, if for a site, $f_{nu} \gg f_{ele}$, then the site is favorable for an electrophilic attack and favorable for nucleophilic attack if $f_{ele} \gg f_{nu}$. A site for which f_{nu} is almost equal to f_{ele} is said to be an amphiphilic site.

3.1.3 Results and Discussion

3.1.3.1 Geometric Structures of Au_6H_n ($n=1-12$) clusters

The planar triangular structure with D_{3h} symmetry for Au_6 cluster has been concluded to be the lowest energy structure from previous works [51,58,59] and the present work utilizes this stable structure (Figure 3.1.1) for further calculations. Based on the optimized lowest energy structure of Au_6 cluster, we perform an extensive minimum energy structural search for a number of hydrogen atoms binding to the Au_6 cluster. The lowest energy structures for Au_6H_n ($n=1-12$) are shown in Figure 3.1.1. The other higher energy isomers obtained during the structural search along with their total and relative energies are summarized in Appendix A. Absence of negative vibrational frequencies indicates the lowest energy optimized structures to be the minima rather than transition states. For all the clusters, Au_6H_n ($n=1$ to 12) both the low spin and high spin states have been considered. The low spin singlet and doublet states are found to be lower in energy compared to the high spin triplet and quartet states for clusters with even and odd number of H-atoms, respectively. The energies of all the clusters in both low spin and high spin states are given in Appendix A. Thus, the clusters are stable in the low spin state irrespective of the number of H-atoms.

Adsorption of the first H atom on the Au_6 cluster was considered in three different sites- outer Au atom, inner Au atom and in the bridge position. It has been found that the Au_6H cluster with H atom adsorbed on the outer Au atom is 0.07 eV higher in energy than the cluster with the H atom adsorbed on the inner Au atom. When the bridge position is considered, during the course of optimization, H atom preferentially adsorbs in the inner Au atom rather than being symmetrically bridged bonded. The Au-H bond lengths of 3.08 Å with outer Au atom and 1.56 Å with the inner Au atom is clearly indicative of this unsymmetrical bridge bonding. Density functional calculations by Rösch and co-workers on binding of one [338] and two [339] hydrogen ligands on Ir_4 cluster showed that the bridging positions are less stable than the terminal coordination sites. When the addition of the second H atom was considered on three sites viz. an outer Au atom, Au atom with adsorbed H atom and an inner Au atom; the

inner Au atom was found to be more preferable as compared to the H addition on an outer Au and the Au atom with adsorbed H atom. These were found to be 1.13 eV higher in energy than the Au_6H_2 cluster obtained from the adsorption of the H atom to an inner Au atom. Preferential adsorption of H atom on the inner Au atom can be correlated with the relative nucleophilicity (f^-/f^+) values. The inner Au atoms possess higher f^-/f^+ value and preference for it by the H atom indicates that H atom is likely to behave as an electrophile. It can be seen from Figure 3.1.1 that the clusters, Au_6H_n ($n=1-6$) are planar without any distortion in the triangular structure of Au_6 . The H atoms bind in a head-on fashion to the Au atoms with the shortest Au-H bond length being 1.52-1.57 Å which can be compared with the experimental Au-H bond length of 1.52 Å in AuH. However, in Au_6H_2 , the H atoms are bridge bonded between the inner Au atoms and the nearby outer Au atom with bond length of 1.73 Å. The average bond length of outer Au-Au bond increases from 2.59 Å in Au_6 to 2.62 Å in Au_6H_6 while the inner Au-Au bond length of 2.73 Å remains unchanged. However, in case of Au_6H_2 , one of the inner Au-Au bonds (dotted bond, Figure 3.1.1 is considerably elongated to 3.97 Å such that the parent Au_6 cluster distorts from the triangular structure. Elongation of Au-Au bond indicates that the binding of H atoms on the Au_6 cluster is made at the cost of metal-metal bond weakening. Zhai *et al.* [340] reported Au-H bond length of 1.72 Å and Au-Au distance of 3.44 Å in Au_2H^- comparable with abnormally long Au-Au distance (3.6 Å) observed in gold nano wires. On further addition of a H atom to the Au_6H_6 cluster that results in the Au_6H_7 , the triangular structure of Au_6 is considerably distorted and such distortion is also observed in Au_6H_8 and Au_6H_9 . However, all the three clusters with the distorted triangular structure are planar. In the Au_6H_7 cluster, migration of two H atoms to an outer Au atom from the nearby Au atoms is observed. Such H atom migration is also observed from the bridge position in Au_6H_8 to the outer Au atom in Au_6H_9 . Both bridge bonded H atoms and atoms bonded in the head-on fashion are observed in the three higher clusters. The shortest Au-H bond length for head-on bonded H atoms is 1.55 Å while for the bridge bonded H atoms the Au-H distance is in the range of 1.66-1.79 Å. One of the inner Au-Au bonds is considerably elongated (3.81 Å in Au_6H_7 , 3.89 Å in Au_6H_8 and 3.46 Å in Au_6H_9) which is comparable with

Au-Au distance in gold nano wires mentioned above. The average bond length of outer Au-Au bonds increase from 2.62 Å in Au_6H_6 to 2.68 Å in Au_6H_9 . Elongation of metal-metal bond indicates weakening of the bond which aid in the binding of H atoms.

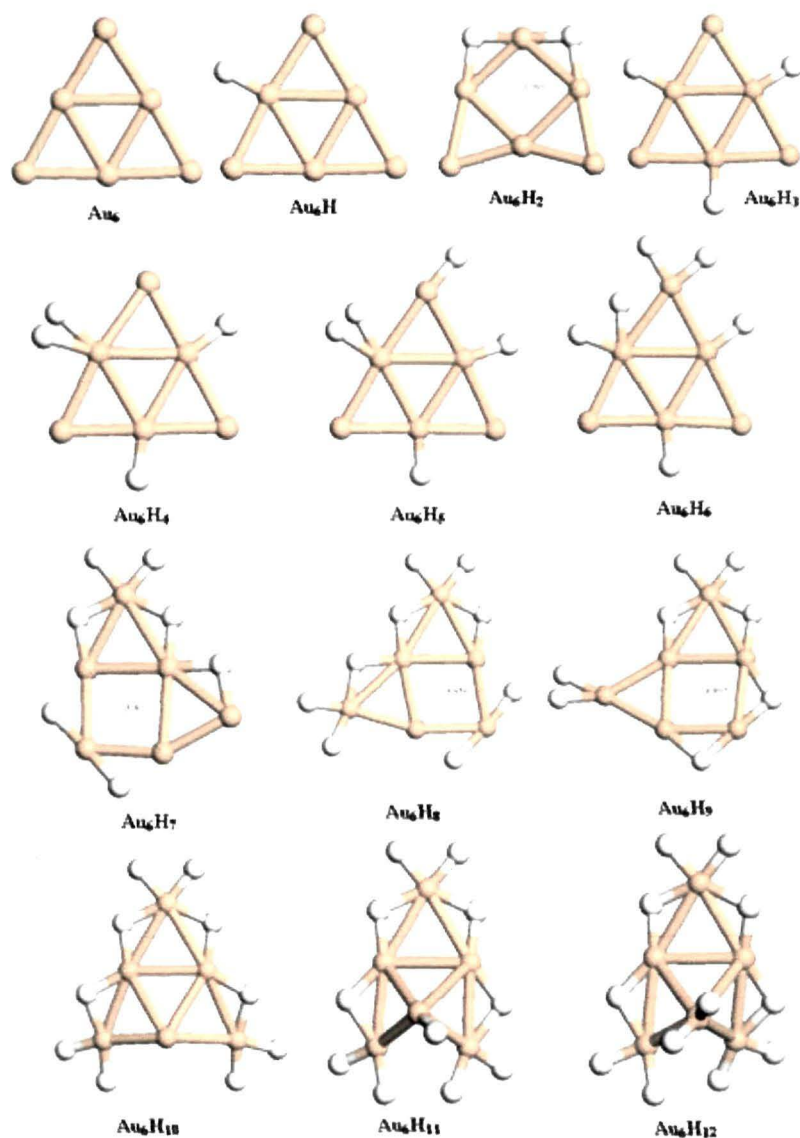


Figure 3.1.1: Optimized structures of the pristine Au_6 cluster and the Au_6H_n ($n=1-12$) clusters at PBE/DNP level of calculation. Yellow and White spheres represent Au and H atoms, respectively.

The planarity of the clusters is lost in Au_6H_{10} , Au_6H_{11} and Au_6H_{12} with one of the inner Au atoms protruding out of the plane of the triangle; however the triangular structure of Au_6 is retained. The average Au-Au bond length of the inner Au atoms increases from 2.68 Å in Au_6H_9 to 2.73 Å in Au_6H_{12} and outer Au-

Au bond length increases from 2.73 Å in Au₆ to 2.80 Å in Au₆H₁₂. The shortest Au-H distance of the head-on bonded H atom is 1.54 Å and in the range of 1.69-1.78 Å for bridge bonded H atom in the three clusters. Table 3.1.1 summarizes the Au-Au and Au-H (both head-on and bridge bonded) distances in Au₆H_n (n=1-12) clusters.

Table 3.1.1: Computed Au-H and Au-Au bond lengths of Au₆H_n (n=1 -12) clusters.

Cluster	Au-H(Å)		Au-Au (Å)	
	Head-on	Bridge	Outer	Inner
Au ₆	-	-	2.59	2.73
Au ₆ H	1.56	-	2.59	2.74
Au ₆ H ₂	1.73	-	2.59	2.73
Au ₆ H ₃	1.57	-	2.58	2.72
Au ₆ H ₄	1.57	-	2.60	2.72
Au ₆ H ₅	1.56	-	2.60	2.73
Au ₆ H ₆	1.54	-	2.62	2.73
Au ₆ H ₇	1.55	1.66-1.75	2.67	2.78
Au ₆ H ₈	1.55	1.66-1.79	2.67	2.74
Au ₆ H ₉	1.55	1.68-1.75	2.68	2.69
Au ₆ H ₁₀	1.54	1.72-1.78	2.69	2.73
Au ₆ H ₁₁	1.55	1.69-1.76	2.73	2.81
Au ₆ H ₁₂	1.54	1.69-1.77	2.73	2.80

3.1.3.2 Variation of Electronic Properties

From the binding energies calculated, it is observed that the binding energy per atom, E_b for the ground states of the Au₆H_n (n=1-12) clusters is higher than that for pristine Au₆ cluster. This indicates that hydrogen adsorption stabilizes the Au₆ cluster. The binding energy per atom and binding energy per H atom increases with the number of H atoms. The clusters with even number of H atoms exhibit higher value of binding energy and thus, possess higher stability compared to the counterparts with odd number of H atoms as evident from the binding

energy values. Both the binding energy per atom and binding energy of per H atom increase till Au_6H_8 while remaining constant with further increase in H-atom. However, exceptionally, Au_6H_2 possess the highest binding energy per H atom among all the clusters. The variation of binding energies of Au_6H_n clusters with the number of H atoms is shown in Figure 3.1.2. The HOMO-LUMO gap shows a definite odd-even oscillation pattern where clusters with even number of H-atoms possess higher values and the highest HOMO-LUMO gap of 2.44 eV is observed in Au_6H_8 such that no increase in the gap on further addition of H atoms is observed. This implicates that the Au_6 cluster with eight hydrogen atoms is more stable compared to the other congeners. The value of hardness, η of a cluster is a measure of the reactivity of that particular cluster. Au_6H_8 also possesses the highest hardness in parity with the highest HOMO-LUMO gap and thus, will be the least reactive from the perspective of highest η value. Figure 3.1.3 illustrates the HOMO and LUMO orbitals of Au_6 , Au_6H_2 , Au_6H_4 , Au_6H_6 , Au_6H_8 , Au_6H_{10} and Au_6H_{12} clusters. A strong s-d orbital hybridization is seen in the Au_6 cluster evident from Figure 3.1.3. The adsorption of different number of hydrogen atoms changes the electron density of the HOMO and LUMO states. Both the HOMO and LUMO states are mainly localized around the Au atoms along with some amount of distribution around the H-atoms.

Distribution around the H- atoms indicates existence of hybridization between the s-orbital of Au and s-orbital of H along with s-d orbital hybridization of Au atoms. Adsorption of H on the inner Au atoms likely results in charge transfer from the HOMO of the Au_6 cluster to the H atom which results in increase in electron density on the later as revealed from the presence of negative charges discussed in the Hirshfeld charge analysis below.

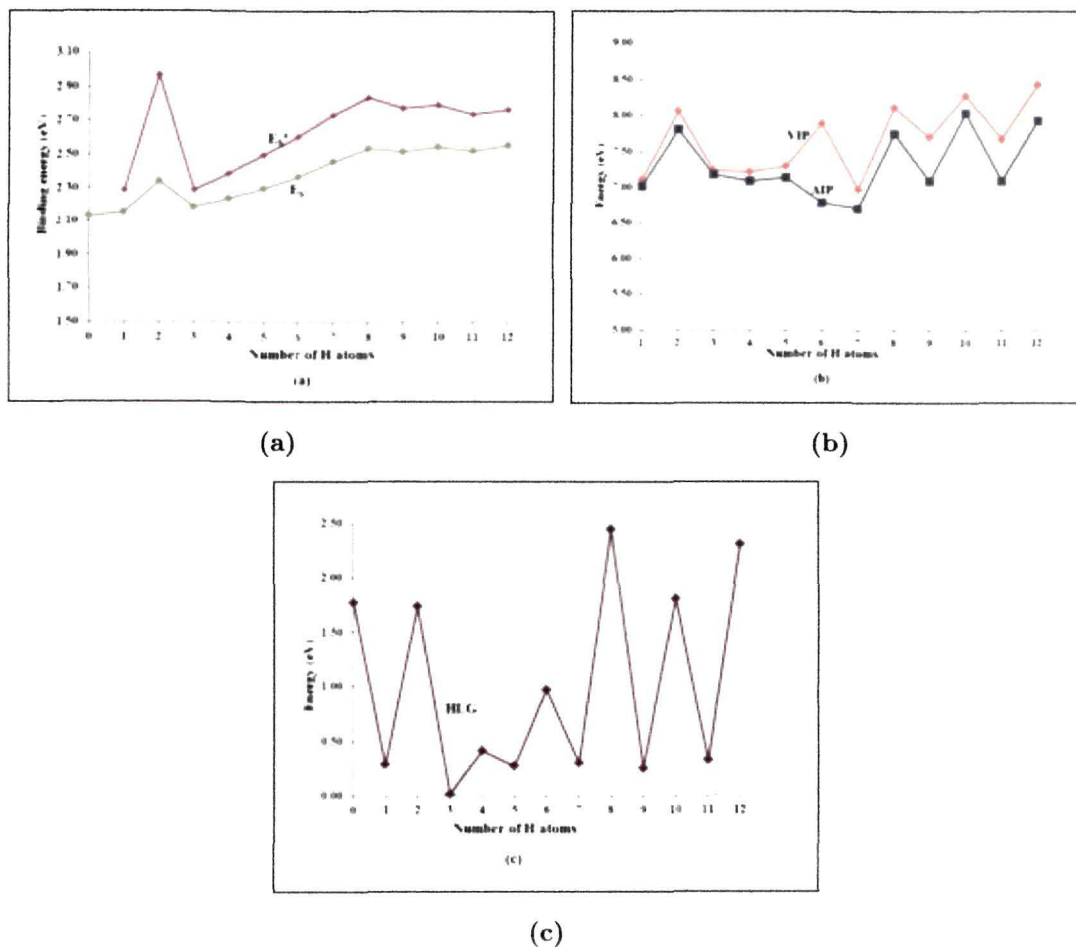


Figure 3.1.2: Variation of (a) binding energy per atom, binding energy per hydrogen atom, (b) vertical ionization potential, adiabatic ionization potential and (c) HOMO-LUMO gap of the Au₆H_n (n=1-12) clusters with the number of hydrogen atoms.

Next, the vertical ionization potential (VIP) and the adiabatic ionization potential (AIP) are considered. The VIP values exhibit an odd-even pattern from Au₆H to Au₆H₃ and then remain constant till Au₆H₅. From Au₆H₆ to Au₆H₁₂, it again exhibits a distinct odd-even oscillation pattern where clusters with even number of H atoms have higher VIP values. Similar odd-even pattern is observed for adiabatic ionization potential values from Au₆H to Au₆H₃ and then remain constant till Au₆H₅. The AIP values decrease in Au₆H₆ and Au₆H₇ while show a definite odd-even oscillation pattern from Au₆H₈ till Au₆H₁₂. The AIP and VIP values indicate Au₆H₂, Au₆H₈, Au₆H₁₀ and Au₆H₁₂ to be more stable compared to other congeners. Table 3.1.2 summarizes the binding energy per atom, E_b; bind-

ing energy per H-atom, E_b^a ; vertical ionization potential, VIP; adiabatic ionization potential, AIP; HOMO-LUMO gap, HLG and hardness, η of the Au_6H_n clusters. Figure 3.1.2 (b) shows the variation of VIP and AIP and (c) shows the variation of HLG values with the number of H atoms.

The averaged atomic Hirshfeld charges on H atoms for the Au_6H_n clusters are listed in Table 3.1.3. The values indicate that the H atoms are negatively charged and the strong interaction between Au and H atoms results from charge transfers. Analysis of Hirshfeld charges on Au atoms of pristine Au_6 cluster reveal that the inner Au atoms carry equal negative charge while the outer Au atoms are positively charged and adsorption of H atom on the inner Au atom results in charge transfer from the Au atom to the H atom. The presence of negative charge on the H atoms in the hydrogenated gold clusters indicates that these are likely to remain as gold hydrides.

Table 3.1.2: Calculated binding energy per atom E_b (eV); binding energy per hydrogen atom E_b^a (eV); vertical ionization potential VIP (eV); adiabatic ionization potential AIP (eV); HOMO-LUMO gap HLG (eV) and hardness η of the Au_6H_n (n=1-12) clusters.

Clusters	E_b	E_b^a	VIP	AIP	HLG	Hardness
Au_6	2.15	-	-	-	1.77	0.885
Au_6H	2.17	2.29	7.10	7.01	0.29	0.145
Au_6H_2	2.36	2.97	8.06	7.80	1.73	0.865
Au_6H_3	2.20	2.29	7.23	7.17	0.01	0.005
Au_6H_4	2.25	2.39	7.21	7.09	0.41	0.205
Au_6H_5	2.31	2.50	7.29	7.14	0.27	0.135
Au_6H_6	2.38	2.61	7.88	6.78	0.97	0.484
Au_6H_7	2.47	2.73	6.96	6.70	0.30	0.150
Au_6H_8	2.54	2.84	8.11	7.75	2.24	1.220
Au_6H_9	2.53	2.78	7.69	7.08	0.25	0.125
Au_6H_{10}	2.56	2.80	8.28	8.03	1.80	0.900
Au_6H_{11}	2.53	2.74	7.66	7.07	0.33	0.165
Au_6H_{12}	2.56	2.77	8.43	7.93	2.30	1.150

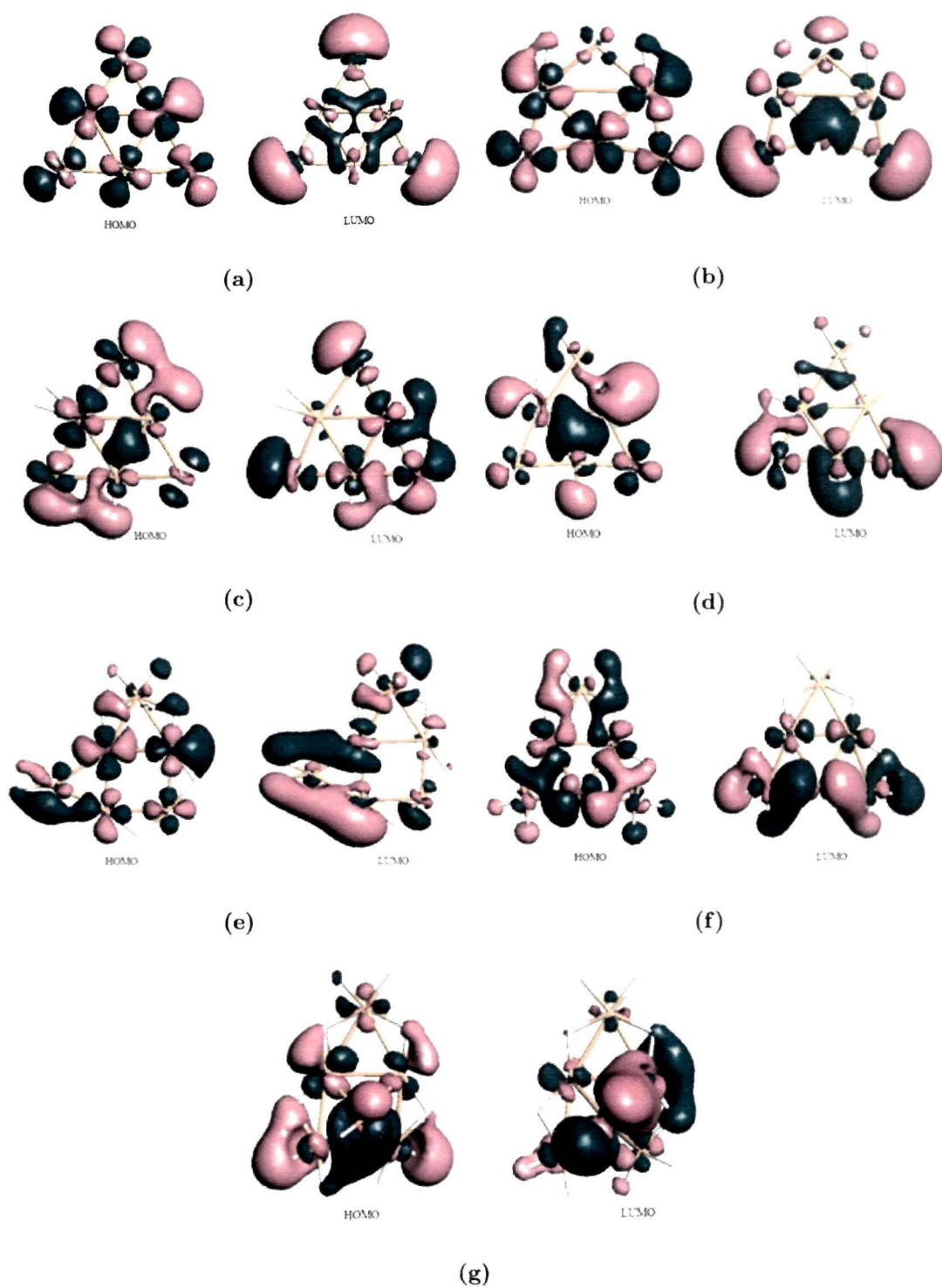


Figure 3.1.3: The HOMO and LUMO orbitals of (a) Au_6 , (b) Au_6H_2 , (c) Au_6H_4 , (d) Au_6H_6 , (e) Au_6H_8 , (f) Au_6H_{10} and (g) Au_6H_{12} clusters.

Table 3.1.3: Averaged atomic Hirshfeld charges on H atom in Au₆H_n (n=1-12) clusters.

Clusters	Charge
Au ₆ H	-0.071
Au ₆ H ₂	-0.085
Au ₆ H ₃	-0.094
Au ₆ H ₄	-0.039
Au ₆ H ₅	-0.042
Au ₆ H ₆	-0.059
Au ₆ H ₇	-0.065
Au ₆ H ₈	-0.043
Au ₆ H ₉	-0.060
Au ₆ H ₁₀	-0.052
Au ₆ H ₁₁	-0.053
Au ₆ H ₁₂	-0.049

3.1.3.3 Fukui Function

Analyzing the f^+/f^- and f^-/f^+ values, i.e. the relative electrophilicity and nucleophilicity, respectively of a site in a cluster helps to predict the response of that particular site towards an impending electrophilic or nucleophilic attack. When we consider the f^+/f^- and f^-/f^+ values for all the six sites present in the Au₆ cluster, we find that on one hand the atoms forming the vertices of the outer triangle have a higher f^+/f^- value while on the other hand, the atoms comprising the vertices of the inner triangle have higher f^-/f^+ value. Thus, the atoms forming the vertices of the outer triangle are prone for a nucleophilic attack like CO and those forming the vertices of the inner triangle are susceptible for an electrophilic attack like O₂. Phala *et al.* [332] and Wu *et al.* [106] have also found CO adsorbed on the outer Au atom of neutral Au₆ cluster to be the most stable configuration. In Au₆H, the Au atom (higher f^-/f^+ value in pristine Au₆) with adsorbed H atom has the highest f^+/f^- value while the remaining two inner Au atoms still have higher f^-/f^+ value. In Au₆H₂, the higher f^+/f^- value is retained on the outer Au atoms and an inner Au atom with no H adsorbed on it has the highest f^-/f^+ value. In Au₆H₃

and Au_6H_4 , all the Au sites are amphiphilic, i.e. all the six Au atoms possess equal f^+/f^- and f^-/f^+ values. These are likely to donate and withdraw electrons thus, participating in both oxidation and reduction reactions. In Au_6H_6 , the reactivity trend of the pristine Au_6 cluster is preserved with one inner Au atom having the highest f^-/f^+ value and a nearby outer Au atom with the highest f^+/f^- value. However, the difference with pristine Au_6 cluster is that in Au_6H_6 specific sites have the highest values unlike having equal values for similar Au sites as in the former. Thus, if we intend to study the CO oxidation on Au_6H_6 cluster, O_2 will adsorb on the inner Au atom while CO on the nearby outer Au atom and will thus serve to be a favorable configuration to investigate the detailed mechanism of the said reaction.

In Au_6H_8 , one Au atom forming the vertex of the inner triangle has the highest f^-/f^+ value while another inner Au atom has the highest f^+/f^- value. On the other hand, in Au_6H_{10} , one Au atom forming the vertex of the outer triangle has the highest f^-/f^+ value while another outer Au atom has the highest f^+/f^- value. Thus, in Au_6H_8 both CO and O_2 will adsorb in the vertices of the inner triangle while in Au_6H_{10} , they will adsorb in the outer Au atoms. The reactivity trend of the Au sites in Au_6H_{11} and Au_6H_{12} is however, similar to Au_6H_8 . Analysis of the reactivity descriptors indicate the adsorption of H atoms do not alter much the reactivity behavior of Au sites towards an impending electrophile or nucleophile except in situations like Au_6H_8 and Au_6H_{10} where the reactivity trend is changed. Relative electrophilicity and relative nucleophilicity for all the clusters are given in Appendix A.

3.1.4 Salient Observation

The geometric structures, binding energies, HOMO-LUMO gap, chemical hardness and the reactivity properties of the Au sites of Au_6H_n ($n=1-12$) clusters have been studied at the generalized gradient approximation level using the PBE functional and DNP basis set. The low spin state structures are found to more stable than the high spin counterparts in all the clusters. The high binding energies indicate that the adsorption of H atoms stabilize the Au_6 cluster. The lowest energy structures obtained from the present investigation shows that the structures are planar till

Au_6H_9 . However, the triangular structure of Au_6 is distorted in Au_6H_7 , Au_6H_8 and Au_6H_9 . Elongation of Au-Au bond length indicates that the metal hydrogen bonding is made at the expense of metal-metal bond weakening. On further addition of H atoms one of the base Au atoms of the Au_6 triangle protrudes out of the plane of Au_6 in Au_6H_{10} , Au_6H_{11} and Au_6H_{12} cluster rendering these clusters non planarity. The averaged Hirshfeld atomic charges indicate the H atoms to be negatively charged in all the clusters indicating charge transfer from Au to H atoms. Odd-even alternation in HOMO-LUMO gap, chemical hardness, vertical ionization potential, adiabatic ionization potential and binding energy is observed with the clusters having even number of H atoms possessing higher values and are observed to be more stable than their congeners with odd number of H atoms. DFT based reactivity descriptors indicate that in Au_6 , the Au atoms forming the vertices of the outer triangle have higher relative electrophilicity value while those forming the vertices of the inner triangle have higher relative nucleophilicity value. This implies that nucleophile such as CO will attack on the outer Au atoms while electrophiles such as O_2 on inner Au atoms. However, in Au_6H_6 , two nearby Au sites forming the vertices of the inner and outer triangle have the highest relative electrophilicity and relative nucleophilicity values. In Au_6H_{12} , these are located in the inner triangle.

3.2 Reverse Hydrogen Spillover on Zeolite Supported Pd₆ and Au₆ clusters

3.2.1 Introduction

Supported transition metal catalysts find widespread application as catalysts in various industrial processes such as production and the transformation of automotive fuels from traditional and new or renewable sources [341]. With the ever increasing efficiency of such catalytic systems and their increased demand for application as a catalyst; it becomes essential to gain an insight into the state and structure of supported metal catalysts. Although experimental studies [159,220,342] have been devoted towards understanding the nature and structure of supported metal clusters, it is difficult to elucidate their exact composition and interaction with the support. Although some indispensable information such as composition of the samples, inter-atomic distances, atomic coordination numbers, and, to some extent, oxidation states of metal center can be obtained from experimental techniques like X-ray absorption near-edge structure spectroscopy (XANES) and extended X-ray absorption fine structure spectroscopy (EXAFS), these techniques do not always yield complete results or unambiguously assess the structure of supported metal clusters. In such situations, complementary theoretical studies based on pertinent models and accurate electronic structure methods have proven to be helpful [343-345]. Zeolites form an interesting class of support for metal clusters and nanoparticles. They are often used as solid catalyst in the petroleum and chemical industries because of their fascinating properties such as Brønsted and Lewis acidities, size-shape-selectivity and thermal stability [346]. Zeolite frameworks possess well-defined chemical composition, structure, pores and cavities of molecular dimensions that facilitate the preparation of uniform small supported metal clusters [347,348]. The structure and aluminum content of the zeolite affect the properties of such supported metal clusters and understanding of how the interaction with the zeolite can modify the structural as well as the electronic properties of these metal clusters is a primary step to rationalize their properties. Computational studies utilizing an accurate electronic structure method can

contribute significantly to clarify these issues.

Transition metal clusters undergo considerable changes in electronic structure and thus in the catalytic behaviour as a result of their interaction with the zeolite framework. Thus, it becomes necessary to first determine the structure, coordination mode and nature of active sites of these transition metal clusters in order to investigate their catalytic activity. Sachtler *et al.* [349,350] carried out experiments that aimed at understanding the catalytic activity of zeolite supported Pd and Rh clusters in hydrocarbon conversion. They suggested the formation of positively charged metal-proton adducts, $[\text{Pd}_n\text{H}_x]^{x+}$ and $[\text{Rh}_n\text{H}_x]^{x+}$ from the interaction of the metal clusters with the protons of the support. The metal moiety in this adducts are partially oxidized. Density functional calculations on Ir_4 cluster supported on faujasite zeolite by Ferrari *et al.* [351] observed notable differences between calculated metal-metal distances and values obtained from EXAFS. Subsequent studies [352] identified reverse spillover of protons from hydroxyl groups of zeolite or metal oxide support to metal clusters as a rationalization for this structural difference. Presence of H impurity atoms on zeolite supported Rh_6 clusters due to reverse hydrogen spillover from the zeolite framework was reported by Vayssilov *et al.* [353]. They found that the supported Rh_6 clusters undergo partial oxidation. When the study was extended to transition metal clusters, M_6 of the platinum and gold groups [343], reverse spillover of hydrogen on to the zeolite supported metal clusters was found to be favourable for all the metals. However, the estimated energy of reverse spillover of hydrogen was reported to be the lowest for the clusters Au_6 and Ag_6 . The isolated cluster models used by them contain six tetrahedral atoms of faujasite zeolite terminated by OH groups, which however, may not be a good model to represent zeolite. The hydrogenated form, $\text{M}_6\text{H}_3/\text{FAU}$ was found to be not necessarily more stable than the bare zeolite supported form, $\text{M}_6/\text{FAU}(3\text{H})$ in case of gold unlike other transition metals in the study made by Shor *et al.* [344]. The energy of reverse hydrogen spillover however, improved to some extent and they found that the process of reverse spillover may be exothermic or endothermic depending upon the initial location of the migrating protons in the zeolite framework. Deka *et al.* [354] performed density functional studies on structure and reverse hydrogen spillover in Au_6 cluster supported on acidic form

of faujasite zeolite. On zeolite support, Au_6 has three dimensional structure with the three apical centres bending towards the support and the hydrogenated clusters, $\text{Au}_6\text{H}_n/\text{FAU}(3-n)\text{H}$ generated by stepwise reverse hydrogen spillover from the bridging OH groups of zeolite were preferred over the $\text{Au}_6/\text{FAU}(3\text{H})$ structure. Investigation of reverse hydrogen spillover on zeolite supported palladium tetramer by Kalita and Deka [355] revealed that the hydrogenated Pd_4 clusters supported on zeolite are favoured over the bare clusters. The transfer of single proton from the zeolite support to the Pd_4 cluster was found to be more favourable than two- and three- proton transfer processes. Successive adsorption of up to twelve hydrogen atoms on gas phase and zeolite supported tetrahedral models of Rh_4 , Ir_4 and Pt_4 has been studied by Petkov *et al.* [356]. They found an increase in the average metal-metal distances for both gas-phase and zeolite supported clusters. However, the adsorption energy decreases with an increase in hydrogen loading on the metal clusters. Motivated by the fair amount of work done by various groups and keeping in view the importance of hydrogenated metal clusters; we studied the process of reverse hydrogen spillover on zeolite supported Au_6 and Pd_6 clusters by stepwise transfer of acidic hydrogens from the bridging OH groups of faujasite zeolite support to the metal clusters using density functional theory.

3.2.2 Computational Details

The faujasite framework employed in the present work (Figure 3.2.1) consists of a six membered ring in which three Si atoms are isomorphously substituted by three Al atoms according to the Löwenstein rule. The excess negative charges generated due to the Al substitution are compensated by adding three protons that form three bridging OH groups with the framework oxygen atoms. The free valences of Si and Al atoms are saturated with hydrogen atoms. At first, only the Si-H, Al-H and O-H bonds have been optimized while fixing the position of other atoms at the crystallographic positions. Subsequently, the optimized positions of the terminating hydrogen atoms have been fixed allowing other atoms to relax.

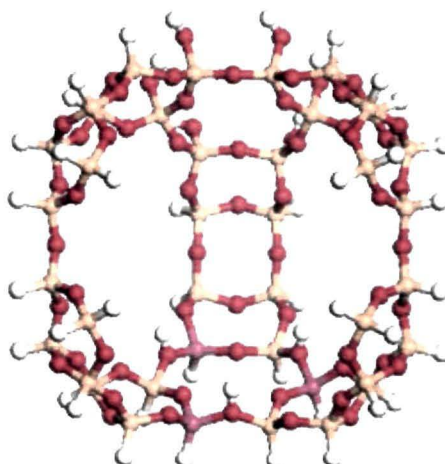


Figure 3.2.1: Faujasite model with three bridging OH groups. Yellow, Magenta, Red and White spheres represent Si, Al, O and H atoms, respectively.

In the present work we have considered Pd_6 and Au_6 clusters supported on the faujasite zeolite. The planar triangular structure of Au_6 cluster has been determined as the most stable structure from density functional calculations [51,58,59]. However, it has been observed that the planar triangular structure undergoes distortion to a distorted octahedron when supported on zeolite. A distorted octahedron has been reported as the lowest energy structure for Pd_6 [357]. In this work, we utilize the distorted octahedral structures for Pd_6 and Au_6 . The geometries of the model clusters are optimized without imposing symmetry constraints. The calculations are performed using DN basis set and VWN functional [271] implemented in the DMol³ program [307]. Hirshfeld population analysis (HPA) has been used to characterize the electronic charge distribution. To investigate the reactivity of the metal clusters with the OH groups of the zeolite fragment, we calculate the energy of reverse hydrogen spillover from bridging OH groups to the metal cluster, M_6 and can be expressed in terms of per transferred hydrogen as:

$$E_{RS} = \frac{\{E[\text{M}_6\text{H}_n/\text{FAU}(3-n)\text{H}] - E[\text{M}_6/\text{FAU}(3\text{H})]\}}{n} \quad (3.2.1)$$

where, $n = 1, 2, 3$. $\{E[\text{M}_6\text{H}_n/\text{FAU}(3-n)\text{H}]\}$ is the energy of the metal cluster with n spillover hydrogen atom(s) and $E[\text{M}_6/\text{FAU}(3\text{H})]\}$ is the energy of the bare M_6 cluster adsorbed on faujasite. A negative E_{RS} value indicates higher stability of the hydrogenated metal clusters, M_6H_n in zeolite support than their dehydrogenated counterpart.

3.2.3 Results and Discussion

3.2.3.1 Zeolite supported bare Pd₆ and Au₆ clusters

The optimized structures of the faujasite supported Pd₆ and Au₆ clusters are shown in Figure 3.2.2. Table 3.2.1 summarizes the important structural parameters and the Hirshfeld charges. The metal atoms of the distorted octahedral structure of the hexamer metal clusters closer to the zeolite framework are assigned as M_z (M=Pd, Au) and the metal atoms that are farther from the zeolite and do not directly interact with the support are assigned as M_t. The framework oxygen atoms are designated as O_z while the oxygen atoms with bridging OH groups are labelled as O_H.

Our calculations reveal that two nearest neighbour Pd_z atoms in the distorted octahedral Pd₆ cluster are at a distance of 2.68Å while the distance between Pd_t atoms is 0.12Å shorter. The distance between Pd atoms belonging to different triangles (Pd_z-Pd_t bond) is found to be similar, differing by at most 0.08Å from the Pd_z-Pd_z length. The Pd_z-Pd_z, Pd_t-Pd_t and Pd_z-Pd_t bond lengths obtained from our calculations are in close agreement with the results reported previously [344]. Interaction of the Pd₆ cluster with the zeolite framework is indicated by the distance between each of the three Pd_z atoms and one framework oxygen atom, O_z with the shortest value of 2.16Å while the Pd_z-O_H bond length is comparatively higher (2.94Å). Thus, the Pd₆ cluster interacts with the zeolite support with an overall of three close Pd-O contacts. The Hirshfeld charge analysis shows that the Pd_z atoms which are in close proximity with the zeolite carry an average charge of 0.168e exhibiting a weak positive character whereas the Pd_t atoms carry 0.090e charge featuring slight neutral behaviour. The weak positive character of the Pd_z atoms can be attributed to their interaction with the zeolite oxygen atoms.

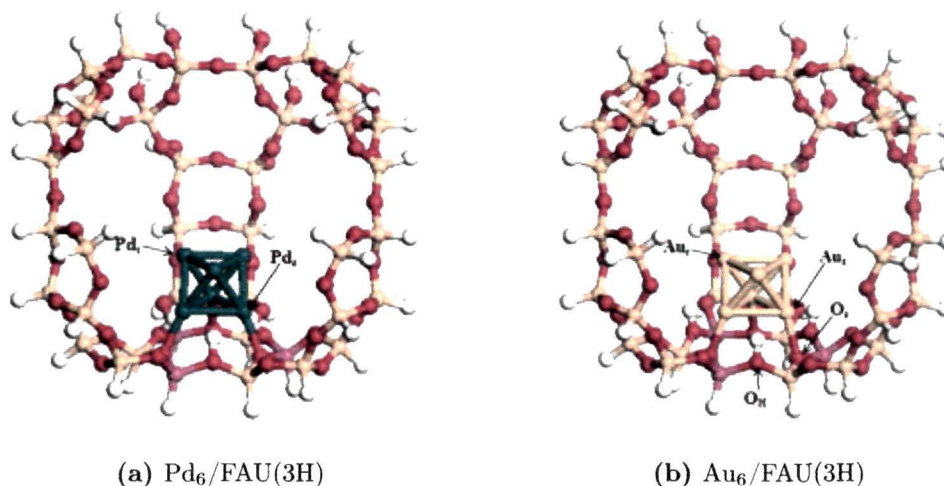


Figure 3.2.2: Optimized structures of faujasite supported bare Pd₆ and Au₆ clusters

Table 3.2.1: Computed geometrical parameters and Hirshfeld charges of selected atoms of faujasite supported bare Pd₆ and Au₆ clusters.

	Pd ₆ /FAU(3H)	Au ₆ /FAU(3H)
Bond Distances(Å)		
M _z - M _z	2.68	2.77
M _t - M _t	2.56	2.72
M _z - M _t	2.60	2.56
M _z - O _z	2.16	2.20
M _z - O _H	2.94	3.06
M _z - Al	3.11	3.04
M _z - Si	3.19	3.21
O-H	1.16	1.02
Charges (Hirshfeld)		
q(M _z)	0.168	0.037
q(M _t)	0.090	-0.040
q(H _O)	0.029	0.153

For the Au₆ cluster with the distorted octahedral structure supported on faujasite, the Au-Au distances of the 'top' and 'bottom' triangles (Au_t-Au_t and Au_z-Au_z bonds) are similar with differences of 0.05Å while the distance between Au atoms belonging to two different triangles (Au_z-Au_t) is 0.21Å shorter than the Au_z-Au_z

distance. Our values are comparable with the results reported earlier [353]. The $\text{Au}_z\text{-O}_z$ distance indicating the interaction of the Au_6 cluster with the zeolite framework has the shortest value of 2.20Å while the $\text{Au}_z\text{-O}_\text{H}$ bond length is much higher (3.06Å). This shows that the Au_6 cluster interacts with the zeolite support via three oxygen atoms, O_z . The Au_z atoms which are in close contact with the zeolite carry an average Hirshfeld charge of 0.037e featuring a slight cationic character whereas the Au_t atoms are weakly negative with a charge of -0.040e. Thus both bare Pd_6 and Au_6 clusters supported on zeolite consist of two type metal centres within the same cluster.

3.2.3.2 Zeolite supported hydrogenated Pd_6 clusters

The optimized structures of the hydrogenated Pd_6 clusters supported on faujasite obtained as a result of stepwise reverse spillover of one, two and three protons from the zeolite to the Pd_6 cluster are shown in Figure 3.2.3. The computed selected geometrical parameters, reverse spillover energy per transferred hydrogen and the Hirshfeld charge of the selected atoms are summarized in Table 3.2.2. It can be perceived that the $\text{Pd}_z\text{-Pd}_z$ and $\text{Pd}_\text{t}\text{-Pd}_\text{t}$ distances do not undergo any significant changes as a result of reverse hydrogen spillover however, the $\text{Pd}_z\text{-Pd}_\text{t}$ bond length decreases from 2.60Å in $\text{Pd}_6/\text{FAU}(3\text{H})$ to 2.51Å in $\text{Pd}_6\text{H}_3/\text{FAU}$. The interaction of the hydrogenated Pd_6 cluster with the zeolite framework increases which is indicated by the decreasing $\text{Pd}_z\text{-O}_z$ distance from 2.16Å in $\text{Pd}_6/\text{FAU}(3\text{H})$ to 2.09Å in $\text{Pd}_6\text{H}_3/\text{FAU}$. The distance between each of the three Pd_z atoms and an oxygen atom with bridging OH group, O_H also decreases considerably from 2.94Å in the dehydrogenated Pd_6 cluster to 2.13Å in the hydrogenated counterpart. Hence, in $\text{Pd}_6\text{H}_3/\text{FAU}$ there are overall six Pd-O contacts unlike three close contacts in the bare Pd_6 cluster supported on zeolite. Thus, reverse hydrogen spillover results in stronger interaction of the Pd_6 cluster with the zeolite support. Decreasing $\text{Pd}_z\text{-Al}$ and $\text{Pd}_z\text{-Si}$ distances to 2.82Å and 2.72Å, respectively also show increased interaction of Pd_6H_3 cluster with the zeolite support. In all the hydrogenated Pd_6 clusters, $\text{Pd}_6\text{H}_n/\text{FAU}(3-n)$; $n=1-3$ the migrated H atoms coordinate with the $\text{Pd}_z\text{-Pd}_\text{t}$ bonds where the distance of the migrated H atom(s), H_{Pd} from the Pd_t atom remains almost similar ($\sim 1.69\text{-}1.70\text{Å}$). The $\text{Pd}_z\text{-H}_{\text{Pd}}$ distance however, decreases from 1.80Å

in Pd₆H/FAU(2H) and Pd₆H₂/FAU(H) to 1.69 Å in Pd₆H₃/FAU. Thus the spilled over hydrogen atoms coordinate in an unsymmetrical fashion in Pd₆H_n/FAU(3-n); n=1,2 whereas in a symmetrical fashion with equal Pd_t-H_{Pd} and Pd_z-H_{Pd} bond lengths in Pd₆H₃/FAU.

The process of reverse hydrogen spillover of two protons from bridging OH groups of the zeolite to the Pd₆ cluster is exothermic, given by a value of -52.60 kJmol⁻¹ for Pd₆H₂/FAU(H). The corresponding processes for the migration of one and three proton(s) are less exothermic with E_{RS} values of -15.87 kJmol⁻¹ and -29.33 kJmol⁻¹, respectively. We can thus, say that the reverse hydrogen spillover process of two proton transfer is energetically more favourable than one and three proton transfer processes for the Pd₆ cluster supported on faujasite. It is seen that the process of reverse hydrogen spillover of two protons from the zeolite support results in the hydrogenated species, Pd₆H₂/FAU(H) which is 105.19 kJmol⁻¹ more stable than the bare Pd₆ cluster supported on faujasite. The other hydrogenated clusters, Pd₆H/FAU(2H) and Pd₆H₃/FAU are 15.87 kJmol⁻¹ and 58.67 kJmol⁻¹, respectively more stable than the dehydrogenated counterpart. Thus, the process of reverse hydrogen spillover enhances the stability of faujasite supported Pd₆ cluster. From the Hirshfeld charges, we observe that the average charge on the Pd_z and Pd_t atoms increases from 0.168e and 0.090e, respectively in Pd₆/FAU(3H) to 0.340e and 0.195e, respectively in the hydrogenated cluster. Increase in the Hirshfeld charge indicates oxidation of both the types of Pd atoms in the Pd₆ cluster as a consequence of reverse hydrogen spillover. The bridging H atoms in the zeolite supported bare Pd₆ cluster carry an average charge of 0.029e which reduces to -0.087e in Pd₆H₃/FAU. The acidic hydrogen atoms, H_O in Pd₆H/FAU(2H) and Pd₆H₂/FAU(H) carry average charges 0.051e and 0.207e, respectively whereas the spilled over hydrogen(s) carry charges -0.107e and -0.087e, respectively. The present investigation allows us to arrive at the conclusion that the process of reverse hydrogen spillover results in formal reduction of hydrogen atoms from H⁺ to H⁻ with a concomitant oxidation of Pd atoms. Both faujasite supported bare and hydrogenated Pd₆ clusters consist of two types of metal centres within the same cluster.

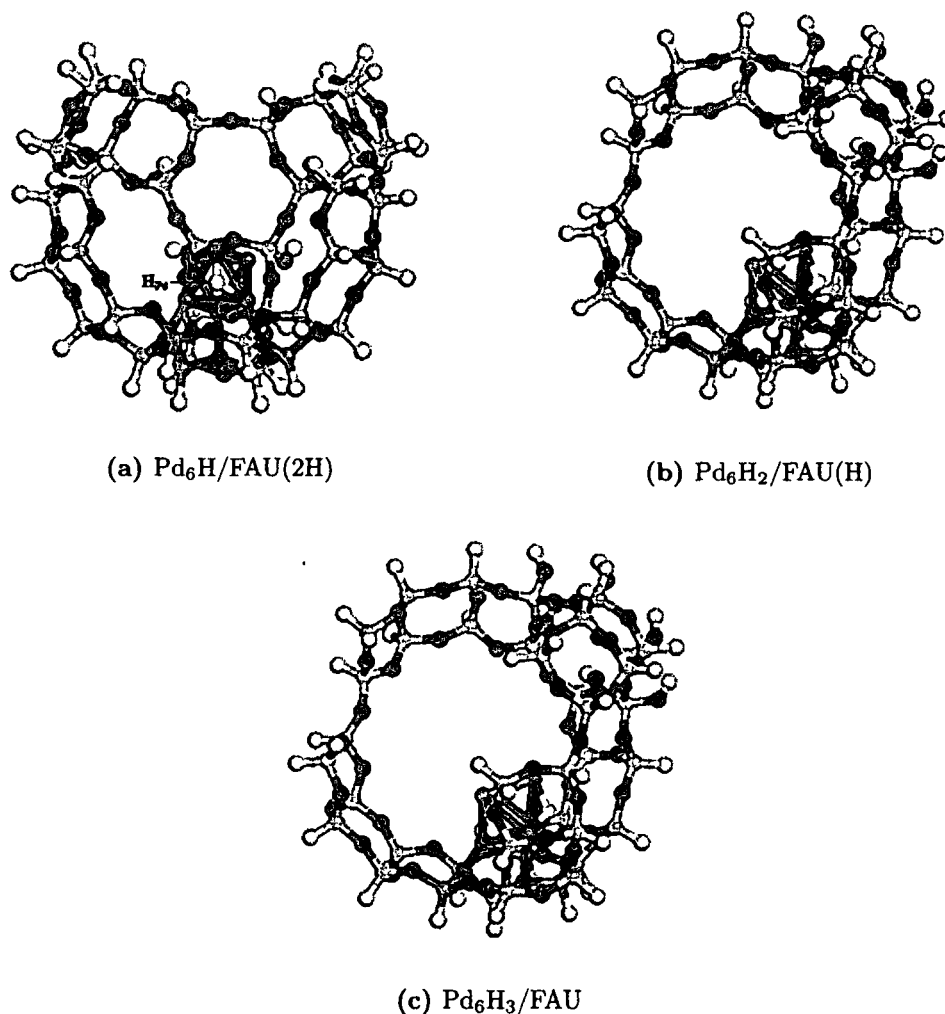


Figure 3.2.3: Optimized structures of faujasite supported hydrogenated Pd_6 clusters, $\text{Pd}_6\text{H}_n/\text{FAU}(3-n)$; $n=1-3$.

3.2.3.3 Zeolite supported hydrogenated Au_6 clusters

The optimized structures of the hydrogenated Au_6 clusters supported on faujasite obtained as a result of stepwise transfer of one, two and three protons from the zeolite to Au_6 cluster are shown in Figure 3.2.4. The computed selected geometrical parameters, reverse spillover energy per transferred hydrogen and the Hirshfeld charges of selected atoms are summarized in Table 3.2.2. The $\text{Au}_z\text{-Au}_z$ distance decreases from 2.77\AA in $\text{Au}_6/\text{FAU}(3\text{H})$ to 2.69\AA in $\text{Au}_6\text{H}_3/\text{FAU}$ as a result of transfer of three protons from the zeolite. The $\text{Au}_t\text{-Au}_t$ and $\text{Au}_z\text{-Au}_t$ bond lengths also decrease in the zeolite supported hydrogenated Au_6 clusters. The $\text{Au}_z\text{-O}_z$ distance decreases from 2.20\AA in $\text{Au}_6/\text{FAU}(3\text{H})$ to 2.09\AA in $\text{Au}_6\text{H}_3/\text{FAU}$. The

Au-O distance obtained by EXAFS for faujasite supported mononuclear gold particles (2.08Å) [220] and for large gold particles supported on alumina (2.04-2.05Å) [358] is close to the value obtained in our calculation for faujasite supported Au₆H₃ cluster. Decreasing Au_z-O_z distance on hydrogenation of the Au₆ cluster is an indication of the increasing interaction of the cluster with the zeolite. The distance between the Au_z atom and the O_H atom decreases from 3.06Å in Au₆/FAU(3H) to 2.22Å in Au₆H₃/FAU. The Au_z-O_z and Au_z-O_H distances indicate that each Au_z atom in the dehydrogenated Au₆ cluster interacts with only one zeolite oxygen atom (O_z) whereas in Au₆H₃/FAU, each Au_z atom interacts with both O_z and O_H atoms. Thus, reverse spillover of hydrogen results in a stronger interaction of the Au₆ cluster with the support with an overall of six close Au-O contacts. Previous computational studies however, evidenced only three close Au-O contacts for hydrogenated Au₆ cluster supported on zeolite. This may be due to the imposed symmetry constraints of the model complex [343]. The Au_z-Si distance also decreases from 3.21Å in Au₆/FAU(3H) to 2.76Å in Au₆H₃/FAU as a consequence of spillover. In all the hydrogenated clusters the H atoms are observed to spillover to the Au_t atoms with Au_t-H bond length of 1.56Å comparable with the value obtained by Deka *et al.* [354].

From Table 3.2.2, we find that the transfer of the first proton from the bridging OH group of the zeolite to the Au₆ cluster is exothermic with the E_{RS} value of -69.56 kJmol⁻¹. The corresponding processes for the migration of two and three acidic hydrogen atoms are less exothermic with E_{RS} values of -47.30 kJmol⁻¹ and -24.50 kJ mol⁻¹, respectively. Thus, the reverse hydrogen spillover process of one proton transfer is energetically more favourable than two and three proton transfer processes for the Au₆ cluster on a faujasite support. The hydrogenated Au₆ cluster supported on faujasite resulting from the migration of two protons is found to be more stable than the bare Au₆ cluster by 94.61 kJmol⁻¹ and is in fact the most stable among all the hydrogenated species, Au₆H_n/FAU(3-n); n=1-3. The other hydrogenated Au₆ clusters, Au₆H₃ and Au₆H are 73.49 kJmol⁻¹ and 69.56 kJmol⁻¹, respectively more stable than the dehydrogenated counterpart. Higher stability of Au₆H₂/FAU(H) is indicated by the shortest Au_z-O_z and Au_z-O_H bond lengths leading to stronger interaction of the cluster with the faujasite

support.

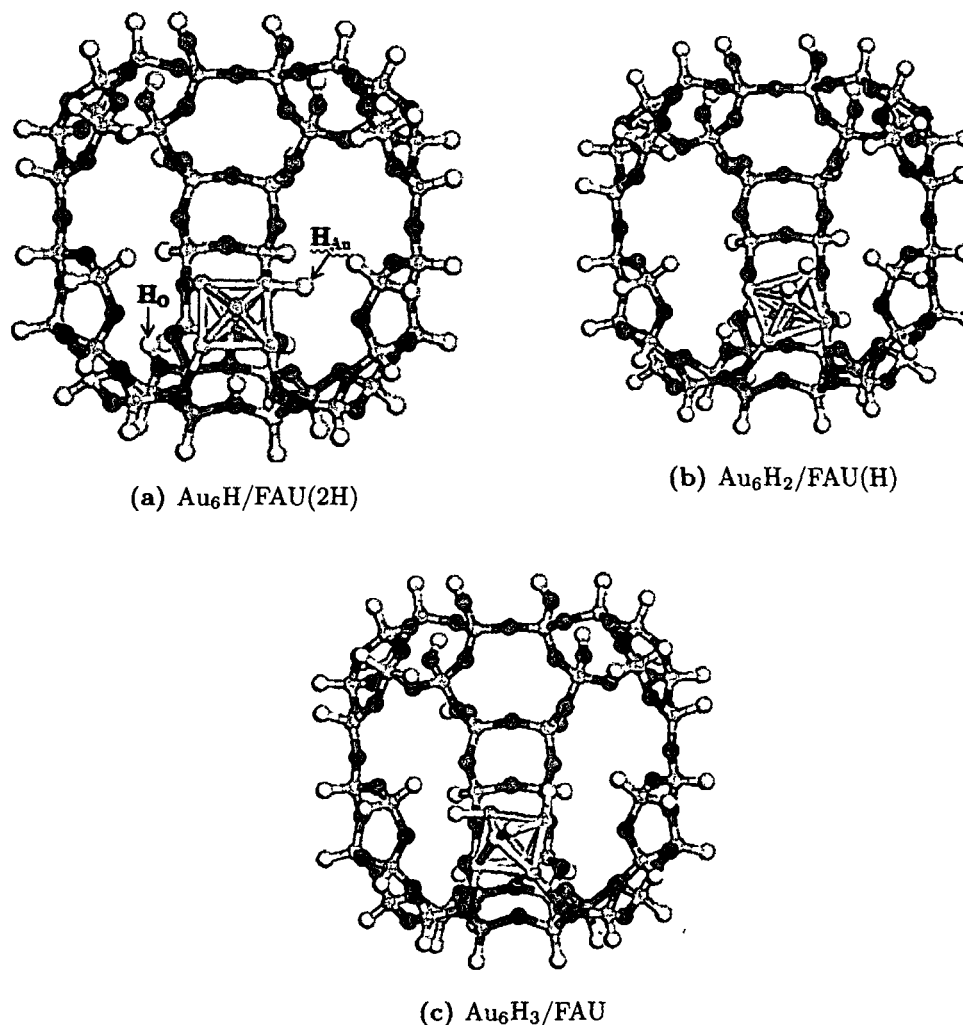


Figure 3.2.4: Optimized structures of faujasite supported hydrogenated Au_6 clusters, $\text{Au}_6\text{H}_n/\text{FAU}(3-n)$; $n=1-3$.

On analyzing the Hirshfeld charges, we observe that the gold atoms are oxidized on hydrogenation which is indicated by the increasing values of the charges being the maximum in $\text{Au}_6\text{H}_3/\text{FAU}$. The Au_z and Au_t atoms in $\text{Au}_6\text{H}_3/\text{FAU}$ carry charges, 0.224e and 0.149e, respectively. The bridging hydrogen atoms in the zeolite supported bare Au_6 cluster carry average charge of 0.153e which reduces to -0.031e in $\text{Au}_6\text{H}_3/\text{FAU}$ indicating a formal reduction of H^+ to H^- during reverse hydrogen spillover. The charges on acidic hydrogen atoms, H_O in $\text{Au}_6\text{H}/\text{FAU}(2\text{H})$ and $\text{Au}_6\text{H}_2/\text{FAU}(\text{H})$ are 0.191e and 0.171e, respectively whereas that of spilled over hydrogen(s), H_Au are -0.030e and -0.038e respectively. Thus, it can be inferred from the present charge analysis that the process of reverse spillover of acidic

hydrogen atoms from the zeolite support to the Au₆ cluster leads to reduction of hydrogen atoms with a concomitant oxidation of gold atoms. Moreover, two types of metal centres exist within the same metal cluster in both faujasite supported bare and hydrogenated Au₆ clusters.

Table 3.2.2: Computed geometrical parameters, Hirshfeld charges of selected atoms and reverse spillover energy per transferred hydrogen of faujasite supported hydrogenated Pd₆ and Au₆ clusters.

	Pd ₆ H/ FAU(2H)	Pd ₆ H ₂ / FAU(H)	Pd ₆ H ₃ / FAU	Au ₆ H/ FAU(2H)	Au ₆ H ₂ / FAU(H)	Au ₆ H ₃ / FAU
Bond Distances (Å)						
M _z - M _z	2.68	2.69	2.70	2.74	2.72	2.69
M _t - M _t	2.56	2.57	2.56	2.57	2.58	2.58
M _z - M _t	2.54	2.52	2.51	2.54	2.53	2.48
M _z - O _z	2.12	2.27	2.09	2.11	2.09	2.09
M _z - O _H	2.97	2.17	2.13	3.17	2.17	2.22
M _z - Al	3.05	2.85	2.82	3.01	2.83	3.41
M _z - Si	3.19	2.78	2.72	3.18	3.07	2.76
M _t - H	1.70	1.69	1.69	1.56	1.56	1.57
M _z - H	1.80	1.80	1.69	-	-	-
O-H	1.09	1.00	-	1.00	0.99	-
Charge (Hirshfeld)						
q(M _z)	0.128	0.280	0.340	0.098	0.184	0.224
q(M _t)	0.127	0.120	0.195	0.018	0.089	0.149
q(H _O)	0.051	0.207	-	0.191	0.171	-
q(H _M)	-0.086	-0.107	-0.087	-0.030	-0.038	-0.031
E _{RS} (kJmol ⁻¹)	-15.87	-52.60	-29.33	-69.56	-47.30	-24.50

3.2.4 Salient Observation

We have studied faujasite supported bare Pd₆ and Au₆ clusters and their interaction with the bridging OH groups of the zeolite support to form hydrogenated Pd₆ and Au₆ clusters. The calculations have been carried out by fixing the op-

timized positions of the terminal hydrogen atoms. In both faujasite supported bare Pd₆ and Au₆ clusters, the metal clusters interact with the support through three close M-O bonds (M=Pd, Au) whereas in their hydrogenated counterparts, Pd₆H₃/FAU and Au₆H₃/FAU, respectively there are overall six close M-O contacts. This indicates the increased interaction of the metal clusters with the zeolite as a consequence of stepwise reverse spillover. The process of proton transfer from the zeolite support to the metal cluster is found to be energetically favourable in both the metals indicated by the exothermic E_{RS} values. The hydrogenated Pd₆ and Au₆ clusters supported on faujasite are more stable than the dehydrogenated clusters also corroborated by the decreasing M-O distances. Pd₆H₂/FAU(H) and Au₆H₂/FAU(H) are 105.19 kJmol⁻¹ and 94.61 kJmol⁻¹, respectively more stable than the faujasite supported bare clusters and are in fact most stable among other hydrogenated congeners. Proton transfer leads to partial oxidation of the metal atoms with a concomitant reduction of H⁺ to H⁻. Both Pd_z and Au_z atoms (atoms in close proximity with the zeolite oxygen atoms) are more strongly oxidized compared to the Pd_t and Au_t atoms. The bare and hydrogenated metal clusters supported on zeolite consist of two types of metal atoms, M_z and M_t with different charges. Thus, there exist metal centres with different oxidation states within the same cluster.

Chapter 4

Adsorption of CO, O₂ on Gas Phase Gold Clusters and CO Oxidation

Overview

One of the major challenges in the field of catalytic research is the removal of poisonous carbon monoxide gas emitted mainly in automobile exhaust. Thus, oxidation of CO ($2\text{CO} + \text{O}_2 \rightarrow 2\text{CO}_2$) has been extensively investigated. In the present chapter, we have studied the adsorption of CO and O₂ on neutral, anionic and cationic gold hexamer, Au₆ clusters using density functional theory. Subsequently, CO oxidation over these clusters was investigated which elucidate the effect of cluster charge state on the catalytic activity. In all the clusters, the conventional bimolecular Langmuir-Hinshelwood mechanism with co-adsorbed CO and O₂ at the neighboring sites has been considered. Among the three clusters, Au₆⁻ entails lower barriers during the various steps of the oxidation mechanism and thus suggests its better catalytic activity as compared to the neutral and cationic counterparts. The stability of all the species including the transition states with respect to the interacting species in Au₆⁻ indicates no thermal activation [Baishya, S. & Deka, R. C. *Int. J. Quantum Chem.* **114** (22), 1559--1566, 2014].

4.1 Introduction

The age old notion regarding the chemical inertness of gold changed drastically when the seminal work of Haruta *et al.* [150,151] demonstrated the catalytic activity of nano-sized gold towards CO oxidation. Following this pioneering work, catalytic activity of both supported and unsupported gold clusters towards CO oxidation has been an integral part of modern research. Catalytic activity of clusters as small as single Au atom [171], Au₂⁻ [172], Au₉ and Au₁₃ (both neutral and cationic) [359,360], Au₁₀ (neutral and anionic) [361,362] towards CO oxidation have been reported by different groups. Density functional theory calculations by Wang *et al.* [363] for CO oxidation promoted by cationic, neutral and anionic Au₃ clusters showed that all the three Au species are able to facilitate the CO oxidation with different mechanisms. Their study demonstrated the catalytic activity of the three differently charged Au clusters and suggested that the highly stable carbonate species need not necessarily be an intermediate in the minimum energy path during CO oxidation. Liu *et al.* [364] proposed a new mechanism called CO self promoting oxidation wherein the co-adsorbed CO molecule at a unique triangular Au₃ active site can act as a promoter for the scission of an O-O bond, leading to the spontaneous formation (due to extremely low energy barrier) of two CO₂ molecules as product. They considered various nanosized gold clusters with sizes ranging from 0.3 to 0.8 nm for their density functional calculations. Yildirim and co-workers [365] reported CO oxidation over anionic gold hexamer and direct coupling of CO and O₂ through a CO-OO intermediate structure was observed leading to the formation of the first CO₂ and Au-O complex. Reaction with another CO molecule resulted in the second CO₂ molecule. The reaction was observed to be more facile when O₂ was bonded to the apex and CO to the nearest lateral site. In the present chapter, we focus on CO oxidation over neutral and charged Au₆ clusters with a motive to exploit the charge effect of the cluster on their catalytic behavior. We have also studied the adsorption of O₂ and CO at different Au sites and their co-adsorption on the three clusters by density functional theory.

4.2 Computational Details

The geometry optimization of the intermediates and the transition states are carried out using functional theory (DFT) methods at the generalized gradient approximation (GGA) with BLYP [280] functional. The BLYP functional incorporates Becke exchange and Lee-Yang-Parr correlation. In the work of Bonacić-Koutecký *et al.* [366] on bimetallic Ag-Au clusters, the authors have revealed the efficiency of BLYP functional in studying gold clusters. Scalar relativistic corrections to valence orbital relevant to atomic bonding properties via a local pseudopotential (VPSR) are implemented with the DNP (Double Numerical Polarization) basis set. DNP basis functions are the double numerical sets containing a polarization d-function on heavy atoms and polarization p-function on hydrogen. Fine grid mesh points are employed for matrix integrations. For self-consistent field procedures on energy and electron density, the convergence criterion is 10^{-6} a.u. The calculations are performed using the DMol³ [307] software package. Binding energy of CO and O₂ adsorbed on Au₆ clusters is calculated using equation (4.1):

$$BE(A) = [E_{Au_6} + E_A] - [E_{Au_6-A}] \quad (4.2.1)$$

BE(A) is the binding energy of CO or O₂ designated as A here, E_{Au_6} is the energy of gas phase Au₆ cluster, E_A is the energy of gas phase free CO or O₂ molecule and E_{Au_6-A} is the total energy of CO or O₂ adsorbed on Au₆. For co-adsorption of CO and O₂ on Au₆ clusters, the interaction energy, E(int) is given as:

$$E(int) = [E_{Au_6-CO-O_2}] - [E_{Au_6} + E_{CO} + E_{O_2}] \quad (4.2.2)$$

$E_{Au_6-CO-O_2}$ is the total energy of the aggregate with both CO and O₂ adsorbed on Au₆, E_{Au_6} is the energy of gas phase Au₆ cluster, E_{CO} and E_{O_2} are the energies of gas phase CO and O₂ molecules, respectively.

4.3 Results and Discussion

4.3.1 Structural features of optimized Au_6^n clusters ($n=0, -1$ and $+1$)

For studying CO oxidation on the neutral and charged clusters, we have considered the lowest energy [51,58,59] planar triangular structure of Au_6 (Figure 4.1). Table 4.1 summarizes the computed selected geometrical parameters for the Au_6^n clusters ($n=0, -1$ and $+1$) optimized at the present level of theory.

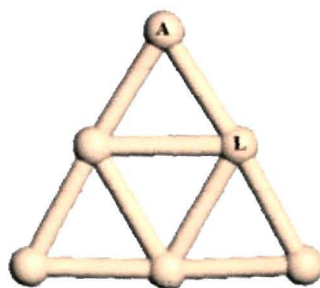


Figure 4.1: Optimized structure of Au_6 cluster at the BLYP/DNP level of calculation. The apex and lateral sites are labeled as A and L in the structure.

Table 4.1: Computed bond lengths (\AA) for Au_6^n clusters ($n=0, -1$ and $+1$).

Cluster	d(Au-Au)	
	Outer	Inner
Au_6^0	2.63	2.78
Au_6^-	2.67	2.76
Au_6^+	2.61	2.78

For both neutral and charged Au_6 clusters, the energy of the low spin state (singlet for neutral and doublet for cationic and anionic) is lower than the high spin counterparts. The high spin triplet state is 1.44 eV higher in energy than the singlet spin state for Au_6^0 ; while the quartet state is 1.49 eV and 2.02 eV higher in Au_6^- and Au_6^+ clusters, respectively than the doublet spin state. The energies of both the spin states for all the three charged clusters are given in Appendix B. Two distinct Au sites exist in the cluster viz. apex (A) and lateral (L) site as

shown in Figure 4.1.

4.3.2 Adsorption of O₂ and CO on Au₆ⁿ clusters (n= 0, -1 and +1)

Investigation of O₂ [90,101,102] and CO [103,110,111] adsorption on gold clusters has been an interesting domain of study in the area of nano-research. As shown in Figure 4.1, we have considered two adsorption sites- apex (A) and lateral (L) on the Au₆ cluster to study the adsorption of CO and O₂ on Au₆⁰, Au₆⁻ and Au₆⁺. The optimized structures of the O₂ adsorption complexes on Au₆ⁿ clusters (n= 0, -1 and +1) clusters are shown in Figure 4.2. Table 4.2 summarizes the computed selected C-O and O-O bond lengths (Å), ν_{C-O} and ν_{O-O} stretching frequencies (cm⁻¹) and binding energies (eV) of CO and O₂ adsorption complexes on the apex and lateral sites of the neutral and charged Au₆ clusters. The bond lengths and vibrational frequencies are reported for the favorable adsorption position. In the neutral and anionic Au₆ clusters, the O-O bond elongates considerably from 1.24Å in the gas phase to 1.30Å in Au₆⁰ and 1.34Å in Au₆⁻ approaching the O-O bond length of superoxide moiety. Thus, the adsorbed O₂ is essentially activated, which is an integral step in CO oxidation process. Red shift in the ν_{O-O} stretching frequency values from 1467.3 cm⁻¹ in O₂ to 1154.7 cm⁻¹ in Au₆⁰-O₂ and 1037.5 cm⁻¹ in Au₆⁻-O₂ further corroborate the O-O bond elongation. However, no activation has been observed in Au₆⁺ wherein the O-O bond length is close to the gas phase distance. For CO adsorption complexes (Figure 4.2), the C-O bond length slightly increases in Au₆⁻ from 1.14Å in gas phase CO to 1.17Å in Au₆⁻-CO; while it remains unchanged in cationic and neutral systems. The ν_{C-O} value shows a red shift from 2112.8 cm⁻¹ in CO to 1932.5 cm⁻¹ in Au₆⁻-CO attributed to the C-O bond elongation. The ν_{C-O} value in Au₆⁰-CO and Au₆⁺-CO systems remains close to the gas phase value. Our study suggests that both the molecules prefer the low-coordination apex site rather than the lateral site for adsorption in all the three clusters, which is in agreement with the previous results [365]. The optimized structures of O₂ and CO adsorbed on the lateral site are given Appendix B.

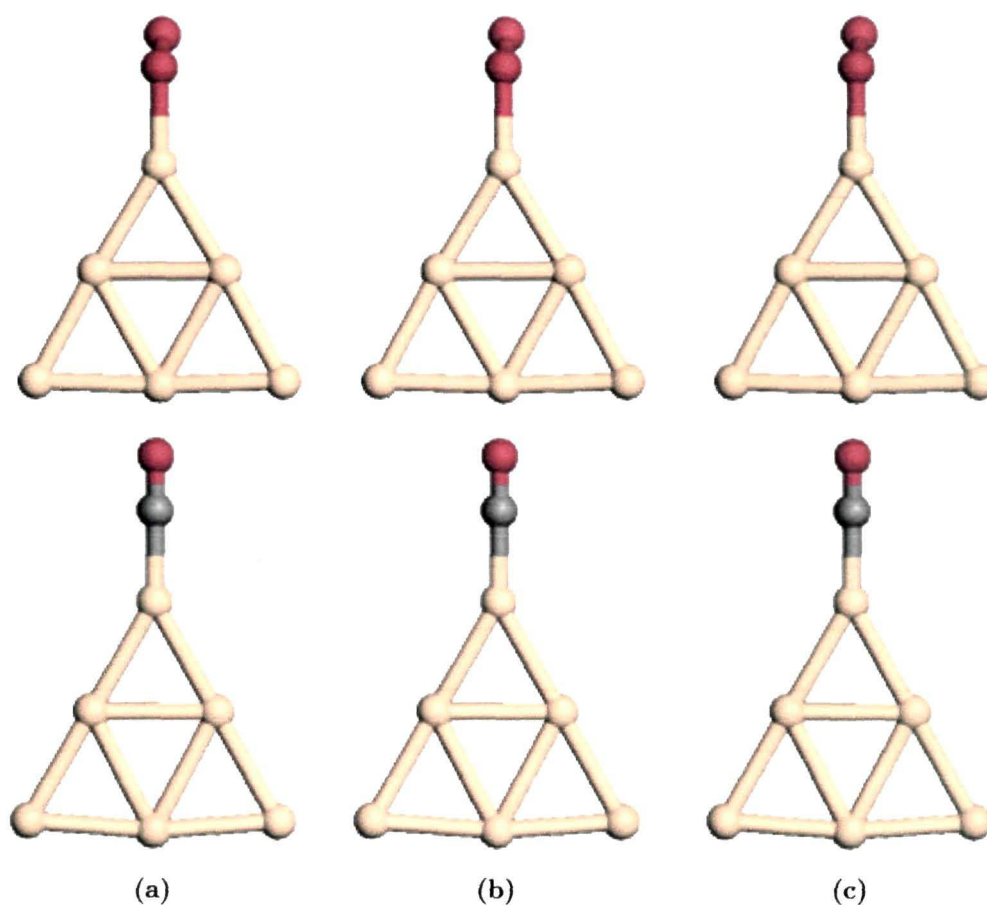


Figure 4.2: Optimized structures of O₂ and CO adsorbed on (a) Au₆⁰ (b) Au₆⁻ (c) Au₆⁺ clusters.

The binding energy values indicate that all the three clusters have strong interaction with both CO and O₂, but the highest binding energy of O₂ is observed in Au₆⁻ and is even more than Au₆⁻-CO. Largest interaction energy of O₂ for anionic gold clusters in the size range of two to eight atoms and maxima for even number of Au atoms was reported by Yoon *et al.* [94]. For CO adsorption, the computed binding energies indicate higher affinity of CO towards positively charged gold species. Prestianni *et al.* [107,360] suggested stronger interaction of O₂ with neutral Au₁, Au₉ and Au₁₃ clusters and CO with the cationic clusters. Reduction of O₂ to superoxide indicated its activation as a consequence of charge transfer. This has been attributed to the electronic charge transfer from gold species to the O₂ π* orbitals. On the other hand, the adsorption characteristic of CO is ascribed to its σ-donating character. The binding energy of O₂ at the apex site calculated in our study for neutral Au₆ cluster (0.54 eV) is in excellent agreement with the

Table 4.2: Computed CO and O₂ binding energies (eV), C-O and O-O distances (Å), C-O and O-O stretching frequencies (cm⁻¹) for Au₆ⁿ clusters (n= 0, -1 and +1).

Au ₆ ⁰				
Cluster	Au ₆ -CO	Au ₆ -CO	Au ₆ -O ₂	Au ₆ -O ₂
Position	Apex	Lateral	Apex	Lateral
BE(CO)	1.21	0.80		
d _{C-O}	1.15			
ν _{C-O}	2047.5			
BE(O ₂)			0.54	0.47
d _{O-O}			1.30	
ν _{O-O}			1154.7	
Au ₆ ⁻				
Cluster	Au ₆ -CO	Au ₆ -CO	Au ₆ -O ₂	Au ₆ -O ₂
Position	Apex	Lateral	Apex	Lateral
BE(CO)	1.33	0.95		
d _{C-O}	1.17			
ν _{C-O}	1932.5			
BE(O ₂)			1.73	1.07
d _{O-O}			1.34	
ν _{O-O}			1037.5	
Au ₆ ⁺				
Cluster	Au ₆ -CO	Au ₆ -CO	Au ₆ -O ₂	Au ₆ -O ₂
Position	Apex	Lateral	Apex	Lateral
BE(CO)	1.44	1.13		
d _{C-O}	1.14			
ν _{C-O}	2117.0			
BE(O ₂)			0.88	0.83
d _{O-O}			1.25	
ν _{O-O}			1307.9	

previous findings [95].

4.3.3 Co-adsorption of CO and O₂ on Au₆ⁿ clusters (n= 0, -1 and +1)

It is apparent from the above results that the molecules (either CO or O₂) will preferably adsorb on the apex site and consequently we consider the co-adsorption of the second molecule at the nearest lateral site so that the reaction takes place with ease. Thus, two co- adsorption configurations of the reactants (CO and O₂) will emerge:

1. CO at the apex site and O₂ at the nearest lateral site.
2. O₂ at the apex site and CO at the nearest lateral site.

In all the co-adsorbed configurations, CO and O₂ adsorb in the linear and bent structure, respectively. The computed interaction energies [E(int)] and selected bond lengths for the co-adsorbed configurations in the three Au₆ clusters are summarized in Table 4.3. The interaction energies indicate the co-adsorbed configuration with CO at the apex site and O₂ at the nearest lateral site to be the preferable configuration for all the three clusters (Figure 4.3). For both neutral and anionic co-adsorption configurations, similar to the corresponding bare O₂ adsorption complexes, O₂ is activated as evident from the elongation of O-O bond. This indicates the lability of O₂ for dissociation in the oxidation reaction. However, no O₂ activation is observed in the cationic aggregate even in the presence of CO. We proceed further to understand the catalytic activity of the neutral, anionic and cationic Au₆ clusters towards CO oxidation with these co-adsorbed structures.

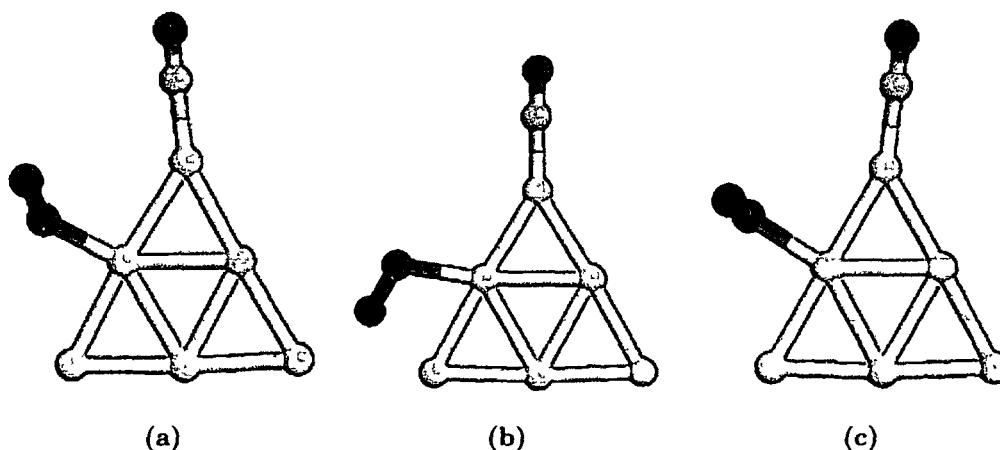


Figure 4.3: Optimized structures of CO and O₂ co-adsorbed complexes of (a) Au₆⁰ (b) Au₆⁻ (c) Au₆⁺ clusters.

Table 4.3: Computed bond lengths (Å) and interaction energies (eV) for the co-adsorbed complexes in the neutral, anionic and cationic Au₆ clusters.

Cluster	Au-C	C-O	Au-O	O-O	E(int)
Au ₆ ⁰					
CO-apex O ₂ -lateral	1.91	1.15	2.14	1.30	-1.53
O ₂ -apex CO-lateral	1.92	1.15	2.06	1.30	-1.36
Au ₆ ⁻					
CO-apex O ₂ -lateral	1.88	1.17	2.22	1.36	-2.81
O ₂ -apex CO-lateral	1.96	1.16	2.10	1.34	-2.30
Au ₆ ⁺					
CO-apex O ₂ -lateral	1.93	1.14	2.20	1.26	-2.26
O ₂ -apex CO-lateral	1.92	1.14	2.12	1.27	-2.09

4.3.4 CO oxidation on neutral Au₆ cluster

The energy profile diagram for CO oxidation on neutral Au₆ cluster is shown in Figure 4.4 and the selected geometrical parameters of the different species involved in the reaction are summarized in Table 4.4. Starting from the preferred co-adsorbed structure where CO is at the apex site and O₂ at the nearest lateral site (R1); the reaction proceeds to form an intermediate (I1). In the species

I1, O₂ bridges between the Au site containing it and the apex Au with CO. This is aided by further elongation of O-O bond from 1.30 Å in R1 to 1.39 Å in I1 which approaches the peroxide bond length thus making it more labile for dissociation. Further, the Au-O bond length decreases from 2.14 Å in R1 to 2.07 Å in I1 indicating increased interaction. On the other hand, the Au-C and C-O bond lengths remain unchanged. The formation of I1 from R1 involves a high energy barrier of 2.50 eV (TS1). The transition state, TS1 is characterized by the presence of a single negative vibrational frequency at -168.6 cm⁻¹. The reaction now, proceeds to release the first CO₂ (P1) from I1 via the barrier, TS2 which involves dissociation of the labile O-O bond [d (O-O): 2.34 Å]. The barrier is calculated to be 1.93 eV (TS2) and the single negative vibrational frequency for TS2 appears at -271.4 cm⁻¹. The C-O bond length in P1 is 1.18 Å and O-C-O angle is 179.9° with a characteristic vibrational frequency of 2314.1 cm⁻¹. It is clear from the energy profile diagram that both the activation barriers in the first oxidation step are above the entrance channel which reflects the undesirability of Au₆⁰ for any catalytic activity towards CO oxidation. Generation of the first CO₂ leaves behind atomic oxygen adsorbed on Au₆ which then reacts further with an incoming CO molecule to form the reactant, R2 where the atomic oxygen species is simultaneously bonded to the apex Au atom and one nearest lateral Au site.

The second product, P2 forms from R2 surpassing a high energy barrier of 2.51 eV indicated by the transition state, TS3. The apex Au atom in TS3 contains both atomic oxygen species and CO which presents a favorable configuration for the formation of the second CO₂. The transition state, TS3 is characterized by the negative frequency at -78.7 cm⁻¹. Further, the product P2 formed from TS3 is characterized by C-O bond length of 1.18 Å, the O-C-O bond angle of 179.9° and the vibrational frequency of 2313.7 cm⁻¹.

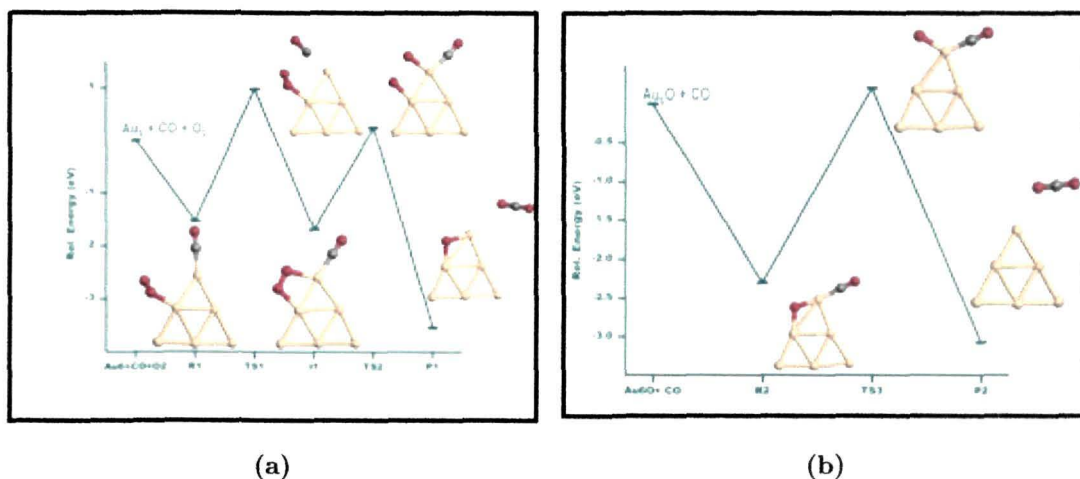


Figure 4.4: Energy profile diagram for CO oxidation [(a) first half (b) second half of the reaction] on neutral Au_6 cluster.

Table 4.4: Bond lengths (\AA) and bond angle for all the species involved in CO oxidation catalyzed by neutral Au_6 cluster.

	Au-O	Au-C	O-O	O-CO	O-C	O-C-O
R1	2.14	1.91	1.29	-	-	-
TS1	2.19	2.44	1.39	2.76	-	-
I1	2.08	1.91	1.38	3.38	-	-
TS2	2.00	1.91	2.34	3.02	-	-
P1	1.95	-	-	-	1.18	179.9°
R2	1.89	1.86	-	3.74	-	-
TS3	2.00	1.86	-	3.43	-	152.5°
P2	-	-	-	-	1.18	179.9°

4.3.5 CO oxidation on anionic Au_6 cluster

Figure 4.5 shows the energy profile diagram for CO oxidation on anionic Au_6 cluster and the selected geometrical parameters of the species involved are summarized in Table 4.5. To study the mechanistic details of the reaction, the co-ordinates of Au_6 are kept fixed during the course of studying the reaction to avoid any complexity during the analysis due to deformities in the relaxed structure. Initially, from the favorable co-adsorbed structure with CO adsorbed at apex Au site and O_2 at

the nearest lateral site (R1), the reaction proceeds to form the intermediate I1. Unlike the neutral counterpart, the I1 species in Au_6^- mediated reaction pathway involves the dissociation of the labile O-O bond of R1 ($d_{\text{O-O}}$: 1.36Å). One of the dissociated oxygen atoms bonds with CO resulting in a partly-formed CO_2 with C-O distances 1.23Å and 1.22Å and O-C-O angle of 143.9°. Our intermediate, I1 reported here is strikingly different from the O-OCO adduct reported earlier [365] and as we shall see later, the barrier for the formation of CO_2 from I1 species is much lower than the value reported there. The other O atom is bonded with the apex Au atom and the nearest lateral site with the shortest Au-O distance of 2.00Å. Formation of I1 from R1 involves a barrier of 0.59 eV indicated by TS1. TS1 is characterized with vibrational frequency of -124.9 cm^{-1} . Our calculated reaction barrier is reasonably close to the values reported for Au_{10} [361], Au (211) and Au (221) surfaces [176]. Careful observation of R1 and TS1 shows that the adsorbed O_2 molecule orients towards the Au site containing CO thereby presenting a more favorable configuration for the formation of CO_2 . The first CO_2 (P1) is formed from I1 via TS2 characterized with vibrational frequency of -119.0 cm^{-1} . The energy barrier involved in the formation of P1 is 0.20 eV which is much lower than the barrier (0.61eV) reported earlier [365] for the reaction pathway starting with similar co-adsorbed structure. This barrier is even lower than the value (0.29 eV) reported in the same study for the pathway with a different co-adsorbed structure that was found to be more favorable. In the product P1, the C-O bond distance is 1.18Å, O-C-O angle is 177.4° and the characteristic vibrational frequency is found to be 2308.0 cm^{-1} . The second half of the reaction initiates from the reactant, R2 that result from the interaction of the second CO with Au_6^- -O. Subsequently, an intermediate I2 forms from R2 via an energy barrier (TS3) of 0.34 eV. The single negative vibrational frequency of TS3 appears at -156.1 cm^{-1} . In the intermediate I2, the oxygen atom is simultaneously bonded to both the apex Au site containing the CO molecule and the nearest lateral site. A barrier of 1.35 eV (TS4) is involved in the second CO_2 formation (P2) from I2 and the single negative frequency appears at -520.5 cm^{-1} . The O...CO distance decreases to 1.74Å in TS4 which indicates interaction between CO and O atom to form the second CO_2 . Meanwhile, the C-O bond elongates to 1.18Å and the

O-C-O angle is 123.6° . The second CO_2 formed (P2) from TS4 has C-O distance of 1.18\AA , O-C-O angle of 171.8° and a vibrational frequency of 2263.6 cm^{-1} .

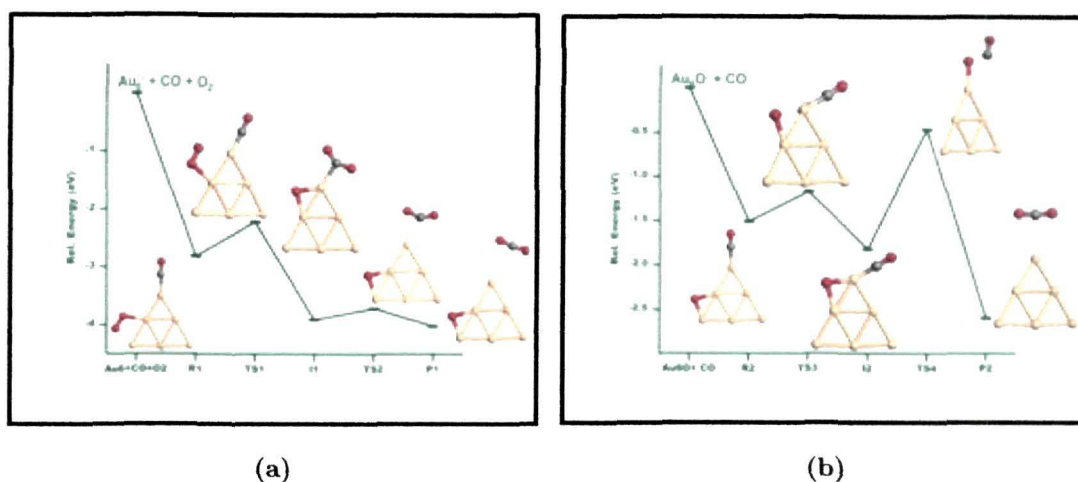


Figure 4.5: Energy profile diagram for CO oxidation [(a) first half (b) second half of the reaction] on anionic Au_6 cluster

Table 4.5: Bond lengths (\AA) and bond angle for all the species involved in CO oxidation catalyzed by anionic Au_6 cluster.

	Au-O	Au-C	O-O	O-CO	O-C	O-C-O
R1	2.22	1.88	1.36	-	-	-
TS1	2.22	1.87	1.36	3.62	-	-
I1	2.00	2.19	-	1.22	-	143.9°
TS2	2.01	-	-	1.25	-	143.3°
P1	2.00	-	-	-	1.18	177.4°
R2	2.01	1.88	-	-	-	-
TS3	1.99	1.85	-	-	-	-
I2	1.94	1.86	-	3.74	-	-
TS4	2.20	3.18	-	1.74	-	123.6°
P2	-	-	-	-	1.18	171.8°

4.3.6 CO oxidation on cationic Au_6 cluster

On similar lines, the reaction starts from the co-adsorbed structure (R1) to form an intermediate, I1 surpassing an energy barrier, TS1 which involves dissociation

of the adsorbed non-activated O_2 and thus entails a high barrier of 3.08 eV. The transition state is characterized with a vibrational frequency of -634.5 cm^{-1} . Similar to Au_6^0 , TS1 involves dissociation of O_2 but the barrier value is comparatively lower in the neutral cluster which can be attributed to the O_2 activation. This indicates that O_2 activation is an essential step in CO oxidation which is also evident in Au_6^- where the highest O-O bond elongation is observed and thus consequently involves lowest barrier among the three clusters. From the intermediate, I1 containing a partly formed CO_2 , the first CO_2 (P1) is released and involves a barrier (TS2) of 0.66 eV. The transition state TS2 has a negative vibrational frequency of -75.2 cm^{-1} . The characteristic vibrational frequency of 2310.9 cm^{-1} is observed for product P1 (CO_2) and with O-C bond length and O-C-O angle of 1.18 \AA and 179.8° , respectively. A second incoming CO molecule adsorbs on the same lateral site with the atomic oxygen (R2) wherein the Au-C (CO) distance in R2 is 1.92 \AA and the Au-O distance is 1.88 \AA . The second product, P2 is formed from R2 via transition state, TS3 indicating a barrier of 1.45 eV. An important observation that can be made from the barriers involved in the formation of the second product, P2 in all the three oxidation states is that the indicated transition state (TS3 in Au_6^0 and Au_6^+ ; TS4 in Au_6^-) is stable with respect to the interacting species only in Au_6^- . This implies that unlike in Au_6^0 and Au_6^+ , no thermal activation will be required in anionic Au_6 . The transition state, TS3 in Au_6^+ comprises a partially formed CO_2 and the single negative vibrational frequency appears at -174.6 cm^{-1} . The distance between $O \cdots CO$ is 1.32 \AA while the C-O bond of CO elongates to 1.29 \AA . Finally, from this transition state the second CO_2 is formed and the characteristic vibrational frequency appears at 2314.8 cm^{-1} . The energy profile diagram for CO oxidation on cationic Au_6 cluster is shown in Figure 4.6 and the selected geometrical parameters of the different species involved are summarized in Table 4.6.

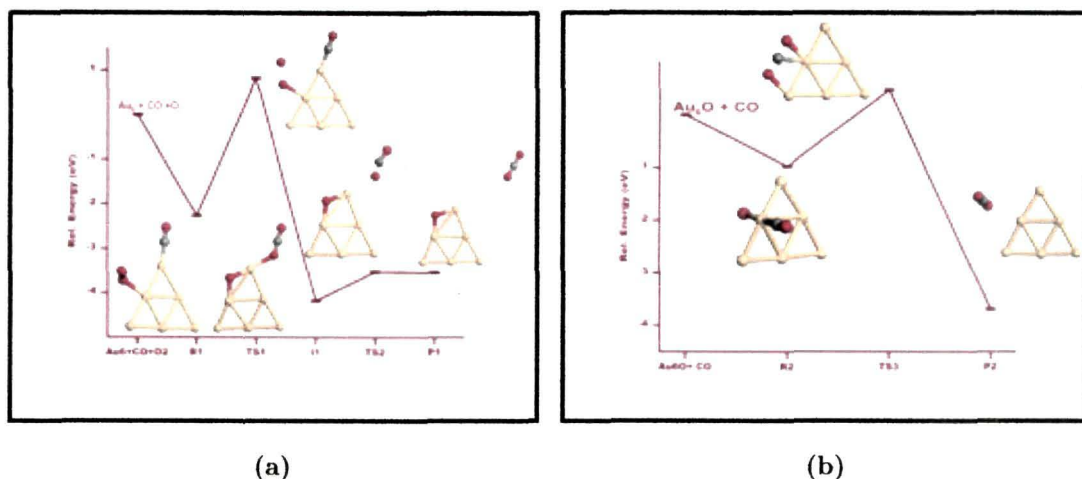


Figure 4.6: Energy profile diagram for CO oxidation [(a) first half (b) second half of the reaction] on cationic Au_6 cluster

Table 4.6: Bond lengths (\AA) and bond angle for all the species involved in CO oxidation catalyzed by cationic Au_6 cluster.

	Au-O	Au-C	O-O	O-CO	O-C	O-C-O
R1	2.20	1.93	1.26	-	1.14	-
TS1	2.17	1.93	1.96	-	1.14	-
I1	1.91	2.18	-	1.20	1.16	177.5°
TS2	1.91	-	-	1.26	1.17	162.9°
P1	1.93	-	-	1.18	1.18	179.8°
R2	1.88	1.92	-	-	1.14	-
TS3	1.97	2.00	-	1.32	1.29	176.6°
P2	-	-	-	1.18	1.17	179.6°

4.4 Salient Observation

We have systematically investigated the conventional bi-molecular Langmuir-Hinshelwood CO oxidation mechanism on neutral, anionic and cationic Au_6 clusters using density functional theory (DFT) calculations. It is observed that both CO and O_2 prefer the low coordinated apex site for adsorption in the Au_6 clusters irrespective of the cluster charge. CO and O_2 adsorption is strongest in the cationic and the

anionic Au_6 clusters, respectively. All the three clusters favor CO at the apex Au site and O_2 at the nearest lateral site for their co-adsorption. However, O_2 activation is observed in the case of Au_6^0 and Au_6^- but not in the cationic counterpart. A comparison of barriers for the different steps in the CO oxidation mechanism over the three clusters is given in Table 4.7. The barriers involved during the CO oxidation on Au_6^- are much lower than those in the neutral and cationic counterparts.

Table 4.7: Comparison of the barriers (eV) involved in the different steps of CO oxidation over neutral and charged Au_6 clusters.

	Au_6^0	Au_6^-	Au_6^+
R1 \rightarrow I1	2.50	0.59	3.08
I1 \rightarrow P1	1.93	0.20	0.66
R2 \rightarrow I2	-	0.34	-
R2/I2 \rightarrow P2	2.51	1.35	1.45

Our calculations indicate that CO oxidation over anionic gold hexamer does not require thermal activation unlike in Au_6^0 and Au_6^+ clusters reflected from the stability of all the species including the transition states with respect to the interacting species. Our study reveals the better catalytic activity of anionic gold hexamer cluster in comparison to neutral and cationic clusters.

Herein, we have considered gas-phase Au clusters as model catalysts in the present work without taking in to consideration the effect of support. However, the conclusions drawn from this study may be inherent for understanding the catalytic activity of realistic catalytic systems and to comprehend the mechanism involved therein.

Chapter 5

Adsorption of CO and O₂ on Zeolite Supported Gold Monomer and the Effect of Moisture

Overview

Single atom catalysis is one of the emerging topics in the field of material research and the catalytic activity of single metal atom with or without support has been investigated extensively. The catalytic activity of single metal atom such as Au, Pt supported on different oxides towards reactions like CO oxidation, alkene hydrogenation, water-gas shift reaction etc. has been established by various studies. Motivated by the growing interest in single atom catalysis, we carried out hybrid quantum mechanics molecular mechanics calculations on the adsorption of small molecules such as CO and O₂ on faujasite supported gold monomer in three oxidation states viz. 0, +1 and +3. It has been observed that the binding energy of CO increases with Au oxidation state. Three different modes viz. top, bridge and dissociative have been considered for O₂ adsorption and it was observed that the unfavourable dissociative mode reverts back to the bridge mode. Activation of O₂ which is an integral part of CO oxidation is observed in our calculations. These results are presented in the first part of this chapter (Section 5.1) [Baishya, S. & Deka, R. C. *J. Chem. Phys.* **135** (24), 244703/1--244703/7, 2011].

The presence of moisture is inevitable in practical catalytic systems and affects the activity of such systems significantly. It is thus, crucial to study the effect of moisture on the adsorption of CO and O₂. In the next part (Section 5.2) of this chapter, we present the results of hybrid quantum mechanics molecular mechanics calculations on the effect of pre-adsorbed water on CO and O₂ adsorption on faujasite supported Au monomer. In the presence of pre-adsorbed H₂O, binding of CO to the Au centre results in the cleavage of the Au-H₂O bond and the highest binding energy of O₂ has been observed in Au⁰/FAU. A hydroperoxyl-hydroxyl species results from the proton sharing between H₂O and O₂ in close proximity and involves low barrier for the transfer of the H atom from H₂O to O₂. In the hydroperoxyl species, the O-O bond is substantially activated which is beneficial for CO oxidation process.

5.1 Adsorption of CO and O₂ on faujasite supported gold monomer

5.1.1 Introduction

Reduction of bulk gold to nano sized clusters makes it catalytically active towards various reactions such as low temperature CO oxidation, water gas shift reaction, etc. The catalytic activity of both supported and unsupported gold clusters towards low temperature CO oxidation has been extensively studied. However, understanding the adsorption behaviour of CO and O₂ is essential to gain insight in to the catalytic mechanism of CO oxidation reaction. Adsorption of CO and O₂ on oxide supported gold clusters has been studied by numerous experimental [115,119,128] and theoretical [120-123,126,131-133] studies; while a handful of these have been made devoted to zeolite supported gold. Rasmussen *et al.* [120] investigated the properties of reduced rutile TiO₂(110) surfaces, as well as the adsorption, diffusion, and dissociation of molecular oxygen by means of density functional theory. Molina and Hammer [121] studied the shape, electronic structure and the affinity for O₂ binding of Au_N clusters (N=1-11) supported either at F or F⁺ centers on the MgO(001) surface. Density functional calculations by

Pacchioni and co-workers [122] showed moderate activation of the O_2 molecule irrespective of being adsorbed on free Au_5 or Au_5^- and suggested that the presence of an extra charge is not sufficient to induce a change in the adsorption mode.

Gates and co-workers [128] provided the first evidence of $Au^0(CO)_3$ species present on the low-coordination zero-valent Au atoms at the surface of gold nanoclusters on zeolite support from IR data. Thomson and co-workers [131] reported favourable adsorption of CO on the Au clusters in TS-1 while studying the interaction of CO with Au_{1-5} located inside TS-1 pores using quantum mechanics/molecular mechanics method. Sierralta *et al.* [132] studied the interaction of CO molecule with Au-exchanged mordenite catalysts, Au/MOR using hybrid quantum mechanics/molecular mechanics method. Deka *et al.* [133] observed an increase in CO binding energy with increase in Au oxidation state in their study on the adsorption of CO on gas phase and faujasite supported gold monomer in three oxidation states 0, +1 and +3 using DFT.

However, to the best of our knowledge, O_2 adsorption on faujasite supported Au monomer has not been investigated till date. In the present work, we have carried out hybrid quantum mechanics/molecular mechanics studies of CO and O_2 adsorption on faujasite supported Au monomer in three oxidation states viz. 0, +1 and +3. For O_2 adsorption, we have considered three different modes of O_2 adsorption viz., top mode in which one oxygen atom is directly bonded to Au, bridging mode with O_2 chelating Au, and dissociative mode in which O_2 adsorbs in a dissociative manner.

5.1.2 Computational Details

Hybrid quantum mechanics/molecular mechanics method SIMOMM [314] (Surface Integrated Molecular Orbital Molecular Mechanics) implemented in GAMESS [316] program has been used to carry out the calculations. This involves partitioning the entire system into a small, chemically active part which is treated quantum mechanically and the larger, outer inactive part modelled using molecular mechanics. Creation of the inner active part from the entire system generates unpaired electrons (dangling bond) on the subsurface atoms in the inner region which must be terminated so that the chemical behaviour of the inner region does

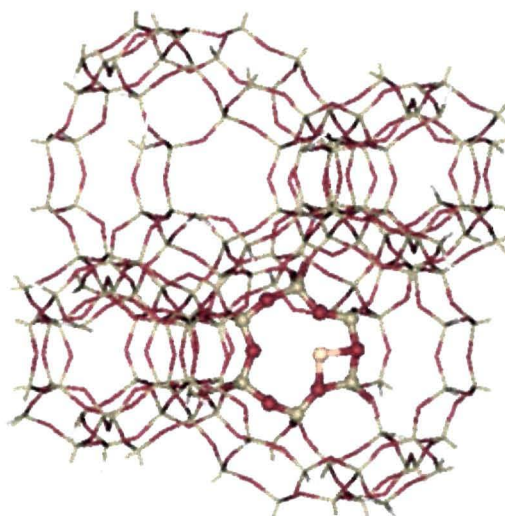


Figure 5.1.1: The faujasite model used in our calculations where the QM part is illustrated by ball and stick and the MM part by line. The H, O, Si and Au atoms are depicted by white, red, green and yellow colour, respectively.

not differ from the real surface. These dangling bonds are saturated with hydrogen atoms known as the linked atoms. The faujasite zeolite model employed in our work comprises of 642 atoms and an extra framework Au atom (Figure 5.1.1). The quantum mechanical part (QM) comprises of a six membered ring of the faujasite zeolite and an Au atom supported on it along with the adsorbed CO or O₂ molecule. The QM part is treated with the DFT based B3LYP functional [278,280,292], 6-31G(d, p) basis set [367] for Si, Al, O, C and H and LANL2DZ [308,309] basis set incorporating relativistic effective core potential for Au atom. When Si atom of the six-member ring is substituted by an Al atom; it generates an excess negative charge. The Au atom added is in the +1 oxidation state in order to retain the charge neutrality of the system. Accordingly, isomorphous substitution of three Si atoms by Al atoms following the Löwenstein rule creates Au³⁺. On the other hand, the outer region is modelled using the MM3 parameter [368]. The binding energy of CO and O₂ adsorbed on faujasite supported Au monomer is calculated using the following equation:

$$BE(A) = [E_{Au/FAU} + E_A] - [E_{Au-A/FAU}] \quad (5.1.1)$$

BE(A) is the binding energy of CO or O₂ designated as A here, E_{Au/FAU} is the energy of the faujasite supported Au monomer system, E_A is the energy of gas phase free CO or O₂ molecule and E_{Au-A/FAU} is the total energy of CO or O₂ adsorbed on Au/FAU. A positive value of binding energy indicates favourable adsorption of CO or O₂. It is to be mentioned here that BSSE (basis set superposition error) corrections have not been incorporated while calculating the binding energies. The quadratic approximation method [369] implemented in GAMESS program was used in the geometry optimizations and transition state searches. Natural bond orbital (NBO) analysis has been performed using GAUSSIAN09 program package [370].

5.1.3 Results and Discussion

5.1.3.1 Faujasite supported gold monomer

The optimized structures of faujasite supported Au monomer in three different oxidation states 0, +1, +3 are shown in Figure 5.1.2 and the selected geometrical parameters are summarized in Table 5.1.1. The Au-O_z (O_z represents framework

Table 5.1.1: Bond lengths (Å) and NBO charges on faujasite supported Au monomer in three oxidation states.

	Au ⁰ /FAU	Au ⁺ /FAU	Au ³⁺ /FAU
	Bond Length(Å)		
Au-O _z	2.76	2.30	2.31
Au-Si	3.32	2.98	2.97
Au-Al	-	3.08	2.96
	NBO Charges		
q(Au)	-0.026	0.714	0.684

zeolite oxygen), Au-Si and Au-Al distances decrease on moving from neutral to cationic systems. This suggests that the interaction of Au monomer with the faujasite support increases on moving to cationic systems. The frontier molecular orbitals shown in Appendix C illustrate the interaction between d-orbital of Au and the p-orbitals of zeolite O-atoms. It can be seen that the overlap of the

orbitals is more pronounced in the cationic systems, thereby accounting for their enhanced interaction with the zeolite framework. NBO charge analysis indicates that anchoring of the Au monomer to the faujasite support causes a withdrawal of charge density from the zeolite to the monomer in both neutral and cationic systems evident from the charge carried by the Au monomer. For instance, the NBO charge for neutral Au has been found to be $-0.06 e$ while for the oxidation state of $+1$, the NBO charge on Au is $0.64 e$.

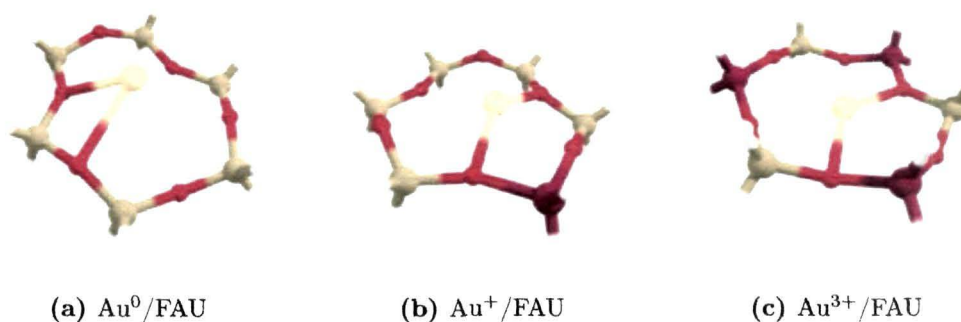


Figure 5.1.2: Optimized structures of faujasite supported Au monomer.

5.1.3.2 CO adsorption on faujasite supported gold monomer

The optimized structures of CO adsorbed on Au^n/FAU ($n=0, +1$ and $+3$) are shown in Figure 5.1.3. Table 5.1.2 summarizes the geometrical parameters, vibrational frequency of CO, binding energies and the NBO charges for the CO adsorbed aggregates.

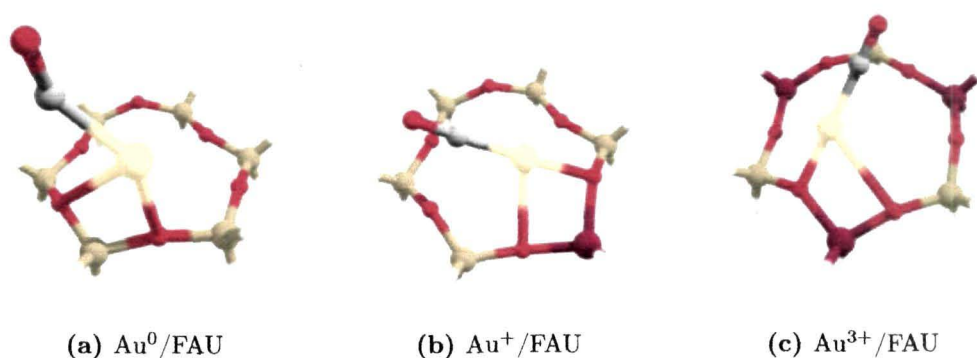


Figure 5.1.3: Optimized structures of CO adsorbed on Au^n/FAU ($n=0, +1$ and $+3$). The H, C, O, Al, Si and Au atoms are depicted by white, grey, red, magenta, green and yellow colours, respectively.

Table 5.1.2: Geometrical parameters, binding energies and vibrational frequency of CO adsorbed on Auⁿ/FAU (n=0, +1 and +3).

	Au ⁰ /FAU	Au ⁺ /FAU	Au ³⁺ /FAU
Bond Length(Å)			
Au-C	2.07	1.91	1.92
C-O	1.18	1.16	1.16
Au-Si	3.38	3.30	3.19
Au-Al	-	2.96	3.09
Au-O _Z	2.82	2.14	2.04
Vibrational frequency (cm ⁻¹)			
ν_{C-O}	1867.22	2086.16	2088.14
Binding Energy(eV)			
B.E.	3.28	4.38	4.59
NBO Charges			
q(Au)	0.067	0.521	0.525
q(C)	0.356	0.507	0.506
q(O)	-0.445	-0.377	-0.365
Δq	0.089	-0.013	-0.141

The Au – O_Z bond length shows a decreasing trend on going to higher oxidation states having a value of 2.04Å in the +3 oxidation state. Our calculated Au – O_Z distances of supported cationic gold monomer are in good agreement with the experimental EXAFS value of 2.08 Å in NaY zeolite supported cationic gold atoms [218]. The increasing interaction of the gold atom with the support on moving to higher oxidation states is also revealed from the decreasing Au-Al and Au-Si distances. The C-O distance does not vary much from the gas phase value (1.16Å) and interaction of CO with the metal atom is stronger in the cationic states as revealed by the shorter Au-C bond lengths. The binding energy of CO increases from 3.28 eV in the neutral monomer to 4.59 eV in the +3 oxidation state. It can be seen from the optimized structures that CO adsorbs in a bent fashion in the neutral monomer while in the cationic systems, it adsorbs as a linear structure. This can be correlated with the red shift in the C-O vibrational frequency in

Au⁰/FAU to 1867.22 cm⁻¹ from a value of 2072.23 cm⁻¹ observed for the free gas phase CO and a blue shift in ν_{C-O} value in the cationic systems. Moreover, NBO charges indicate transfer of 0.089e charge to the CO molecule (represented by Δq) as a result of interaction with the gold monomer in Au⁰/FAU and the transferred charge goes to the antibonding orbital of CO. On the other hand, in the cationic systems, there is withdrawal of charge from CO reflected from the negative values of Δq . This further contributes to the red shift of ν_{C-O} in neutral monomer and blue shift in case of cationic systems. The adsorbed CO interacts with the Au centre via the C atom and it involves overlap of the Au d-orbital and p-orbital of C as depicted in the frontier orbitals shown in Appendix C.

5.1.3.3 O₂ adsorption in the top mode on faujasite supported gold monomer

The optimized structures of O₂ adsorbed in the top mode on Auⁿ/FAU (n=0, +1 and +3) are depicted in Figure 5.1.4. Computed geometrical parameters, vibrational frequencies, binding energies are summarized in Table 5.1.3 and the NBO charges are given in Table 5.1.4. The shortest Au-O bond distance (2.13Å) in Au³⁺-O₂ system indicates that interaction of O₂ with the gold monomer is strongest as compared to the neutral and Au⁺/FAU systems. This is reflected in concomitant increase of the O-O bond length with a value of 1.41Å in the Au³⁺/FAU system which approaches the O-O bond length in peroxide moiety. The O-O bond also elongates (1.36Å) in the neutral Au system as a consequence of interaction with the metal centre. O₂ adsorbed in the top mode on Au⁰/FAU and Au³⁺/FAU is thus, highly activated. However, no such activation is realized in Au⁺/FAU where, the O-O bond length (1.29 Å) is comparable to that in free O₂ (1.22 Å). Activation of O₂ can be attributed to the charge transferred to the O₂ molecule as a result of interaction with the zeolite supported Au monomer (Δq). The charge transferred goes to the antibonding orbital of O₂ thereby the lowering of the vibrational frequency of O-O bond. The ν_{O-O} value red shifts from 1643.04 cm⁻¹ in the free gas phase O₂ to 781.40 cm⁻¹ in Au³⁺/FAU. The frontier molecular orbitals shown in Appendix C illustrate the interaction of O₂ with Au which involves interaction of the p-orbital centred on O₂ and d-orbital

of Au. Another observation that can be perceived from the NBO charges is the increase in charge of Au^0 and Au^{3+} centres on adsorption of O_2 as compared to the bare monomer (Table 5.1.1) while it remains almost similar in Au^+/FAU .

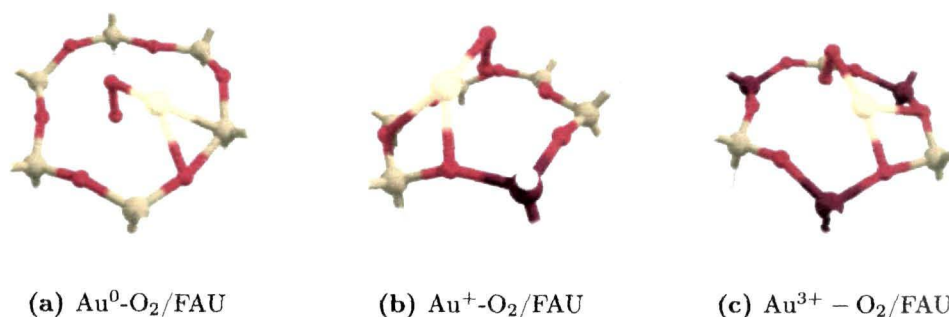


Figure 5.1.4: Optimized structures of O_2 adsorbed in the top mode on Au^n/FAU ($n=0, +1$ and $+3$).

This indicates charge transfer in the former systems while mere electrostatic interaction in the later. The highest binding energy of O_2 is observed in $\text{Au}^{3+}/\text{FAU}$ which results from strong charge transfer interaction while the binding energy is lower in Au^+/FAU where the interaction is merely electrostatic in nature. The $\text{Au}-\text{O}_z$ distance indicating interaction of the Au monomer with the zeolite support decreases with the increase in Au oxidation state having a value of 1.99\AA in $\text{Au}^{3+}/\text{FAU}$. Comparing this $\text{Au}-\text{O}_z$ bond length with the value observed in bare supported systems, it is evident that on adsorption of O_2 , interaction of the metal centre with the zeolite support increases. In all systems, O_2 adsorbs in a bent fashion with the O-O bond pointing towards the zeolite plane.

5.1.3.4 O_2 adsorption in the bridge mode on faujasite supported gold monomer

Figure 5.1.5 shows the optimized structures of O_2 adsorbed in the bridge mode on faujasite supported Au monomer in three oxidation states viz. 0, +1 and +3 and the frontier molecular orbitals are depicted in Appendix C.

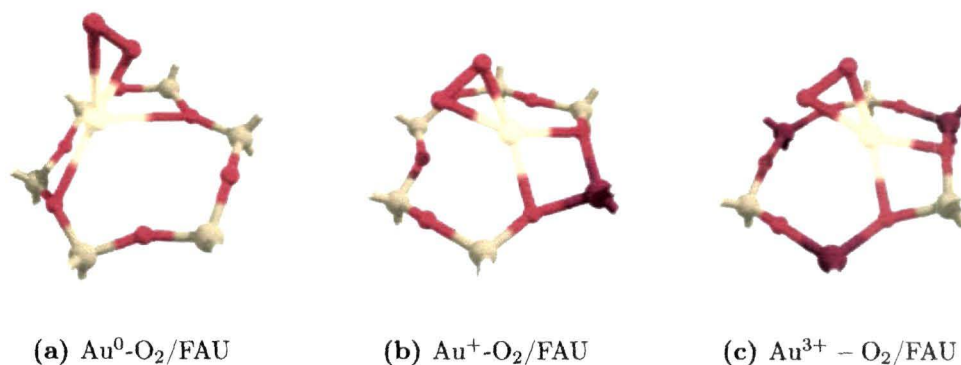


Figure 5.1.5: Optimized structures of O_2 adsorbed in the bridge mode on Au^n/FAU ($n=0, +1$ and $+3$).

The bridge mode is favourable in both neutral and charged systems which is evident from the positive, high binding energies. The highest binding energy (3.23 eV) is observed in the neutral monomer while the energies are comparable in the cationic systems. Substantial charge transfer to O_2 (Δq) in the three systems results in significant elongation of the O-O bond that approaches the bond length of peroxide moiety. As a consequence, the corresponding vibrational frequency, $\nu_{\text{O-O}}$ is considerably lowered ($< 1000 \text{ cm}^{-1}$) compared to the gas phase value. Thus, O_2 adsorbed in the bridge mode on faujasite supported neutral and cationic Au monomer is highly activated. Increase in NBO charge on Au on adsorption of O_2 as compared to the bare monomer supported on faujasite also indicates charge transfer to O_2 . However, as it appears from the Au- O_z distance, which indicates weak interaction of the Au monomer with the zeolite support in Au^0/FAU , the charge transfer to O_2 occurs solely from the metal centre while in the cationic systems, strong interaction with the zeolite support assists in the charge transfer. The Au-O distances indicate strong interaction of the adsorbed O_2 with the supported Au monomer which is reflected in the high O_2 binding energies. The frontier molecular orbitals indicate participation of the p-orbitals of the zeolite O atoms in the cationic system along with the d-orbital of Au and p-orbital of O while in the neutral system, no contribution from the zeolite O-atoms is encountered in the respective orbital. In the lowest energy structures, O_2 binds in a chelating manner to the Au centre and hence is described as the bridge mode of adsorption. Table 5.1.3 summarizes the geometrical parameters, vibrational frequencies, binding energies and the NBO charges are given in Table 5.1.4.

5.1.3.5 O₂ adsorption in the dissociative mode on faujasite supported gold monomer

The dissociative mode of O₂ adsorption is considered next, where, two dissociated O atoms are considered to adsorb on the faujasite supported Au monomer. The optimized structures of O₂ adsorbed in the dissociative mode on faujasite supported neutral and cationic Au monomer are shown in Figure 5.1.6.

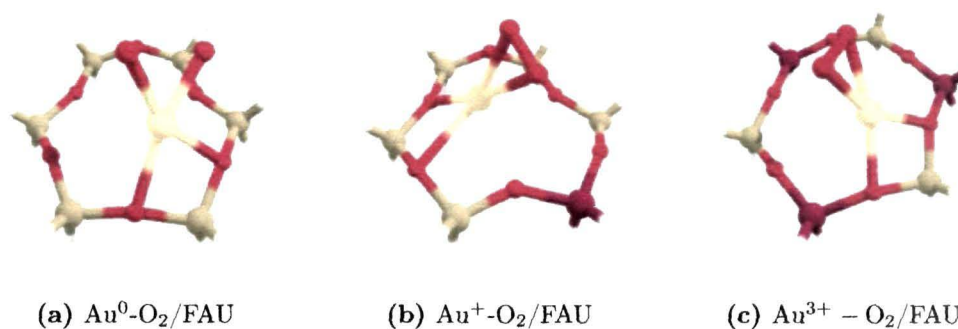


Figure 5.1.6: Optimized structures of O₂ adsorbed in the dissociative mode on Auⁿ/FAU (n=0, +1 and +3).

On Au⁰/FAU, the calculated binding energy indicates favourable adsorption of O₂ as two dissociated O atoms. However, this binding energy (0.31 eV) is rather significantly lower than the binding energy when O₂ adsorbs in the bridge mode. The distance between the O atoms is observed to be 2.09 Å which implies no interaction between the atoms and thus remain separated. Both the O atoms adsorb on Au with a distance of 1.95 Å signifying strong interaction with the metal centre. Analysis of the NBO charges indicates transfer of 0.91e charge to O₂ and concomitant increase in Au charge to 0.75e. Absence of O-O bond is attributed to the occupancy of the σ^* orbital of O₂ and the HOMO-1 orbital showing the occupancy of σ^* orbital is shown in Appendix C. In the cationic systems, when O₂ adsorption was considered in the dissociative mode, it reverts back to the bridge mode with O-O bond length of ~ 1.4 Å. The interaction of O₂ with the faujasite supported Au centre is shown in Appendix C. Red shift in the corresponding ν_{O-O} (< 1000 cm⁻¹) from the gas phase value (1643.04 cm⁻¹) indicates considerable elongation of the O-O bond. The binding energies calculated are comparable with the values observed in the bridge mode. NBO charges indicate transfer of similar

amount of charge to O₂ in both the bridge and dissociative modes for both the cationic systems which further corroborate reversal of the dissociated O atoms to the bridge mode of adsorption. The zero occupancy of σ^* and the π^* orbitals in free gas phase O₂ molecule shows O=O double bond (1.22 Å). When O₂ is adsorbed on Au³⁺/FAU an increase in occupancy of the π^* orbital of O₂ from 0 to 0.67556 is observed which contributes to the elongation of the O-O bond (1.41 Å) in Au³⁺-O₂/FAU. NBO analysis on Au⁺-O₂/FAU system shows a slight increase in occupancy of σ^* orbital of O₂ from 0 to 0.00772 resulting further elongation of O-O bond (1.42 Å). The computed geometrical parameters, vibrational frequencies, binding energies are given in Table 5.1.3 and Table 5.1.4 summarizes the NBO charges. This work has been published with 6-31G basis set for Si, Al, O, C and H atoms while LANL2DZ basis set for Au in the QM part [Baishya, S. Deka, R. C. *J. Chem. Phys.* **135** (24), 244703/1--244703/7, 2011].

5.1.4 Salient Observation

Using hybrid quantum mechanics/molecular mechanics method, we have investigated adsorption of CO and O₂ on faujasite supported neutral and cationic (+1 and +3) gold monomer. Our calculations indicate favourable binding of CO in the three Au oxidation states and the highest binding energy value is observed in Au³⁺/FAU. Top, bridge and dissociative modes of O₂ adsorption is considered in the present study. The top mode of O₂ adsorption is favourable in the cationic systems and higher O₂ binding energy is observed in Au³⁺/FAU. Charge transfer to O₂ in Au⁰/FAU and Au³⁺/FAU results in its activation evident from O-O bond elongation. Interaction of O₂ with the faujasite supported Au⁺ monomer is suggested to be merely electrostatic in nature and involves no O₂ activation. The bridge mode is favourable in the three oxidation systems and is accompanied by high binding energies and with substantial O-O bond activation. Adsorption of O₂ as two dissociated O atoms is designated as the dissociative mode and appears to be interesting. In Au⁰/FAU, O₂ remains as two dissociated O atoms albeit with low binding energy. On the other hand, in the cationic systems, it reverts back to the bridge mode instead of remaining as dissociated O atoms. It appears from the present calculations that the bridge mode is preferred over top and dissociative

Table 5.1.3: Geometrical parameters, binding energies and vibrational frequency of O₂ adsorbed on Auⁿ/FAU (n=0,+1 and +3)

	<i>Top</i>			<i>Bridge</i>			<i>Dissociative</i>		
	Au ⁰ /FAU	Au ⁺ /FAU	Au ³⁺ /FAU	Au ⁰ /FAU	Au ⁺ /FAU	Au ³⁺ /FAU	Au ⁰ /FAU	Au ⁺ /FAU	Au ³⁺ /FAU
	Bond Length (Å)								
Au-O	2.19	2.29	2.13	2.07	2.04	2.05	1.95	2.05	2.06
O-O	1.36	1.29	1.41	1.38	1.42	1.40	2.09	1.42	1.41
Au-Si	2.43	2.90	2.85	3.36	3.21	2.84	2.85	3.26	2.88
Au-Al	-	3.11	2.93	-	2.89	3.30	-	2.96	3.42
Au-O _z	2.27	2.04	1.99	2.71	2.14	2.26	2.40	2.28	2.31
	Vibrational Frequency (cm ⁻¹)								
ν_{O-O}	946.62	1150.37	781.40	880.53	901.60	901.97	-	900.11	910.96
	Binding Energy (eV)								
BE	-1.07	0.90	0.95	3.23	2.46	2.25	0.31	2.45	2.11

Table 5.1.4: Computed NBO charges in the different modes of O₂ adsorption on Auⁿ/FAU (n=0, +1 and +3).

	<i>Top</i>			<i>Bridge</i>			<i>Dissociative</i>		
	Au ⁰	Au ⁺	Au ³⁺	Au ⁰	Au ⁺	Au ³⁺	Au ⁰	Au ⁺	Au ³⁺
q(Au)	0.59	0.63	0.84	0.39	0.97	0.96	0.75	0.97	0.97
q(O)	-0.36	-0.16	-0.29	-0.17	-0.25	-0.22	-0.40	-0.24	-0.23
q(O)	-0.22	0.04	0.07	-0.33	-0.24	-0.21	-0.51	-0.22	-0.21
Δq	0.58	0.12	0.22	0.50	0.49	0.43	0.91	0.46	0.43
q(O _z)	-1.21	-1.22	-1.13	-1.24	-1.23	-1.21	-1.23	-1.23	2.31

modes of O₂ adsorption on faujasite supported neutral and cationic Au monomer which also accompanies significant O₂ activation.

5.2 Role of water on the adsorption of CO and O₂ on faujasite supported gold monomer

5.2.1 Introduction

The presence of certain amount of water is inevitable in practical catalytic systems and can significantly affect the adsorption of CO and O₂ on such systems. It thus, becomes indispensable to study the effect of water on the adsorption of CO and O₂. The role of water on the CO oxidation pathway has been investigated at large by different groups [139,141,142] and it has been observed that the presence of water can have both positive as well as negative effect on the catalytic activity of supported gold catalysts.

Various studies have investigated the co-adsorption of O₂/CO and H₂O or the effect of pre-adsorbed water on adsorption of O₂ and CO [137-146]. Gao *et al.* [139] suggested that the promotional effect of water on the catalytic activity of TiO₂ supported Au particles is mainly due to activation of molecular oxygen rather than carbonate decomposition. However, the binding energy of CO decreased in presence of water. DFT calculations by Zhang and Lindan [140] on the co-adsorption of water and oxygen on the TiO₂ (110) surface indicated enhancement in water binding in presence of co-adsorbed O. The dissociation of water along (-110) was observed to be harder and a new path along the (001) direction became more feasible. Hu and co-workers [141] presented the first density functional calculations on the effect of water on both adsorption and diffusion of O₂ on TiO₂(110). O₂ adsorption on TiO₂(110) was observed in the presence of OH groups; even in low coverage of OH and the effect of OH is demonstrated to be a long-range effect. First-principle investigations by Bongiorno and Landman [142] revealed a significant enhancement of the binding and activation of O₂ resulting from the co-adsorption of O₂ and water on small Au clusters (Au₈) supported on defect-free MgO(100), as well as on gas-phase neutral clusters (Au₈ and Au₃₀). The water enhanced activity of gold clusters towards CO oxidation has been attributed to the formation of a complex which involves partial sharing of a proton between the co-adsorbed molecules resulting in a hydroperoxyl-like intermediate.

The O-O bond is observed to be highly activated in this complex attaining bond length values characteristic of superoxo or peroxy like states. Recently, Ito *et al.* [145] demonstrated the enhancement in the adsorption of CO and O₂ molecules on gold dimer cation, Au₂⁺ due to pre-adsorption of a H₂O molecule using tandem mass spectrometry and ion trap methods. Adsorption and dissociation of H₂O on Au (111) surface was studied by Liu using DFT calculations [371]. It was observed that H₂O preferred the top site for adsorption and in the presence of adsorbed O atom the high energy barrier for water dissociation on clean gold surface reduces considerably.

Here, we present the results obtained from density functional theory calculations on the adsorption of carbon monoxide and oxygen on faujasite supported Au monomer in presence of water. We also discuss the formation of a hydroperoxyl-hydroxyl species as a consequence of proton transfer from H₂O to O₂ and the role of the zeolite framework in H₂O activation.

5.2.2 Computational Details

We have performed hybrid quantum mechanics/ molecular mechanics calculations using the SIMOMM [314] (Surface Integrated Molecular Orbital Molecular Mechanics) method implemented in GAMESS [316] program. The method has been elaborated in Section 5.1.2 and the zeolite model employed to study the adsorption of CO and O₂ on faujasite supported Au monomer has been utilized here (Figure 5.1.1). DFT based B3LYP functional [278,280,292], 6-31G(d, p) basis set [367] for Si, Al, O, C and H and LANL2DZ [308,309] basis set incorporating relativistic effective core potential for Au atom has been utilized for the quantum mechanical part and the molecular mechanical part is modelled using MM3 parameter [368]. The binding energy of H₂O adsorbed on Auⁿ/FAU (n=0, +1 and +3) is calculated using equation 5.2.1:

$$BE(H_2O) = (E_{Au/FAU} + E_{H_2O}) - (E_{Au-H_2O/FAU}) \quad (5.2.1)$$

BE(H₂O) is the binding energy of H₂O, E_{Au-H₂O/FAU} is the energy of H₂O adsorbed complex on faujasite supported Au monomer, E_{Au/FAU} is the energy of the faujasite supported Au monomer system, E_{H₂O} is the energy of gas phase free H₂O molecule.

The binding energy of the CO and O₂ molecule in presence of pre-adsorbed H₂O on faujasite supported Au atom is calculated using the following equation:

$$BE(A) = (E_{Au-H_2O/FAU} + E_A) - (E_{Au-H_2O,A/FAU}) \quad (5.2.2)$$

BE(A) is the binding energy of CO or O₂ designated as A here, $E_{Au-H_2O/FAU}$ is the energy of H₂O adsorbed on faujasite supported Au monomer system, E_A is the energy of gas phase free CO or O₂ molecule and $E_{Au-H_2O,A/FAU}$ is the energy of the aggregate containing H₂O and CO or O₂ on faujasite supported Au monomer. Favourable adsorption of CO or O₂ on water pre-adsorbed Auⁿ/FAU (n=0, +1 and +3) is indicated by a positive binding energy value. BSSE (basis set superposition error) corrections have not been incorporated while calculating the binding energies. The quadratic approximation method [369] implemented in GAMESS program was used in the geometry optimizations and transition state searches. The transition states are characterized with the presence of single negative vibrational frequency.

5.2.3 Results and Discussion

5.2.3.1 Water adsorption on faujasite supported gold monomer

The optimized structures of H₂O adsorbed on faujasite supported Au monomer in three oxidation states viz. 0, +1 and +3 are shown in Figure 5.2.1. The various structural parameters and the binding energy of H₂O in the three oxidation states of Au are listed in Table 5.2.1. The binding energy of H₂O increases with Au oxidation state and the strongest H₂O binding is observed in Au³⁺/FAU. The binding energy values calculated in our work are in good agreement with the values (0.2-0.6 eV) reported by Bongiorno and Landman for Au₈ and Au₃₀ clusters supported on defect-free MgO surface [142]. H₂O binds to the supported Au metal centre via the O atom and the interaction of Au and H₂O can be further understood qualitatively in terms of the frontier molecular orbital which shows considerable overlap between the d-orbital of Au and p-orbital centred on O atom of H₂O as shown in Appendix C. The role of zeolite framework in the adsorption of H₂O on faujasite supported Au monomer can be appraised from the activation of H₂O indicated by its elongated O-H bonds; particularly observed in the cationic

systems (both O-H bonds in $\text{Au}^{3+}/\text{FAU}$ and one O-H bond in Au^+/FAU). This activation of H_2O can be attributed to the H-bonding interaction between the nearest framework O atoms and the H atoms of H_2O which is persistent in the cationic Au systems (shown as dotted bonds in Figure 5.2.1). We next focus on the adsorption behaviour of CO and O_2 in the presence of H_2O on Au^n/FAU , $n=0, +1$ and $+3$. As described earlier, we consider three different modes viz. top, bridge and dissociative for O_2 adsorption in the presence of pre-adsorbed H_2O .

Table 5.2.1: Computed bond length (\AA), binding energy (eV) and NBO charges of H_2O adsorbed on Au^n/FAU , $n=0, +1$ and $+3$.

	Au^0/FAU	Au^+/FAU	$\text{Au}^{3+}/\text{FAU}$
Bond Length (\AA)			
Au-O	2.26	2.29	2.10
O-H	0.98, 0.98	0.98, 1.01	1.00, 1.03
H(H_2O)... O_z	1.99, 2.05	1.68, 2.65	1.61, 1.86
Au... O_z	3.39	2.03	1.98
Binding Energy (eV)			
BE	0.51	0.68	0.95
NBO Charges			
q(Au)	-0.070	0.580	0.752
q(O)	-1.000	-0.971	-0.972
q(H)	0.525, 0.525	0.526, 0.538	0.547, 0.549
q(O_z)	-1.248	-1.243	-1.222

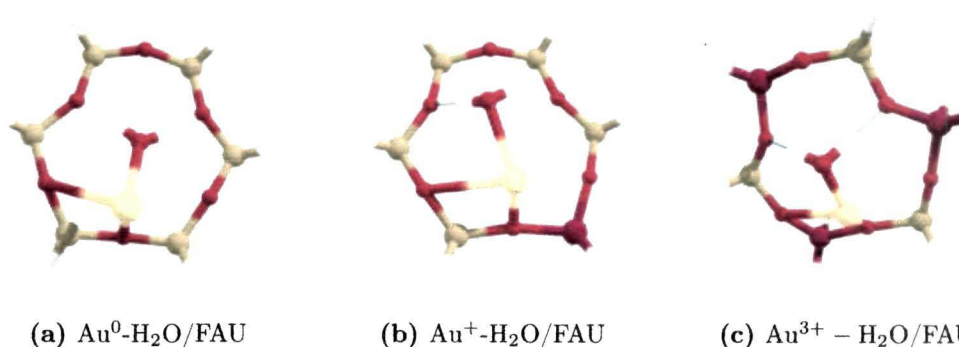


Figure 5.2.1: Optimized structures of H₂O adsorbed on Auⁿ/FAU (n=0, +1 and +3).

H, O, Al, Si and Au atoms are depicted with white, red, magenta, green and yellow colours.

5.2.3.2 Adsorption of CO on faujasite supported gold monomer in presence of pre-adsorbed H₂O

The optimized structures of CO adsorbed on Auⁿ/FAU (n=0, +1 and +3) in presence of pre-adsorbed H₂O are given in Figure 5.2.2. Our calculations indicate that the binding energy of CO in presence of pre-adsorbed water increases with the Au oxidation state and the highest binding energy value is observed in Au³⁺/FAU. The increasing CO binding energy with the Au oxidation state can be correlated with the decreasing Au-C distance with the shortest value of 1.91 Å in Au³⁺/FAU. The interaction of the metal centre with the zeolite framework given by the Au-O_z distance also decreases with the oxidation state. Our work shows that as CO binds with the metal centre, it results in cleavage of the Au-H₂O bond which is indicated by the elongated Au-O(H₂O) distance in all the oxidation states. In the neutral system, adsorption of CO even results in the displacement of the pre-adsorbed H₂O molecule from the zeolite plane. On Au₂⁺, Ito *et al.* [145] also indicated that adsorption of CO in presence of pre-adsorbed H₂O is assisted by the cleavage of Au-H₂O bond. In the three oxidation states, it is observed that no interaction exists between the CO and H₂O molecules. On the other hand, a weak interaction between the nearest zeolite oxygen atoms and the H atoms of the H₂O molecule prevails in all the structures which can be identified as H-bonding interaction. The shortest O_z..H(H₂O) distance of 1.70 Å is observed in Au⁰/FAU revealing the strongest interaction between H₂O and the zeolite framework among the three

Au oxidation states. The computed selected geometrical parameters and the CO binding energy in presence of pre-adsorbed H₂O on Auⁿ/FAU (n=0, +1 and +3) are summarized in Table 5.2.3.

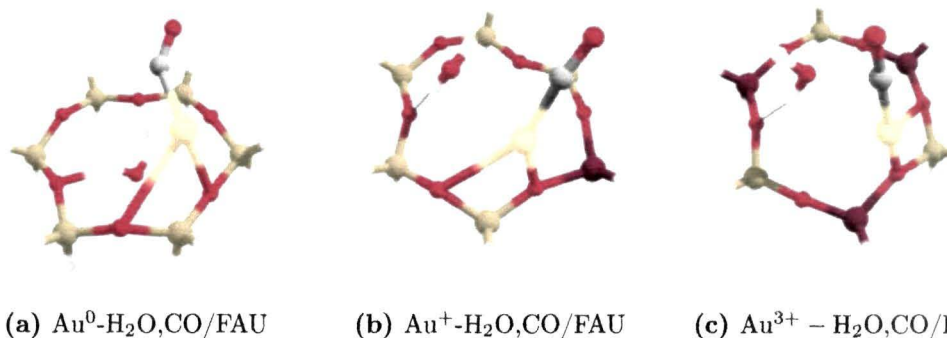


Figure 5.2.2: Optimized structures of CO adsorbed on Auⁿ/FAU (n=0, +1 and +3) in the presence of pre-adsorbed H₂O. H, C, O, Al, Si and Au atoms are depicted with white, grey, red, magenta, green and yellow colours.

5.2.3.3 Adsorption of O₂ in the top mode on faujasite supported gold monomer in presence of pre-adsorbed H₂O

Adsorption of O₂ in the top mode on Auⁿ/FAU, n=0, +1 and +3 in presence of pre-adsorbed H₂O is shown in Figure 5.2.3 and Table 5.2.3 lists the selected geometrical parameters and binding energy of O₂. The shortest Au-O distance is observed in Au⁰/FAU which reveals the strongest interaction of O₂ with Au⁰/FAU having a pre-adsorbed H₂O molecule and concomitantly the highest binding energy of O₂. The NBO charge analysis summarized in Table 5.2.4 indicates transfer of 0.545e charge to O₂ thereby, populating the antibonding orbital and consequently O₂ activation as illustrated by the elongated O-O distance of 1.40Å. The activation of O₂ is also reflected in the red shift of ν_{O-O} value from 1643.04 cm⁻¹ in gas phase to 899.57 cm⁻¹ in Au⁰/FAU. The O-O bond is slightly elongated as an outcome of the small quantity of charge transfer in the cationic counterparts. A weak interaction prevails between the adsorbed H₂O and O₂ in Au⁺/FAU (2.87Å) and Au³⁺/FAU (2.29Å) and can be recognized as hydrogen bonded interaction. However, as it appears from the co-adsorbed structures, there is apparently no interaction between the molecules (4.98Å) in Au⁰/FAU.

Table 5.2.2: Computed bond lengths (Å), stretching frequency, ν_{C-O} (cm^{-1}), binding energy of CO (eV) and NBO charges for CO adsorption on Au^n/FAU , $n=0, +1$ and $+3$ with pre-adsorbed H_2O .

	Au^0/FAU	Au^+/FAU	$\text{Au}^{3+}/\text{FAU}$
Bond Lengths (Å)			
Au- O_z	2.85	2.08	2.02
C-O	1.17	1.16	1.16
Au-C(CO)	2.10	1.96	1.91
Au-O(H_2O)	3.36	2.69	2.72
C(CO)..O(H_2O)	3.81	3.01	2.37
H(H_2O)... O_z	1.70	1.82	1.9
H...OH	0.98	0.99	0.99
Vibrational frequency(cm^{-1})			
ν_{C-O}	1917.08	2063.09	2084.96
Binding energy (eV)			
CO	2.27	3.66	3.84
NBO charge			
q(Au)	0.05	0.525	0.505
q(C)	0.385	0.497	0.524
q(O)	-0.442	-0.387	-0.39
Δq	0.057	-0.11	-0.134
q[O(H_2O)]	-0.984	-0.972	-0.975
q(H)	0.505	0.513	0.527
q(H)	0.497	0.497	0.502
q(O_z)	-1.245	-1.242	-1.237

With the framework zeolite oxygen atoms being in close proximity to the H atoms of the H₂O molecule; one cannot rule out the possibility of H-bonded interaction between them. The H(H₂O)···O_z distance reveals presence of such interaction in all the three oxidation state. The interaction of the metal centre with the zeolite framework (Au – O_z bond) increases with the oxidation state in the co-adsorbed structures. The frontier molecular orbitals illustrated in Appendix C show the contribution of the d-orbital of Au, p-orbitals of O(O₂) and O(H₂O) in bonding.

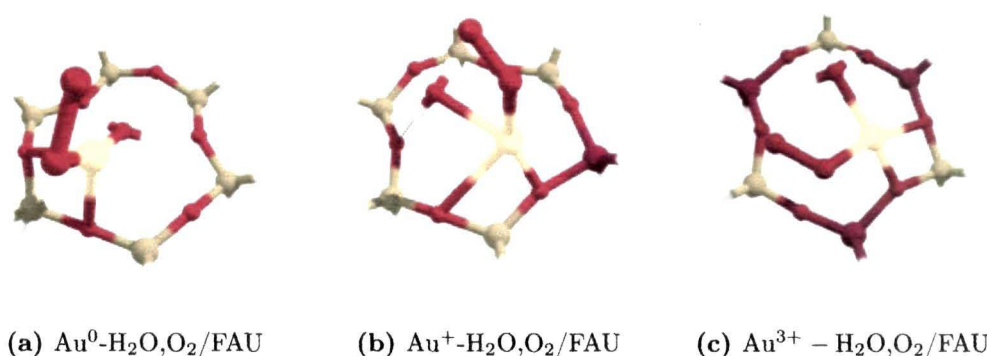


Figure 5.2.3: Optimized structures of O₂ adsorbed in the top mode on Auⁿ/FAU (n=0, +1 and +3) in the presence of pre-adsorbed H₂O.

From a chemical point of view, one cannot rule out the possibility of proton sharing when O₂ and H₂O are in close proximity. Thus, in the next step we consider the feasibility of dissociation of the adsorbed H₂O molecule and consequently formation of the hydroperoxyl and hydroxyl species due to the transfer of the dissociated H atom from H₂O to O₂. Our calculations indicate a high barrier value of 1.53eV in Au³⁺/FAU (TS₃) and a barrier as low as 0.20eV (TS₁) in Au⁺/FAU for the dissociation of the H atom from H₂O. The dissociated H atom bonds with O₂ and OH concomitantly as the distance between H···OH increases while the O₂···H distance decreases. The high barrier involved in Au³⁺/FAU can be attributed to the strong interaction of the H₂O molecule with the metal centre and also to the non-activation of the O-H bond which does not dissociate readily. On the other hand, the low barrier in Au⁺/FAU can possibly be attributed to the weak interaction of H₂O and Au atom even though Au⁺/FAU also involve no O-H activation. As a consequence of the dissociation of the H atom from H₂O, a hy-

Table 5.2.3: Computed bond lengths (Å), stretching frequency, $\nu_{\text{C-O}}$ (cm^{-1}) and binding energy of O_2 (eV) for O_2 adsorption on Au^n/FAU , $n=0, +1$ and $+3$ with pre-adsorbed H_2O .

	<i>Top</i>			<i>Bridge</i>			<i>Dissociative</i>		
	Au^0/FAU	Au^+/FAU	$\text{Au}^{3+}/\text{FAU}$	Au^0/FAU	Au^+/FAU	$\text{Au}^{3+}/\text{FAU}$	Au^0/FAU	Au^+/FAU	$\text{Au}^{3+}/\text{FAU}$
	Bond lengths (Å)								
Au- O_z	3.10	2.05	1.99	2.69	2.09	1.94	2.45	2.05	1.91
O-O	1.40	1.29	1.29	1.38	1.41	1.28	1.37	3.25	2.51
Au-O(O_2)	2.05	2.25	2.13	2.27	2.01	2.3	2.28	1.86	1.95
Au-O(H_2O)	2.14	2.31	2.09	2.30	2.14	2.09	2.67	2.36	2.09
$\text{O}(\text{O}_2) \cdots \text{H}(\text{H}_2\text{O})$	4.98	2.87	2.29	1.60	3.53	2.84	3.85	2.62	3.43
$\text{H}(\text{H}_2\text{O}) \cdots \text{O}_z$	1.91,1.99	1.72,2.77	1.63,2.13	2.38,2.95	1.79,1.83	1.67,1.53	2.91,3.44	2.00,3.17	1.54,1.85
$\text{H} \cdots \text{OH}$	0.98	0.99	0.99	0.97	1.00	1.03	0.98	0.98	1.05
	Vibrational Frequency (cm^{-1})								
$\nu_{\text{O-O}}$	899.57	1175.3	1103.57	969.19	909.31	1159.82	836.15	-	-
	Binding energy (eV)								
B.E	3.58	1.68	1.93	2.7	2.52	0.97	2.47	-1.56	-3.12

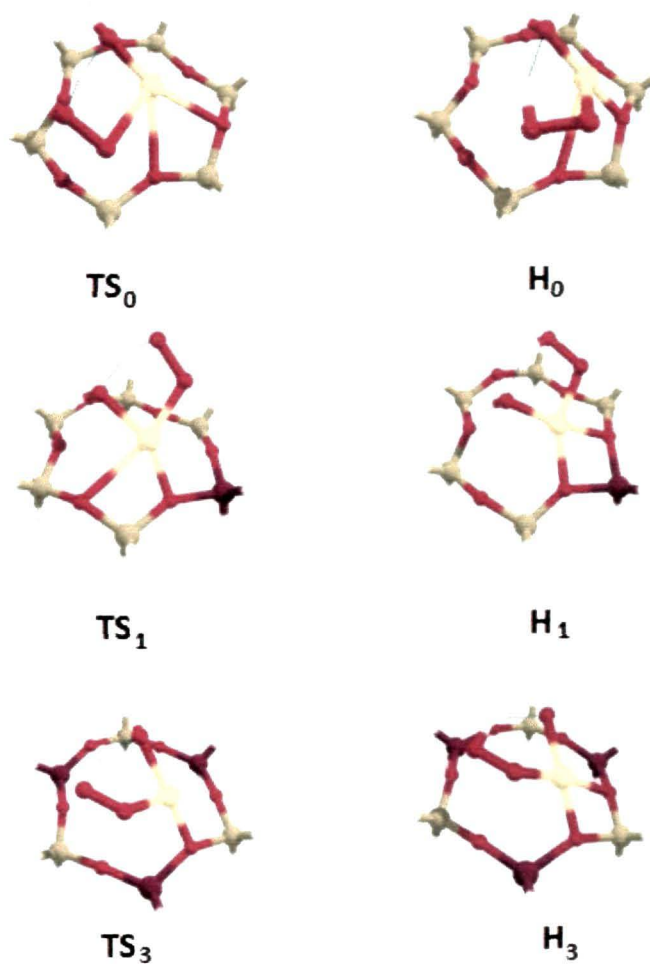


Figure 5.2.4: Energy profile diagram (above) and the structure of the transition states and the hydroperoxyl species (below) for the formation of hydroperoxyl-hydroxyl species from O₂ (adsorbed in the top mode) and H₂O on Auⁿ/FAU (n=0, +1 and +3)

droperoxyl (O_2H) and hydroxyl containing species results from the transfer of the dissociated H atom to the O_2 molecule in the three oxidation states. Exothermicity involved in the hydroperoxyl-hydroxyl species formation and its enhanced stability than the initial O_2 - H_2O co-adsorbed structure is observed only in Au^+ /FAU which implies that the adsorbed O_2 on Au^+ /FAU prefers the hydroperoxyl state when H_2O is in close proximity. The O-O bond is significantly elongated in the hydroperoxyl species in all the oxidation states and the highest elongation is perceived in Au^+ /FAU which can be attributed to the highest amount of charge transfer to O_2 (Δq is $0.764e$, Table 5.2.4). The O-O bond elongation implies activation of O_2 and thereby making the bond highly susceptible to dissociation. It is believed that such highly activated O_2 will be beneficial for oxidation reactions where activation of O_2 is an essential step. Previous work on O_2 and H_2O co-adsorption on Au_8 /MgO has also reported such O-O bond activation and the formation of hydroperoxyl group [142]. Figure 5.2.4 shows the energy profile diagram for the three oxidation states and Table 5.2.5 summarizes the geometrical parameters, the barriers involved and the imaginary frequency associated with the transition states.

Table 5.2.4: Computed NBO charges for O_2 adsorption in the top mode in presence of pre-adsorbed H_2O (R), the hydroperoxyl-hydroxyl species formed (H) and the transition state involved (TS) in Au^n /FAU ($n=0, +1$ and $+3$).

		q(Au)	q(O)	q(O)	Δq	q[O(H_2O)]	q(H)	q(H)	q(O_2)
Au^0	R	0.414	-0.353	-0.192	0.545	-0.979	0.539	0.54	-1.248
	TS ₀	0.530	-0.268	-0.348	0.616	-1.036	0.518	0.503	-1.237
	H	0.447	-0.175	-0.408	0.583	-0.993	0.505	0.482	-1.238
Au^+	R	0.697	-0.133	-0.02	0.153	-0.955	0.534	0.528	-1.243
	TS ₁	0.885	-0.192	-0.237	0.429	-0.973	0.54	0.536	-1.235
	H	1.081	-0.317	-0.447	0.764	-0.887	0.507	0.501	-1.227
Au^{3+}	R	0.911	-0.082	-0.042	0.124	-0.949	0.549	0.55	-1.233
	TS ₃	0.936	-0.191	-0.278	0.469	-0.963	0.524	0.533	-1.217
	H	1.04	-0.216	-0.354	0.570	-0.933	0.527	0.513	-1.223

5.2.3.4 Adsorption of O₂ in the bridge mode on faujasite supported gold monomer in presence of pre-adsorbed H₂O

The optimized structures for adsorption of O₂ in the bridge mode on Auⁿ/FAU, n=0, +1 and +3 in presence of pre-adsorbed H₂O are shown in Figure 5.2.5 and the computed geometrical parameters, O-O vibrational frequency and binding energy are listed in Table 5.2.3. The activation of O₂ as indicated by the elongation of the O-O bond and consequently red shift in the $\nu_{\text{O-O}}$ values is observed in Au⁰/FAU and Au⁺/FAU whereas in Au³⁺/FAU, the bond length increases slightly. Analysis of NBO charges summarized in Table 5.2.6 shows a charge transfer of 0.55e and 0.48e to O₂ in Au⁰/FAU and Au⁺/FAU, respectively which populates the antibonding orbital resulting in O₂ activation. The highest binding energy of O₂ (2.70eV) in the bridge mode in presence of pre-adsorbed H₂O is observed in Au⁰/FAU. The H-bonded interaction between O₂ and H₂O is most prevalent in the faujasite supported neutral Au system as revealed by the shortest O (O₂)...H (H₂O) distance (1.60Å) and is negligible in Au⁺/FAU (3.53Å). Moreover, such H-bonding also exists with the zeolite oxygen atoms which are in close proximity to the adsorbed H₂O molecule and can be recognized from the O_z...H(H₂O) distances summarized in Table 5.2.3.

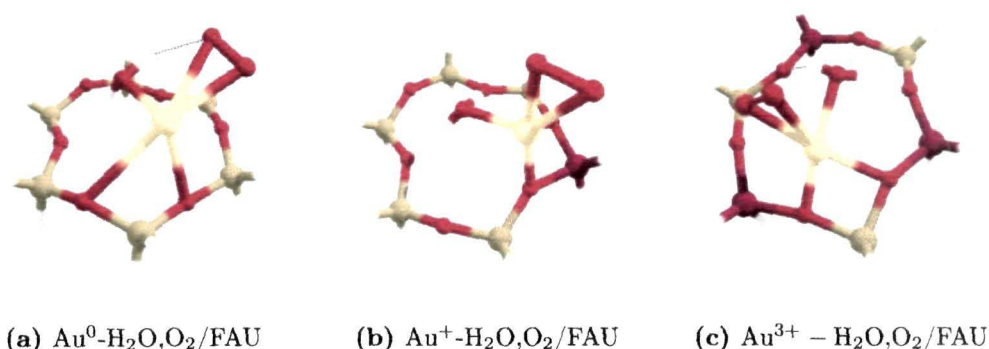


Figure 5.2.5: Optimized structures of O₂ adsorbed in the bridge mode on Auⁿ/FAU (n=0, +1 and +3) in the presence of pre-adsorbed H₂O.

As an outcome of this interaction, the O-H bond of H₂O elongates to 1.03Å (in Au³⁺/FAU) indicating activation of the adsorbed H₂O molecule. In these co-adsorbed structures, the interaction of the metal centre with the zeolite framework increases with the oxidation state. The frontier molecular orbitals are shown in

Table 5.2.5: Computed bond lengths (Å) of the transition states and the hydroperoxyl species, the barriers involved, ΔE (eV) and the imaginary frequency for the transition states in Au^n/FAU , $n=0, +1$ and $+3$.

		<i>O₂ (top mode)</i>						
		O-O	Au-O	Au-O(H ₂ O)	O(O ₂)..H	H..OH	ΔE	-ve freq
Au^0/FAU	TS ₀	1.39	2.67	2.10	1.17	1.24	0.80	-262.98
	O ₂ H	1.40	2.70	2.02	1.07	1.57		
Au^+/FAU	TS ₁	1.41	2.06	2.03	1.03	1.63	0.20	-126.88
	O ₂ H	1.49	2.00	2.00	1.01	1.89		
$\text{Au}^{3+}/\text{FAU}$	TS ₃	1.38	2.12	2.06	1.22	1.26	1.53	-1427.26
	O ₂ H	1.42	2.07	1.96	1.02	1.85		
		<i>O₂ (bridge mode)</i>						
		O-O	Au-O	Au-O(H ₂ O)	O(O ₂)..H	H..OH	ΔE	-ve freq
Au^0/FAU	TS' ₀	1.41	2.37	2.12	1.08	1.39	0.61	-134.52
	O ₂ H	1.44	2.64	2.06	0.99	3.85		
Au^+/FAU	TS' ₁	1.43	1.95	2.11	1.11	1.61	2.95	-1027.72
	O ₂ H	1.49	2.27	1.97	0.99	3.82		
$\text{Au}^{3+}/\text{FAU}$	TS' ₃	1.37	2.67	1.94	1.01	1.97	0.36	-222.01
	O ₂ H	1.44	2.05	2.04	1.03	1.75		

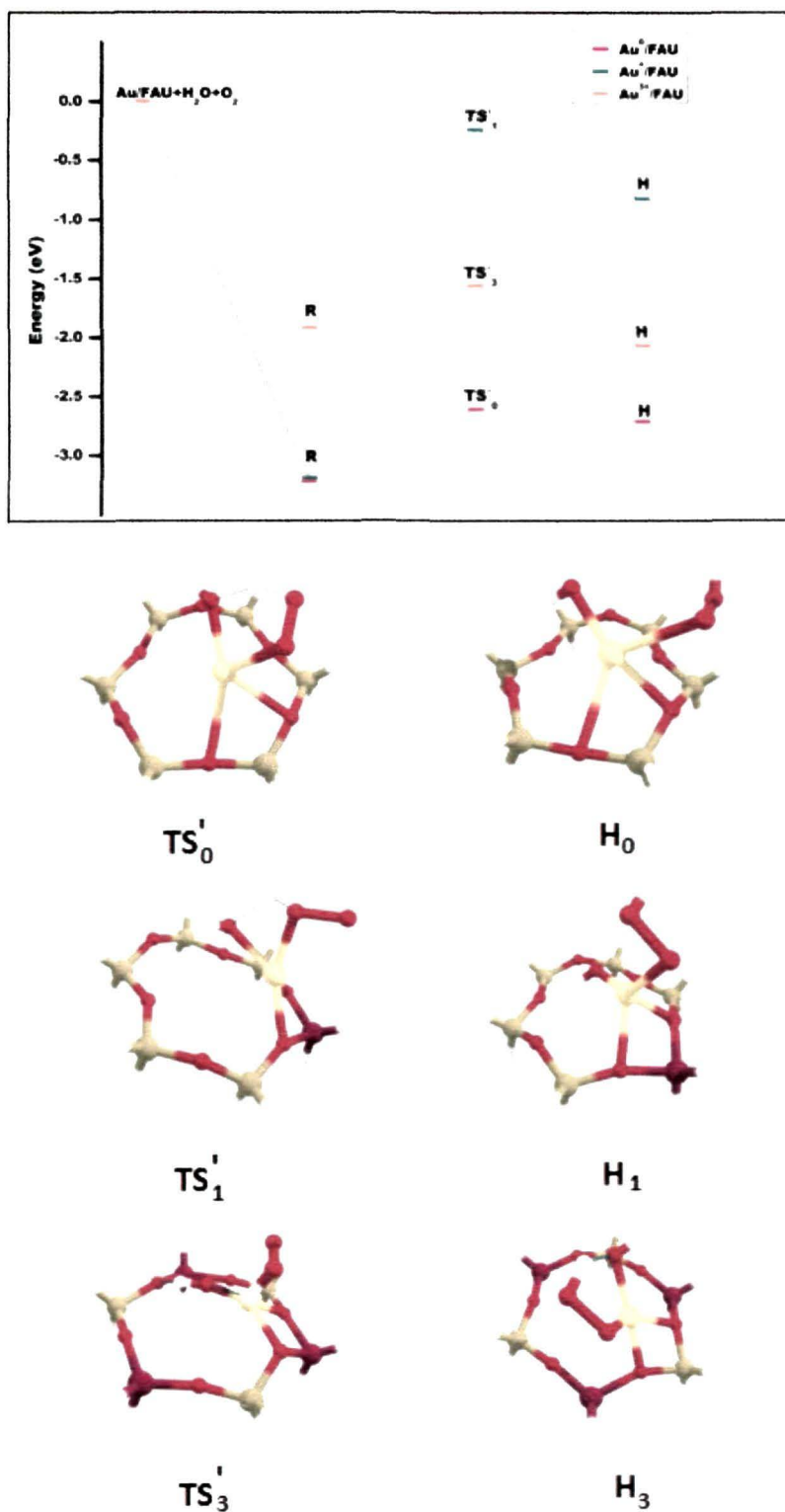


Figure 5.2.6: Energy profile diagram (above) and the structure of the transition states and the hydroperoxyl species (below) for the formation of hydroperoxyl-hydroxyl species from O_2 (adsorbed in the bridge mode) and H_2O on Au^n/FAU ($n=0, +1$ and $+3$).

Appendix C. As discussed earlier, H-bonded interaction exists between O_2 and H_2O and also between the zeolite oxygen atoms and H_2O that results in H_2O activation. As a consequence of such activation initiated by the zeolite framework indicated by the O-H bond elongation which is much effective in Au^{3+}/FAU , the barrier involved (TS'_3) in the dissociation of H_2O is the lowest (0.36 eV) among the three oxidation states. In the transition state (TS'_3), one of the H atoms dissociates partially from the H_2O molecule and forms a weak bond with the O_2 molecule. In other words, we can say that the H atom is shared between the co-adsorbed H_2O and O_2 molecules. The highest barrier (2.95 eV) in Au^+/FAU can be attributed to the larger distance between the adsorbed molecules which apparently indicates no H-bonded interaction. Moreover, higher O_2 binding energy in Au^+/FAU than in the Au^{3+} counterpart implies stable adsorption of O_2 in the bridge mode in the former in presence of pre-adsorbed H_2O . In Au^0/FAU , presence of H-bonded interaction between O_2 and H_2O lowers the barrier for H_2O dissociation. The dissociated H atom then forms a hydroperoxyl (O_2H) and hydroxyl (OH) species in all the oxidation states which is however, more stable than the initial co-adsorbed species only in Au^{3+}/FAU . The higher stability of the hydroperoxyl-hydroxyl species can be related with the lowest binding energy of O_2 (0.97 eV) in the co-adsorbed structure in Au^{3+}/FAU which implies that adsorbed O_2 on Au^{3+}/FAU prefers the hydroperoxyl state when H_2O is in close proximity. A high degree of O-O bond activation is observed in the hydroperoxyl state which is reflected by the elongated O-O bond in all the three oxidation states. The highest O-O bond elongation (1.49Å) is observed in Au^+/FAU that can be correlated with the transfer of highest amount of charge (0.73e) as shown by the charge analysis given in Table 5.2.6. The overall process of the formation of hydroperoxyl species from co-adsorbed H_2O and O_2 (in the bridge mode) on faujasite supported Au atom is exothermic only in the +3 oxidation state. The energy profile diagram for the three oxidation states is shown in Figure 5.2.6 and Table 5.2.5 summarizes the geometrical parameters, the barriers involved and the imaginary frequency associated with the transition states.

Table 5.2.6: Computed NBO charges for O₂ adsorption in the bridge mode in presence of pre-adsorbed H₂O (R), the hydroperoxyl-hydroxyl species formed (H) and the transition state involved (TS') in Auⁿ/FAU, n=0, +1 and +3.

		q(Au)	q(O)	q(O)	Δq	q[O(H ₂ O)]	q(H)	q(H)	q(O ₂)
	R	0.464	-0.279	-0.274	0.553	-0.99	0.512	0.522	-1.238
Au ⁰	TS' ₀	0.518	-0.374	-0.254	0.628	-1.053	0.497	0.521	-1.237
	H	0.439	-0.425	-0.144	0.569	-0.943	0.464	0.505	-1.235
	R	0.965	-0.264	-0.215	0.479	-0.952	0.544	0.547	-1.243
Au ⁺	TS' ₁	0.999	-0.41	-0.182	0.592	-0.861	0.508	0.563	-1.236
	H	0.97	-0.418	-0.31	0.728	-0.822	0.512	0.511	-1.222
	R	1.042	-0.011	0.028	-0.017	-0.916	0.559	0.553	-1.201
Au ³⁺	TS' ₃	1.153	-0.261	-0.102	0.363	-0.82	0.521	0.532	-1.192
	H	1.044	-0.376	-0.251	0.627	-0.92	0.518	0.493	-1.215

5.2.3.5 Adsorption of O₂ in the dissociative mode on faujasite supported gold monomer in presence of pre-adsorbed H₂O

The optimized structures of O₂ adsorbed in the dissociative mode in presence of pre-adsorbed water in Auⁿ/FAU (n=0, +1 and +3) are shown in Figure 5.2.7. For studying the dissociative mode of O₂ adsorption, we have considered the O₂ molecule as two dissociated O atoms on Auⁿ/FAU (n=0, +1 and +3) with pre-adsorbed H₂O as the initial structure. However, during the course of optimization, the dissociated O atoms revert to the bridged O₂ with O-O distance of 1.39 Å in Au⁰/FAU. On the other hand, in the cationic systems, O₂ remains as two dissociated O atoms in presence of pre-adsorbed H₂O.

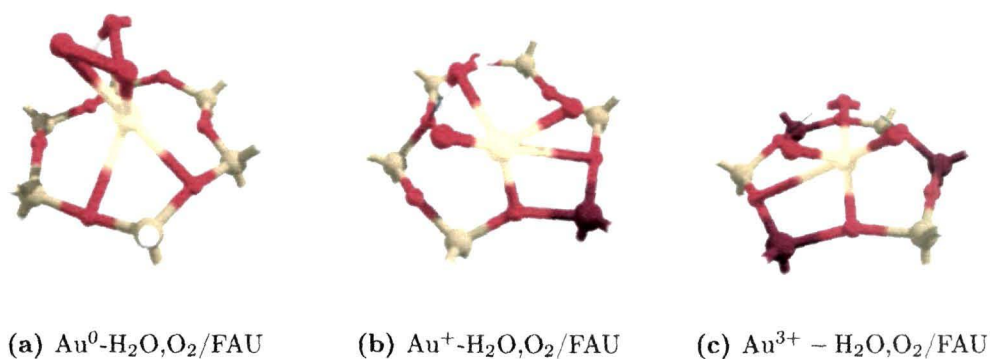


Figure 5.2.7: Optimized structures of O_2 adsorbed in the dissociative mode on Au^n/FAU ($n=0, +1$ and $+3$) in the presence of pre-adsorbed H_2O .

Table 5.2.7: Computed NBO charges for O_2 adsorption in the dissociative mode on Au^n/FAU ($n=0, +1$ and $+3$) in the presence of pre-adsorbed H_2O .

	Au^0/FAU	Au^+/FAU	$\text{Au}^{3+}/\text{FAU}$
$q(\text{Au})$	0.573	1.149	1.228
$q(\text{O})$	-0.377	-0.452	-0.37
$q(\text{O})$	-0.304	-0.441	-0.418
Δq	0.681	0.893	0.788
$q[\text{O}(\text{H}_2\text{O})]$	-1.003	-0.927	-0.924
$q(\text{H})$	0.537	0.521	0.557
$q(\text{H})$	0.547	0.521	0.554
$q(\text{O}_z)$	-1.239	-1.218	-1.191

NBO analysis (Table 5.2.7) reveals transfer of larger amount of charge to O_2 in Au^+ (0.89e) and Au^{3+} (0.79e) assisting in the O_2 dissociation. The HOMO-1 orbital of Au^+/FAU system and HOMO-2 orbital of $\text{Au}^{3+}/\text{FAU}$ system depicted in Appendix C shows the occupancy of the σ^* orbital with respect to the O-O bond and thus breaking the O-O bond. The interaction of the metal centre with the zeolite framework increases with the Au oxidation state which is indicated by the shortest $\text{Au} - \text{O}_z$ distance (1.91Å) for $\text{Au}^{3+}/\text{FAU}$. The presence of strong H-bonding between H atoms of adsorbed H_2O and the nearest framework oxygen atoms is revealed by the shortest $\text{O}_z \cdots \text{H}(\text{H}_2\text{O})$ distance of 1.54Å in $\text{Au}^{3+}/\text{FAU}$. As an outcome of such interaction, O-H bond of H_2O elongates re-

flecting H₂O activation. The O-H distance increases to 1.05Å and H-O-H angle to 111.82° in Au³⁺/FAU. Meanwhile, in Au⁺/FAU weak H-bonding between framework O atoms and H₂O exists and consequently no H₂O activation is noticed. Unlike the earlier modes of adsorption, herein no H-bonding is observed between the dissociated O atoms of O₂ and the H₂O. Since, O₂ is adsorbed as two dissociated O atoms and as discussed above no interaction is observed between H₂O and O atoms, thus we rule out the possibility of formation of O₂H type species on Au⁺/FAU and Au³⁺/FAU. The calculated binding energies indicate that the binding of O₂ in the dissociative mode is unfavourable in the cationic systems indicated by the negative binding energy values whereas the binding is favourable in Au⁰/FAU wherein it reverts back to the bridge bonded mode.

5.2.4 Salient Observation

Hybrid quantum mechanics/molecular mechanics calculations have been carried out to comprehend the effect of water on the adsorption of CO and O₂ on faujasite supported neutral and cationic gold monomer. It is observed that the binding energy of H₂O on faujasite supported gold monomer increases with the Au oxidation state. However, adsorption of CO on this H₂O pre-adsorbed faujasite supported monomer results in cleavage of the Au-H₂O bond and no interaction exists between CO and H₂O. The binding energy of CO increases with the oxidation state. Three modes of O₂ adsorption viz. top, bridge and dissociative has been considered on H₂O pre-adsorbed Auⁿ/FAU, n=0, +1 and +3. Our calculations indicate that the top and the bridge modes are favourable in all the oxidation states and the highest binding energy is observed in Au⁰/FAU. On the other hand, it is observed that the dissociative mode is unfavourable in the cationic systems and reverts back to the favourable bridge mode of adsorption in Au⁰/FAU. A weak interaction prevails between O₂ and H₂O and also between the nearest zeolite oxygen atoms and the H atoms of H₂O which can be recognized as hydrogen bonded interaction. As a consequence, activation of H₂O is observed which is indicated by the elongation of the O-H bond of H₂O. Further, transfer of a proton from H₂O to O₂ results in a hydroperoxyl-hydroxyl species which involves a barrier as low as 0.20 eV. The transition state involves proton sharing between the O₂ and H₂O molecules. It

is believed that the results obtained here for the atomic level calculations will be beneficial in understanding similar fundamental aspects in more realistic larger clusters.

Chapter 6

Activity of Zeolite Supported Gold Monomer Towards CO Oxidation and Water Gas Shift Reaction

Overview

In this chapter, we have presented the results of the activity of faujasite supported gold monomer towards CO oxidation and water gas shift reactions. In the first part of this chapter (Section 6.1), we have investigated the activity of Auⁿ/FAU (n=0, +1 and +3) towards CO oxidation. The most favourable oxidation pathway among the different pathways considered involves Eley-Rideal mechanism with CO adsorbed on the supported Au centre and O₂ reacting from the gas phase. The most stable CO and O₂ adsorption configurations obtained in Chapter 5 have been used for investigating their co-adsorption, necessary to study CO oxidation mechanism. Our calculations indicate that the initial configurations containing CO and O₂ with substantial interaction energies are not appreciable as they lead to oxidation pathways which entail high reaction barriers. It is observed that Au³⁺/FAU exhibits better catalytic activity among the three systems considered here, and the stability of all the species including the transition states with respect to the interacting species indicates no thermal activation.

In Section 6.2, we present the results for the activity of Auⁿ/FAU (n=0, +1

and +3) towards water-gas shift reaction. We have considered two CO-H₂O co-adsorption configurations and it has been observed that CO adsorption on Auⁿ/FAU (n=0, +1 and +3) in presence of pre-adsorbed H₂O presents a more favourable configuration. Our calculations indicate the formation of a carboxyl intermediate in the water-gas shift reaction mechanism which is the rate limiting step in Au⁺/FAU. The occurrence of high barriers in dissociation of water and the endothermicity of the overall reaction observed in the cationic systems will diminish their activity towards water-gas shift reaction. On the other hand, comparatively lower barriers and exothermicity of the reaction in Au⁰/FAU indicates it to be a better catalyst. The stability of all the species including the transition states with respect to the interacting species indicates no thermal activation in faujasite supported neutral Au monomer.

6.1 CO oxidation on faujasite supported gold monomer

6.1.1 Introduction

Pioneering work of Haruta *et al.* [150,151] on low temperature CO oxidation by ultrafine gold particles dispersed on metal oxides stimulated the use of gold clusters and nanoparticles as efficient catalysts for various reactions. Oxidation of carbon monoxide is an environmentally important reaction and has been widely studied. Various experimental [178-185] and theoretical [186-195] studies have unveiled the catalytic activity of gold clusters supported on various oxides towards CO oxidation. Apart from metal oxides, zeolites form a fascinating class of solid support which can be attributed to the presence of pores and cavities of molecular dimensions and adjustable acidic properties. The catalytic activity of gold nanoparticles supported on zeolites towards CO oxidation has been studied using various experimental methods [212-222]. Chen *et al.* [215] prepared nano-gold in Y, β and mordenite zeolites and observed that Y-zeolite with more aluminium loading showed no aggregation of the gold particles with size around 1 nm. The high activity of Au/Y catalyst and its stability for CO oxidation has

been attributed to the cage-like pores in Y-zeolite with high aluminium content that prevented sintering of gold and the hydrophilic surface favoured activation of gold species. Fierro-Gonzalez and Gates observed higher activity of the NaY supported Au^{III} complex towards CO oxidation compared to the Au^I complex [218]. The catalytic activity was found to decrease with a concomitant reduction of the initially present Au^{III} to Au^I. They have identified the catalytic site as atomically dispersed gold catalyst with atomic resolution STEM complemented by spectroscopy [220]. Simakov *et al.* [219] identified two types of active sites viz. partly reduced gold species, Au_n^{δ+} for low temperature activity and gold nanoparticles, Au_m⁰ for high temperature activity while investigating CO oxidation over mordenite supported Au. Thus, it appears that the catalytic activity of zeolite supported gold clusters is greatly influenced by its oxidation state. In comparison to the large volume of the experimental work on the catalytic activity of zeolite supported Au towards CO oxidation, theoretical investigations are quite scarcer. Griffe *et al.* implemented density functional calculations to study CO oxidation on silicoaluminophosphates (SAPO) molecular sieves supported Au, Au₂ [224] and Au₃₋₅ [225]. Their results indicated exothermicity of the oxidation reaction and involve Eley-Rideal mechanism where gas phase O₂ reacts with adsorbed CO on both Au/SAPO-11 species [224]. CO adsorption and oxidation was studied on Au₃₋₅/SAPO-11 using hybrid QM/MM method [225].

Moreover, catalytic activity of gold clusters as small as single Au atom has also been demonstrated by different studies [171,218,220,262-264]. The catalytic activity of a single Au atom embedded in a 2D h-BN monolayer towards CO oxidation was observed by Mao *et al.* [262] using density functional calculations along with molecular dynamics and micro-kinetic analysis. They have proposed a new tri-molecular Eley-Rideal mechanism with two CO molecules and one O₂ molecule and the formation of two CO₂ molecules from an OOCAuCOO intermediate is the rate limiting step with activation energy of 0.47 eV. Fang *et al.* [171] performed calculations at the CCSD(T)/aug-cc-pVTZ//mPW2PLYP/aug-cc-pVTZ level of theory and showed that even the single gold atom is a good catalyst for CO oxidation involving a barrier of 4.8 kcal mol⁻¹ at 0K for the first oxidation step and 1.6 kcal mol⁻¹ for the second step. In the present chapter, we have focussed on un-

derstanding the CO oxidation mechanisms on faujasite supported gold monomer in three oxidation states viz. 0, +1 and +3.

6.1.2 Computational Details

All the calculations are performed using hybrid quantum mechanics/ molecular mechanics method, SIMOMM [314] (Surface Integrated Molecular Orbital Molecular Mechanics) which is implemented in the GAMESS program [316]. Details of this hybrid method have been described in Chapter 5 and the same zeolite model has been employed to study CO oxidation pathways on faujasite supported Au monomer (Figure 5.1.1). The reaction is modelled within the chemically active quantum mechanical part which comprises of a six membered zeolite ring and the Au monomer. DFT based B3LYP functional [278,280,292], 6-31G(d, p) basis set [367] for Si, Al, O, C and H and LANL2DZ [308,309] basis set incorporating relativistic effective core potential for Au atom has been utilized for the quantum mechanical part while the MM3 parameter [368] is employed for the molecular mechanical part. The quadratic approximation method [369] implemented in GAMESS program was used in the geometry optimizations and transition state searches. The transition states are characterized with the presence of single negative vibrational frequency. The results for adsorption of CO and O₂ on faujasite supported Au monomer in three oxidation states viz. 0, +1 and +3 are presented in Chapter 5. Interaction between the initial reactants Au/FAU, CO and O₂ is considered from the interaction energy, calculated using equation (6.1.1).

$$E(int) = (E_{Au-A,B/FAU}) - (E_{Au/FAU} + E_A + E_B) \quad (6.1.1)$$

$E(int)$ is the interaction energy, $E_{Au-A,B/FAU}$ is the energy of the adsorption complex with both CO and O₂ adsorbed on faujasite supported Au, $E_{Au/FAU}$ is the energy of faujasite supported Au monomer, E_A and E_B are energies of the free A and B molecules. A and B represent CO and O₂ molecules.

6.1.3 Results and Discussion

6.1.3.1 Adsorption of CO and O₂ on faujasite supported Au monomer

The adsorption of CO and O₂ on faujasite supported neutral and cationic Au monomer has been studied earlier and the results are summarized in Chapter 5. Here, we present the results for different initial configurations containing CO and O₂ on Auⁿ/FAU (n=0, +1 and +3) that have been adopted to investigate CO oxidation mechanism. These configurations are:

- i. CO in the gas phase and O₂ adsorbed (three different modes of O₂ coordination viz. top, bridge and dissociative).
- ii. O₂ in the gas phase and CO adsorbed.
- iii. Both CO and O₂ adsorbed.

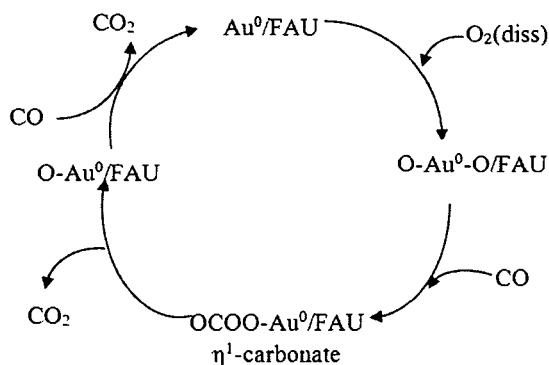
Table 6.1.1: Computed interaction energies (in eV) for different initial configurations containing CO and O₂ on Auⁿ/FAU (n=0, +1 and +3).

	ER mechanism			LH mechanism			
	CO (gas), O ₂ (ads)			CO (ads), O ₂ (gas)	CO (ads), O ₂ (ads)		
	Top	Bridge	Dissociative		Top	Bridge	Dissociative
Au ⁰ /FAU	-9.03	-6.3	-9.33	-6.30	-6.14	-6.31	-9.28
Au ⁺ /FAU	-7.33	-5.33	-8.90	-5.71	-5.2	-6.19	-8.85
Au ³⁺ /FAU	-7.24	-4.86	-8.21	-4.72	-5.64	-6.04	-8.16

The interaction energies calculated using equation (6.1.1) for the different initial configurations are given in Table 6.1.1. In the three Au systems, interaction energies indicate the configuration with O₂ adsorbed in the dissociative mode and CO in the gas phase to be more preferable. The configuration with both CO and O₂ (dissociative mode) adsorbed also has comparable interaction energy. We proceed further to investigate the CO oxidation mechanism with the most favourable configuration i.e. O₂ adsorbed in the dissociative mode and CO in the gas phase. In addition to this, we also consider other mechanistic pathways with intermediate interaction energies.

6.1.3.2 CO oxidation reaction energy profile with dissociated O₂

- (a) Oxidation pathway on Au⁰/FAU: The various intermediate steps in the oxidation pathway on Au⁰/FAU involving O₂ adsorbed in the dissociative mode and gas phase CO (Eley-Rideal mechanism) can be represented as:

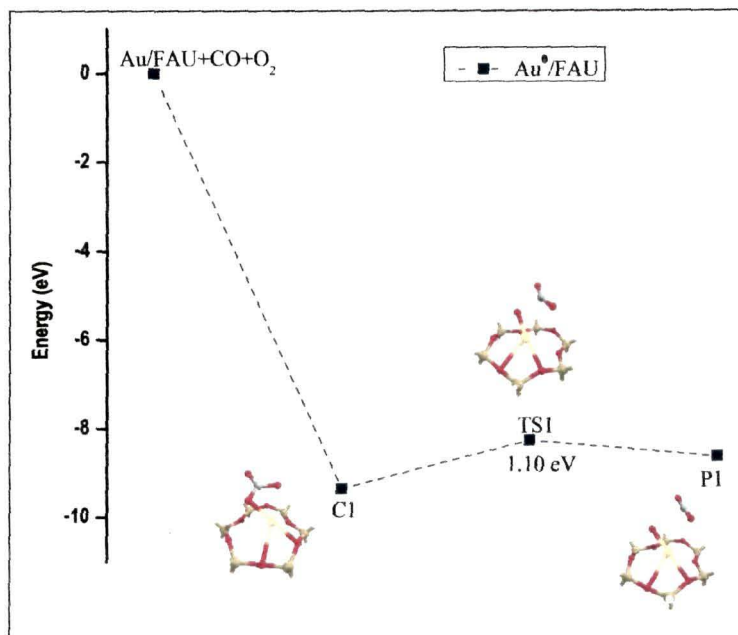


The first step involves formation of a highly exothermic carbonate-like structure which is attached to the metal centre via one O atom with a distance of 2.01 Å and hence is denoted as a η^1 -carbonate (C1) species. Subsequently, one of the C-O bonds breaks to form the first CO₂ (P1) while one oxygen atom remains adsorbed on faujasite supported Au. The transition state, TS1 for P1 formation involves considerable elongation of one of the C-O bonds which dissociates later and the single negative vibrational frequency is observed at -180.33 cm^{-1} . High barrier value of 1.10 eV observed in our calculations reflects the undesirability of Au⁰/FAU as a catalyst for the first oxidation step. The interaction of the metal centre with the zeolite framework, given by the Au-O_z distance is observed to be 2.37 Å in P1. The CO₂ formed has C-O bond length of 1.19 Å, O-C-O angle of 177.6° and a characteristic vibrational frequency of 2258.73 cm^{-1} . To complete the full catalytic cycle, a second gas phase CO molecule reacts with Au⁰-O/FAU (Eley-Rideal mechanism) initially to form an entity (R2) containing the oxygen atom adsorbed on the metal centre and the CO molecule. However, no interaction exists between the oxygen atom and the CO molecule apparent from the large separation between them. The second CO₂ forms from the species R2 surpassing an energy barrier of 0.41 eV indicated by the transition state, TS2. The single negative vibrational frequency for TS2 appears at -311.79 cm^{-1} .

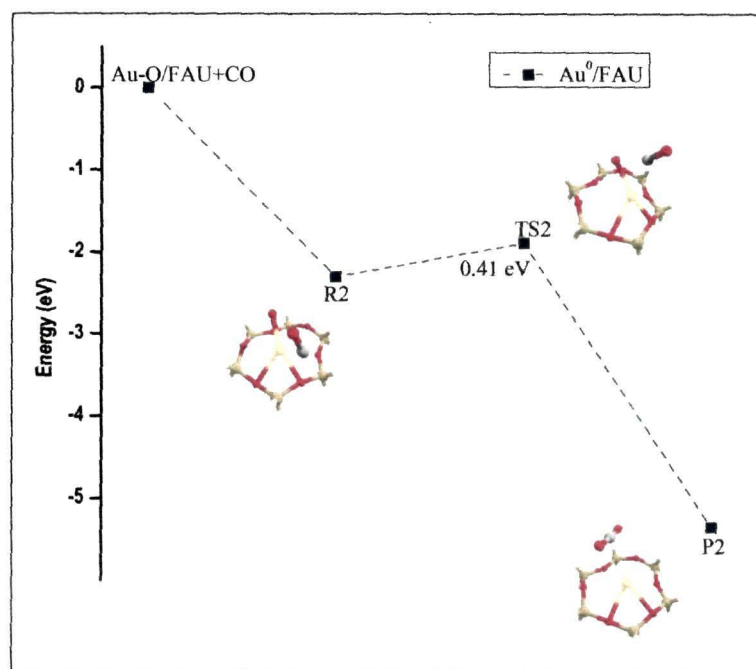
Table 6.1.2: Computed geometrical parameters (Å), barriers values (eV) and the imaginary frequency (cm⁻¹) for transition states in the Eley-Rideal pathway with dissociated O₂ on Au⁰/FAU.

	Au-O _z	Au-O	O-C	O-C (CO)	O-C-O	ΔE	-ve freq
C1	2.37	2.01	1.35, 1.33	1.25	-		
TS1	2.37	1.96	1.92, 1.23	1.2	152.45°	1.10	-180.33
P1	2.37	1.97	1.19	1.19	177.62°		
R	2.4	2.01	2.50	1.16	-		
TS2	2.4	2.08	2.05	1.17	157.13°	0.41	-311.79
P2	2.78	-	1.20	1.19	174.53°		

A weak interaction crops up between the oxygen atom and the CO molecule in TS2, which is evident from the decreasing distance between them to 2.05 Å, while the C-O bond of CO elongates to 1.17 Å, thereby, representing a partially formed CO₂ with O-C-O angle of 157.1°. Further, the product P2 formed from TS2 is characterized with C-O bond length of 1.19 Å, O-C-O angle of 174.5° and a characteristic vibrational frequency of 2191.90 cm⁻¹. The barriers calculated above indicate that the second CO₂ formation is not the rate determining step; instead, the first step with high barrier for CO₂ formation appears to be the rate limiting step. The energy profile diagram for CO oxidation on Au⁰/FAU is shown in Figure 6.1.1 and the geometrical parameters, energy barriers and vibrational frequencies are summarized in Table 6.1.2.



(a)

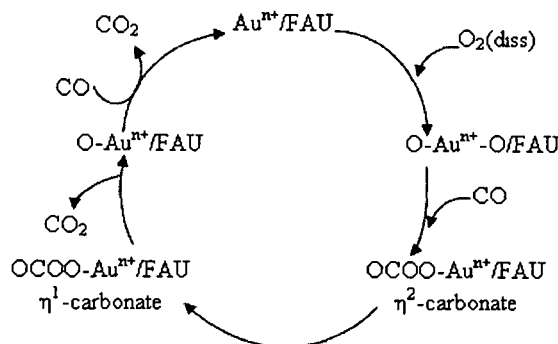


(b)

Figure 6.1.1: Energy profile diagram and the structures of the different species involved in the Eley-Rideal pathway with dissociated O_2 on Au^0/FAU .

- (b) Oxidation pathway on Au^+/FAU and Au^{3+}/FAU : η^1 -carbonate pathway:
 On the cationic systems viz. Au^+/FAU and Au^{3+}/FAU , this pathway involves the formation of a η^2 -carbonate species initially which then transforms

in to η^1 -carbonate subsequently. We identify this pathway as η^1 -carbonate pathway and involve the following steps:

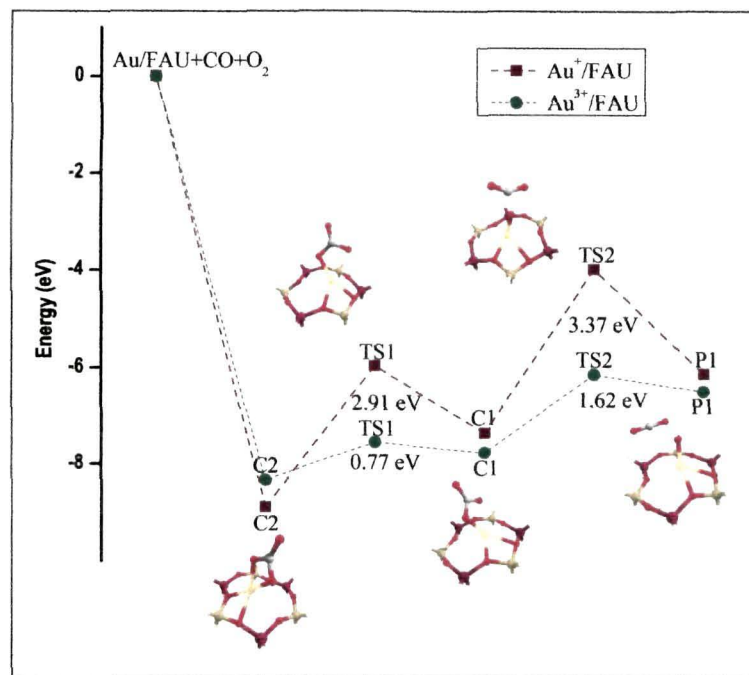


The first step entails the formation of a η^2 -carbonate species (C2) resulting from insertion of the gas phase CO molecule in to the activated O-O bond of O₂ adsorbed on Au⁺/FAU and Au³⁺/FAU. It is necessary to keep in mind while considering the dissociative mode of O₂ adsorption that it reverts to the bridge mode in the cationic systems. This carbonate species is bonded to the Au centre via two oxygen atoms and hence is denoted as η^2 -carbonate species. Interaction of the metal centre with the zeolite framework is given by the Au-O_z bond with a distance of 2.08 Å in Au⁺/FAU. The C2 species transforms in to a η^1 -carbonate species (C1) as one of the Au-O bonds elongates such that the carbonate entity now has a single Au-O linkage. The formation of C1 involves a high barrier of 2.91 eV indicated by TS1 in Au⁺/FAU while much lower (0.71 eV) in Au³⁺/FAU. The single negative vibrational frequencies appear at -349.98 cm⁻¹ and -137.08 cm⁻¹ in Au⁺/FAU and Au³⁺/FAU, respectively. However, in both the systems the formation of η^1 -carbonate is endothermic which is implicit of the fact that the η^2 -carbonate species with double Au-O linkage is preferred over the η^1 -carbonate counterpart. The double Au-O linkage provides additional stabilization to the η^2 -carbonate intermediate. Similar conclusions have been made by Liu et al. [364] where the OCOO intermediate with double Au-O linkage on Au₃ triangular sites are more stable than intermediate with a single Au-O linkage. Table 6.1.3 lists the geometrical parameters of the different species involved in the CO oxidation pathway on Au³⁺/FAU. Subsequent to

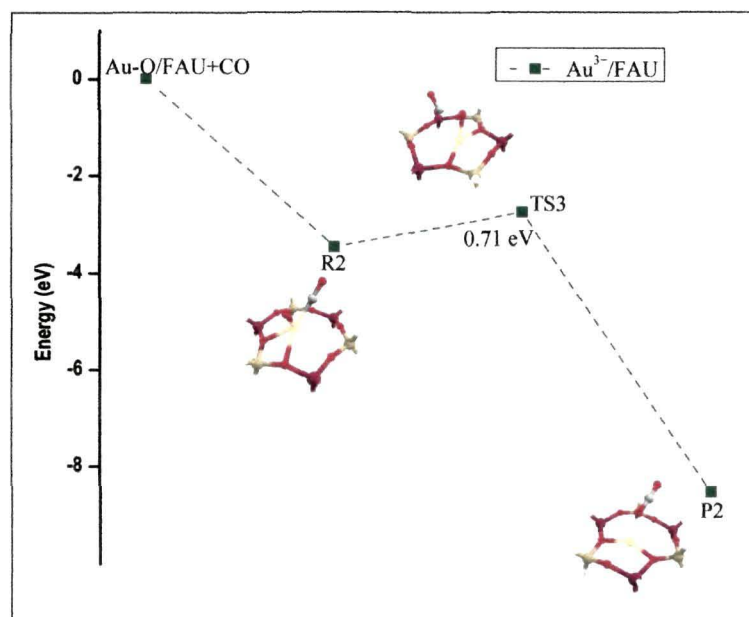
the formation of the C1 intermediate, the more labile C-O bond breaks via energy barrier (TS2) of 3.37 eV and 1.72 eV in Au⁺/FAU and Au³⁺/FAU, respectively resulting in a free CO₂ molecule and an atomic O adsorbed on the faujasite supported Au atom. The single negative vibrational frequency appears at -659.64 cm⁻¹ and -433.45 cm⁻¹ in Au⁺/FAU and Au³⁺/FAU, respectively. Formation of the first CO₂ from η¹-carbonate species is thus, the rate limiting step in Au³⁺/FAU. The energy gain during the reaction will assist in overcoming the barrier in Au³⁺/FAU however, the barriers for both the steps in Au⁺/FAU are much higher and thereby prohibiting any catalytic activity towards CO oxidation. The second incoming CO molecule reacts off the adsorbed atomic O to form the second CO₂ molecule, thereby closing the catalytic cycle (Eley-Rideal mechanism).

Table 6.1.3: Computed geometrical parameters (Å), barriers values (eV) and the imaginary frequency (cm⁻¹) for transition states in the Eley-Rideal (η¹-carbonate) pathway with dissociated O₂ on Au³⁺/FAU.

	Au-O _z	Au-O	O-C	O-C (CO)	O-C-O	ΔE	-ve freq
C2	2.34	2.00, 2.09	1.38, 1.37	1.21			
TS1	2.38	2.02, 2.58	1.37, 1.31	1.25		0.77	-137.08
C1	2.18	1.99	1.38, 1.30	1.24			
TS2	2.26	1.95	1.69	1.25, 1.19	153.2°	1.62	-433.57
P1	2.29	1.89	-	1.20, 1.18	179.3°		
R	2.37	2.01	2.40	1.15			
TS3	2.05	1.98	2.00	1.16	116.0°	0.71	-412.21
P2	2.06	-	-	1.18, 1.19	176.7°		



(a)



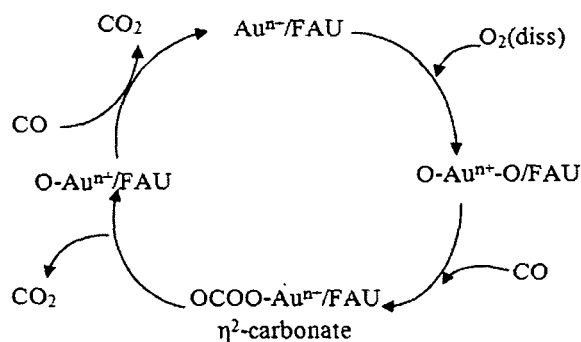
(b)

Figure 6.1.2: Energy profile diagram and the structures of the different species involved in the Eley-Rideal (η^1 -carbonate) pathway with dissociated O_2 on cationic systems.

The calculated activation energy barrier (TS3) for this final step is observed to be 0.71eV in Au^{3+}/FAU . The transition state is characterized with the single negative vibrational frequency at -412.21 cm^{-1} . This last reaction step

in general, does not entail high reaction barrier and is not the rate limiting step which is consistent with earlier reports. The energy profile diagram for CO oxidation on the cationic systems via the η^1 -carbonate pathway and the structures of the different species involved in the reaction on $\text{Au}^{3+}/\text{FAU}$ are shown in Figure 6.1.2. The structures of the intermediates, transition states and products formed in Au^+/FAU and the various geometrical parameters are given in Appendix D.

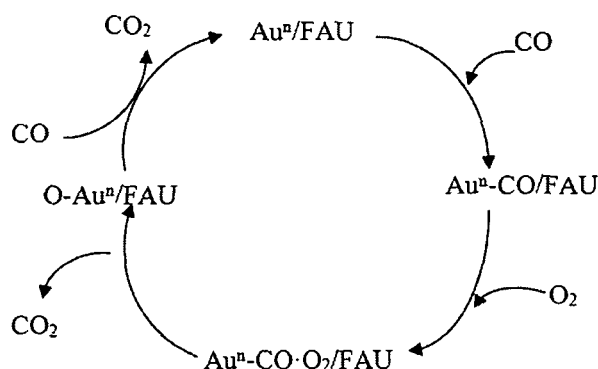
η^2 -carbonate pathway: It is also probable that the reaction can proceed directly from the initially formed η^2 -carbonate species without transforming to the η^1 -carbonate species. We identify this as the η^2 -carbonate pathway and involve the following steps:



Initially, a η^2 -carbonate species (C2) results from insertion of the CO molecule into the activated O-O bond and is attached to the Au centre via two O atoms i.e. two Au-O linkages. The product CO_2 (P1) is obtained from C2 via the activation barrier, TS1 and the calculated energy barrier is significantly higher (3.53 eV and 2.86 eV for Au^+/FAU and $\text{Au}^{3+}/\text{FAU}$, respectively) for both the cationic Au systems which implicate that the η^2 -carbonate pathway is not a favourable route for CO oxidation. We thus, rule out the possibility of the existence of this pathway for CO oxidation. The energy profile diagram for the η^2 -carbonate pathway and the geometrical parameters are given in Appendix D.

6.1.3.3 CO oxidation reaction energy profile with gas phase O₂

Experimental reports [218] have assigned the appearance of a 2169 cm⁻¹ band in the IR spectrum to CO bonded gold in the presence of CO + O₂ leading to the replacement of the CH₃ ligand by CO. This is implicit of the fact that the reaction involves the CO chemisorbed Au species and gas phase O₂ (from the CO + O₂ gas mixture) corresponding to the Eley-Rideal mechanism. The steps involved in the mechanism can be represented as given below. The first step in both the neutral

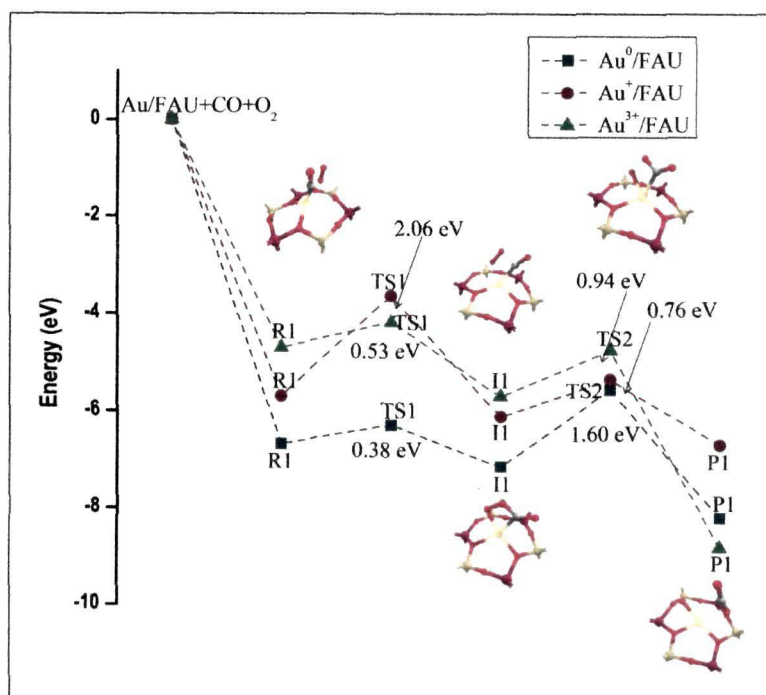


and cationic systems involves the formation of a species, R1 where CO is adsorbed on the faujasite supported Au centre while O₂ barely exhibits any interaction with Au. Activation of the O-O bond of O₂ in Au⁰/FAU ($d_{\text{O-O}}$: 1.38Å) can be correlated with the presence of a weak interaction between CO and O₂ ($d_{\text{C-O}}$: 1.74Å). However, no such activation is observed in the cationic systems. The HOMO-1 orbital of the R1 entity shown in Appendix D is clearly indicative of the absence of any interaction between CO and O₂ in the cationic systems while overlap of p orbitals centred on O₂ and CO account for the weak interaction in the neutral counterpart. In the next step, CO and O₂ move closer to form an OCOO intermediate (I1) after crossing the first energy barrier, TS1 in the three oxidation states. Au⁺/FAU entails a high barrier of 2.06 eV, thereby reducing its chances to act as a catalyst for the reaction while Au⁰ and Au³⁺ involve lower barriers; 0.38 and 0.53 eV, respectively. The imaginary frequencies associated with the transition states and the geometrical parameters for the various species involved in the reaction on Au³⁺/FAU are summarized in Table 6.1.4. In the vicinity of the transition state TS1, the O-O bond length expands uniformly to a value close to peroxide bond length with a concomitant decrease in the distance between

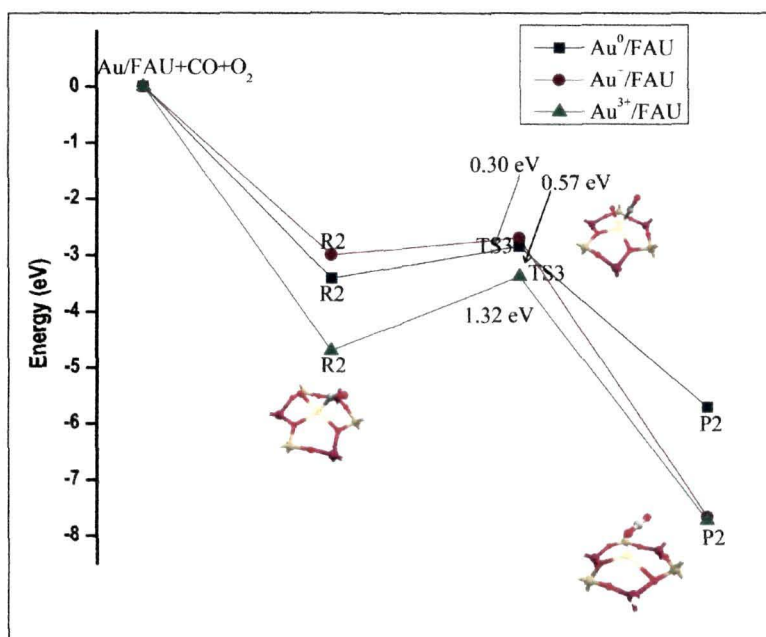
CO and O₂. In the four-centre intermediate I1 this distance further decrease to below 1.60 Å which implies that a moderate interaction now exists between CO and O₂. The intermediate I1 interacts with the metal centre via two bonds viz. Au-C and Au-O, thus accounting for its enhanced stabilization compared to R1. Further elongation of the O-O bond from the peroxide bond length to ~1.6Å in the cationic systems indicates that the bond is now more labile for dissociation. This is reflected from the energy barrier values (TS2) involved in the formation of CO₂. In the vicinity of TS2, the O-O bond dissociates resulting in the formation of a partly-formed CO₂ while one O atom is attached to the Au centre. As a consequence of the formation of a new bond between C atom of CO and O atom of O₂, the C-O bond length increases to ~1.20Å in TS2. This implies that the C-O bond formation causes two structural modifications: O-O bond dissociation and expansion of C≡O bond. The highest TS2 barrier value (1.60 eV) is observed in Au⁰/FAU which can be attributed to the less propensity of the O-O bond to dissociate as compared to the cationic counterparts. The reaction further proceeds to release the first CO₂ (P1) and leaving behind one O atom attached to the Au centre.

Table 6.1.4: Computed geometrical parameters (Å), barriers values (eV) and the imaginary frequency (cm⁻¹) for transition states in the Eley-Rideal pathway with gas phase O₂ on Au³⁺/FAU.

	Au-O ₂	Au-C	Au-O	O-O (O ₂)	O-C	O-C (CO)	O-C-O	ΔE	-ve freq
R1	2.16	2.06	2.28	1.29	2.44	1.15			
TS1	2.15	2.00	2.31	1.38	1.93	1.17		0.53	-392.36
I1	2.24	2.26	2.11	1.59	1.59	1.19			
TS2	2.2	2.07	2.26	1.67	1.35	1.2	132.09°	0.94	-319.31
P1	2.14	-	2.09	-	1.18	1.19	173.95°		
R2	2.15	2.24	2.08	-	-	1.15			
TS3	2.18	2.03	1.96	-	2.14	1.15	124.38°	1.32	-414.86
P2	2.24	-	-	-	1.19	1.19	177.93°		



(a)



(b)

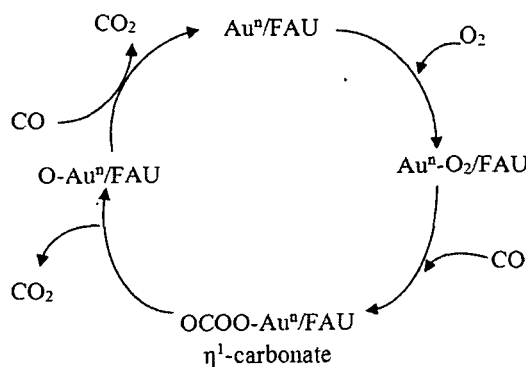
Figure 6.1.3: Energy profile diagram for the Eley-Rideal pathway with gas phase O_2 on Au^n/FAU ($n=0, +1$ and $+3$) and the structures of the different species involved in Au^{3+}/FAU .

The second half of the reaction proceeds when the second CO molecule attaches to $Au^n - O/FAU$ ($n=0, +1$ and $+3$) resulting in a reactant, R2 where no

interaction between O atom and CO is observed. Further, in TS3, O and CO interact weakly; this is evident from the decreasing separation ($\sim 2\text{\AA}$) between them. The highest barrier involved in the formation of the second CO_2 (TS3) is observed in $\text{Au}^{3+}/\text{FAU}$ among the three oxidation states. However, the energy gain during the various steps of the oxidation process will assist in overcoming the barrier. It is observed that the complete oxidation reaction is below the entrance channel which reflects exothermicity of the reaction on all the three Au oxidation systems. The energy profile for this reaction pathway on all the three Au systems are shown in Figure 6.1.3. The structures of the different species and the various geometrical parameters for Au^0/FAU and Au^+/FAU are given in Appendix D.

6.1.3.4 CO oxidation reaction energy profile with gas phase CO

In addition to the mechanisms discussed above, we have also considered another pathway where the reactants CO and O_2 have intermediate interaction energies. The various steps involved in this pathway with CO in the gas phase and O_2 adsorbed on faujasite supported Au monomer can be represented as:

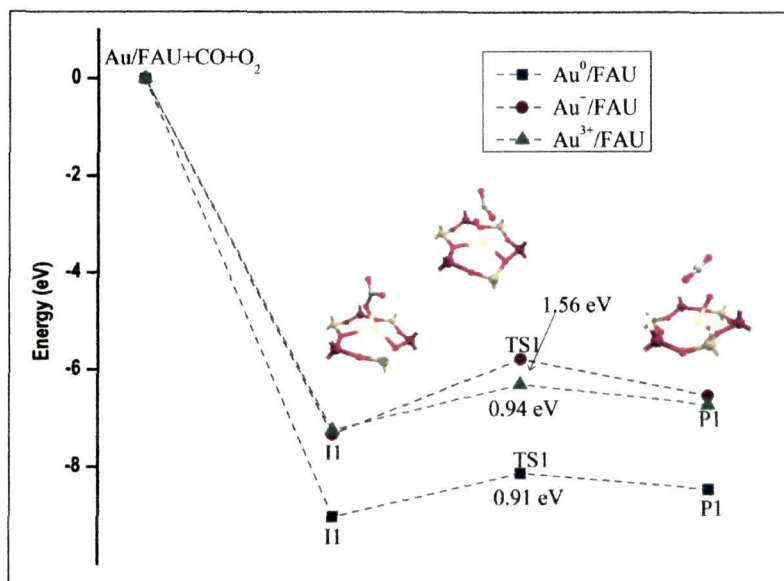


The first step involves the exothermic formation of a η^1 -carbonate (I1) species in the three supported systems resulting from O_2 adsorbed in the top mode and CO reacting from the gas phase. The formation of I1 can be viewed as the insertion of the gas phase CO molecule into the O_2 molecule. The carbonate moiety is attached to the Au centre via one Au-O linkage with distance $\sim 2.06\text{\AA}$ and hence designated as η^1 -carbonate. The first CO_2 (P1) can be obtained from I1 via crossing the energy barrier TS1. The high energy barrier (1.56 eV) in Au^+/FAU will limit its catalytic activity. On the other hand, Au^0/FAU and $\text{Au}^{3+}/\text{FAU}$ have

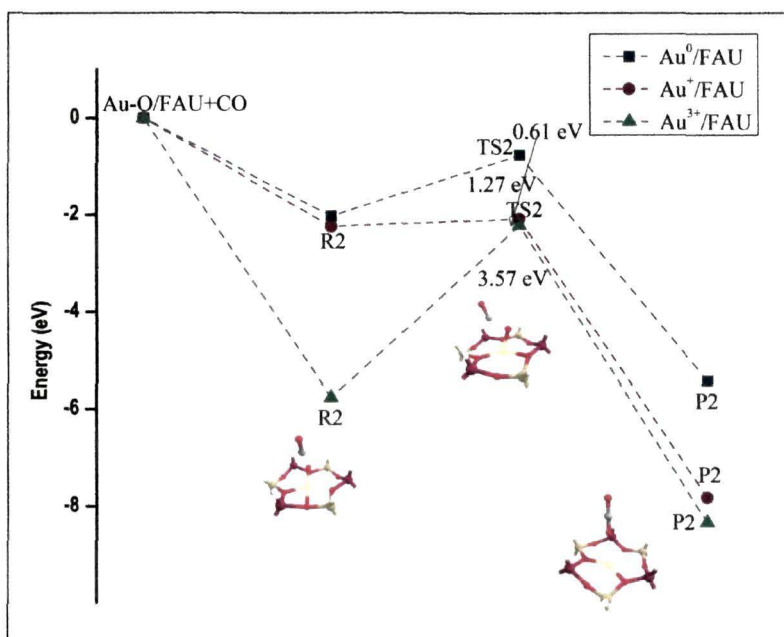
comparable barriers. In all the three cases, TS1 involves breaking of one of the C-O bonds so that a partly-formed CO₂ results and the dissociated O atom remains attached to the Au centre. Formation of the product, P1 is exothermic in all the systems and involves generation of one CO₂ molecule. The O atom that is left attached to the Au centre will be reacted off by another CO molecule so that the second CO₂ forms, thereby completing the full catalytic cycle. As the gas phase CO molecule approaches Auⁿ - O/FAU (n=0, +1 and +3), it results in a co-adsorbed species, R2 wherein no interaction is observed between the adsorbed O atom and the CO molecule. This R2 species then gives the second CO₂ molecule (P2) via crossing the energy barrier, TS2. Unlike in R2, a weak interaction appears between O and CO in TS2 which is evident from the decreasing O...CO to below 2.0Å. Contrary to the first oxidation step, high barrier value is observed in Au⁰/FAU and Au³⁺/FAU systems while Au⁺/FAU entails much lower barrier. Figure 6.1.4 shows the energy profile diagram for this pathway in all the three Au oxidation states and Table 6.1.5 summarizes the geometrical parameters and the single negative vibrational frequencies characterizing transition states in Au³⁺/FAU. The structures of the different species involved in the reaction on Au⁰/FAU and Au⁺/FAU and the various geometrical parameters are given in Appendix D.

Table 6.1.5: Computed geometrical parameters (Å), barriers values (eV) and the imaginary frequency (cm⁻¹) for transition states in the Eley-Rideal pathway with gas phase CO on Au³⁺/FAU.

	Au-O _z	Au-O	O-C	O-C (CO)	O-C-O	ΔE	-ve freq
I1	2.32	2.03	1.37, 1.29	1.25			
TS1	2.22	1.97	1.91, 1.24	1.20	153.59°	0.94	-563.62
P1	2.06	1.96	1.19	1.19	178.96°		
R	2.03	2.02	3.27	1.15			
TS2	2.09	1.98	2.02	1.16	119.40°	3.57	-397.76
P2	2.06	-	1.19	1.18	179.39°		



(a)



(b)

Figure 6.1.4: Energy profile diagram for the Eley-Rideal pathway with gas phase CO on Au^n/FAU ($n=0, +1$ and $+3$) and the structures of the different species involved in $\text{Au}^{3+}/\text{FAU}$.

6.1.4 Salient Observation

The present hybrid QM/MM study aims to investigate the preferential mechanistic pathway for CO oxidation on faujasite supported Au monomer in three oxidation

states viz. 0, +1 and +3. Different initial configurations containing CO and O₂ were considered to determine the interaction energies. The highest interaction energies were observed for O₂ adsorbed in the dissociative mode and a gas phase CO molecule, thereby, indicating this to be the most favourable initial configuration for CO oxidation. While, the configuration with CO adsorbed on the supported Au centre and O₂ in the gas phase yielded much lower interaction energies in all the oxidation states. A comparison of the energy barriers involved in the various pathways is given in Table 6.1.6.

Table 6.1.6: Comparison of the barriers involved in the different pathways for CO oxidation on Auⁿ/FAU (n=0, +1 and +3).

	Au ⁰ /FAU	Au ⁺ /FAU	Au ³⁺ /FAU
<i>Eley-Rideal</i> mechanism with dissociated O ₂ and gas phase CO			
C2 → C1	-	2.91	0.77
C1 → P1	1.10	3.37	1.62
R2 → P2	0.41	-	0.71
<i>Eley-Rideal</i> mechanism with gas phase O ₂ and adsorbed CO			
R1 → I1	0.38	2.06	0.53
I1 → P1	1.60	0.76	0.94
R2 → P2	0.57	0.30	1.32
<i>Eley-Rideal</i> mechanism with gas phase CO and adsorbed O ₂			
I1 → P1	0.91	1.56	0.94
R2 → P2	1.27	0.61	3.57

Our calculations indicate that high barriers are involved in the pathway initiating from the most favourable initial CO-O₂ configuration (*Eley-Rideal* mechanism with dissociated O₂) compared to the pathway with initial CO-O₂ containing configuration having moderate interaction energies. This implies that too strong interaction energy is energetically not appreciable for CO oxidation. The *Eley-Rideal* mechanism with CO adsorbed on the supported Au centre and O₂ in the gas phase is the preferred pathway. Among the three faujasite supported Au systems, Au³⁺/FAU exhibits better catalytic activity. Experiments on catalytic activity of NaY supported mononuclear Au complexes also indicated superior activity of Au^{III}

compared to Au^I and reduction of Au^{III} to Au^I resulted in decreasing catalytic activity [218]. It is necessary to keep in mind that we have considered a simple model of zeolite supported Au catalyst for CO oxidation. However, the conclusions drawn from this study may be inherent for understanding the catalytic activity of larger realistic catalytic system so as to apprehend the mechanism involved.

6.2 Water Gas Shift reaction on faujasite supported Au monomer

6.2.1 Introduction

The water gas shift reaction, WGS ($\text{CO} + \text{H}_2\text{O} \rightarrow \text{CO}_2 + \text{H}_2$) is crucial in providing clean hydrogen for fuel cell applications [226,227]. In order to overcome the innumerable drawbacks [228,229] suffered by the commercially available low-temperature heterogeneous WGS catalysts, designing catalysts with high activity and stability has been one of the central tenants in the field of catalytic research [232-236].

Excellent WGS catalyst resulting from Au supported on ceria [228,235-239], titania [242-244], ZrO_2 , Al_2O_3 etc. as well as mixed oxides [245-247] have been investigated using experimental and theoretical studies. Although the WGS reaction on different supported gold catalysts has been extensively studied, no definite consensus on the mechanism as well as the active gold site has been reached. The various factors affecting the WGS reaction on supported gold catalysts such as the effect of particle size, effect of the support, preparation method, active site [248,249], location of the gold species which is critical both in terms of stability and low temperature activity, detailed insight into the reaction mechanism [250] have been reviewed in detail.

Mohamed and Ichikawa [251] characterized a monodentate formate species on Au/H-mordenite and reaction was observed to be more facile when Au is encapsulated in the H-mordenite zeolite. They observed the highest activity towards WGS reaction was observed for Au supported on NaY among NaY, Na-mordenite, and Na-ZSM-5 [252]. Participation of the Au^+ and Au^0 dual site for WGS reaction when encapsulated inside NaY zeolite was suggested. Much higher concentration of water was found to decrease the catalytic activity because of the masking of the active sites.

Wang *et al.* [253] reported a density functional study on the WGS reaction promoted by neutral and charged gold dimer clusters. Dissociation of water into OH and H was identified as the rate determining step with a barrier of 45.53 kcal

mol⁻¹. They proposed that the charge of the cluster does affect the catalytic activity towards WGS reaction and on all the three clusters, irrespective of the charge state, the formate mechanism was feasible rather than the redox mechanism. From DFT calculations, Liu and Rodriguez [254] proposed higher activity of the Au and Cu nanoparticles than their parent bulk surfaces and the enhanced activity has been attributed to the low coordinated corner and edge sites in addition to the fluxionality of the particles. The associative carboxyl mechanism was found to be preferred pathway in the nanoparticles as well as in the Au surface. In all the systems, water dissociation remained the rate limiting step. DFT study on the catalytic activity of Au₃₈ cluster towards WGS reaction indicated better activity of this cluster when compared to Au(100) and Au₂₉ based on the lower barrier associated with the rate limiting water dissociation step (Au₃₈: 31.41 kcal mol⁻¹; Au(100): 35.28 kcal mol⁻¹ and Au₂₉: 32.05 kcal mol⁻¹). Desorption of H₂ was observed to occur more readily on the Au₃₈ cluster [255].

6.2.2 Computational Details

The calculations are performed using hybrid quantum mechanics/ molecular mechanics method, SIMOMM [314] (Surface Integrated Molecular Orbital Molecular Mechanics) which is implemented in the GAMESS [316] program. Details of this hybrid method have been described in Chapter 5 and the same zeolite model has been employed to study WGS reaction on faujasite supported Au monomer (Figure 5.1.1). The reaction is modelled within the chemically active quantum mechanical part which comprises of a six membered zeolite ring and the Au monomer. DFT based B3LYP functional [278,280,292], 6-31G(d, p) basis set [367] for Si, Al, O, C and H and LANL2DZ [308,309] basis set incorporating relativistic effective core potential for Au atom has been utilized for the quantum mechanical part while the MM3 parameter [368] is employed for the molecular mechanical part. The quadratic approximation method [369] implemented in GAMESS program was used in the geometry optimizations and transition state searches. The transition states are characterized with the presence of single negative vibrational frequency. The results for adsorption of CO and H₂O on faujasite supported Au monomer in three oxidation states viz. 0, +1 and +3 are presented in Chapter 5. In the

CO-H₂O co-adsorbed aggregates, binding energy is calculated using:

$$BE(B) = (E_{Au-A/FAU} + E_B) - (E_{Au-A,B/FAU}) \quad (6.2.1)$$

BE(B) is the binding energy of B (CO or H₂O) in the co-adsorbed aggregates, $E_{Au-A/FAU}$ is the energy of Au/FAU with a pre-adsorbed A molecule, E_B is the energy of free gas phase B molecule and $E_{Au-A,B/FAU}$ is the energy of the co-adsorbed aggregate. Favourable adsorption of B on Auⁿ/FAU (n=0, +1 and +3) in the presence of pre-adsorbed A is indicated by positive binding energy value.

6.2.3 Results and Discussion

6.2.3.1 Adsorption of CO and H₂O on faujasite supported Au monomer

The results for adsorption of CO and H₂O on faujasite supported neutral and cationic Au monomer has been summarized in Chapter 5. Here, we consider the co-adsorption of CO and H₂O on Auⁿ/FAU (n=0, +1 and +3) and the following two co-adsorption aggregates can be appraised:

- i. CO adsorbed on H₂O pre-adsorbed Auⁿ/FAU (n=0, +1 and +3) [R1⁰, R1⁺, R1³⁺]
- ii. H₂O adsorbed on CO pre-adsorbed Auⁿ/FAU (n=0, +1 and +3) [R1⁰, R1⁺, R1³⁺].

The adsorption of CO in presence of pre-adsorbed H₂O on Auⁿ/FAU (n=0, +1 and +3) has been discussed in Chapter 5. The optimized structures (designated as R1⁰, R1⁺, R1³⁺ here) are given in Figure 5.2.3. The computed selected geometrical parameters and the CO binding energy in presence of pre-adsorbed H₂O on Auⁿ/FAU (n=0, +1 and +3) are summarized in Table 5.2.3.

Our calculations indicate that the adsorption of H₂O in presence of pre-adsorbed CO is accompanied by negative binding energy in Au⁰/FAU and Au³⁺/FAU, thereby rendering this co-adsorbed configuration unfavourable. Adsorption of H₂O results in the cleavage of Au-CO bond in these oxidation states. However, on Au⁺/FAU, the adsorption of H₂O is favourable, albeit with low binding energy. Table 6.2.1 summarizes the geometrical parameters and the binding energy of H₂O

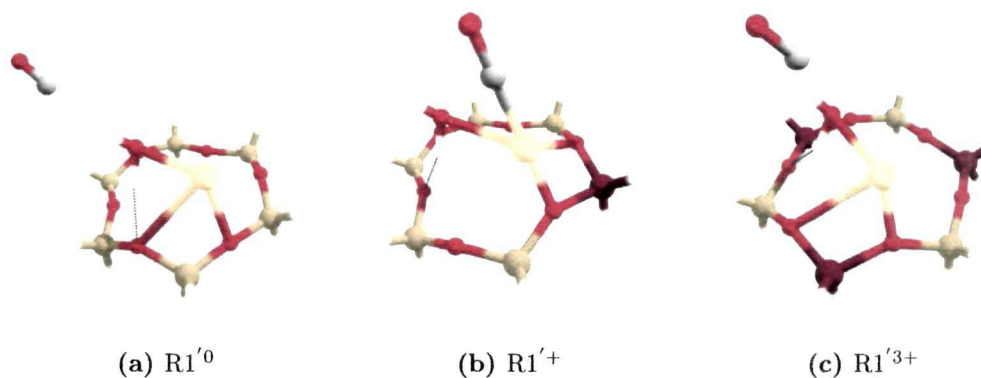


Figure 6.2.1: Optimized structures of H₂O adsorbed on CO pre-adsorbed Auⁿ/FAU (n=0, +1 and +3).

in presence of pre-adsorbed CO and the optimized structures of the co-adsorbed structures are given in Figure 6.2.1. The high binding energies calculated for CO on Auⁿ/FAU (n=0, +1 and +3) in presence of pre-adsorbed H₂O (R1) indicate it to be the preferred configuration over adsorption of H₂O on CO pre-adsorbed Auⁿ/FAU (n=0, +1 and +3) (R1′). In the subsequent sections, we discuss the water gas shift reaction on Auⁿ/FAU (n=0, +1 and +3) with the more favourable CO-H₂O co-adsorbed configuration.

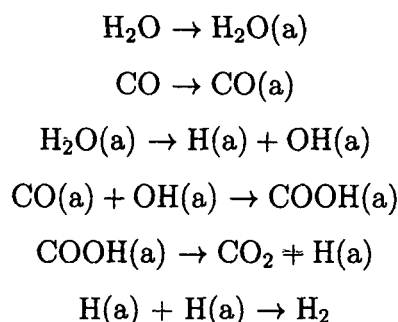
Table 6.2.1: Computed geometrical parameters and the binding energy of water in the CO pre-adsorbed Auⁿ/FAU (n=0, +1 and +3) (R1′).

	Au-O _z	C-O	Au-C(CO)	Au-O(H ₂ O)	C(CO)..O(H ₂ O)	H(H ₂ O)...O _z	H...OH	BE
Au ⁰	2.29	1.15	-	2.32	3.11	2.05	0.98	-0.18
Au ⁺	2.01	1.16	1.91	2.72	2.40	1.94	0.97	0.29
Au ³⁺	2.05	1.15	-	2.65	2.98	2.19	0.98	-1.59

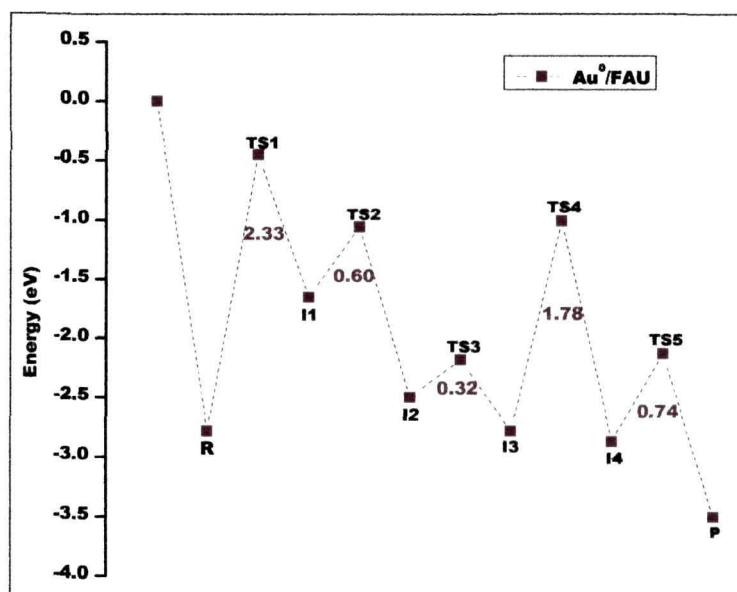
6.2.3.2 Water gas shift reaction on Au⁰/FAU

We first consider the water gas shift reaction on faujasite supported neutral Au monomer. The energy profile diagram along with the structures of the intermediates and transition states is shown in Figure 6.2.2. The geometrical parameters, energy barriers and the single negative vibrational frequency characterizing tran-

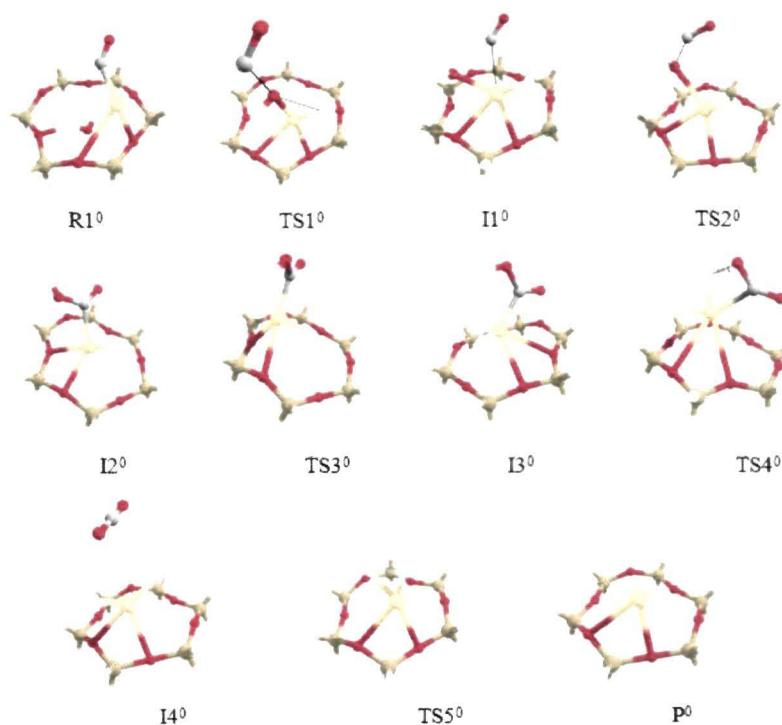
sition states are summarized in Table 6.2.2. The steps involved in the reaction can be outlined as:



The reaction commences with the more preferable co-adsorbed structure resulting from CO adsorption on H₂O pre-adsorbed Au⁰/FAU (R1⁰). The next step involves rupture of one O-H bond of H₂O to form an intermediate I1⁰ such that it contains CO, H and OH. This endothermic step of O-H bond rupture involves a high energy barrier (TS1⁰) of 2.33 eV and unlike in R1⁰, the Au-CO bond elongates substantially while two new bonds Au-OH and Au-H emerges in TS1⁰. The single negative vibrational frequency of TS1⁰ appears at -151.46 cm⁻¹. In I1⁰, formation of Au-OH and Au-H bonds is accompanied by the scission of Au-CO bond. Following this, CO and OH recombine to form a *cis*-COOH intermediate (I2⁰) via an energy barrier (TS2⁰) of 0.60 eV. TS2⁰ is characterized with a single negative vibrational frequency at -530.13 cm⁻¹ and involves a moderate interaction between OH and CO as recognized from the decreasing distance to 1.74 Å. The *cis*-COOH intermediate (I2⁰) is attached to the metal centre via the C atom which is reflected from the overlap of the d-orbital centred on Au and p-orbital of C as illustrated in the frontier molecular orbital (HOMO) shown in Figure 6.2.3. The *cis*-COOH intermediate then isomerizes to the more stable *trans*-COOH intermediate (I3⁰) such that the O-H bond is now directed towards the metal centre and involves a barrier of 0.32 eV (TS3⁰). Subsequently, the O-H bond elongates to 1.60 Å with a concomitant decrease in the OC··OH bond length to 1.29 Å in the transition state, TS4⁰, involved in the formation of CO₂ from the *trans*-COOH intermediate. This barrier is calculated to be 1.78 eV and the single negative vibrational frequency appears at -1042.71 cm⁻¹. Further, the O-H bond dissociates resulting in the exothermic formation of CO₂ (I4⁰) and two H atoms attached to the Au metal centre. In the last step, these H atoms recombine to form H₂ (P⁰)



(a) Energy profile diagram for water-gas shift reaction on faujasite supported neutral Au monomer.



(b) Structures of various intermediates and transition states observed during the reaction on Au^0/FAU .

Figure 6.2.2: Energy profile diagram and the structures of various intermediates and transition states observed during the water-gas shift reaction on Au^0/FAU .

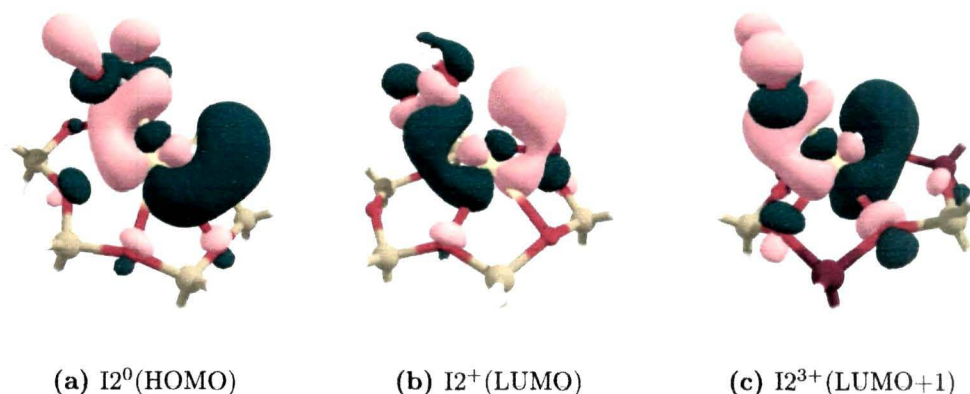


Figure 6.2.3: Frontier molecular orbitals illustrating interaction between the Au centre and C atom in the *cis*-COOH intermediate ($I2^{0,+ ,3+}$).

and the barrier involved ($TS5^0$) is calculated to be 0.74 eV. $TS5^0$ is characterized by the single negative vibrational frequency that appears at -1285.54 cm^{-1} corresponding to the appearance of a modest interaction between the H atoms. This last reaction step is highly exothermic which implies stable formation of H_2 and thereby regenerating the supported metal atom. It is apparent from the energy profile diagram that the overall reaction is exothermic on Au^0/FAU and the rate limiting step is the dissociation of water which is however, endothermic in nature.

6.2.3.3 Water gas shift reaction on Au^+/FAU and Au^{3+}/FAU

We first present the results for the reactivity of Au^+/FAU towards water gas shift reaction. As suggested above, the more favourable H_2O -CO co-adsorbed structure ($R1^+$) has been considered for studying the water gas shift reaction. Our calculations indicate the presence of a barrier ($TS1^+$) as high as 3.71 eV involved in the dissociation of H_2O into H and OH. The H-OH bond of H_2O elongates to 1.79 \AA in $TS1^+$ and the single negative vibrational frequency appears at -863.95 cm^{-1} . The intermediate $I1^+$ containing CO, OH and H species is much less stable than $R1^+$ which accounts for the observed endothermicity associated with its formation. Further, a weak interaction develops between OH and CO as reflected from the decreasing distance to 1.77 \AA in $TS2^+$ and further to 1.39 \AA in $I2^+$ which results in the recombination of CO and OH to form a *cis*-COOH intermediate. Formation of $I2^+$ involves a barrier of 1.94 eV ($TS2^+$), is the only

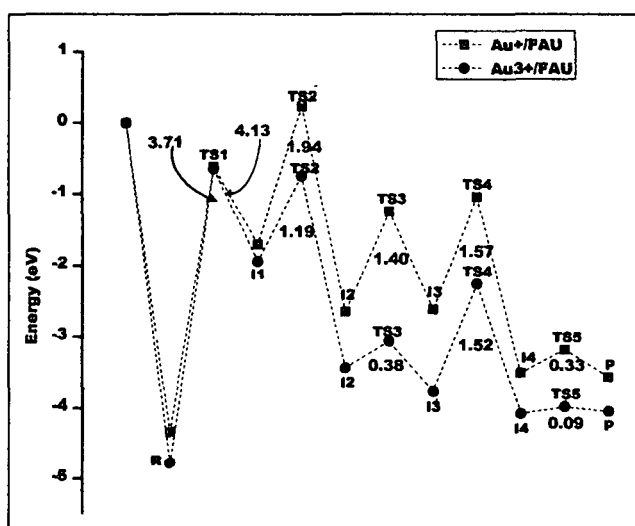
step with energy above the entrance channel and thus, is the rate limiting step. Interaction of Au with the C atom in the *cis*-COOH intermediate is depicted by the overlap of d-orbital centred on Au and p-orbital of C as shown in Figure 6.2.3. In the subsequent steps, *cis*-COOH isomerizes to the *trans*-COOH (I3⁺) via an energy barrier of 1.40 eV (TS3⁺). The transition state, TS4⁺ involved in the formation of CO₂ (I4⁺) from I3⁺ is associated with structural modifications such that the OC···OH bond length reduces with a concomitant elongation of the O-H bond to 1.31 Å. As a consequence of this O-H bond elongation, the H atom is now simultaneously bonded to the O atom and the Au centre also reflected from the decreasing Au···H distance to 1.71 Å. It can be thus said that, TS4⁺ involves a partially formed CO₂ and the single negative vibrational frequency appears at -1668.03 cm⁻¹. This barrier associated with the formation of CO₂ is calculated to be 1.57 eV. With the formation of CO₂, two H atoms are now attached to the metal centre which are however, separated by large distance indicating lack of interaction between them. In the next step, this distance reduces to 1.20 Å in TS5⁺ implying that a moderate interaction develops between them and the barrier involved in the formation of H₂ is calculated to be 0.33 eV. The overall reaction on Au⁺/FAU is endothermic as apparent from the energy profile diagram depicted in Figure 6.2.4. The geometrical parameters, energy barriers involved in the different steps and the negative vibrational frequencies associated with the transition states are summarized in Table 6.2.3.

On Au³⁺/FAU, the first step i.e the dissociation of H₂O into OH and H (I1³⁺) from the H₂O-CO co-adsorbed structure (R1³⁺) involves still higher barrier (4.13 eV) and is endothermic. In the transition state, TS1³⁺, the Au-CO bond ruptures while Au-OH and Au-H appears and the single negative vibrational frequency appears at -123.33 cm⁻¹. Further, the distance between OH and CO decreases to 1.56 Å which implies that a modest interaction develops in TS2³⁺. This barrier involved in the formation of *cis*-COOH intermediate (I2³⁺) is calculated to be 1.19 eV and the single negative vibrational frequency appears at -500.27 cm⁻¹. The CO···OH distance decreases further to 1.36 Å such that CO and OH recombine to form a *cis*-COOH intermediate. However, unlike in Au⁺/FAU, this step of COOH formation from I1³⁺ is below the entrance channel and is exothermic which

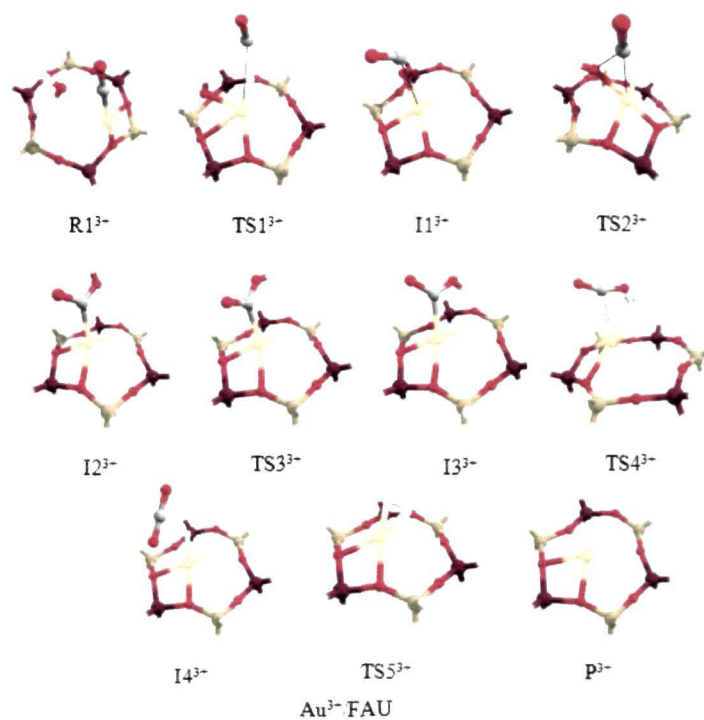
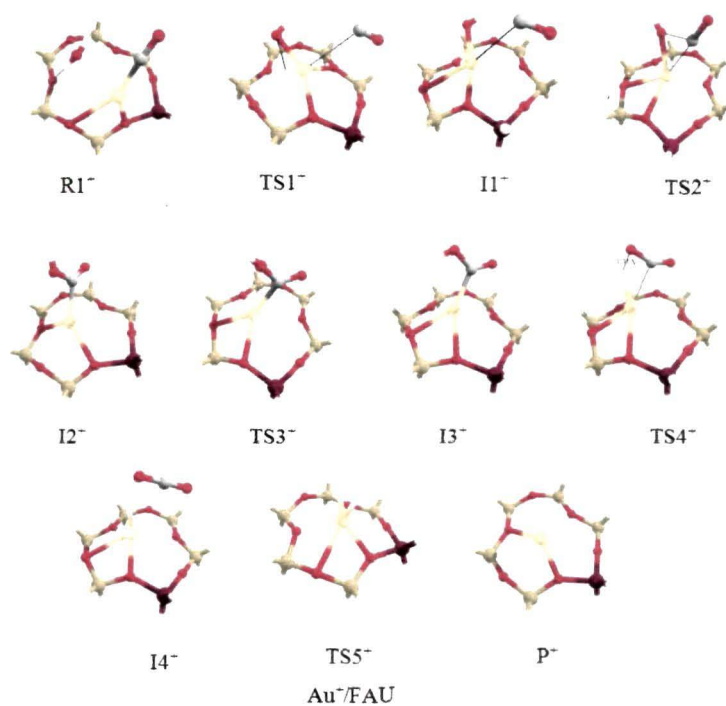
Table 6.2.2: Computed geometrical parameters (Å), energy barriers (eV) and the imaginary frequency (cm^{-1}) associated with the transition states in the various steps of the water gas shift reaction on Au^0/FAU .

	Au-O _z	Au-C	Au-OH	Au-H	C-O	OC··OH	H··OH	H-H	ΔE	-ve freq
R1 ⁰	2.85	2.10	-	-	1.17	-	0.98	-		
TS1 ⁰	2.43	4.43	2.27	1.61	1.16	-	2.5	-	2.33	-151.46
I1 ⁰	2.87	3.24	2.03	1.6	1.16	-	-	-		
TS2 ⁰	2.69	-	2.28	1.58	1.18	1.74	-	-	0.6	-530.13
I2 ⁰	2.62	2.14	-	1.64	1.22	1.4	-	-		
TS3 ⁰	2.78	1.99	-	1.69	1.21	1.37	-	-	0.32	-116.75
I3 ⁰	2.88	2.08	-	1.64	1.22	1.38	-	-		
TS4 ⁰	3.24	2.18	-	1.62	1.22	1.29	-	-	1.78	-1042.71
I4 ⁰	2.96	-	-	1.63,1.64	1.19	-	-	2.81		
TS5 ⁰	2.94	-	-	1.57,2.03	-	-	-	1.45	0.74	-1285.54
P ⁰	2.90	-	-	-	-	-	-	0.74		

indicates that the *cis*-COOH intermediate is more stable than the intermediate $I1^{3+}$. The interaction of Au with the C atom of COOH intermediate is depicted by the overlap of the Au-d-orbital and C-p-orbital as illustrated in Figure 6.2.3. Isomerisation of $I2^{3+}$ to *trans*-COOH ($I3^{3+}$) intermediate entails a barrier of 0.38 eV ($TS3^{3+}$) and the negative frequency appears at -216.80 cm^{-1} . The O-H bond elongates to 1.21 \AA while the Au-H distance decreases to 1.89 \AA in the transition state, $TS4^{3+}$ observed in the formation of CO_2 ($I4^{3+}$) from $I3^{3+}$. The $CO \cdots OH$ distance decreases to 1.27 \AA and the O-C-O angle is observed to 156.81° which represents a partially formed CO_2 . The barrier involved is calculated to be 1.52 eV and single negative frequency appears at -1627.16 cm^{-1} . With the formation of CO_2 ($I4^{3+}$), two H atoms are now attached to the Au centre and the distance between them is 1.93 \AA which indicates lack of any interaction between them. The distance however, reduces to 1.12 \AA implying appearance of interaction between the H atoms in $TS5^{3+}$ and the single negative vibrational frequency appears at -861.79 cm^{-1} . This barrier involved in the formation of H_2 is calculated to be 0.09 eV. The overall reaction is endothermic as reflected from the energy profile diagram shown in Figure 6.2.4. Table 6.2.4 summarizes the geometrical parameters, energy barriers involved in the different steps and the negative vibrational frequencies associated with the transition states.



(a) Energy profile diagram for water-gas shift reaction on faujasite supported cationic Au systems.



(b) Structures of various intermediates and transition states observed during the reaction on Au⁺/FAU and Au³⁺/FAU.

Figure 6.2.4: Energy profile diagram and the structures of various intermediates and transition states observed during the water-gas shift reaction on Au⁺/FAU and Au³⁺/FAU.

6.2.4 Salient Observation

Hybrid quantum mechanics/molecular mechanics calculations have carried out to investigate the activity of faujasite supported neutral and cationic Au monomer towards water-gas shift reaction. It has been observed that CO adsorption on Au^n/FAU ($n=0, +1$ and $+3$) in presence of pre-adsorbed H_2O is more favourable than the adsorption of H_2O on Au^n/FAU ($n=0, +1$ and $+3$) in presence of pre-adsorbed CO and thus, has been appraised as the starting configuration for investigating the reaction mechanism. The reaction mechanism involves the formation of a carboxyl intermediate in all the oxidation states from the recombination of CO and OH. However, carboxyl formation step is above the entrance channel in Au^+/FAU and is thus, the rate limiting step. The overall reaction is found to be endothermic in both the cationic systems while is exothermic in Au^0/FAU . Comparing the activity of the three Au monomer species, it is observed that neutral Au exhibits better catalytic activity towards water-gas shift reaction. The dissociation of H_2O into OH and H is the rate limiting step in Au^0/FAU . Substantially high barriers associated with the cationic systems and endothermicity of the reaction will limit their catalytic activity. However, reducing the water dissociation barrier observed in the neutral monomer will improve the catalytic activity further.

It seems from the present calculations that faujasite supported Au monomer posses the better potential to act as a catalyst for CO oxidation whereas significantly high barrier involved in water dissociation will inhibit its catalytic activity towards water gas shift reaction. The conclusions drawn from this study with a simple model of zeolite supported Au catalyst may be inherent for understanding the catalytic activity of larger realistic catalytic system so as to apprehend the mechanism involved. Further, designing improved catalysts with enhanced potential for water gas shift reaction will open up a new dimension for water gas shift reaction catalysts.

Table 6.2.3: Computed geometrical parameters (Å), energy barriers (eV) and the imaginary frequency (cm^{-1}) associated with the transition states in the various steps of the water gas shift reaction on Au^+/FAU .

	Au-O _z	Au-C	Au-OH	Au-H	C-O	OC··OH	H··OH	H-H	ΔE	-ve freq
R1 ⁺	2.08	1.96	-	-	1.16	-	0.99	-		
TS1 ⁺	2.35	3.04	2.10	1.54	1.16	-	1.79	-	3.71	-863.95
I1 ⁺	2.07	3.56	2.03	1.53	1.16	-	-	-		
TS2 ⁺	2.57	2.50	2.25	1.52	1.18	1.77	-		1.94	-529.55
I2 ⁺	2.51	2.04	-	1.56	1.21	1.39	-	-		
TS3 ⁺	2.43	2.05	-	1.55	1.21	1.34	-	-	1.40	-1196.3
I3 ⁺	2.54	2.06	-	1.57	1.21	1.36	-	-		
TS4 ⁺	2.46	2.46	-	1.61	1.18	1.28	-	-	1.57	-1668.03
I4 ⁺	2.23	-	-	1.55,156	1.19	-	-	2.41		
TS5 ⁺	2.28	-	-	1.62	-	-	-	1.20	0.33	-965.11
P ⁺	2.28	-	-	1.80	-	-	-	0.85		

Table 6.2.4: Computed geometrical parameters (Å), energy barriers (eV) and the imaginary frequency (cm^{-1}) associated with the transition states in the various steps of the water gas shift reaction on $\text{Au}^{3+}/\text{FAU}$.

	Au-O _z	Au-C	Au-OH	Au-H	C-O	OC··OH	H··OH	H-H	ΔE	-ve freq
R1 ³⁺	2.02	1.91	-	-	1.16	-	0.99	-		
TS1 ³⁺	2.33	3.46	1.99	1.55	1.15	-	2.29	-	4.13	-123.33
I1 ³⁺	1.22	3.37	1.94	1.53	1.15	-	-	-		
TS2 ³⁺	2.13	2.65	2.2	1.54	1.19	1.56	-	-	1.19	-500.27
I2 ³⁺	2.31	2.02	-	1.56	1.23	1.36	-	-		
TS3 ³⁺	2.33	2.04	-	1.57	1.22	1.36	-	-	0.38	-216.8
I3 ³⁺	2.32	2.05	-	1.58	1.21	1.34	-	-		
TS4 ³⁺	2.33	2.53	-	1.57	1.18	1.27	1.21	-	1.52	-1627.16
I4 ³⁺	2.25	-	-	1.55,1.56	1.19	-	-	1.93		
TS5 ³⁺	2.28	-	-	1.65,1.63	-	-	-	1.12	0.09	-861.79
P ³⁺	2.34			1.76,1.78	-	-	-	0.84		

Chapter 7

Conclusions and Future Scopes

Conclusions

The work presented in this thesis aims at: first, to investigate the structure, electronic and reactivity properties of hydrogenated gold clusters and the phenomenon of reverse hydrogen spillover on zeolite supported Pd₆ and Au₆ clusters; second, to study the adsorption of carbon monoxide and oxygen on gas phase gold cluster and carbon monoxide oxidation on neutral and charged gold clusters; third, to study the adsorption of carbon monoxide and oxygen on zeolite supported gold monomer in three oxidation states and to incorporate the effect of pre-adsorbed water on their adsorption; fourth, to investigate the activity of zeolite supported gold monomer in three oxidation states towards carbon monoxide oxidation and water gas shift reaction. Density functional theory (DFT) has been employed to carry out the calculations. The calculations associated with gas phase gold clusters as well as the phenomenon of reverse hydrogen spillover has been performed with the help of DMol³ program while hybrid QM/MM method, SIMOMM implemented in GAMESS program has been used to study zeolite supported gold clusters. Gaussian 09 program has been used for natural bond orbital (NBO) analysis.

At the outset of this work, we present a general definition of clusters, their properties and classification based on nature of constituents and the type of bonding. Special emphasis has been laid on gold clusters and their structures in various

size regimes studied by different groups have been discussed. The unique properties of gold such as aurophilic interaction and relativistic effect have been also considered. Bulk gold is a noble metal however, its unusual and unanticipated catalytic properties when the size is reduced to nanometre range, makes it very interesting. Gold clusters, whether supported or unsupported, find widespread application as catalysts for reactions such as carbon monoxide oxidation, water gas shift reaction. The numerous reports on such catalytic activity of bare and supported gold clusters as well as adsorption of small molecules such as CO, O₂ on gold clusters have been discussed elaborately. Above all, we have also reviewed the recent developments in the field of single atom catalysis.

Various computational methods used for modelling surfaces, nanoparticle etc. have been discussed under two categories- Molecular Mechanics and Quantum Mechanics. A brief overview of the molecular mechanics method along with its advantages and disadvantages has been laid out. Quantum mechanics has been particularly stressed upon, since our calculations are mostly based on it. One of the most popular electronic structure methods, density functional theory (DFT) has been discussed in detail with reference to various functionals, basis sets available in the domain of computational chemistry. A part of our work related to zeolite supported gold systems utilizes hybrid QM/MM method and thereby, we have also included hybrid methods along with the various computational methods.

The geometric structures, electronic and reactivity properties of Au₆H_n (n=1-12) clusters have been studied at the generalized gradient approximation level using the PBE functional and DNP basis set. In all the hydrogenated Au₆ clusters, the low spin state structures are found to be more stable than their high spin counterparts. Adsorption of H atoms stabilizes the Au₆ cluster which is reflected from the high binding energies. Our calculations indicate that planarity is retained till Au₆H₉ but the triangular structure of Au₆ distorts in Au₆H₇, Au₆H₈ and Au₆H₉. Further addition of H atoms removes planarity of the clusters such that one of the base Au atoms of the Au₆ triangle protrudes out of the plane of Au₆ in Au₆H₁₀, Au₆H₁₁ and Au₆H₁₂ cluster rendering these clusters non planar. The H atoms are found to be negatively charged in all the clusters indicating charge transfer from Au to H atoms. Clusters with even number of H atoms possess higher

HOMO-LUMO gap, chemical hardness, vertical ionization potential, adiabatic ionization potential and binding energy and are thus, suggested to be more stable than their congeners with odd number of H atoms. The Au atoms forming the vertices of the outer triangle in Au_6 have higher relative electrophilicity value while those forming the vertices of the inner triangle have higher relative nucleophilicity value as revealed by the DFT based reactivity descriptors. However, in Au_6H_6 , two nearby Au sites forming the vertices of the inner and outer triangle have the highest relative electrophilicity and relative nucleophilicity values, respectively while in Au_6H_{12} , these are located in the inner triangle.

The structures of faujasite supported bare Pd_6 and Au_6 clusters and their interaction with the bridging OH groups of the zeolite support to form hydrogenated Pd_6 and Au_6 clusters has been studied using density functional theory. During calculations, the optimized positions of the terminal hydrogen atoms have been fixed. The faujasite supported bare metal clusters, Pd_6 and Au_6 interact with the support through three close M-O bonds (M= Pd , Au) whereas in their hydrogenated counterparts, $\text{Pd}_6\text{H}_3/\text{FAU}$ and $\text{Au}_6\text{H}_3/\text{FAU}$, respectively there are overall six close M-O contacts. This implies that interaction of the metal clusters with the zeolite is enhanced as a consequence of stepwise reverse spillover. The hydrogenated Pd_6 and Au_6 clusters supported on faujasite are more stable than the dehydrogenated clusters and exothermic E_{RS} values indicate that the process of proton transfer from the zeolite support to the metal cluster is energetically favourable in both the metals. Our calculations reveal that $\text{Pd}_6\text{H}_2/\text{FAU}(\text{H})$ and $\text{Au}_6\text{H}_2/\text{FAU}(\text{H})$ are the most stable among other hydrogenated congeners. Proton transfer leads to partial oxidation of the metal atoms with a concomitant reduction of H^+ to H^- . In case of both the metals, atoms which are in close proximity with the zeolite oxygen atoms are more strongly oxidized compared to the metal atoms that do not interact directly with the zeolite framework and thus there exists metal centres with different oxidation states within the same cluster in both bare and hydrogenated metal clusters.

With a view to delineate the effect of cluster charge on the catalytic activity of gas phase gold cluster towards CO oxidation, we have considered the conventional bi-molecular Langmuir-Hinshelwood CO oxidation mechanism on Au_6^0 , Au_6^- and

Au_6^+ clusters using density functional theory (DFT) calculations. Adsorption of CO and O_2 has been considered initially and our calculations indicate that both CO and O_2 prefer the low coordination apex site for adsorption in the Au_6 clusters irrespective of the cluster charge. On considering their co-adsorption on the three clusters viz. Au_6^0 , Au_6^- and Au_6^+ , it is observed that CO preferentially adsorbs at the apex Au site and O_2 at the nearest lateral site. However, O_2 activation is observed in the case of Au_6^0 and Au_6^- but not in the cationic counterpart. Investigation of the CO oxidation pathway on the three clusters reveal that the barriers observed for the reaction on Au_6^- are much lower than those with the neutral and cationic counterparts. CO oxidation over anionic gold hexamer does not require thermal activation unlike in Au_6^0 and Au_6^+ clusters which is reflected from the stability of all the species including the transition states with respect to the interacting species. It can be thus concluded that Au_6^- exhibits better catalytic activity compared to neutral and cationic clusters.

We have employed hybrid quantum mechanics/molecular mechanics method to treat the faujasite supported gold monomer in three oxidation states viz. 0, +1 and +3 model system considered in our work. Initially, we have investigated the adsorption of CO and O_2 on faujasite supported neutral and cationic (+1 and +3) gold monomer. CO adsorption was found to be favourable in all the oxidation states and the highest CO binding energy is observed in $\text{Au}^{3+}/\text{FAU}$. On the neutral monomer, CO adsorbs in a bent fashion while in the cationic systems, it adsorbs linearly. O_2 adsorption was considered in three modes viz. top, bridge and dissociative. Our calculations indicate that the top mode of O_2 adsorption is favourable in the cationic systems and higher O_2 binding energy is observed in $\text{Au}^{3+}/\text{FAU}$. Charge transfer to O_2 results in O-O bond elongation and consequently its activation. On the other hand, O_2 adsorbs in the bridge mode with high binding energy in both neutral and cationic systems. This mode of O_2 adsorption is favourable in the three oxidation systems and involves substantial O-O bond activation. Adsorption of O_2 as two dissociated O atoms is designated as the dissociative mode and is quite interesting. In Au^0/FAU , the dissociative mode is observed to be favourable albeit with low binding energy. However, in cationic systems, the dissociative mode reverts back to the bridge mode rather

than remaining as dissociated O atoms. The present calculations imply that the bridge mode is preferred over top and dissociative modes of O₂ adsorption on faujasite supported neutral and cationic Au monomer which also accompanies substantial O₂ activation.

Further, as a certain amount of moisture is inevitably present in practical catalytic systems, we have investigated the effect of water on the adsorption of CO and O₂ on faujasite supported neutral and cationic gold monomer. Our calculations indicate that the adsorption of CO on faujasite supported monomer in presence of pre-adsorbed water results in cleavage of the Au-H₂O bond and no interaction exists between CO and H₂O. The binding energy of CO increases with the Au oxidation state. In the optimized structures, bonding of CO on water pre-adsorbed Auⁿ/FAU changes from bent to linear mode with increase in Au oxidation state. This can be correlated with the decrease in ν_{C-O} value observed in the neutral monomer and blue shift in case of cationic systems. In presence of pre-adsorbed water, the top and bridge modes of O₂ adsorption are favourable in all the oxidation states and the highest binding energy is observed in Au⁰/FAU. The dissociative mode reverts back to the favourable bridge mode in Au⁰/FAU while in the cationic systems where it remains in the dissociative mode, the adsorption of O₂ is observed to be unfavourable. Activation of H₂O observed in our calculations can be attributed to the hydrogen bonded interaction that prevails between O₂ and H₂O and also between the nearest zeolite oxygen atoms and the H atoms of H₂O. Further, we consider the feasibility of dissociation of the adsorbed H₂O molecule and consequently formation of a hydroperoxyl and hydroxyl species from the transfer of the dissociated H atom from H₂O to O₂ when O₂ and H₂O are in close proximity. Transfer of a proton from H₂O to O₂ that results in a hydroperoxyl-hydroxyl species was found to involve a barrier as low as 0.20 eV.

Next, we attempted to investigate the activity of faujasite supported neutral and cationic Au monomer towards CO oxidation using hybrid QM/MM method. Initially, we considered different CO-O₂ containing configurations and the corresponding interaction energies were determined. It was observed that high barriers are involved in the pathway initiating from the most favourable initial CO-O₂ configuration (Eley-Rideal mechanism with dissociated O₂) compared to the pathway

with initial CO-O₂ containing configuration having moderate interaction energies. Our calculations indicated that the Eley-Rideal mechanism with CO adsorbed on the supported Au centre and O₂ in the gas phase is the preferred pathway. Among the three faujasite supported Au systems, Au³⁺/FAU exhibits better catalytic activity and the stability of all the species including the transition states with respect to the interacting species indicates no thermal activation. Superior activity of NaY supported mononuclear Au^{III} complex towards CO oxidation as compared to Au^I has also been observed in experiments. The conclusions drawn from this simple model of zeolite supported Au catalyst for CO oxidation may be inherent for understanding the catalytic activity of larger realistic catalytic system so as to apprehend the mechanism involved.

The study was further extended to investigate the activity of faujasite supported neutral and cationic gold monomer towards water-gas shift reaction using hybrid quantum mechanics/molecular mechanics calculations. Initially, two different CO-H₂O co-adsorbed configurations have been considered and our calculations indicated that CO adsorption on Auⁿ/FAU (n=0, +1 and +3) in presence of pre-adsorbed H₂O is more favourable than the adsorption of H₂O on Auⁿ/FAU (n=0, +1 and +3) in presence of pre-adsorbed CO. Subsequently, this configuration has been appraised as the starting configuration for investigating water-gas shift reaction mechanism. The reaction involves formation of a carboxyl intermediate in all the oxidation states from the recombination of CO and OH. However, carboxyl formation is above the entrance channel in Au⁺/FAU and is thus, the rate limiting step. The overall reaction is found to be endothermic in both the cationic systems while is exothermic in Au⁰/FAU. Comparing the activity of the three Au monomer species, it is observed that neutral Au exhibits better catalytic activity towards water-gas shift reaction and the dissociation of H₂O into OH and H is the rate limiting step. Substantially high barriers associated with the cationic systems and endothermicity of the reaction will inhibit their catalytic activity. Stability of all the species including the transition states with respect to the interacting species indicates no thermal activation in faujasite supported neutral Au monomer. However, reducing the water dissociation barrier observed in the neutral monomer will improve the catalytic activity further.

Our calculations indicate that faujasite supported Au monomer possesses the potential to act as a catalyst for CO oxidation but significantly high barrier involved in water dissociation will inhibit its catalytic activity towards water gas shift reaction. It is believed that designing improved catalysts with enhanced potential for water gas shift reaction will open up a new dimension for water gas shift reaction catalysts. The conclusions drawn from this study may be inherent for understanding the catalytic activity of larger realistic catalytic system so as to apprehend the mechanism involved.

Future Scopes

With the emerging advancement in the field of material research and nanotechnology, there has been a growing interest in diverse applications of nanoclusters. Gold nanoclusters are appreciated largely because of their appealing role as a catalyst for a large number of both industrially and environmentally important reactions such as CO oxidation, propene epoxidation, water gas shift reaction and so on. The work presented in the thesis attempts to provide an insight into the structure, energetics and properties of gas phase and zeolite supported hydrogenated gold clusters. Moreover, we have investigated the catalytic activity of gas phase and zeolite supported gold cluster towards CO oxidation and water gas shift reaction. The effect of moisture on the adsorption of CO and O₂ on zeolite supported Au and consequently the process of proton transfer between H₂O and O₂ has also been considered. This work can be further extended in various directions, some of which are:

1. Single gold atom or small gold clusters supported on materials such as graphene can be utilized to study reactions such as NO_x reduction, alkene hydrogenation etc.
2. Reaction mechanisms can be modelled on small gold clusters entrapped in a larger zeolite cavity to obtain a more realistic model.
3. The detailed mechanism of H atom transfer during the process of reverse hydrogen spillover from bridging OH groups of zeolite to metal clusters can

be investigated.

4. The study can be extended to gold clusters doped with other transition metals such as Ag, Pt etc.
5. Molecular dynamics simulations can be implemented to study reaction mechanisms on gold clusters.

Bibliography

1. Castleman, Jr., A. W. & Jena, P. *Proc. Natl. Acad. Sci. U.S.A.* **103** (28), 10552--10553, 2006.
2. Jena, P. & Castleman, Jr., A. W. *Proc. Natl. Acad. Sci. U.S.A.* **103** (28), 10560--10569, 2006.
3. Heer, W. A. de *Rev. Mod. Phys.* **65** (3), 611--676, 1993.
4. Bentley, P. G. *Nature* **190** (4774), 432--433, 1961.
5. Henkes, V. W. *Z. Naturforsch.* **16A**, 842, 1961.
6. Robbins, E.J., et al. *Adv.Phys.* **16** (64), 739--744, 1967.
7. Leckenby, R. E., et al. *Proc. R. Soc. Lond. A* **280** (1382), 409--429, 1964.
8. Milne, T. A. & Greene, F. T. *J. Chem. Phys.* **47** (10), 4095--4101, 1967.
9. Arshadi, M., et al. *J. Phys. Chem.* **74** (7), 1475--1482, 1970.
10. Calo, J. M. *Nature* **248** (5450), 665--667, 1967.
11. Pradeep, T. *Nano: The essentials*, Tata McGraw-Hill Publishing Company Limited, New Delhi, 2008.
12. Wilcoxon, J. P. & Abrams, B. L. *Chem. Soc. Rev.* **35** (11), 1162--1194, 2006.
13. Chakraborty, P. *J. Mater. Sci.* **33** (9), 2235--2259, 1998.
14. Brongersma, M. L. *Nat. Mater.* **2** (5), 296--297, 2003.
15. Lee, T., et al. *J. Nano. Res.* **2** (4), 345--362, 2000.

16. Gudiksen, M. S., et al. *Nature* **415** (6872), 617--620, 2002.
17. Shang, L., et al. *Nano Today* **6** (4), 401--418, 2011.
18. Jain, P. K., et al. *Acc. Chem. Res.* **41** (12), 1578--1586, 2008.
19. Beale, A. M. & Weckhuysen, B. M. *Phys. Chem. Chem. Phys.* **12** (21), 5562--5574, 2010.
20. Daniel, M.-C. & Astruc, D. *Chem. Rev.* **104** (1), 293--346, 2004.
21. Hutchings, G. J., et al. *Chem. Soc. Rev.* **37** (9), 1759--1756, 2008.
22. Faraday, M. *Philos. Trans. R. Soc. London* **147**, 145--181, 1857.
23. Schmidbaur, H. & Schier, A. *Chem. Soc. Rev.* **41** (1), 370--412, 2012.
24. Pyykkö, P., et al. *Faraday Discuss.* **152**, 169--178, 2011.
25. Scherbaum, F., et al. *Angew. Chem., Int. Ed. Engl.* **27** (11), 1544--1546, 1988.
26. Pyykkö, P. *Chem. Rev.* **97** (3), 597--636, 1997.
27. Schmidbaur, H. *Gold Bull.* **33** (1), 3--10, 2000.
28. Pyykkö, P. & Mendizabal, F. *Chem. Eur. J.* **3** (9), 1458--1465, 1997.
29. Pyykkö, P. & Runeberg, N. *J. Chem. Soc. Chem. Commun.* (24), 1812--1813, 1993.
30. Schneider, W., et al. *Organometallics* **15** (26), 5445--5446, 1996.
31. Codina, A., et al. *J. Am. Chem. Soc.* **124** (23), 6781--6786, 2002.
32. Pyykkö, P. & Zhao, Y. *Angew. Chem., Int. Ed. Engl.* **30** (5), 604--605, 1991.
33. Pyykkö, P., et al. *Chem. Phys. Lett.* **218** (1-2), 133--138, 1994.
34. Bayler, A., et al. *J. Am. Chem. Soc.* **118** (29), 7006--7007, 1996.
35. Tripathi, U. M., et al. *Chem. Soc., Dalton Trans.* (17), 2865--2868, 1997.

36. Spicer, W.E., et al. *Phys. Rev.* **115** (1), 57--62, 1959.
37. Moore, C.E. *Atomic Energy Levels*, Vol. III, Natl. Bur. Stand. (U.S.)
Circ. 467, U.S. Government Printing Office, Washington, D.C., 1958.
38. Christensen, N. E. & Seraphin, B. O. *Phys. Rev. B* **4** (10), 3321--3344,
1971.
39. Bartlett, N. *Gold Bull.* **31** (1), 22--25, 1998.
40. Schwerdtfeger, P. *Heter. Chem.* **13** (6), 578--584, 2002.
41. Pyykkö, P. *Angew. Chem. Int. Ed.* **43** (34), 4412--4456, 2004.
42. Autschbach, J. *J. Chem. Phys.* **136** (15), 150902/1--150902/15, 2012.
43. Taylor, K. J., et al. *J. Chem. Phys.* **93** (10), 7515--7518, 1990.
44. Xing, X. et al. *Phys. Rev. B* **74** (16), 165423/1--165423/6, 2006.
45. Gu, X., et al. *J. Phys. Chem. C* **111** (23), 8228--8232, 2007.
46. Huang, W., et al. *ACS Nano* **3** (5), 1225--1230, 2009.
47. Lechtken, A., et al. *Phys. Chem. Chem. Phys.* **11** (21), 4344--4350, 2009.
48. Schoss, D., et al. *Phil. Trans. R. Soc. A* **368** (1915), 1211--1243, 2010.
49. Huang, W., et al. *J. Chem. Phys.* **132** (5), 054305/1--054305/5, 2010.
50. Zhu, M., et al. *Nano Lett.* **11** (9), 3963--3969, 2011.
51. Häkkinen, H. & Landman, U. *Phys. Rev. B* **62** (4), R2287--R2290, 2000.
52. Wang, J., et al. *Phys. Rev. B* **66** (3), 035418/1--035418/6, 2002.
53. Han, Y.-K. *J. Chem. Phys.* **124** (2), 024316/1--024316/3, 2006.
54. Martínez, A. *J. Phys. Chem. C* **114** (49), 21240--21246, 2010.
55. Mukhamedzyanova, D. F., et al. *J. Phys. Chem. C* **116** (21), 11507--11518,
2012.

-
56. Zanti, G. & Peeters, D. *Theor. Chem. Acc.* **132** (1), 11507--11518, 2012.
57. Dufour, F., et al. *J. Phys. Chem. C* **118** (8), 4362--4376, 2014.
58. Li, X.-B., et al. *J. Chem. Phys.* **126** (8), 084505/1--084505/8, 2007.
59. Deka, A. & Deka, R. C. *J. Mol. Str.: Theochem* **870** (1-3), 83--93, 2008.
60. Johansson, M. P., et al. *Phys. Rev. A* **77** (5), 053202/1--053202/7, 2008.
61. Johansson, M. P., et al. *J. Phys. Chem. C* \dx.doi.org/10.1021/jp505776d, 2014.
62. Assadollahzadeha, B. & Schwerdtfeger, P. *J. Chem. Phys.* **131** (6), 064306/1 -- 064306/11, 2009.
63. Häkkinen, H., et al. *J. Phys. Chem. A* **107** (32), 6168--6175, 2003.
64. Furche, F., et al. *J. Chem. Phys.* **117** (15), 6982--6990, 2002.
65. Gilb, S., et al. *J. Chem. Phys.* **116** (10), 4094--4101, 2002.
66. Ferrighi, L., et al. *J. Am. Chem. Soc.* **131** (30), 10605--10609, 2009.
67. Bulusu, S. & Zeng, X. C. *J. Chem. Phys.* **125** (15), 154303/1--154303/5, 2006.
68. Fa, W., et al. *Phys. Rev. B* **72** (20), 205428/1--205428/4, 2005.
69. Yang, A., et al. *Phys. Lett. A* **374** (44), 4506--4511, 2010.
70. Aprò, E., et al. *Phys. Rev. B* **73** (20), 205414/1--205414/5, 2006.
71. Krishnamurty, S., et al. *J. Phys. Chem. A* **111** (42), 10769--10775, 2007.
72. Gruene, P., et al. *Science* **321** (5889), 674--676, 2008.
73. De, H. S., et al. *J. Phys. Chem. C* **113** (17), 7101--7106, 2009.
74. Bulusu, S., et al. *J. Phys. Chem. C* **111** (11), 4190--4198, 2007.
75. Shao, N., et al. *J. Am. Chem. Soc.* **132** (18), 6596--6605, 2010.

-
76. Jalbout, A. F., et al. *J. Phys. Chem. A* **112** (3), 353--357, 2008.
 77. Johansson, M. P., et al. *J. Phys. Chem. C* **112** (49), 19311--19315, 2008.
 78. Shao, N., et al. *J. Phys. Chem. C* **118** (13), 6887--6892, 2014.
 79. Gu, X., et al. *Phys. Rev. B* **70** (20), 205401/1--205401/5, 2004.
 80. Ji, M., et al. *Angew. Chem. Int. Ed.* **44** (43), 7119--7123, 2005.
 81. Knight, W. D., et al. *Phys. Rev. Lett.* **52** (24), 2141--2143, 1984.
 82. Gao, Y., et al. *J. Chem. Phys.* **129** (8), 084703/1--084703/6, 2008.
 83. Pyykkö, P. *Nat. Nanotechnol.* **2** (5), 273--274, 2007.
 84. Tsunoyama, H. & Tsukuda, T. *J. Am. Chem. Soc.* **131** (51), 18216--18217, 2009.
 85. Li, J., et al. *Science* **299** (5608), 864--867, 2003.
 86. Salisbury, B.E., et al. *Chem. Phys.* **262** (1), 131--141, 2000.
 87. Jiang, P., et al. *J. Am. Chem. Soc.* **132** (9), 2858--2859, 2010.
 88. Huang, W., et al. *J. Am. Chem. Soc.* **132** (12), 4344--4351, 2010.
 89. Wallace, W. T. & Whetten, R. L. *J. Am. Chem. Soc.* **124** (25), 7499--7505, 2002.
 90. Woodham, A. P., et al. *Angew. Chem. Int. Ed.* **51** (18), 4444--4447, 2012.
 91. Woodham, A. P., et al. *J. Am. Chem. Soc.* **135** (5), 1727--1730, 2013.
 92. Mills, G., et al. *Chem. Phys. Lett.* **359** (5-6), 493--499, 2002.
 93. Mills, G., et al. *J. Chem. Phys.* **118** (9), 4198--4205, 2003.
 94. Yoon, B., et al. *J. Phys. Chem. A* **107** (20), 4066--4071, 2003.
 95. Fernández, E. M., et al. *Chem. Phys. Lett.* **408** (4-6), 252--257, 2005.

-
96. Ding, X., et al. *J. Chem. Phys.* **120** (20), 9594--9600, 2004.
 97. Boronat, M. & Corma, A. *Dalton Trans.* **39** (36), 8538--8546, 2010.
 98. Roldán, A., et al. *Phys. Chem. Chem. Phys.* **12** (36), 10723--10729, 2010.
 99. Staykov, A., et al. *J. Phys. Chem. C* **116** (30), 15992--16000, 2012.
 100. Sun, K., et al. *J. Phys. Chem. A* **116** (38), 9568--9573, 2012.
 101. Pal, R., et al. *J. Am. Chem. Soc.* **134** (22), 9438--9445, 2012.
 102. Zhai, H.-J. & Wang, L.-S. *J. Chem. Phys.* **122** (5), 051101/1--051101/4, 2005.
 103. Neumaier, M., et al. *J. Chem. Phys.* **122** (10), 104702/1--104702/11, 2005.
 104. Kimble, M.L., et al. *Int. J. Mass Spectrom.* **254** (3), 163--167, 2006.
 105. Veldeman, N., et al. *J. Phys. Chem. A* **109** (51), 11793--11801, 2005.
 106. Wu, X., et al. *J. Chem. Phys.* **117** (8), 4010--4015, 2002.
 107. Prestianni, A., et al. *J. Phys. Chem. B* **110** (25), 12240--12248, 2006.
 108. Yang, X.-F., et al. *Phys. Chem. Chem. Phys.* **12** (12), 3038--3043, 2010.
 109. Manzoor, D., et al. *J. Phys. Chem. C* **117** (40), 20982--20990, 2013.
 110. Zhai, H.-J., et al. *J. Am. Chem. Soc.* **127** (34), 12098--12106, 2005.
 111. McKenna, K. P. & Shluger, A. L. *J. Phys. Chem. C* **111** (51), 18848--18852, 2007.
 112. Schwerdtfeger, P., et al. *J. Chem. Phys.* **128** (12), 124302/1--124302/10, 2008.
 113. Wang, Y.-L., et al. *J. Phys. Chem. A* **114** (3), 1247--1254, 2010.
 114. Morrow, B. H., et al. *J. Phys. Chem. C* **115** (13), 5637--5647, 2011.

-
115. Stiehl, J. D., et al. *J. Am. Chem. Soc.* **126** (6), 1606--1607, 2004.
116. Weiher, N., et al. *J. Am. Chem. Soc.* **129** (8), 2240--2241, 2007.
117. Schaub, R., et al. *Science* **299** (5605), 377--379, 2003.
118. van Bokhoven, J. A., et al. *Angew. Chem. Int. Ed.* **45** (28), 4651--4654, 2006.
119. Rodríguez, J. A., et al. *J. Am. Chem. Soc.* **132** (9), 3177--3186, 2010.
120. Rasmussen, M. D., et al. *J. Chem. Phys.* **120** (2), 988--997, 2004.
121. Molina, L. M. & Hammer, B. *J. Chem. Phys.* **123** (16), 161104/1--161104/5, 2005.
122. Roldán, A., et al. *J. Phys. Chem. C* **114** (40), 16973--16978, 2010.
123. Liu, L., et al. *Chem. Phys. Chem.* **14** (5), 996--1002, 2013.
124. Chrétien, S. & Metiu, H. *J. Chem. Phys.* **129** (7), 074705/1--074705/16, 2008.
125. Kong, X., et al. *Phys. Chem. Chem. Phys.* **14** (39), 13564--13568, 2012.
126. Chen, X., et al. *Molecules* **18** (3), 3279--3291, 2013.
127. Meier, D. C. & Goodman, D. W. *J. Am. Chem. Soc.* **126** (6), 1892--1899, 2004.
128. Anderson, B. G., et al. *Langmuir* **22** (9), 4310--4314, 2006.
129. Lin, X., et al. *J. Am. Chem. Soc.* **132** (22), 7745--7749, 2010.
130. Kadossov, E. & Burghaus, U. *Catal. Lett.* **134** (3-4), 228--232, 2010.
131. Joshi, A. M., et al. *J. Phys. Chem. C* **111** (30), 11424--11436, 2007.
132. Sierraalta, A., et al. *J. Phys. Chem. A* **114** (25), 6870--6878, 2010.
133. Deka, A., et al. *Chem. Phys. Lett.* **490** (4-6), 184--188, 2010.
134. Sierraalta, A., et al. *J. Mol. Catal. A: Chemical* **301** (1-2), 61--66, 2009.

135. Deka, A. *Rev. Appl. Phys.* **2** (2), 33--38, 2013.
136. Fernández, E. M. & Balbás, L. C. *J. Phys. Chem. B* **110** (21), 10449--10454, 2006.
137. Wallace, W. T., et al. *J. Am. Chem. Soc.* **125** (27), 8408--8414, 2003.
138. Wallace, W. T., et al. *Phys. Chem. Chem. Phys.* **7** (5), 930--937, 2005.
139. Gao, F., et al. *Catal. Lett.* **134** (1-2), 9--12, 2010.
140. Zhang, C. & Lindan, P. J. D. *J. Chem. Phys.* **121** (8), 3811--3815, 2004.
141. Liu, L. M., et al. *J. Am. Chem. Soc.* **128** (12), 4017--4022, 2006.
142. Bongiorno, A. & Landman, U. *Phys. Rev. Lett.* **95** (10), 106102/1--106102/4, 2005.
143. Su, H.-Y., et al. *J. Phys. Chem. C* **112** (44), 17303--17310, 2008.
144. Okumura, M., et al. *Gold Bull.* **40** (1), 40--44, 2007.
145. Ito, T., et al. *J. Phys. Chem. A* **118** (37), 8293--8297, 2014.
146. Gao, Y. & Zeng, X. C. *ACS Catal.* **2** (12), 2614--2621, 2012.
147. Bone, W. A. & Wheeler, R. V. *Phil. Trans. R. Soc. Lond. A* **206** (402-412), 1--67, 1906.
148. Bone, W. A. & Andrew, G. W. *Proc. R. Soc. Lond. A* **109** (751), 459--476, 1925.
149. Huber, H., et al. *Inorg. Chem.* **16** (5), 975--979, 1977.
150. Haruta, M., et al. *Chem. Lett.* **16** (2), 405--408, 1987.
151. Haruta, M., et al. *J. Catal.* **115** (2), 301--309, 1989.
152. Haruta, M., et al. *Catal. Today* **36** (1), 153--166, 1997.
153. Chen, M. & Goodman, D. W. *Acc. Chem. Res.* **39** (10), 739--746, 2006.
154. Lim, D. C., et al. *Angew. Chem. Int. Ed.* **45** (15), 2413--2415, 2006.

155. Chen, M. & Goodman, D. W. *Catal. Today* **111** (1-2), 22--33, 2006.
156. Grabow, L. C. & Mavrikakis, M. *Angew. Chem. Int. Ed.* **47** (39), 7390--7392, 2008.
157. Hutchings, G. J., et al. *Chem. Soc. Rev.* **37** (9), 1759--1765, 2008.
158. Fu, L., et al. *J. Phys. Chem. B* **109** (9), 3704--3706, 2005.
159. Guzman, J. & Gates, B. C. *J. Am. Chem. Soc.* **126** (9), 2672--2673, 2004.
160. Park, E. D. & Lee, J. S. *J. Catal.* **186** (1), 1--11, 1999.
161. Lemire, C., et al. *Angew. Chem. Int. Ed.* **43** (1), 118--121, 2004.
162. Mills, G., et al. *J. Chem. Phys.* **118** (9), 4198--4205, 2003.
163. Taylor, K. J., et al. *J. Chem. Phys.* **96** (4), 3319--3329, 1992.
164. Pyykkö, P. *Angew. Chem. Int. Ed.* **43** (23), 4412--4456, 2004.
165. Pyykkö, P. *Chem. Soc. Rev.* **37** (9), 1967--1997, 2008.
166. Min, B. K. & Friend, C. M. *Chem. Rev.* **107** (6), 2709--2724, 2007.
167. Kung, M. C., et al. *J. Phys. Chem. C* **111** (32), 11767--11775, 2007.
168. Wallace, W. T. & Whetten, R. L. *J. Am. Chem. Soc.* **124** (25), 7499--7505, 2002.
169. Socaciu, L. D., et al. *J. Am. Chem. Soc.* **125** (34), 10437--10445, 2003.
170. Mikami, Y., et al. *Catal. Sci. Technol.* **3** (1), 58--69, 2013.
171. Fang, H.-C., et al. *Phys. Chem. Chem. Phys.* **13** (29), 13358--13369, 2011.
172. Häkkinen, H. & Landman, U. *J. Am. Chem. Soc.* **123** (39), 9704--9705, 2001.
173. Gao, Y., et al. *ACS Nano* **5** (10), 7818--7829, 2011.

-
174. Tang, D. & Hu, C. *J. Phys. Chem. Lett.* **2** (23), 2972--2977, 2011.
175. Liu, W., et al. *J. Phys. Chem. C* **114** (49), 21094--21099, 2010.
176. Liu, Z.-P., et al. *J. Am. Chem. Soc.* **124** (49), 14770--14779, 2002.
177. Chang, C. M., et al. *J. Chem. Phys.* **128** (12), 124710/1--124710/4, 2008.
178. Aguilar-Guerrero, V. & Gates, B.C. *Chem. Commun.* **30** (12), 3210--3212, 2007.
179. Chen, M. S. & Goodman, D. W. *Chem. Soc. Rev.* **37** (9), 1860--1870, 2008.
180. Sanchez, A., et al. *J. Phys. Chem. A* **103** (48), 9573--9578, 1999.
181. Yoon, B., et al. *Science* **307** (5708), 403--407, 2005.
182. Costello, C. K., et al. *Appl. Catal. A: General* **232** (1-2), 159--168, 2002.
183. Schubert, M. M., et al. *J. Catal.* **197** (1), 113--122, 2001.
184. Comotti, M., et al. *J. Am. Chem. Soc.* **128** (3), 917--924, 2006.
185. Valden, M., et al. *Science* **281** (5383), 1647--1650, 1998.
186. Remediakis, I. N., et al. *Appl. Catal. A: General* **291** (1-2), 13--20, 2005.
187. Remediakis, I. N., et al. *Angew. Chem. Int. Ed.* **44** (12), 1824--1826, 2005.
188. Kim, H. Y., et al. *J. Am. Chem. Soc.* **134** (3), 1560--1570, 2012.
189. Li, L., et al. *J. Am. Chem. Soc.* **135** (51), 19336--19346, 2013.
190. Molina, L. M. & Hammer, B. *Phys. Rev. Lett.* **90** (20), 206102/1--206102/4, 2003.
191. Wang, C.-M., et al. *J. Am. Chem. Soc.* **129** (9), 2642--2647, 2007.
192. Gao, M., et al. *Catalysts* **1** (1), 18--39, 2011.
193. Sun, C. & Smith, S. C. *J. Phys. Chem. C* **116** (5), 3524--3531, 2012.

194. Green, I. X., et al. *J. Am. Chem. Soc.* **134** (30), 12717--12723, 2012.
195. Camellone, M. F. & Fabris, S. *J. Am. Chem. Soc.* **131** (30), 10473--10483, 2009.
196. Chakrabarty, D. K. & Viswanathan, B. *Catalysis by Acidic Solids*, in *Heterogeneous Catalysis*, New Age International (P) Limited, Publishers, New Delhi, 2008, 145--169.
197. Gates, B. C. *Catalysis in Molecular-Scale Cavities*, in *Catalytic Chemistry*, Wiley, New York, 1991, 254--304.
198. Kung, H. H., et al. *Top. Catal.* **10** (1-2), 59--64, 2000.
199. Smit, B. & Maesen, T. L. M. *Nature* **451** (7179), 671--678, 2008.
200. Barone, G., et al. *J. Chem. Theory Comput.* **5** (5), 1274--1283, 2009.
201. Swisher, J. A., et al. *J. Phys. Chem. C* **114** (22), 10229--10239, 2010.
202. Rahimi, N. & Karimzadeh, R. *Appl. Catal. A: General* **398** (1-2), 1--17, 2011.
203. Briend-Faure, M., et al. *Appl. Catal. A: General* **38** (1), 71--87, 1988.
204. Pfeifer, H. *Colloids Surf.* **36** (2), 169--177, 1989.
205. Phung, T. K., et al. *Appl. Catal. A: General* **470** (1), 72--80, 2014.
206. Li, S., et al. *J. Phys. Chem. Lett.* **5** (17), 3068--3072, 2014.
207. Lewis, D. W., et al. *J. Phys. Chem.* **99** (8), 2377--2383, 1995.
208. Sierka, M., et al. *J. Phys. Chem. B* **102** (33), 6397--6404, 1998.
209. Deka, R. C., et al. *J. Phys. Chem. B* **107** (33), 8574--8577, 2003.
210. Suzuki, K., et al. *J. Phys. Chem. C* **113** (14), 5672--5680, 2009.
211. Zhang, J., et al. *J. Phys. Chem. C* **116** (17), 9666--9674, 2012.
212. Boudart, M. & Meitzner, G. *EXAFS and Near Edge Structure III*, Springer, Berlin, 1984.

-
213. Guillemot, D., et al. *Catal. Lett.* **41** (3-4), 143--148, 1996.
214. Lin, J. -N. & Wan, B. -Z. *Appl. Catal. B* **41** (1-2), 83--95, 2003.
215. Chen, J.-H., et al. *Appl. Catal. A: General* **291** (1-2), 162--169, 2005.
216. Qu, Z., et al. *Chem. Commun.* (23), 2507--2509, 2006.
217. Tuzovskaya, I. V., et al. *Catal. Commun.* **8** (7), 977--980, 2007.
218. Fierro-Gonzalez, J. C. & Gates, B. C. *J. Phys. Chem. B* **108** (44), 16999--17002, 2004.
219. Simakov, A., et al. *Catal. Commun.* **9** (6), 1277--1281, 2008.
220. Fierro-Gonzalez, J. C., et al. *J. Phys. Chem. C* **111** (18), 6645--6651, 2007.
221. Lu, J., et al. *Angew. Chem. Int. Ed.* **51** (24), 5842--5846, 2012.
222. Okumura, K., et al. *J. Phys. Chem. B* **109** (25), 12380--12386, 2005.
223. Sierraalta, A., et al. *J. Phys. Chem. B* **110** (36), 17912--17917, 2006.
224. Griffe, B., et al. *Int. J. Quant. Chem.* **110** (13), 2573--2582, 2010.
225. Griffe, B., et al. *Comput. Theor. Chem.* **1042**, 69--83, 2014.
226. Song, C. *Catal. Today* **77** (1-2), 17--49, 2002.
227. Suh, D. J., et al. *J. Power Sources* **142** (1-2), 70--74, 2005.
228. Fu, Q., et al. *Science* **301** (5635), 935--938, 2003.
229. Deng, W., et al. *J. Phys. Chem. C* **112** (33), 12834--12840, 2008.
230. Yao, H. C. & Yao, Y. F. Y. *J. Catal.* **86** (2), 254--265, 1984.
231. Zalc, J. M., et al. *J. Catal.* **206** (1), 169--171, 2002.
232. Li, Y., et al. *Appl. Catal. B: Environmental* **27** (3), 179--191, 2000.
233. Andreeva, D., et al. *J. Catal.* **158** (1), 354--355, 1996.

234. Andreeva, D., et al. *Appl. Catal. A: General* **134** (2), 275--283, 1996.
235. Fu, Q., et al. *Catal. Lett.* **77** (1-3), 87--95, 2001.
236. Deng, W., et al. *J. Phys. Chem. C* **112** (33), 12834--12840, 2008.
237. Wen, C., et al. *ACS Nano* **6** (10), 9305--9313, 2012.
238. Rodriguez, J. A., et al. *Acc. Chem. Res.* **47** (3), 773--782, 2014.
239. Grinter, D. C., et al. *J. Phys. Chem. C* **118** (33), 19194--19204, 2014.
240. Liu, Z.-P., et al. *Phys. Rev. Lett.* **94** (19), 196102/1--196102/4, 2005.
241. Song, W. & Hensen, E. J. M. *ACS Catal.* **4** (6), 1885/1--1892, 2014.
242. Sakurai, H., et al. *Chem. Commun.* (3), 271/1--272, 1997.
243. Williams, W. D., et al. *J. Am. Chem. Soc.* **132** (40), 14018--14020, 2010.
244. Yang, M., et al. *J. Am. Chem. Soc.* **135** (10), 3768--3771, 2013.
245. Li, J., et al. *Gold Bull.* **42** (1), 48--60, 2009.
246. Lessard, J. D., et al. *Chem. Commun.* **48** (40), 4857--4859, 2012.
247. Menegazzo, F., et al. *Chem. Sus. Chem.* **1** (4), 320--326, 2008.
248. Andreeva, D. *Gold Bull.* **35** (3), 82--88, 2002.
249. Flytzani-Stephanopoulos, M. *Acc. Chem. Res.* **47** (3), 783--792, 2014.
250. Burch, R. *Phys. Chem. Chem. Phys.* **8** (47), 5483--5500, 2006.
251. Mohamed, M. M. & Ichikawa, M. *J. Colloid Interface Sci.* **232** (2), 381--388, 2000.
252. Mohamed, M. M., et al. *J. Colloid Interface Sci.* **224** (2), 366--371, 2000.
253. Wang, Y., et al. *J. Phys. Chem. C* **113** (15), 6215--6220, 2009.
254. Liu, P. & Rodriguez, J. A. *J. Chem. Phys.* **126** (165), 164705/1--164705/8, 2007.

255. Lin, R.-J., et al. *J. Phys. Chem. C* **116** (1), 336--342, 2012.
256. Risse, T., et al. *Acc. Chem. Res.* **41** (8), 949--956, 2008.
257. Böhme, D. K. & Schwarz, H. *Angew. Chem. Int. Ed.* **44** (16), 2336--2354, 2005.
258. Liu, Z.-P., et al. *Angew. Chem. Int. Ed.* **45** (41), 6865--6868, 2006.
259. Yu, X., et al. *J. Phys. Chem. C* **116** (19), 10632--10638, 2012.
260. Yang, X.-F., et al. *Acc. Chem. Res.* **46** (8), 1740--1748, 2013.
261. Qiao, B., et al. *Nat. Chem.* **3** (8), 634--641, 2011.
262. Mao, K., et al. *Sci. Rep.* **4**, 5441/1--5441/7, 2014.
263. Li, Z.-Y., et al. *J. Am. Chem. Soc.* 0.1021/ja508547z.
264. Gao, M., et al. *J. Phys. Chem. C* **116** (16), 9054--9062, 2012.
265. Argaman, N. & Makov, G. *Am. J. Phys.* **68** (1), 69--79, 2000.
266. Koch, W. & Holthausen, M. C. *A Chemist's Guide to Density Functional Theory*, Wiley-VCH, Weinheim, Germany, Second Edition, 2000.
267. Hohenberg P. & Kohn, W. *Phys. Rev. B* **136** (3B), B864--B871, 1964.
268. Kohn, W. & Sham, L. J. *Phys. Rev. A* **140** (4A), A1133--A1138, 1965.
269. Sousa, S. F., et al. *J. Phys. Chem. A* **111** (42), 10439--10452, 2007.
270. Dirac, P. A. M. *Proc. Camb. Phil. Soc.* **26** (3), 376--385, 1930.
271. Vosko, S. J., et al. *Can. J. Phys.* **58** (8), 1200--1211, 1980.
272. Perdew, J. P., et al. *Phys. Rev. B* **46** (11), 6671--6687, 1992.
273. Slater, J. C. *Phys. Rev.* **81** (3), 385--390, 1951.
274. Becke, A. D. *J. Chem. Phys.* **84** (8), 4524--4529, 1986.
275. Becke, A. D. *J. Chem. Phys.* **96** (3), 2155--2160, 1992.

-
276. Becke, A. D. *J. Chem. Phys.* **97** (12), 9173--9177, 1992.
277. Becke, A. D. *J. Chem. Phys.* **98** (7), 5648--5652, 1993.
278. Becke, A. D. *J. Chem. Phys.* **104** (3), 1040--1046, 1996.
279. Becke, A. D. *J. Chem. Phys.* **107** (20), 8554--8560, 1997.
280. Becke, A. D. *Phys. Rev. A* **38** (6), 3098--3100, 1988.
281. Perdew, J. P. & Wang, Y. *Phys. Rev. B* **33** (12), 8800--8802, 1986.
282. Adamo, C. & Barone, V. *J. Chem. Phys.* **108** (2), 664--675, 1998.
283. Handy, N. C. & Cohen, A. J. *Mol. Phys.* **99** (5), 403--412, 2001.
284. Xu, X. & Goddard III, W. A. *Proc. Natl. Acad. Sci. U.S.A.* **101** (9), 2673--2677, 2004.
285. Wang, Y. & Perdew, J. P. *Phys. Rev. B* **43** (11), 8911--8916, 1991.
286. Perdew, J. P. *Phys. Rev. Lett.* **55** (16), 1665--1668, 1985.
287. Perdew, J. P. *Phys. Rev. B* **33** (12), 8822--8824, 1986.
288. Perdew, J. P., et al. *Phys. Rev. Lett.* **77** (18), 3865--3868, 1996.
289. Adamo, C. & Barone, V. *J. Chem. Phys.* **116** (14), 5933--5940, 2002.
290. Becke, A. D. *J. Chem. Phys.* **88** (2), 1053--1062, 1988.
291. Perdew, J. P. *Unified Theory of Exchange and Correlation Beyond the Local Density Approximation In Electronic Structure of Solids '91*, Akademie Verlag, Berlin, Germany, 1991.
292. Lee, C., et al. *Phys. Rev. B* **37** (2), 785--789, 1988.
293. Langreth, D. C. & Mehl, M. J. *Phys. Rev. B* **28** (4), 1809--1834, 1983.
294. Atkins, P. & Fredman, R. *Molecular Quantum Mechanics*, Oxford University Press, Fourth Edition, 2010.

-
295. Tao, J. M. & Perdew, J. P. *J. Chem. Phys.* **122** (11), 114102/1--114102/7, 2005.
296. Patton, D. C. & Pederson, M. R. *Phys. Rev. A* **56** (4), R2495--R2498, 1997.
297. Krieger, J. B., Chen, J., Iafrate, G. J., Savin, A. *Electron Correlations and Materials Properties*, Kluwer Academic/Plenum Publishers, New York, 1999.
298. Tao, J., et al. *Phys. Rev. Lett.* **91** (14), 146401--146405, 2003.
299. Voorhis, T. V. & Scuseria, G. E. *J. Chem. Phys.* **109** (2), 400--410, 1998.
300. Zhao, Y., et al. *J. Phys. Chem. A* **108** (14), 2715--2719, 2004.
301. Zhao, Y., et al. *J. Phys. Chem. A* **108** (33), 6908--6918, 2004.
302. Perdew, J. P. & Schmidt, K. *AIP Conf. Proc.* **577**, 1--20, 2001.
303. Perdew, J. P. *MRS Bull.* **38** (9), 743--750, 2013.
304. Slater, J. C. *Phys. Rev.* **36** (9), 57--64, 1930.
305. Boys, S. F. *Proc. R. Soc. A* **200** (1063), 542--554, 1950.
306. Cramer, C. J. *Essentials of Computational Chemistry, Theories and Models*, 2nd ed., John Wiley and Sons, Ltd, England, 2004.
307. Delly, B. *J. Chem. Phys.* **92** (1), 508--517, 1990.
308. Hay, P. J. & Wadt, W. R. *J. Chem. Phys.* **82** (1), 299--310, 1985.
309. Hay, P. J. & Wadt, W. R. *J. Chem. Phys.* **82** (1), 270--283, 1985.
310. Warshel, A. & Levitt, M. *J. Mol. Biol.* **103** (2), 227--249, 1976.
311. Nasluzov, V. A., et al. *J. Chem. Phys.* **115** (17), 8157--8171, 2001.
312. Nasluzov, V. A., et al. *J. Phys. Chem. B* **107** (10), 2228--2241, 2003.
313. Sauer, J. *Chem. Rev.* **89** (1), 199--255, 1989.

314. Shoemaker, J. R. et al. *J. Phys. Chem. A* **103** (17), 3245--3251, 1999.
315. Ponder, J.W. & Richards, F.M. *J. Comput. Chem.* **8** (7), 1016--1024, 1987.
316. Schmidt, M.W., et al. *J. Comput. Chem.* **14** (11), 1347--1363, 1993.
317. Schmidbaur, H., et al. *Chem. Soc. Rev.* **43** (1), 345--380, 2014.
318. Ito, H., et al. *Org. Lett.* **7** (14), 3001--3004, 2005.
319. Hashmi, A. S. K. & Hutchings, G. J. *Angew. Chem. Int. Ed.* **45** (47), 7896--7936, 2006.
320. Tsui, E. Y., et al. *Angew. Chem. Int. Ed.* **47** (46), 8937--8940, 2008.
321. González-Arellano, C., et al. *Chem. Commun.* (27), 3451--3453, 2005.
322. Ito, H., et al. *Chem. Commun.* (11), 981--982, 2000.
323. Wei, C. & Li, C.-J. *J. Am. Chem. Soc.* **125** (32), 9584--9585, 2003.
324. Conte, M., et al. *J. Am. Chem. Soc.* **131** (20), 7189--7196, 2009.
325. Kiran, B., et al. *J. Chem. Phys.* **125** (13), 133204/1--133204/7, 2006.
326. Buckart, S., et al. *J. Am. Chem. Soc.* **125** (46), 14205--14209, 2003.
327. Hay, P. J., et al. *J. Chem. Phys.* **69** (3), 984--997, 1978.
328. Schwerdtfeger, P., et al. *J. Chem. Phys.* **91** (3), 1762--1774, 1989.
329. Wang, Y. & Gong, X. G. *J. Chem. Phys.* **125** (12), 124703/1--124703/12, 2006.
330. Guichemerre, M. G. & Chambaud, G. *J. Chem. Phys.* **122** (20), 204325/1 -- 204325/11, 2005.
331. Ghebriel, H. W. & Kshirsagar, A. *J. Chem. Phys.* **126** (24), 244705/1 -- 244705/9, 2007.
332. Phala, N. S., et al. *Chem. Phys. Lett.* **395** (1-3), 33--37, 2004.

333. Buckart, S. et al. *J. Am. Chem. Soc.* **125** (46), 14205--14209, 2003.
334. Zhang, M. et al. *J. Mol. Struct: Theochem* **911** (1-3), 65--69, 2009.
335. Delley, B. *Int. J. Quant. Chem.* **69** (3), 423--433, 1998.
336. Yang, W. & Mortier, W. J. *J. Am. Chem. Soc.* **108** (19), 5708--5711, 1986.
337. Roy, R. K., et al. *J. Phys. Chem. A* **102** (21), 3746--3755, 1998.
338. Bussai, C., et al. *Phys. Chem. Chem. Phys.* (13), 2656--2663, 2005.
339. Krüger, S., et al. *Phys. Chem. Chem. Phys.* (29), 3391--3398, 2006.
340. Zhai, H.-J., et al. *J. Chem. Phys.* **121** (17), 8231--8236, 2004.
341. Huber, G. W., et al. *Chem. Rev.* **106** (9), 4044--4098, 2006.
342. Häkkinen, H., et al. *Angew. Chem. Int. Ed.* **42** (11), 1297--1300, 2003.
343. Vayssilov, G. N. & Rösch, N. *Phys. Chem. Chem. Phys.* (23), 4019--4026, 2005.
344. Shor, E. A. I., et al. *J. Phys. Chem. C* **111** (33), 12340--12351, 2007.
345. Bromley, S. T., et al. *Micro. Meso. Mater.* **44-45**, 395--399, 2001.
346. Catlow, C. R. A.; Bell, R. G.; Gale, J. D.; Lewis, D. W. Modelling of Structure and Reactivity in Zeolites, in *Zeolites: A Refined Tool for Designing Catalytic Sites*, C. R. A. Catlow, eds., Academic Press, London, 1992, 87-100.
347. Kubelkova, L., et al. *J. Chem. Soc., Faraday Trans.* (11), 2035--2041, 1996.
348. Guzman, J. & Gates, B. C. *Dalton Trans.* (17), 3303--3318, 2003.
349. Sachtler, W. M. H. & Zhang, Z. *Adv. Catal.* **39**, 129--220, 1993.
350. Bai, X. & Sachtler, W. M. H. *J. Catal.* **129** (1), 121--129, 1991.

-
351. Ferrari, A. M., et al. *J. Phys. Chem. B* **103** (25), 5311--5319, 1999.
352. Vayssilov, G.N. & Rösch, N. *J. Phys. Chem. B* **108** (1), 180--192, 2004.
353. Vayssilov, G. N., et al. *Angew. Chem., Int. Ed.* **42** (12), 1391--1394, 2003.
354. Deka, R. C., et al. *Cat. Lett.* **131** (1-2), 155--159, 2009.
355. Kalita, B. & Deka, R. C. *J. Phys. Chem. C* **113** (36), 16070--16076, 2009.
356. Petkov, P. St., et al. *J. Phys. Chem. C* **114** (18), 8500--8506, 2010.
357. Kalita, B. & Deka, R. C. *J. Chem. Phys.* **127** (24), 244306/1--244306/10, 2007.
358. Weiher, N., et al. *J. Catal.* **240** (2), 100--107, 2006.
359. Prestianni, A., et al. *J. Phys. Chem. C* **112** (46), 18061--18066, 2008.
360. Prestianni, A., et al. *J. Mol. Str.: Theochem* **903** (1-3), 34--40, 2009.
361. Nikbin, N., et al. *J. Phys. Chem. C* **115** (41), 20192--20200, 2011.
362. Lopez, N. & Nørskov, J. K. *J. Am. Chem. Soc.* **124** (38), 11262--11263, 2002.
363. Wang, F., et al. *J. Phys. Chem. C* **113** (42), 18032--18039, 2009.
364. Liu, C., et al. *J. Am. Chem. Soc.* **135** (7), 2583--2595, 2013.
365. Davran -Candan, T., et al. *J. Mol. Cat. A: Chemical* **306** (1-2), 118--122, 2009.
366. Bonačić-Koutecký, V., et al. *J. Chem. Phys.* **117** (7), 3120--3130, 2002.
367. Frisch, M. J., et al. *J. Chem. Phys.* **80** (7), 3265--3269, 1984.
368. Allinger, N. L., et al. *J. Am. Chem. Soc.* **111** (8), 8551--8556, 1989.
369. Culot, P., et al. *Theor. Chim. Acta* **82** (3-4), 189--205, 1992.

370. Frisch, M. J., et al. Gaussian 09, Revision A.1, Gaussian, Inc., Wallingford CT, 2009.
371. Liu, R. *Comp. Theor. Chem.* **1019**, 141--145, 2013.

List Of Publications

1. Baishya, S. & Deka, R. C. Activity of Faujasite Supported Gold Monomer towards Water Gas Shift Reaction: Hybrid Density Functional Theory/Molecular Mechanics Approach (*Under preparation*).
2. Baishya, S. & Deka, R. C. Unraveling CO oxidation mechanism on faujasite supported Au monomer: Hybrid density functional and molecular mechanics study (*Communicated*).
3. Baishya, S. & Deka, R. C. Role of Water on the Adsorption of CO and O₂ on Zeolite Supported Au Atom: Hybrid Density Functional Theory and Molecular Mechanics Study (*Under revision*).
4. Baishya, S. & Deka, R. C. Catalytic Activities of Au₆, Au₆, and Au₆⁺ Clusters for CO oxidation: A density functional study, *Int. J. Quantum Chem.* **114** (22), 1559--1566, 2014.
5. Baishya, S. & Deka, R. C. Exploring Structures, Electronic and Reactivity properties of Au₆H_n (n = 1-12) Clusters: A DFT Approach, *Comput. Theor. Chem.* **1002**, 1--8, 2012.
6. Deka, R. C. & Baishya, S. Density Functional Investigation of Reverse Hydrogen Spillover on Zeolite Supported Pd₆ and Au₆ Clusters, *Catal. Today* **198** (1), 110--115, 2012.
7. Baishya, S. & Deka, R. C. Hybrid density functional/molecular mechanics studies on activated adsorption of oxygen on zeolite supported gold monomer, *J. Chem. Phys.* **135** (24), 244703/1--244703/7, 2011.

List Of Conferences Attended

1. **Poster Presentation** in "14th Theoretical Chemistry Symposium" at CSIR-National Chemical Laboratory, Pune from 18-21st December, 2014.
2. **Poster Presentation** in "8th Mid-Year CRSI National Symposium in Chemistry" at CSIR-North East Institute of Science and Technology from 10-12th July, 2014. (*Best Poster Award*).
3. **Oral Presentation** in "21st National Symposium on Catalysis for Sustainable Development (CATSYMP-21)" at CSIR-Indian Institute of Chemical Technology from 11-13th February, 2013.
4. **Poster Presentation** in "International Symposium on Chemistry and Complexity" at Indian Association for the Cultivation of Science from 6-8th December, 2011.
5. **Poster Presentation** in "National Conference on Chemistry, Chemical Technology and Society" at Department of Chemical Sciences, Tezpur University from 11-12th November, 2011.
6. **Poster Presentation** in "National Symposium on Recent Developments and Trends in Computational Chemistry (RDTCC-2010)" at Department of Chemistry, North-Eastern Hill University, Shillong from 12-13th March, 2010.

Participated in:

1. 20th National Magnetic Resonance Society Symposium cum Annual Meeting (NMRS-2014) at Department of Chemical Sciences, Tezpur University from 2nd- 5th February, 2014.

2. Science Academies Lecture Workshop on Modern Trends in Chemistry at Department of Chemical Sciences, Tezpur University from 20-22nd November, 2013.
3. Workshop on Spectroscopic Tools and their Applications at Department of Chemical Sciences, Tezpur University on 6th April, 2013.
4. Indo-Finnish Symposium on Role of Catalysts on Production of Green Fuel at Department of Energy, Tezpur University on 1st February, 2013.
5. International Congress on Renewable Energy at Tezpur University from 2-4th November, 2011.
6. Workshop on Integrated Arsenic and Iron Removal from Groundwater: *Arsiron Nilogon* at Tezpur University on 25th June, 2011.
7. Workshop on Intellectual Property Rights Sensitization (IPRSW-2010) at Tezpur University on 23rd December, 2010.

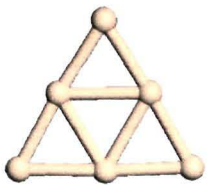
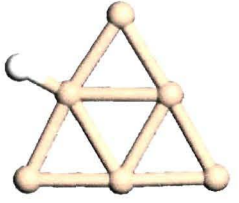
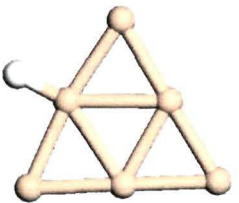
APPENDICES

Appendix A

Structural Isomers of Au_6H_n

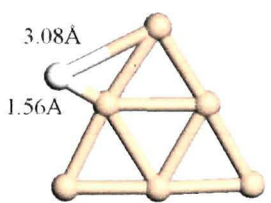
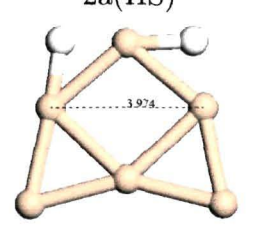
($n=1-12$) clusters

Table A.1: Energies of low-spin and high-spin states (hartree) and relative energies (eV) of the structural isomers of Au_6H_n ($n=1-12$) clusters.

Cluster	Structures	E(LS)	E(HS)	Relative Energy
Au_6		-110387.9082	110387.8540	
Au_6H	 1a(LS)	-110388.4886		0.00
	 1a(HS)	-	-110388.4283	

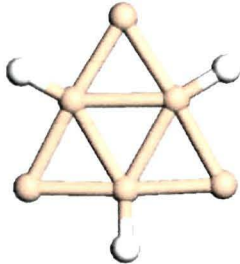
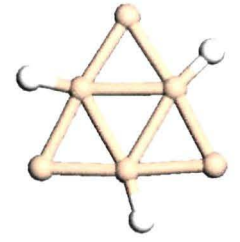
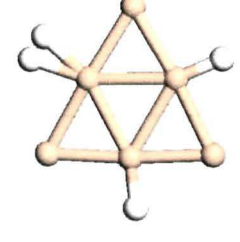
Continued on next page

Table A.1 – continued from previous page

Cluster	Structures	E(LS)	E(HS)	Relative Energy	
Au ₆ H ₂		-110388.4886		0.00	
	lb	-110388.4861		0.07	
	lc	-110389.1191		0.00	
	2a(LS)		-110389.0659		
	2a(HS)		-110389.0776		1.13
	2b	-110389.0776		1.13	
	2c				

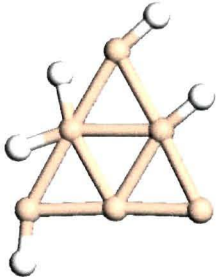
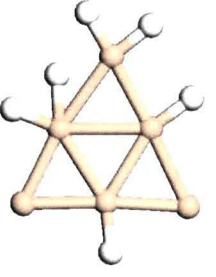
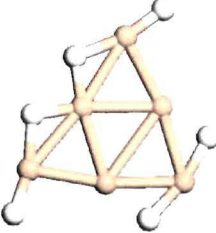
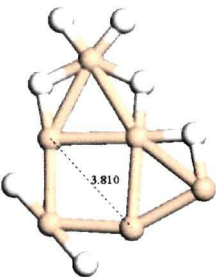
Continued on next page

Table A.1 – continued from previous page

Cluster	Structures	E(LS)	E(HS)	Relative Energy
Au ₆ H ₃		-110389.6495		0.00
	3a(LS)			
Au ₆ H ₄		-110390.2444	-110389.6256	0.00
	3a(HS)			
	4a(LS)			
Au ₆ H ₅		-110390.8488		0.00
	4a(HS)			
	5a(LS)			

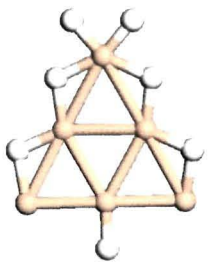
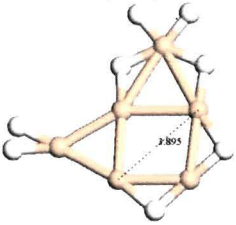
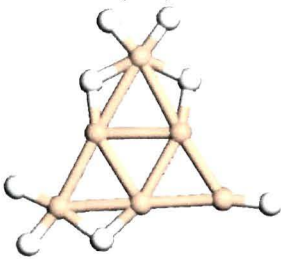
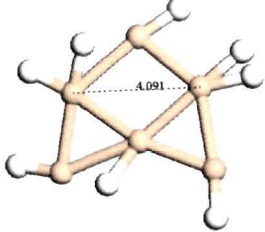
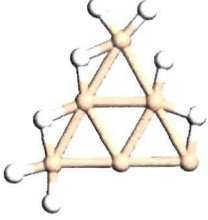
Continued on next page

Table A.1 – continued from previous page

Cluster	Structures	E(LS)	E(HS)	Relative Energy
Au ₆ H ₆			-110390.8421	
	5a(HS)			
			-110391.4611	
	6a(LS)			
Au ₆ H ₇			-110391.4558	
	6a(HS)			
			-110392.0862	
	7a(LS)			

Continued on next page

Table A.1 – continued from previous page

Cluster	Structures	E(LS)	E(HS)	Relative Energy	
Au ₆ H ₈			-110390.8421		
	7a(HS)				
		8a(LS)	-110392.7136		0.00
		8a(HS)		-110392.6650	
		8b	-110392.6657		1.30
	8c	-110392.7066		0.19	

Continued on next page

Table A.1 – continued from previous page

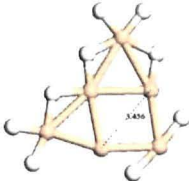
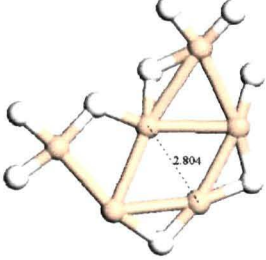
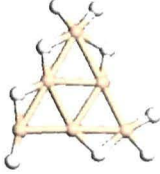
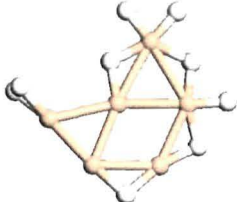
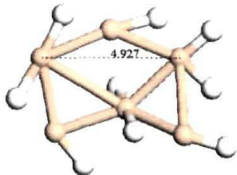
Cluster	Structures	E(LS)	E(HS)	Relative Energy
Au ₆ H ₉	 9a(LS)	-110393.294		0.00
	 9a(HS)		-110393.2181	
	 9b	-110393.2905		0.09
	 9c	-110393.2756		0.50
	 9d	-110393.2722		0.59
Continued on next page				

Table A.1 – continued from previous page

Cluster	Structures	E(LS)	E(HS)	Relative Energy
Au ₆ H ₁₀	 10a(LS)	-110393.8986		0.00
	 10a(HS)		-110393.8601	
	 10b	-110393.8587		1.06
	 11a(LS)	-110394.4746		0.00
Au ₆ H ₁₁	 11a(HS)		-110394.4156	

Continued on next page

Table A.1 – continued from previous page

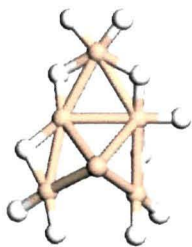
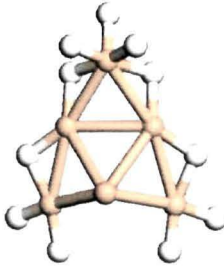
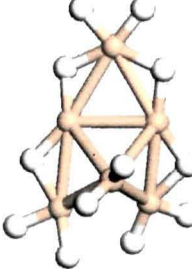
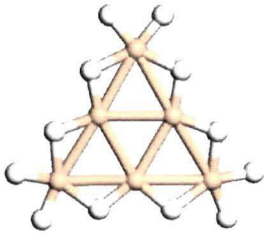
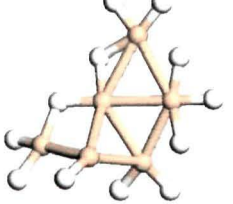
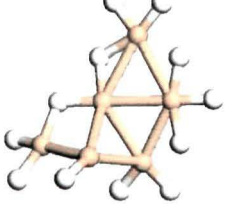
Cluster	Structures	E(LS)	E(HS)	Relative Energy
Au ₆ H ₁₂	 11b	-110394.4579		0.46
	 11b	-110394.4389		0.97
	 11b	-110395.0850		0.00
	 12a(LS)		-110395.0625	
	 12a(HS)		-110395.0787	0.17
	 12b			

Table A.2: Fukui functions of the Au_6H_n ($n=1-12$) clusters

Au_6			Au_6H		
Atom	f^-/f^+	f^+/f^-	Atom	f^-/f^+	f^+/f^-
Au (1)	0.84	1.19	Au (1)	0.97	1.03
Au(2)	1.38	0.72	Au(2)	0.85	1.18
Au(3)	1.38	0.72	Au(3)	1.25	0.80
Au(4)	0.84	1.19	Au(4)	0.97	1.03
Au(5)	1.38	0.72	Au(5)	1.26	0.80
Au(6)	0.84	1.19	Au(6)	0.93	1.08

Au_6H_2			Au_6H_3		
Atom	f^-/f^+	f^+/f^-	Atom	f^-/f^+	f^+/f^-
Au(2)	0.84	1.19	Au(2)	0.98	1.02
Au(2)	1.25	0.80	Au(2)	1.01	0.99
Au(3)	1.25	0.80	Au(3)	1.01	0.99
Au(4)	0.84	1.19	Au(4)	0.98	1.02
Au(5)	1.32	0.76	Au(5)	1.00	1.00
Au(6)	0.84	1.19	Au(6)	0.98	1.02

Au_6H_4			Au_6H_5		
Atom	f^-/f^+	f^+/f^-	Atom	f^-/f^+	f^+/f^-
Au(1)	1.00	1.00	Au(1)	1.02	0.98
Au(2)	1.03	0.97	Au(2)	1.28	0.78
Au(3)	1.00	1.00	Au(3)	0.91	1.10
Au(4)	1.00	1.00	Au(4)	1.02	0.98
Au(5)	1.00	1.00	Au(5)	0.92	1.09
Au(6)	0.99	1.01	Au(6)	0.90	1.11

Au ₆ H ₆		
Atom	f ⁻ /f ⁺	f ⁺ /f ⁻
Au(1)	0.99	1.01
Au(2)	1.08	0.93
Au(3)	1.38	0.73
Au(4)	0.92	1.09
Au(5)	0.90	1.11
Au(6)	0.84	1.19

Au ₆ H ₇		
Atom	f ⁻ /f ⁺	f ⁺ /f ⁻
Au(1)	1.03	0.97
Au(2)	1.24	0.81
Au(3)	1.02	0.98
Au(4)	0.97	1.03
Au(5)	1.04	0.96
Au(6)	0.97	1.03

Au ₆ H ₈		
Atom	f ⁻ /f ⁺	f ⁺ /f ⁻
Au(1)	0.90	1.11
Au(2)	1.40	0.72
Au(3)	1.88	0.53
Au(4)	0.89	1.12
Au(5)	0.67	1.48
Au(6)	1.02	0.98

Au ₆ H ₉		
Atom	f ⁻ /f ⁺	f ⁺ /f ⁻
Au(1)	1.05	0.96
Au(2)	0.98	1.03
Au(3)	0.89	1.12
Au(4)	1.03	0.97
Au(5)	1.11	0.90
Au(6)	0.99	1.01

Au ₆ H ₁₀		
Atom	f ⁻ /f ⁺	f ⁺ /f ⁻
Au (1)	1.44	0.70
Au(2)	1.42	0.71
Au(3)	1.39	0.72
Au(4)	0.67	1.49
Au(5)	1.28	0.78
Au(6)	0.67	1.49

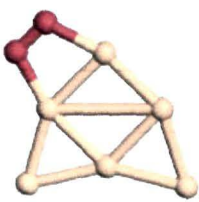
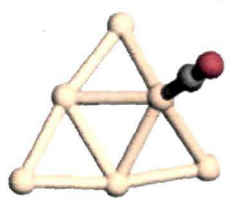
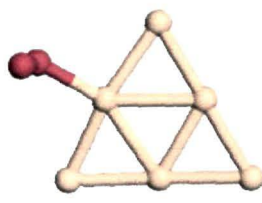
Au ₆ H ₁₁		
Atom	f ⁻ /f ⁺	f ⁺ /f ⁻
Au (1)	0.95	1.05
Au(2)	0.80	1.25
Au(3)	1.39	0.72
Au(4)	1.12	0.89
Au(5)	0.95	1.05
Au(6)	0.94	1.07

Au ₆ H ₁₂		
Atom	f ⁻ /f ⁺	f ⁺ /f ⁻
Au(1)	1.14	0.88
Au(2)	1.86	0.54
Au(3)	0.64	1.57
Au(4)	1.41	0.71
Au(5)	0.55	1.82
Au(6)	1.74	0.58

Appendix B

Structures of O₂ and CO adsorption on Au₆ⁿ (n=0,-1 and +1) Clusters

Table B.1: Optimized structures of O₂ and CO adsorbed on the less preferred lateral sites of neutral, anionic and cationic Au₆ clusters.

Cluster	Structure
Au ₆ ⁰ - O ₂	
Au ₆ ⁰ - CO	
Au ₆ ⁻ - O ₂	

Continued on next page

Table B.1 – continued from previous page

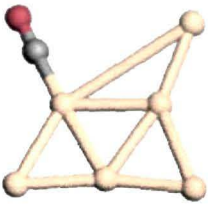
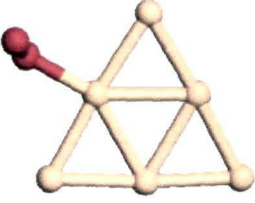
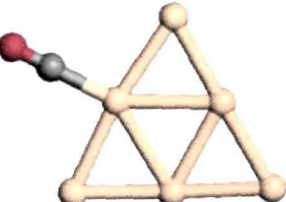
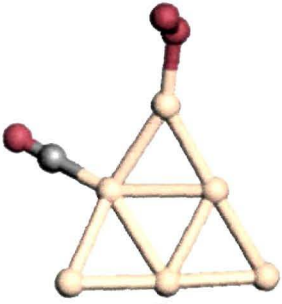
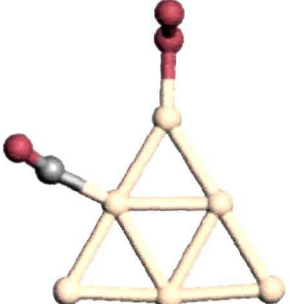
Cluster	Structure
$\text{Au}_6^- - \text{CO}$	
$\text{Au}_6^+ - \text{O}_2$	
$\text{Au}_6^+ - \text{CO}$	

Table B.2: Optimized structures of co-adsorption configurations with O_2 at the apex site and CO at the nearest lateral site of neutral, anionic and cationic Au_6 clusters.

Cluster	Structure
Au_6^0	
Au_6^-	

Continued on next page

Table B.2 – continued from previous page

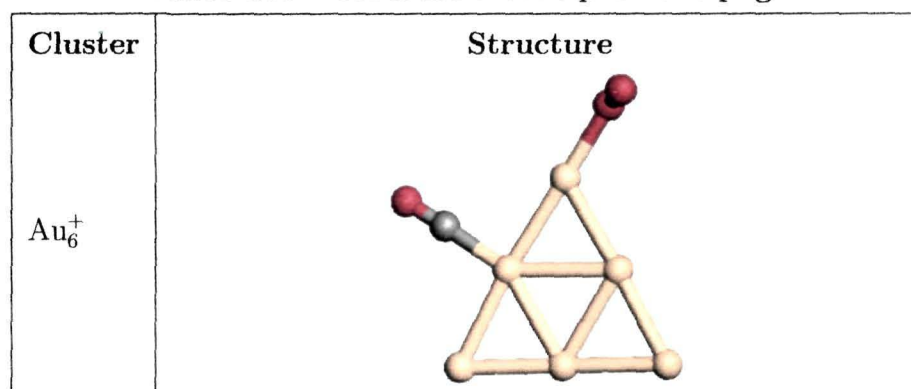


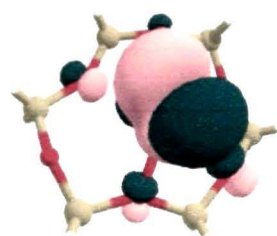
Table B.3: Total energies (eV) of both low spin and high spin states of neutral and charged Au_6 clusters.

Cluster	E(LS)	E(HS)
Au_6^0	-110392.85	-110392.79
Au_6^-	-110392.93	-110392.87
Au_6^+	-110392.56	-110392.48

Appendix C

Frontier Molecular Orbitals for Different Au^n/FAU ($n=0, +1$ and $+3$) systems

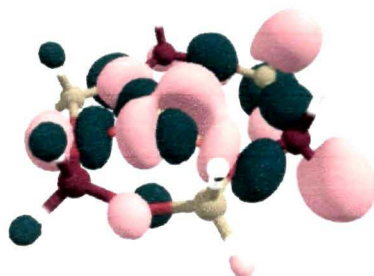
Figure C.1: Interaction between Au and the zeolite O atoms in Au^n/FAU ($n=0, +1$ and $+3$).



(a) Au^0/FAU , HOMO-2



(b) $\text{Au}^{-1}/\text{FAU}$, HOMO-1



(c) $\text{Au}^{3+}/\text{FAU}$, HOMO-2

Figure C.2: Interaction between CO and faujasite supported Au centre in the CO adsorbed complexes of Auⁿ/FAU (n=0, +1 and +3).

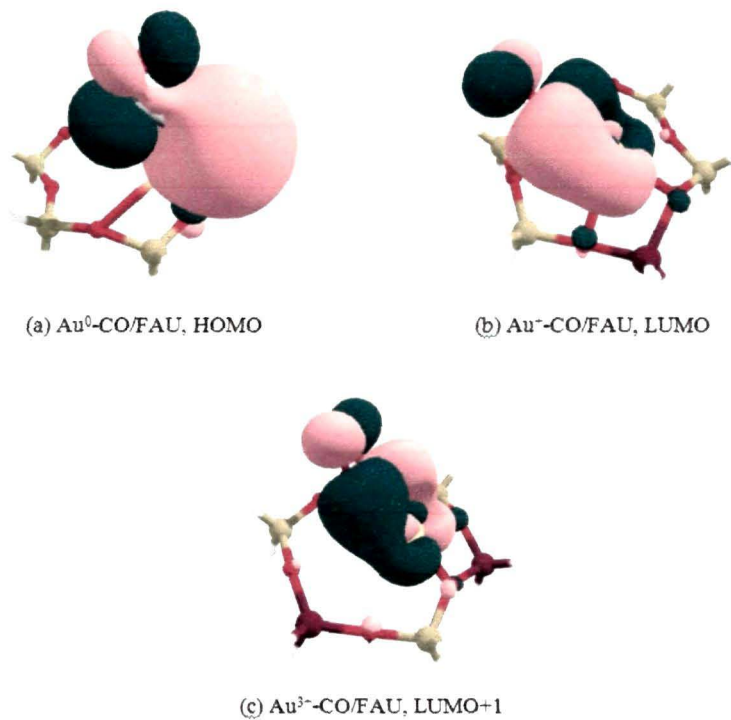


Figure C.3: Interaction between O₂ and faujasite supported Au centre in the top mode O₂ adsorbed complexes of Auⁿ/FAU (n=0, +1 and +3).

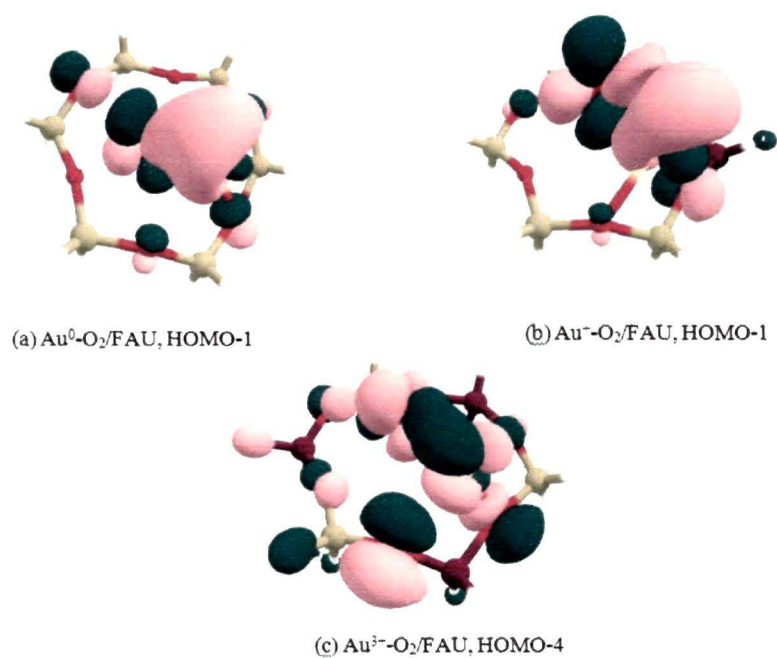


Figure C.4: Interaction between O₂ and faujasite supported Au centre in the bridge mode O₂ adsorbed complexes of Auⁿ/FAU (n=0, +1 and +3).

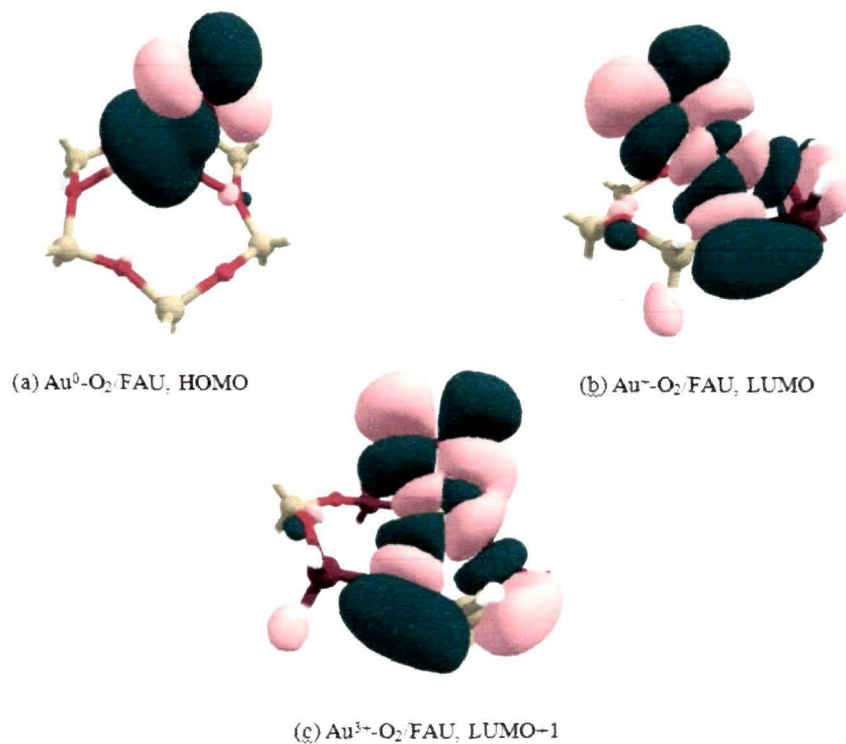


Figure C.5: Interaction between O₂ and faujasite supported Au centre in the dissociative mode O₂ adsorbed complexes of Auⁿ/FAU (n=0, +1 and +3).

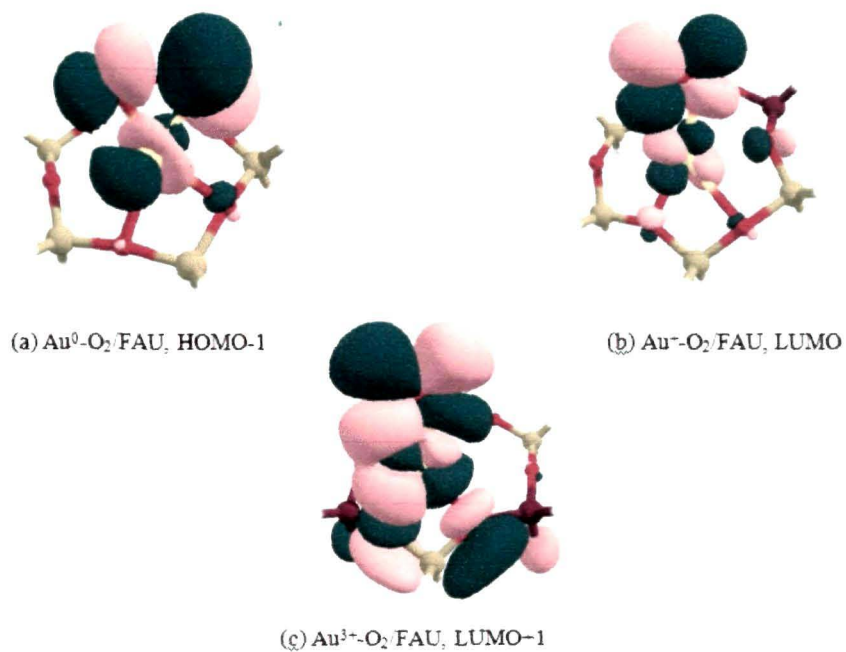


Figure C.6: Interaction between H₂O and faujasite supported Au centre in the H₂O adsorbed complexes of Auⁿ/FAU (n=0, +1 and +3).

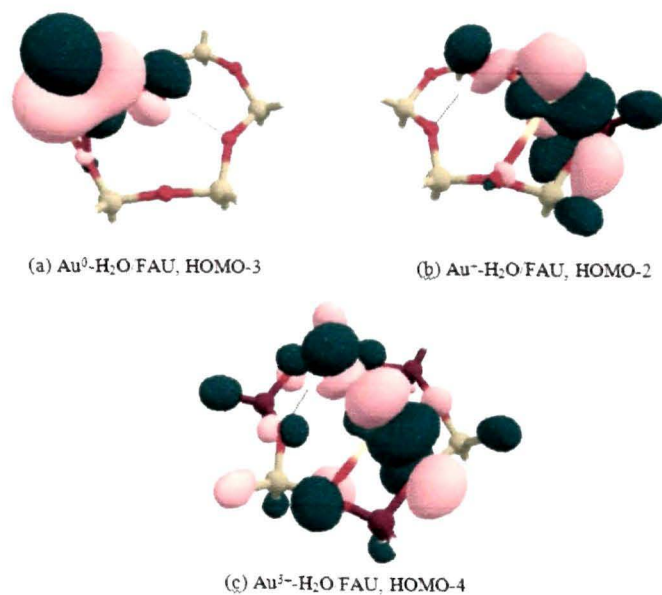


Figure C.7: Interaction between CO and faujasite supported Au centre in the CO adsorbed complexes of Auⁿ/FAU (n=0, +1 and +3) in the presence of pre-adsorbed H₂O.

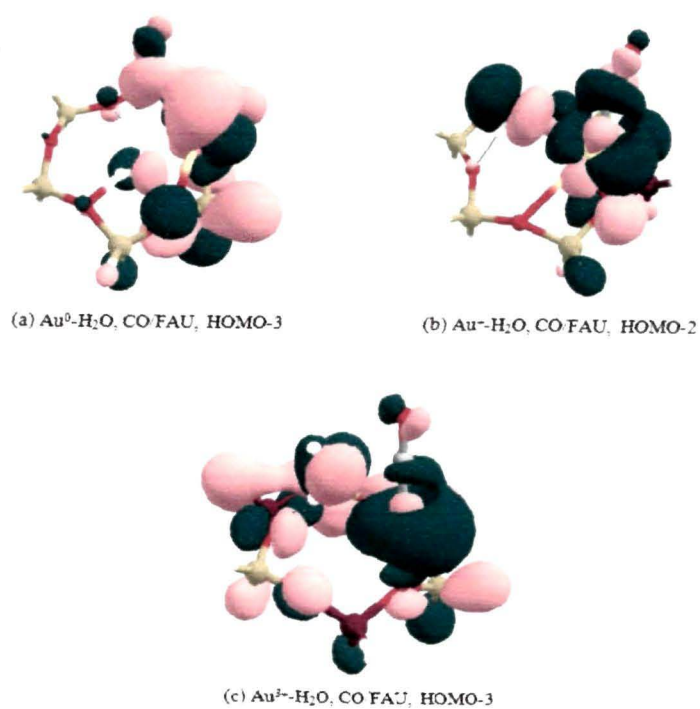


Figure C.8: Interaction between O_2 , H_2O and faujasite supported Au centre in top mode O_2 adsorbed complexes of Au^n/FAU ($n=0, +1$ and $+3$) in the presence of pre-adsorbed H_2O .

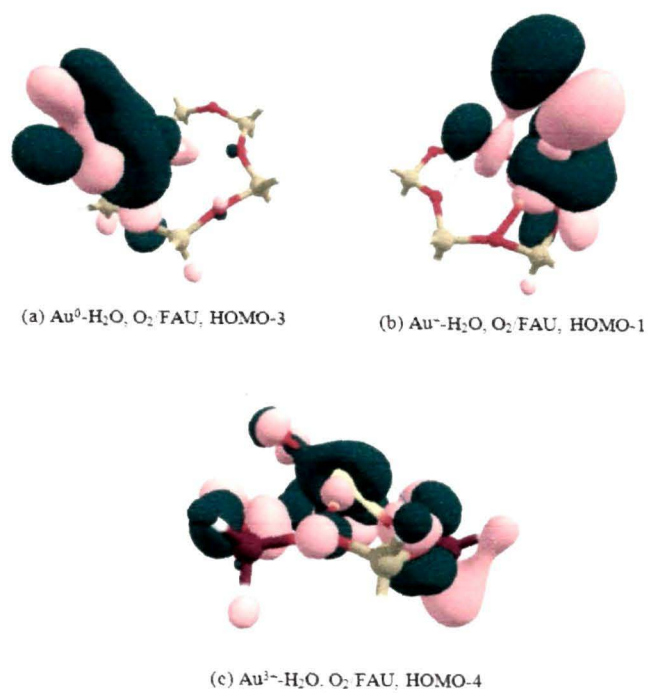


Figure C.9: Interaction between O_2 , H_2O and faujasite supported Au centre in bridge mode O_2 adsorbed complexes of Au^n/FAU ($n=0, +1$ and $+3$) in the presence of pre-adsorbed H_2O .

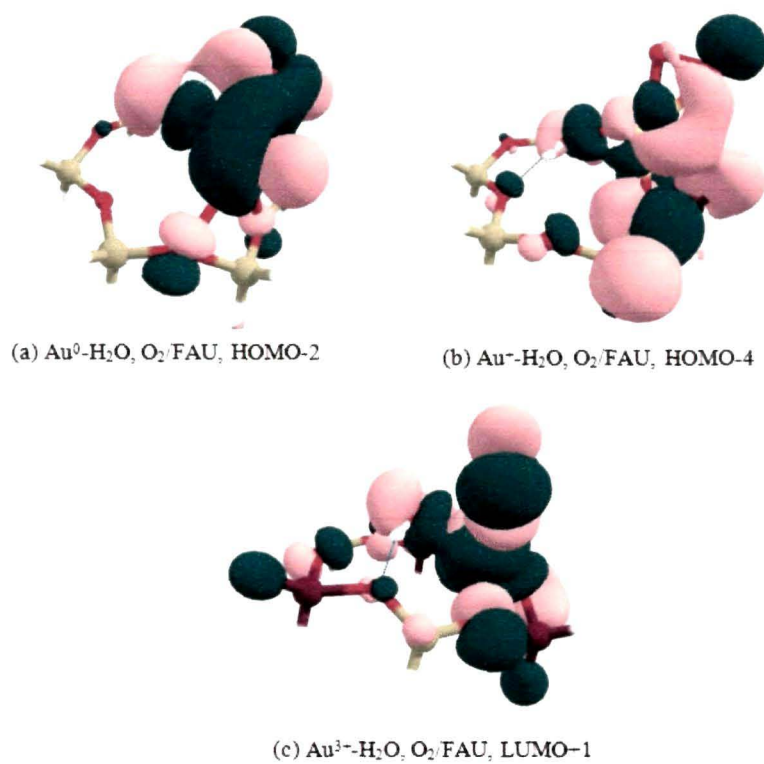
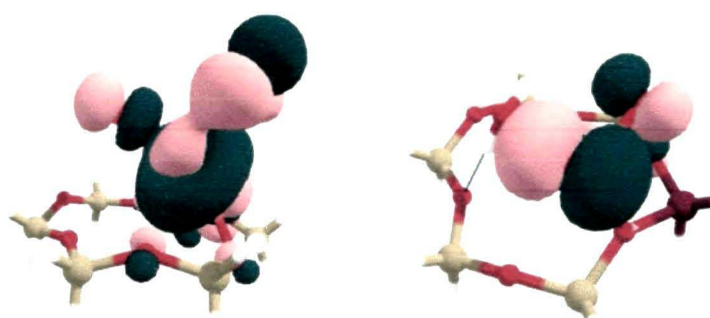
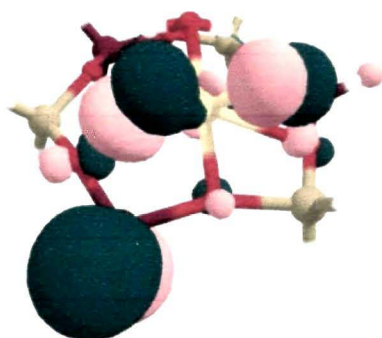


Figure C.10: Interaction between O_2 , H_2O and faujasite supported Au centre in Au^0/FAU and dissociation of O_2 due to occupancy of antibonding orbital in Au^+/FAU and Au^{3+}/FAU in the presence of pre-adsorbed H_2O .



(a) $Au^0-H_2O, O_2/FAU, HOMO-3$

(b) $Au^+-H_2O, O_2/FAU, HOMO-1$



(c) $Au^{3+}-H_2O, O_2/FAU, HOMO-2$

Appendix D

Structures of Different Species for CO Oxidation pathways

Optimized structures of various intermediates, transition states, products obtained during CO oxidation on faujasite supported neutral and cationic Au monomer

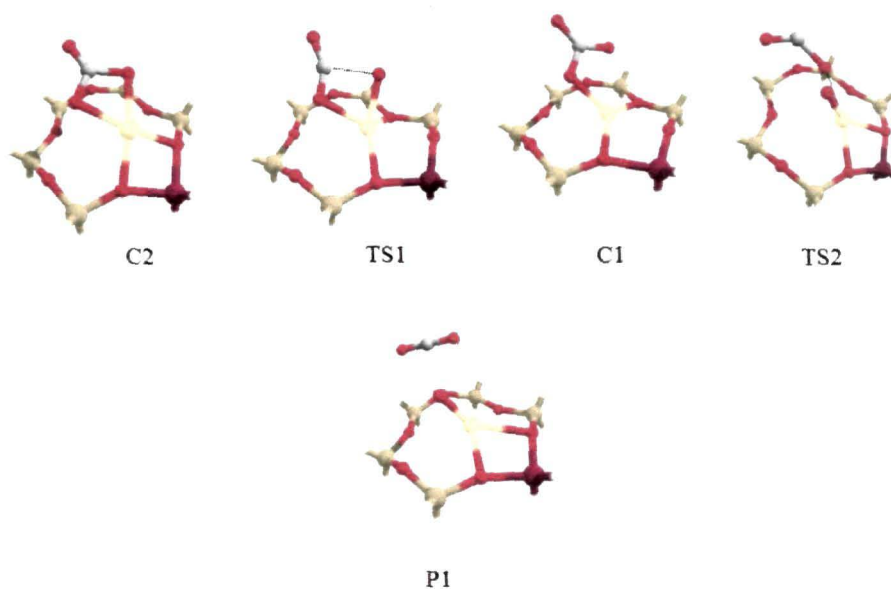
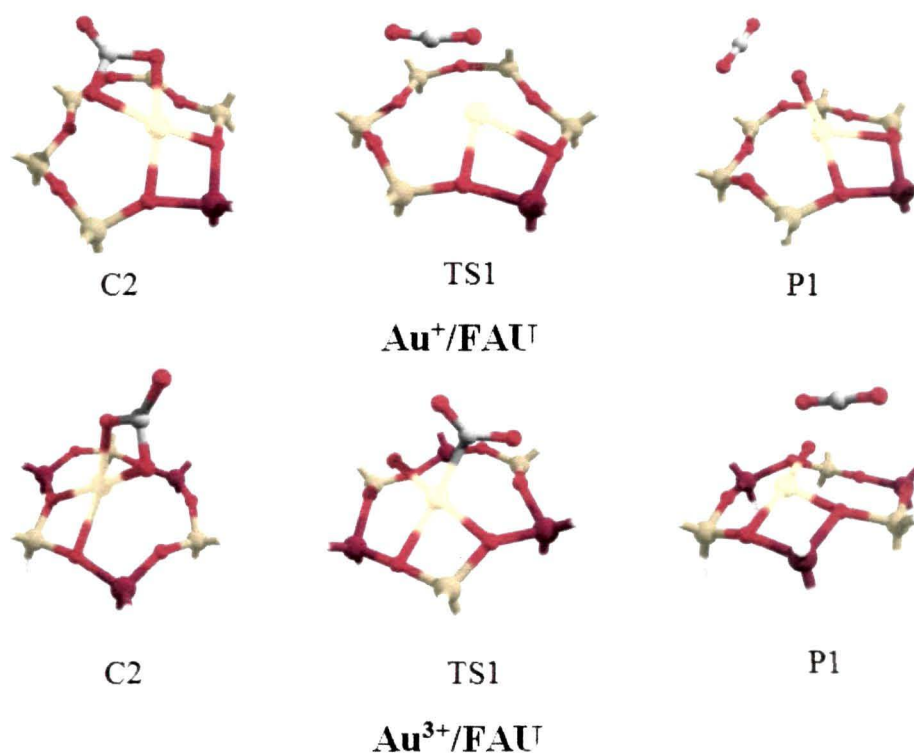


Figure D.1: Structures of different species involved in the Eley-Rideal (η^1 -carbonate) pathway with dissociated O₂ on Au⁺/FAU.



(b) Structures of the different species involved in the reaction pathway on the cationic systems.

Figure D.2: Energy profile diagram (a) and the structures of different species (b) involved in the Eley-Rideal (η^2 -carbonate) pathway with dissociated O_2 on Au^+/FAU and $\text{Au}^{3+}/\text{FAU}$.

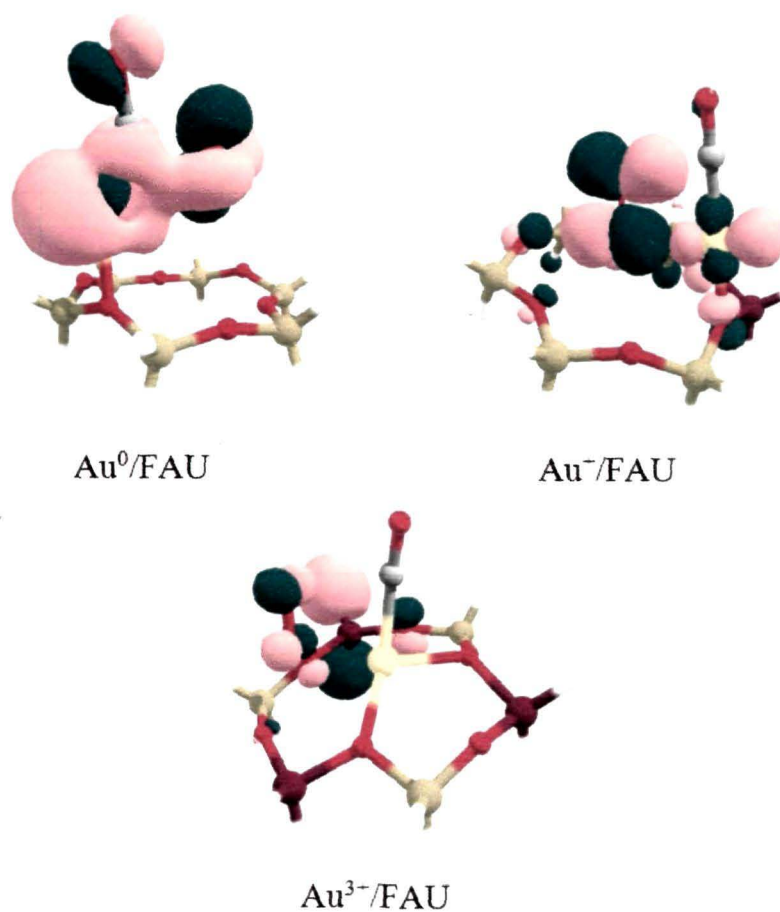
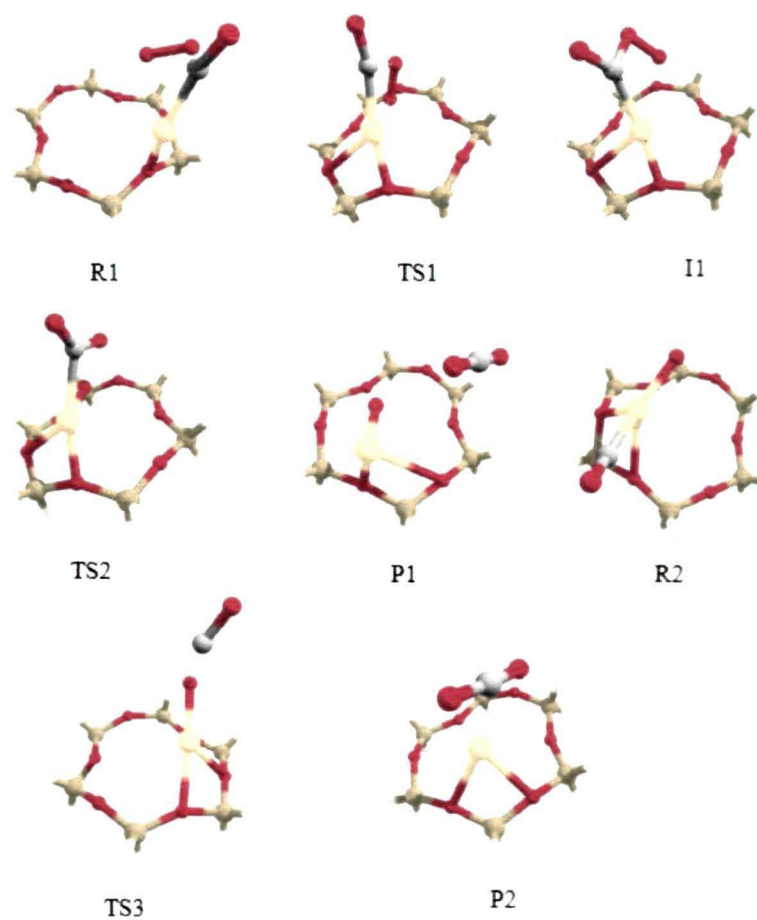


Figure D.3: Frontier molecular orbitals (HOMO-1) of the R1 species in Au^n/FAU ($n=0, +1$ and $+3$). Overlap of p orbitals centred on O_2 and CO account for the weak interaction in the neutral counterpart while absence of such overlap ensue no interaction between O_2 and CO in the cationic systems.



Au⁰/FAU

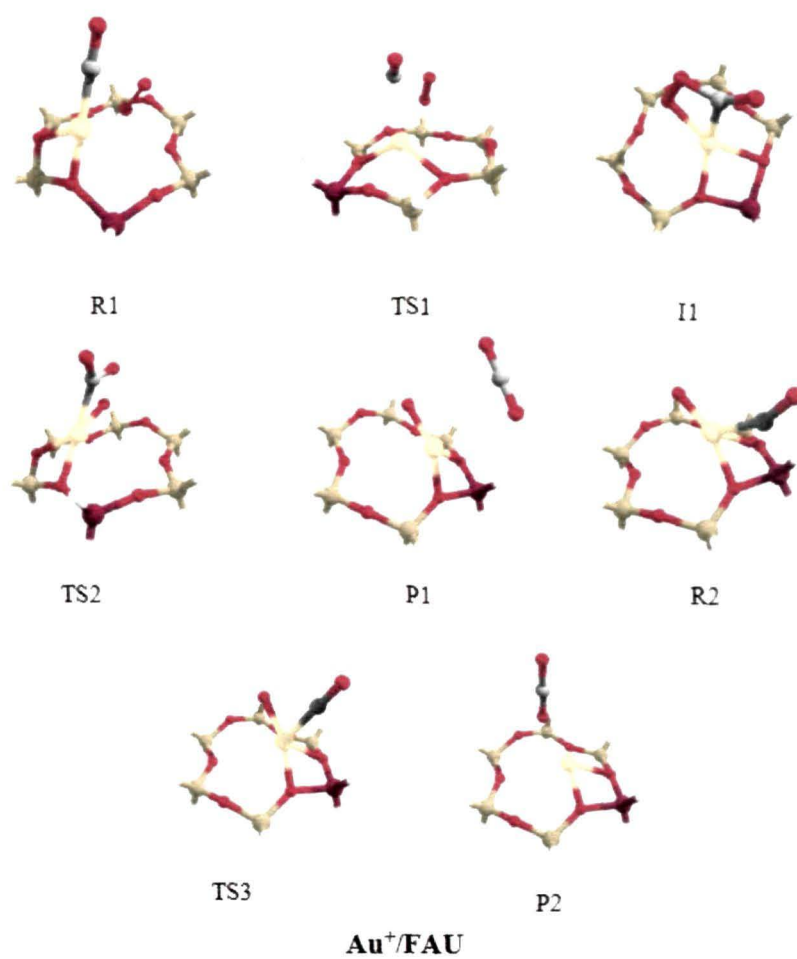


Figure D.4: Structures of the different species involved in the Eley-Rideal pathway with gas phase O₂ on Au⁰/FAU and Au⁺/FAU.

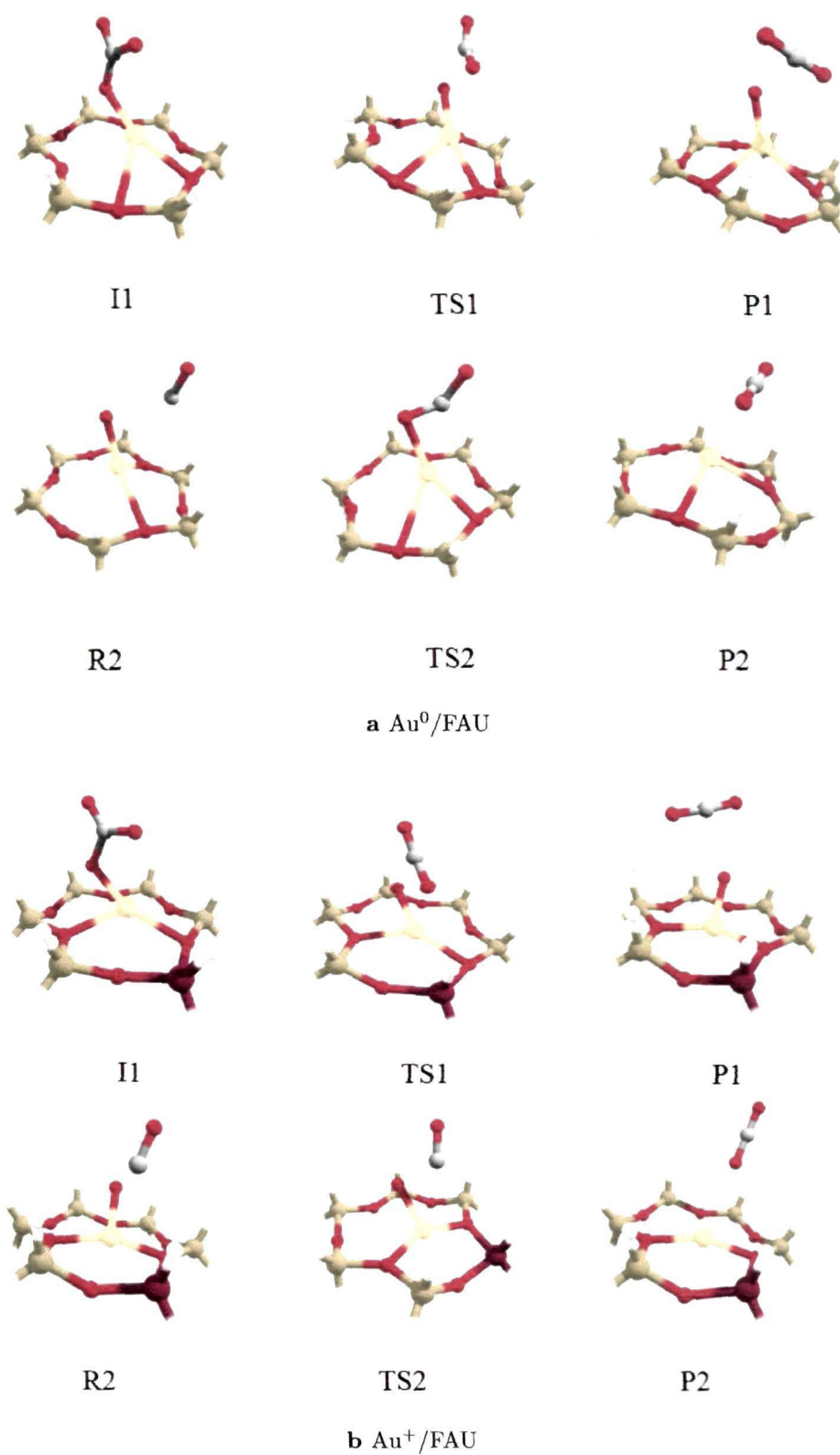


Figure D.5: Structures of the different species involved in the Eley-Rideal pathway with gas phase CO on Au⁰/FAU and Au⁺/FAU.

Table D.2: Computed geometrical parameters (\AA), barriers values (eV) and the imaginary frequency (cm^{-1}) for transition states in the Eley-Rideal (η^2 -carbonate) pathway with dissociated O_2 on Au^+/FAU and $\text{Au}^{3+}/\text{FAU}$.

Au^+/FAU	Au- O_2	Au-O	O-C	O-C (CO)	O-C-O	ΔE	-ve freq
C2	2.08	2.03,2.08	1.33, 1.38	1.22			
TS1	2.35	2.22	1.21,1.83	1.18	178.8°	3.53	-255.62
P1	2.33	1.91	1.19	1.19	176.2°		

$\text{Au}^{3+}/\text{FAU}$	Au- O_2	Au-O	O-C	O-C (CO)	O-C-O	ΔE	-ve freq
C2	2.34	2.00, 2.09	1.38, 1.37	1.21			
TS1	2.14	2.01	1.31	1.22	135.5°	2.86	-434.56
P1	2.11	2.01	1.20	1.18	178.5°		

Table D.3: Computed geometrical parameters (\AA), barriers values (eV) and the imaginary frequency (cm^{-1}) for transition states in the Eley-Rideal pathway with gas phase O_2 on Au^0/FAU and Au^+/FAU .

Au^0/FAU	Au-O_z	Au-C	Au-O	$\text{O...O (O}_2)$	O-C	O-C (CO)	O-C-O	ΔE	-ve freq
R1	2.35	1.97	2.65	1.38	1.74	1.19			
TS1	2.10	1.96	2.36	1.39	1.93	1.18		0.38	-84.18
I1	2.10	2.00	2.68	1.37	1.55	1.21			
TS2	2.17	2.07	2.19	1.83	1.30	1.23	138.20°	1.60	-1166.39
P1	2.89	-	1.93	-	1.19	1.19	178.62°		
R2	2.81	1.97	2.00	-	-	1.16	-		
TS3	2.38	-	1.97	-	2.03	1.16	129.33°	0.57	-286.41
P2	2.80	-	-	-	1.19	1.18	176.38°		

$\text{Au}^+/\bar{\text{FAU}}$	Au-O_z	Au-C	Au-O	$\text{O...O (O}_2)$	O-C	O-C (CO)	O-C-O	ΔE	-ve freq
R1	2.02	1.92	2.67	1.27	2.74	1.16			
TS1	2.38	2.60	2.29	1.37	1.71	1.17		2.06	-618.26
I1	2.28	2.04	2.02	1.60	1.34	1.21			
TS2	2.07	2.07	2.12	1.64	1.34	1.21	128.66°	0.76	-242.92
P1	2.06	-	1.88	-	1.19	1.20	178.44°		
R2	2.13	2.03	1.87	-	-	1.16	-		
TS3	2.10	1.94	1.97	-	2.51	1.15	131.07°	0.30	-223.87
P2	2.07	-	-	-	1.21	1.17	177.37°		

Table D.4: Computed geometrical parameters (Å), barriers values (eV) and the imaginary frequency (cm^{-1}) for transition states in the Eley-Rideal pathway with gas phase CO on Au^0/FAU and Au^+/FAU .

Au^0/FAU	Au- O_z	Au-O	O-C	O-C (CO)	O-C-O	ΔE	-ve freq
I1	2.36	2.06	1.33,1.29	1.28			
TS1	2.37	2.02	1.86,1.22	1.20	154.39°	0.91	-527.94
P1	2.72	1.98	1.19	1.19	177.86°		
R2	2.75	1.98	2.47	1.16			
TS2	2.40	2.18	1.29	1.21	138.42°	1.27	-304.22
P2	2.78	-	1.20	1.19	179.0°		

Au^+/FAU	Au- O_z	Au-O	O-C	O-C (CO)	O-C-O	ΔE	-ve freq
I1	2.33	2.03	1.37, 1.30	1.25			
TS1	2.20	2.00	2.21, 1.18	1.21	172.59°	1.56	-159.56
P1	1.98	1.94	1.19	1.19	174.13°		
R2	1.99	1.95	2.58	1.16			
TS2	2.03	2.00	1.87	1.18	114.84°	0.61	-526.63
P2	2.00	-	1.18	1.19	179.43°		